POLARIZED ON HIGGS?

MEASUREMENT OF THE HIGGS COUPLINGS TO POLARIZED VECTOR BOSONS

LUCREZIA STELLA BRUNI

POLARIZED ON HIGGS?

LUCREZIA STELLA BRUNI

Polarized on Higgs?

Measurement of the Higgs couplings to polarized vector bosons

Lucrezia Stella Bruni

Polarized on Higgs?

Measurement of the Higgs couplings to polarized vector bosons

DISSERTATION

to obtain

the degree of doctor at the University of Twente,

on the authority of the rector magnificus

prof. dr. T.T.M. Palstra

on account of the decision of the Doctorate Board,

to be publicly defended

on Wednesday 27th February 2019 at 16.45

by

Lucrezia Stella Bruni

born on August 23, 1989
in Rome, Italy

This dissertation has been approved by:

Supervisor: prof. dr. ing. B. van Eijk

Co-supervisor: dr. P. Ferrari

Per mamma e papà

La bimba osserva dal vetro
il naso incollato
le mani appoggiate

enorme la macchina dentro
appena si muove e scintilla
accelera nella sua pancia
i suoni dell'infinito
rincorre minimi abissi
proietta invisibili corpi

la bimba li conta additando
intuisce i percorsi del nulla
infila la sua fantasia
e canta una filastrocca

la macchina è docile e attenta
ascolta la grazia di voce
la assimila agli altri comandi

poi dona una coda di numeri
che sembrano omerici versi
atteso e affettuoso responso
regalo per il suo stupore.

Antonio Bruni

Contents

Preface

The theoretical framework of particle physics, the Standard Model, has revealed itself successful in explaining most of the observed particle physics phenomena, the latest being the recently discovered Higgs boson. Nevertheless, it does not include some observations such as, for example, neutrino oscillations and the presence of dark matter and dark energy in the universe. The large and unique dataset collected at the Large Hadron Collider (LHC) may contain information that will shed light on these and other phenomena, thus constituting an invaluable source of information.

Several strategies can be followed to search for beyond Standard Model (BSM) physics. For example, one could look for new resonances predicted by theoretical models or generically hunt for excesses in the data collected at the LHC. A different approach is to use these data to study the properties of known particles and look for deviations from their SM values. This thesis follows this last path and focuses on the Higgs boson. Some of its properties (such as mass, spin and CP) have been analyzed in detail with the dataset collected during 2010-2012 by the ATLAS and CMS collaborations. However, other attributes have not been investigated yet.

One of these properties, the coupling of the Higgs boson to polarized vector bosons, is discussed in this thesis. This is studied in the vector boson fusion production mechanism (VBF) and in the $H \to WW^* \to \ell\nu\ell\nu$ decay, in order to have two HWW vertices. The Higgs is responsible for the unitarization of the cross-section for longitudinal vector boson scattering ($W_L W_L \to W_L W_L$). An incomplete unitarization could re-emerge from possible deviations from the SM values of the HWW coupling, hinting to new physics. A simple theoretical framework is adopted to represent such deviations. This approach has the advantage of being model independent, even if not gauge nor Lorentz invariant. In addition, results are mapped into more generic frameworks such as pseudo-observables and effective field theories, that intrinsically obey these

symmetries.

The data analyzed have been collected by the ATLAS experiment during 2015 and 2016, corresponding to 36.1 fb^{-1} of integrated luminosity. With this dataset, also the gluon-gluon fusion (ggF) and vector boson fusion (VBF) production cross-section measurements have been performed in the $H \to WW^* \to \ell\nu\ell\nu$ channel.

The thesis is organized as follows:

Chapter 1   contains two parts. After a brief theoretical explanation of the Standard Model, the Higgs boson production mechanisms at the LHC, decay modes and properties are discussed.

Chapter 2   outlines the motivations for the analysis of Higgs boson couplings to polarized vector bosons, explaining the simple model adopted and its translation into more generic frameworks. In this context, I performed generator-level studies to identify physical quantities suitable to disentangle different polarization states.

Chapter 3   gives an overview of the main components of the ATLAS detector.

Chapter 4   describes the test beam campaigns performed to investigate the performance of prototype silicon strip modules for the upgrade of the ATLAS tracking system, ITk (Inner Tracker). I have been actively involved in the test beam set up and in data acquisition. Furthermore, I have been in charge of track reconstruction and the analysis of the prototype performance. The tests were successful and their results were published as part of ATLAS Inner Tracker Strip Detector Technical Design Report [1].

Chapter 5   starts with an explanation of the phenomenology behind a proton-proton collision at LHC and its implementation in Monte Carlo (MC) generators. Next, focus is on the description of the dedicated Monte Carlo signal samples that I produced with an event generator for the polarized couplings studies.

Chapter 6   outlines the reconstruction algorithms and techniques employed to identify final state objects relevant for the analysis discussed in this thesis.

Chapter 7 is structured in three main components. First, a complete description of the $H \to WW^* \to \ell\nu\ell\nu$ event topology and of the main background processes is given. Then, VBF event selection is discussed, followed by the evaluation of systematic uncertainties. I performed trigger studies for both VBF and ggF channels. Furthermore, I worked on signal region optimization, where I employed multivariate techniques to enhance the sensitivity to the polarized signals. I studied the discriminating variables and I verified their modeling in dedicated control regions. Finally, I evaluated theoretical uncertainties for all processes involved.

Chapter 8 begins with a description of the statistical methods employed in the analyses. The outcomes in terms of cross-section and signal strength, published as an ATLAS paper [2], are presented for the VBF and ggF channels. Finally, in the second part of this chapter, the measurement of polarized couplings is discussed. I used the analytic Lagrangian method to obtain a continuous description for the physical observables in the parameter space studied. Then, I performed likelihood fits to the data to estimate the significance on these couplings. The results will be published by the ATLAS collaboration.

The Higgs boson

The undisputed protagonist of this thesis is the Higgs boson. This chapter is organized in two parts: in the first one, the formulation of the theoretical framework of particle physics, the Standard Model (SM) is outlined, with special attention to the Higgs Mechanism of electroweak symmetry breaking (EWSB). More comprehensive descriptions are given in References [3–6]. The second part is meant to describe the production mechanisms at LHC and decay modes of the Higgs boson and the properties of this recently discovered particle.

1.1   Fundamental particles

The discovery of the Higgs boson in 2012, by the ATLAS and CMS collaborations at the center-of-mass energies of 7 and 8 TeV [7–9], made a breakthrough for particle physics, confirming the efficacy of the Standard Model (SM) [10–13]. This model is the theoretical framework that describes the interactions between fundamental particles and their properties. It is one of the most successful theories in physics, which has resisted decades of experimental scrutiny.

Matter and anti-matter particles described by the SM are called *fermions*. These particles have an half integer spin and their interactions happen through exchange of force carrying particles, called the *gauge bosons*, that have integer spin. The SM successfully combines three out of four interactions known in nature: the weak, the strong and the electromagnetic interactions, leaving out only gravitation, that, at subatomic scales, is negligible.

The mediator of the electromagnetic interaction is the photon, γ, a neutral particle which couples to particles that carry electric charge. The charged W bosons, W^+ and W^-, and the neutral Z boson are the mediators of the weak

Interaction	Gauge boson	Mass Mass [GeV]	EM charge [e]	Weak Charge [Isospin]	Strong Charge [Color]
Electromagnetic	Photon (γ)	0	0	no	no
Weak	W^+ , W^-	80.4 GeV	±1	yes	no
	Z^0	91.2 GeV	0	yes	no
Strong	Eight gluons (g)	0	0	no	r/g/b

TABLE 1.1: Table listing the gauge bosons of the SM. Mass values from [14].

interactions and they interact with particles through the third component of the weak isospin. The W bosons are the mediators of the charged current while the Z boson is the mediator of the neutral current. The range of the weak interaction is very short, because of the large mass of the gauge bosons ($m_W \approx$ 80.4 GeV, $m_Z \approx$ 91.2 GeV).

The last interaction, the strong one, is instead mediated by eight different massless gluons (g). Gluons are electrically neutral and carry color charge: red (r), green (g) and blue (b). As a result, they can couple to each other and this fact leads, even if they are massless, to a short range of the strong interaction.

All gauge bosons and their properties are listed in Table 1.1.

The fermions are divided into two families, the leptons and quarks. Leptons do not carry color charge and therefore can interact only through the electromagnetic and weak forces. The electron, the muon and the tau (e, μ, τ) have electric charge -1, while the neutrinos (ν_e, ν_μ, ν_τ) do not carry any charge and therefore can interact only weakly. In the SM neutrinos are treated as massless particles. The discovery of their oscillations [15] has given proof of their tiny mass.

Quarks can have charge of $+2/3$, $-1/3$ and interact via all three forces. The hadrons are colorless, being color singlet states. There are two kinds of hadrons: barions, that consist of quarks triplets ($qqq - \bar{q}\bar{q}\bar{q}$), and mesons that are formed by quarks doublets ($q\bar{q}$). Combined states with four and five quarks (anti-quarks), referred to as tetra-quarks and penta-quarks, have recently been observed [16–18].

All fermions have an anti-particle, that has the exact same mass but with conjugated charge and parity. There are three generations of fermions. The first one is responsible for visible and stable matter in the Universe and it is formed by the electron, the electron neutrino (e, ν_e), and the quarks up and

Generation	Particle	Electric charge [Q/e]	Color [r,g,b]	Mass [MeV]
1st	e	-1	No	0.511
	ν_e	0	No	$<2 \cdot 10^{-6}$
	u	2/3	Yes	2.2
	d	-1/3	Yes	4.7
2nd	μ	-1	No	105.6
	ν_μ	0	No	< 0.19
	c	2/3	Yes	$1.275 \cdot 10^3$
	s	-1/3	Yes	95
3rd	τ	-1	No	1776.86
	ν_τ	0	No	< 18.2
	t	2/3	Yes	$173.0 \cdot 10^3$
	c	-1/3	Yes	$4.18 \cdot 10^3$

TABLE 1.2: Table summarizing the main characteristics of fermions of the Standard Model. Mass values from [14].

down (u, d). The proton is formed by two up-quarks and a down-quark (**uud**), while the neutron by two down-quarks and an up-quark (**ddu**). The fermions of the 2nd and 3rd generation (leptons μ, τ, ν_μ and ν_τ and quarks c, s, b and t) can decay via the weak force into fermions of the lower generations. A scheme with fermion properties is given in Table 1.2.

1.2 The Standard Model

The weak and electromagnetic interactions between leptons and quarks are described by the electroweak theory by Glashow-Weinberg-Salam [10–12], that is a Yang–Mills theory [19] based on the symmetry group $SU(2)_L \times U(1)_Y$. The QCD gauge theory that describes the strong interactions between the colored quarks is based on the symmetry group $SU(3)_C$. The mathematical framework of the Standard Model is given by the combinations of these three interactions, hence the Standard Model is a quantum field theory based on the gauge symmetry $SU(2)_L \times U(1)_Y \times SU(3)_C$. The Standard Model Lagrangian $\mathcal{L}_{SM}$ can be split into four different components:

$$\mathcal{L}_{SM} = \mathcal{L}_G + \mathcal{L}_F + \mathcal{L}_{Higgs} + \mathcal{L}_{Yukawa}, \tag{1.1}$$

$\mathcal{L}_G$ encloses the dynamics of the gauge bosons, while $\mathcal{L}_F$ describes the behavior of the matter fermions as foreseen by the unbroken gauge symmetry. The

latter two, $\mathcal{L}_{Higgs}$ and $\mathcal{L}_{Yukawa}$, involve the Higgs field.

Fermions are divided into the three generations of left–handed and right–handed chiral quarks and leptons and they present different representations of the gauge group. Hence, a distinction between left- and right-handed fields is necessary. The left- and right-handed chiral fields are defined as follows:

$$\psi_L = \frac{1-\gamma_5}{2}\psi\,, \quad \psi_R = \frac{1+\gamma_5}{2}\psi\,. \tag{1.2}$$

The right-handed fermion fields of each lepton and quark family are grouped into singlets, while the left-handed into $SU(2)$ doublets[1]:

$$I_f^{3L,3R} = \pm\frac{1}{2},0\ :\ \begin{array}{l} L_1 = \left(\begin{array}{c} \nu_e \\ e^- \end{array}\right)_L, \ e_{R_1} = e_R^-, \ Q_1 = \left(\begin{array}{c} u \\ d \end{array}\right)_L, \ u_{R_1} = u_R\,, \ d_{R_1} = d_R, \\[12pt] L_2 = \left(\begin{array}{c} \nu_\mu \\ \mu^- \end{array}\right)_L, \ e_{R_2} = \mu_R^-, \ Q_2 = \left(\begin{array}{c} c \\ s \end{array}\right)_L, \ u_{R_2} = c_R\,, \ d_{R_2} = s_R, \\[12pt] L_3 = \left(\begin{array}{c} \nu_\tau \\ \tau^- \end{array}\right)_L, \ e_{R_3} = \tau_R^-, \ Q_3 = \left(\begin{array}{c} t \\ b \end{array}\right)_L, \ u_{R_3} = t_R\,, \ d_{R_3} = b_R. \end{array} \tag{1.3}$$

In Table 1.3 the electric charge Q, the isospin I_3 and the hypercharge Y for the left- and right-handed leptons and quarks are summarized.

The fermion hypercharge of the fermions is connected to the electric charge Q_f and of the third component of the weak isospin I_f^3, by

$$Q = I_3 + \frac{Y}{2}\,. \tag{1.4}$$

	ν_L	e_L	e_R	u_L	d_L	u_R	d_R
I_3	+1/2	-1/2	0	+1/2	-1/2	0	0
Y	-1	-1	-2	+1/3	+1/3	+4/3	-2/3
Q	0	-1	-1	+2/3	-1/3	+2/3	-1/3

TABLE 1.3: Table lists the electric charge Q, the isospin I_3 and the hypercharge Y for the left- and right-handed leptons and quarks.

The generators of the $SU(2)_L \times U(1)_Y$ group are the isospin operators T^a (with $a = 1,2,3$) and the hypercharge Y. A vector field is associated to each of these generalized charges $W_\mu^{1,2,3}$ to $I_{1,2,3}$, and a singlet field B_μ to Y. These

---

[1]The neutrinos in the SM are assumed to have zero mass and occur with their left–handed components only.

can be expressed in terms of the non–commuting 2×2 Pauli matrices

$$T^a = \frac{1}{2}\tau^a ; \quad \tau_1 = \begin{pmatrix} 0 & 1 \\ 1 & 0 \end{pmatrix}, \ \tau_2 = \begin{pmatrix} 0 & -i \\ i & 0 \end{pmatrix}, \ \tau_3 = \begin{pmatrix} 1 & 0 \\ 0 & -1 \end{pmatrix} \tag{1.5}$$

and the commutation relations between the generators are given by

$$[T^a, T^b] = i\epsilon^{abc} T_c \quad \text{and} \quad [Y, Y] = 0. \tag{1.6}$$

In these relations ϵ^{abc} represents the antisymmetric tensor. In QCD, the gluon field octet $G_\mu^{1,\cdots,8}$, which coincides with the eight generators of the SU(3)$_\mathrm{C}$ group, obeys:

$$[T^a, T^b] = i f^{abc} T_c \quad \text{with} \quad \mathrm{Tr}[T^a T^b] = \frac{1}{2}\delta_{ab}. \tag{1.7}$$

Here, the same notation as for the SU(2) generation has been used while the tensor f^{abc} is the structure constant of SU(3)$_\mathrm{C}$.

Defining g_s, g_2 and g_1 respectively as the coupling constants of SU(3)$_\mathrm{C}$, SU(2)$_\mathrm{L}$ and U(1)$_\mathrm{Y}$, the field strengths can be written as:

$$\begin{aligned} G_{\mu\nu}^a &= \partial_\mu G_\nu^a - \partial_\nu G_\mu^a + g_s f^{abc} G_\mu^b G_\nu^c, \\ W_{\mu\nu}^a &= \partial_\mu W_\nu^a - \partial_\nu W_\mu^a + g_2 \epsilon^{abc} W_\mu^b W_\nu^c, \\ B_{\mu\nu} &= \partial_\mu B_\nu - \partial_\nu B_\mu. \end{aligned} \tag{1.8}$$

The SU(2) and SU(3) groups have a non-abelian nature, therefore self-interactions between their gauge fields, $V_\mu \equiv W_\mu$ or G_μ, will occur. This leads to triple gauge boson couplings

$$i g_i \, \mathrm{Tr}(\partial_\nu V_\mu - \partial_\mu V_\nu)[V_\mu, V_\nu]$$

and quartic couplings

$$\frac{1}{2} g_i^2 \, \mathrm{Tr}[V_\mu, V_\nu]^2. \tag{1.9}$$

The covariant derivative contains the interaction between the fermionic fields and the gauge fields. In case of quarks it is defined as:

$$D_\mu \psi = \left(\partial_\mu - i g_s T_a G_\mu^a - i g_2 T_a W_\mu^a - i g_1 \frac{Y_q}{2} B_\mu \right) \psi. \tag{1.10}$$

The unique fermion-gauge boson coupling is defined as:

$$- g_i \bar{\psi} V_\mu \gamma^\mu \psi. \tag{1.11}$$

The SM Lagrangian, neglecting mass terms for fermions and gauge bosons, is then given by

$$\begin{aligned}
\mathcal{L}_G + \mathcal{L}_F \;=\; & -\frac{1}{4} G^a_{\mu\nu} G^{\mu\nu}_a - \frac{1}{4} W^a_{\mu\nu} W^{\mu\nu}_a - \frac{1}{4} B_{\mu\nu} B^{\mu\nu} & (1.12) \\
& + \bar{L}_i \, i D_\mu \gamma^\mu \, L_i + \bar{e}_{Ri} \, i D_\mu \gamma^\mu \, e_{R_i} & (1.13) \\
& + \; \bar{Q}_i \, i D_\mu \gamma^\mu \, Q_i + \bar{u}_{Ri} \, i D_\mu \gamma^\mu \, u_{R_i} \; + \bar{d}_{Ri} \, i D_\mu \gamma^\mu \, d_{R_i}
\end{aligned}$$

and is invariant under local $SU(3)_C \times SU(2)_L \times U(1)_Y$ gauge transformations for fermion and gauge fields and thus describes massless particles.

When massive terms for the gauge bosons, $\frac{1}{2} M_V^2 W_\mu W^\mu$, are added the local SU(2)×U(1) gauge invariance is violated. If a fermionic mass term instead is added, the gauge invariance is explicitly broken, due to a mixing of left- and right-handed fields as, for example, in $m_e(\bar{e}_L e_R + \bar{e}_R e_L)$. The mass terms for the vector bosons of the weak interaction will be introduced by breaking the electroweak symmetry spontaneously with the help of the Higgs mechanism, while fermionic terms will be introduced with the help of gauge-invariant Yukawa interactions of the fermions with the Higgs field.

1.2.1   The Higgs mechanism

The invariance under local gauge transformations in the SM Lagrangian is preserved due to spontaneous symmetry breaking, which also allows the introduction of mass terms for the particles. The symmetry is not broken by a term added by hand, but it is a peculiar characteristic of the fields involved in the theory.

The introduction of a new $SU(2)_L$ doublet of complex scalar fields ϕ represents the simplest way to introduce this mechanism into the SM Lagrangian:

$$\Phi = \begin{pmatrix} \phi^+ \\ \phi^0 \end{pmatrix}. \tag{1.14}$$

The additional term that involves this new field is

$$\mathcal{L}_H = (D^\mu \Phi)^\dagger (D_\mu \Phi) - V(\Phi), \tag{1.15}$$

where the covariant derivative is defined as

$$D_\mu = \left(\partial_\mu - i g_2 \frac{\tau_a}{2} W_\mu^a - i g_1 \frac{Y_q}{2} B_\mu \right).$$ (1.16)

In this equation, W_μ^a are three gauge fields and B_μ another gauge field with coupling strengths g_2 and g_1. The τ_a are the Pauli matrices and Y the hyper-charge. The complex scalar doublet in Eq. 1.14 is chosen in such a way that the hyper-charge is $+1$ and the weak isospin is $1/2$.
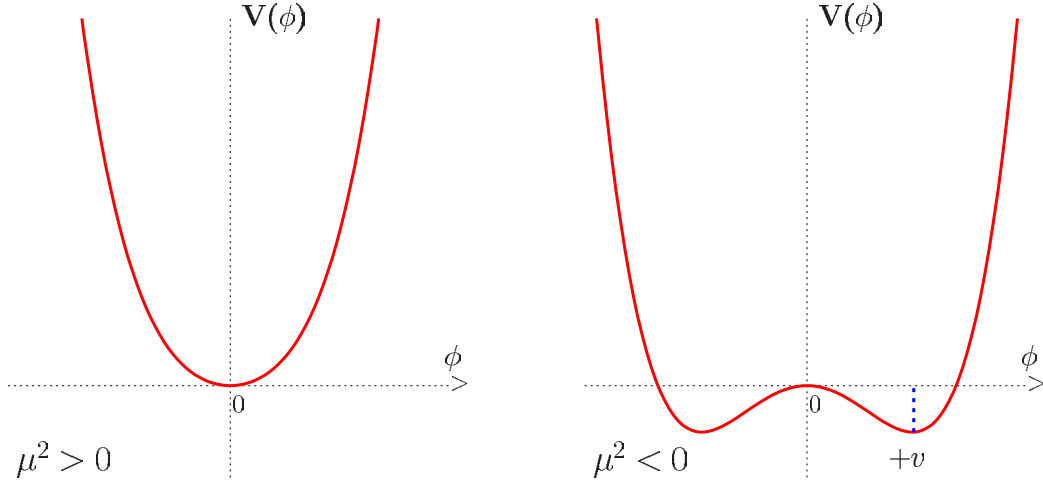
FIGURE 1.1: Scalar field ϕ potential V in the case $\mu^2 > 0$ (left) and $\mu^2 < 0$ (right). Figure from [4]

The potential $V(\phi)$ can be written as:

$$V(\phi) = \mu^2 \Phi^\dagger \Phi + \lambda (\Phi^\dagger \Phi)^2 = \mu^2 |\Phi|^2 + \lambda |\Phi|^4.$$ (1.17)

The shape of the potential depends solely on the values of λ and μ. $\lambda > 0$ is required to ensure the potential is bounded from below, guaranteeing the presence of a ground state. In case of positive μ^2, the potential has its minimum at $\langle 0|\phi|0 \rangle \equiv \phi_0 = 0$ as shown in the left–hand side graph of Fig. 1.1. $\mathcal{L}$ is the Lagrangian of a particle with mass μ and spin zero. For $\mu^2 < 0$ the symmetry of the potential will be broken and the minimum of the potential V will be at

$$\langle \Phi \rangle_0 \equiv \langle 0| \Phi |0 \rangle = \left(-\frac{\mu^2}{2\lambda} \right)^{1/2} \equiv \frac{v}{\sqrt{2}}.$$ (1.18)

The quantity v is called the vacuum expectation value (vev) of the scalar field ϕ:

$$v = \langle 0|\Phi|0 \rangle = 2 \sqrt{\frac{\mu^2}{\lambda}}.$$ (1.19)

The shape of the potential is shown in the right-hand side graph of Fig. 1.1. As the vacuum has to be electrically neutral, the upper component of Φ_0 disappears. In this way, Φ_0 is fixed up to a phase:

$$\Phi_0 = (0, v/\sqrt{2})^{\mathrm{T}} . \tag{1.20}$$

Despite the fact that the Lagrangian is symmetric under gauge transformations of the $\mathrm{SU(2)_I \times U(1)_Y}$ group, this symmetry is not maintained by the vev, and it has been spontaneously broken. However, $\langle 0|\Phi|0 \rangle$ preserves the symmetry under transformations of the electromagnetic subgroup $U(1)$, generated by the charge Q, keeping the electromagnetic gauge symmetry. The field Φ can be parametrized in terms of the unphysical complex fields $\theta_{1,2,3}(x)$ and the physical real field $H(x)$. At first order Φ reads:

$$\Phi(x) = \begin{pmatrix} \theta_2 + i\theta_1 \\ \frac{1}{\sqrt{2}}(v+H) - i\theta_3 \end{pmatrix} = e^{i\theta_a(x)\tau^a(x)/v} \begin{pmatrix} 0 \\ \frac{1}{\sqrt{2}}(v+H(x)) \end{pmatrix}. \tag{1.21}$$

The $\theta_{1,2,3}(x)$ fields are referred to as Goldstone bosons that arise when a global symmetry is spontaneously broken (*Goldstone theorem*). They are non-physical states because they are connected to the vev by gauge transformations, i.e. there exists a gauge transformation (referred to as "unitary gauge"), that makes the two fields vanish:

$$\Phi(x) \rightarrow e^{-i\theta_a(x)\tau^a(x)} \Phi(x) = \frac{1}{\sqrt{2}} \begin{pmatrix} 0 \\ v + H(x) \end{pmatrix}. \tag{1.22}$$

In the unitary gauge, the $\theta^i(x) = 0$ and unphysical degrees of freedom become longitudinal modes of the massive gauge bosons.

The term $|D_\mu\Phi)|^2$ of the Lagrangian can be expanded as:

$$
\begin{aligned}
|D_\mu\Phi)|^2 &= \frac{1}{2}\left|\left(\partial_\mu - ig_2\frac{\tau_a}{2}W_\mu^a - ig_1\frac{1}{2}B_\mu\right)\begin{pmatrix} 0 \\ v+H \end{pmatrix}\right|^2 = \\
&= \frac{1}{2}(\partial_\mu H)^2 + \frac{1}{8}g_2^2(v+H)^2|W_\mu^1 + iW_\mu^2|^2 + \frac{1}{8}(v+H)^2|g_2W_\mu^3 - g_1B_\mu|^2.
\end{aligned}
\tag{1.23}
$$

Defining the new fields $W_\mu^\pm$, Z_μ and A_μ:

$$W^\pm = \frac{1}{\sqrt{2}}(W_\mu^1 \mp iW_\mu^2) \,, \ Z_\mu = \frac{g_2W_\mu^3 - g_1B_\mu}{\sqrt{g_2^2 + g_1^2}} \,, \ A_\mu = \frac{g_2W_\mu^3 + g_1B_\mu}{\sqrt{g_2^2 + g_1^2}} \,. \tag{1.24}$$

Bilinear terms can be isolated:

$$M_W^2 W_\mu^+ W^{-\mu} + \frac{1}{2} M_Z^2 Z_\mu Z^\mu + \frac{1}{2} M_A^2 A_\mu A^\mu \tag{1.25}$$

and also the mass components:

$$M_W = \frac{1}{2} v g_2 \ , \ M_Z = \frac{1}{2} v \sqrt{g_2^2 + g_1^2} \ , \ M_A = 0. \tag{1.26}$$

With the spontaneous breaking of the $SU(2)_L \times U(1)_Y \to U(1)_Q$ symmetry, the $W^\pm$ and Z bosons acquired masses to form their longitudinal components by absorbing the Goldstone bosons. The $U(1)_Q$ symmetry stays unbroken and its generator, the photon, remains massless. Inserting the mass terms, the parameters μ^2, λ and v can be eliminated from the Lagrangian:

$$\mathcal{L}_{Higgs} = \frac{1}{2}(\partial H)^2 - \frac{1}{2} M_H^2 H^2 + M_W^2 W_\mu^+ W^{-,\mu} + \frac{1}{2} M_Z^2 Z_\mu Z^\mu \tag{1.27}$$

$$+ g M_W H W_\mu^+ W^{-,\mu} + \frac{g^2}{4} H^2 W_\mu^+ W^{-,\mu} \tag{1.28}$$

$$+ \frac{g M_Z}{2 c_w} H Z_\mu Z^\mu + \frac{g^2}{4 c_w^2} H^2 Z_\mu Z^\mu \tag{1.29}$$

$$- \frac{g M_H^2}{4 M_W} H^3 - \frac{g^2 M_H^2}{32 M_W^2} H^4 + \text{const..} \tag{1.30}$$

The real field $H(x)$ in the potential describes physical neutral scalar particles, the Higgs bosons, with mass $M_H = \frac{\mu}{\sqrt{2}}$ and triple and quartic self interactions with couplings proportional to M_H^2. The couplings to the gauge fields imply tri-linear HWW, HZZ and quadri-linear $HHWW$, $HHZZ$ vertices. $\mathcal{L}_{Higgs}$, together with Eq 1.26, gives the coupling strength at the HW^+W^- vertex:

$$g_{HWW} = \frac{1}{2} g_2^2 v = g_2 M_W. \tag{1.31}$$

The HWW coupling is proportional to the W-boson mass. In the same way, the HZZ coupling is proportional to M_Z.

The fermion masses can be generated with the same scalar field Φ, and the isodoublet $\tilde{\Phi} = i\tau_2 \Phi^*$. The $SU(2)_L \times U(1)_Y$ invariant Yukawa Lagrangian for any fermion generation becomes:

$$\mathcal{L}_F = -\lambda_e \bar{L} \Phi e_R - \lambda_d \bar{Q} \Phi d_R - \lambda_u \bar{Q} \tilde{\Phi} u_R + h.c. \tag{1.32}$$

where the $\lambda_{e,d,u}$ are the individual Yukawa coupling constants. For example, for the electron one obtains:

$$
\begin{aligned}
\mathcal{L}_F &= -\frac{1}{\sqrt{2}} \lambda_e \, (\bar{\nu}_e, \bar{e}_L) \begin{pmatrix} 0 \\ v+H \end{pmatrix} e_R \; + \cdots \\
&= -\frac{1}{\sqrt{2}} \lambda_e \, (v+H) \, \bar{e}_L e_R \; + \cdots
\end{aligned}
\tag{1.33}
$$

The constant terms in front of $\bar{f}_L f_R$ with the fermion mass are:

$$
m_e = \frac{\lambda_e \, v}{\sqrt{2}} \quad , \; m_u = \frac{\lambda_u \, v}{\sqrt{2}} \quad , \; m_d = \frac{\lambda_d \, v}{\sqrt{2}} \; .
\tag{1.34}
$$

The same isodoublet Φ of generates the masses of the fermions and of the weak vector bosons $W^\pm, Z$ by spontaneously breaking the SU(2)×U(1) gauge symmetry, and keeping unbroken the electromagnetic U(1)$_Q$ symmetry and the SU(3) color symmetry. The Standard Model is based on a SU(3)×SU(2)×U(1) symmetry, which is gauge invariant.

1.3 Beyond the Standard Model

Over the years, the Standard Model has been experimentally validated. However, it is known to be an incomplete theory. Open issues are:

- **Dark matter and dark energy**: the presence of dark matter and dark energy in the Universe, proven by astronomical observations, is not explained in the SM.

- **Gravity**: the SM unifies three out of four interactions, excluding the gravitational force.

- **Neutrino masses**: in the SM neutrinos are massless, but recent observations of neutrino oscillations have proven that indeed they have a tiny mass.

- **CP violation**: the imbalance between matter and antimatter in the Universe cannot be sufficiently explained by the CP-violation incorporated in the SM.

- **The hierarchy problem**: the Standard Model is an effective theory, i.e. it is a theory valid up to the EW energy scale $\Lambda_{cut-off}$. For larger scales, such as the Plank scale (10^{19} GeV), a more complete theory is

required (*hierarchy problem*). Radiative corrections to the Higgs mass have a quadratic dependence on the cut-off scale. For scales $\Lambda >> \Lambda_{cut-off}$, these corrections become much larger than the Higgs mass, demanding a fine tuning to almost completely cancel these quantum corrections. This unnatural fine-tuning is referred to as *naturalness problem.*

Several theoretical solutions have been proposed to address these issues. One of the most popular models is Supersymmetry (SUSY) [20]. SUSY demands that each particle (bosons and fermions) has a *superpartner*, with spin that differs by a half-integer. All the quantum corrections to the Higgs boson mass are canceled by the superpartner, solving at the same time the hierarchy problem and providing a natural dark matter candidate. In the Higgs sector, SUSY also introduces additional CP-violating sources. Moreover, it is a prerequisite for String Theory, that includes the gravitational interaction.

Several other models to extend the Standard Model affect more directly the Higgs sector. One of those is called *The Two Higgs Doublet Model (2HDM)* [21, 22]. The 2HDM adds an electroweak doublet to the SM and foresees the existence of five Higgs bosons: a pseudo-scalar neutral boson (A), two scalar Higgs (h^0 and H), where h^0 is the lighter of the two, and two charged scalar Higgs bosons ($H^{\pm}$).

Other theories foresee the Higgs boson as a composite particle such as the *Strongly Interacting Light Higgs (SILH)* [23]. In this regard, a new strongly interacting QCD-like force above the electroweak scale is introduced, while the SM is seen as an effective theory.

All these models among others directly affect the Higgs boson properties and so far no experimental evidence of any BSM theory has been found. Any deviations from the SM values would boost the scientific community to the right direction in understanding the mysteries of the Universe.

1.4 The Higgs boson at the LHC

After the discovery of the Higgs boson, that was found to be consistent with the SM expectations, one of the main goals of the ATLAS and CMS experiments has been to probe its properties. With the large amount of data collected from 2015 to 2018, a precision era for the Higgs boson cross-section and properties measurements has started. The rise of the center-of-mass energy causes an increase of the production cross-sections, implying an improved sensitivity to several physics processes.

1.4.1   Higgs boson production mechanisms
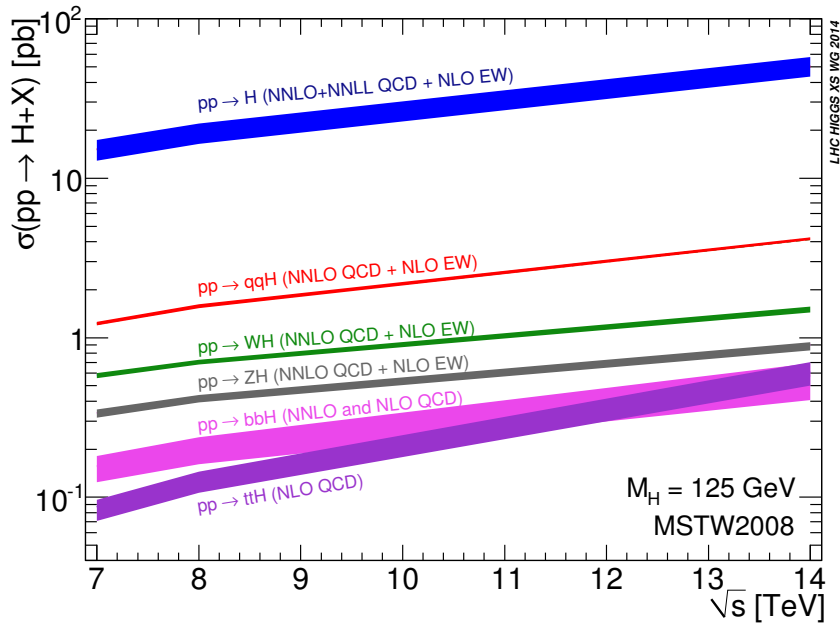
FIGURE 1.2: Standard Model cross-sections for the Higgs bo-
son as a function of the center-of-mass energy [24].

The SM production cross-sections as a function of the center-of-mass en-
ergy are shown in Figure 1.2. The Higgs production at the LHC center-of-
mass energies happens mainly through the fusion of two gluons or two vector
bosons, or through the associated production with a vector boson or with two
heavy quarks. In this section, an overview of these production mechanisms is
given, listed in order of decreasing cross-section.

Gluon fusion   The gluon-gluon fusion (or ggF) is the production mecha-
nism with the highest cross-section. This process happens mainly through
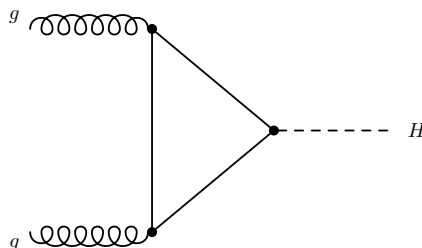
FIGURE 1.3: Lowest order Feynman diagram for the Higgs
boson production mechanism through gluon-gluon fusion.

a loop of heavy quarks, as shown in the Feynman diagram in Fig 1.3. The
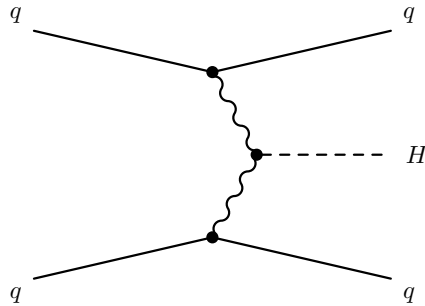
FIGURE 1.4: Lowest order Feynman diagram for the Higgs boson production mechanism through vector boson fusion.
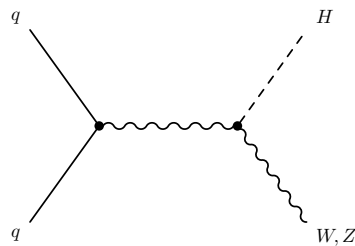
FIGURE 1.5: Lowest order Feynman diagram for the $qq \to VH$ process.

couplings of the Higgs boson to heavy quarks are probed directly: since the coupling is directly proportional to the quark mass, the most likely quark in the loop is the heaviest one, the top-quark, followed by the b-quark. In this channel the Higgs boson is produced alone, resulting in no distinctive experimental signature. Therefore, a clear identification of the Higgs boson decay products is the only way to detect this process. However, the first and second order real emission corrections to the gluon fusion process can result in a final state with a Higgs boson plus one or two jets (ggF+1j/ggF+2j).

Vector Boson Fusion The fusion of two vector bosons (or VBF) is the second most important production mechanism. Two W or Z bosons, radiated by quarks, fuse to create an Higgs boson, as shown in the Feynman diagram in Fig 1.4. The VBF production cross-section measures the strength of the HVV coupling, probing the Higgs mechanism as the source of the EWSB. VBF shows a distinctive kinematic signature: the final state characterized by the presence of two light jets, with high invariant mass, directed predominantly in the forward region of the detector. The peculiarities of this production mechanism will be described more in detail in Chapter 7.
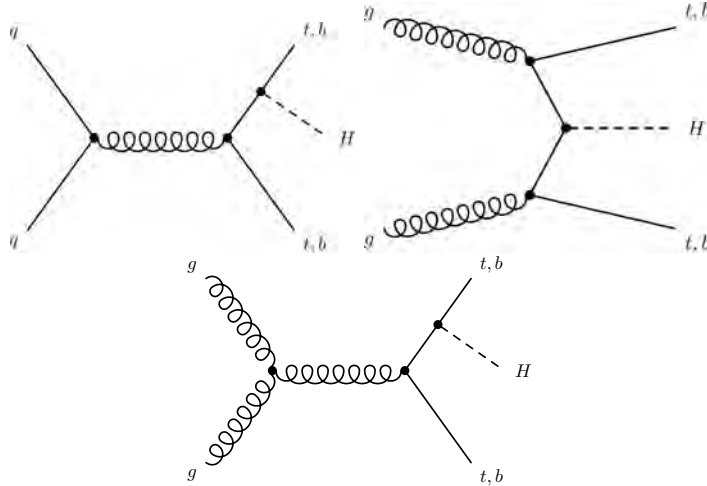
FIGURE 1.6:   Lowest order Feynman diagrams for the
$qq/gg \rightarrow ttH$ and the $qq/gg \rightarrow bbH$ processes.

Higgs-strahlung   The Higgs-strahlung or Higgs boson associated production with a vector boson ($W^{\pm}$ or Z), represents the third larger cross-section at LHC. This mode probes the coupling between the Higgs and the vector bosons. The associated Feynman diagram is shown in Fig 1.5.

Associated production with heavy quarks   The Higgs boson can also be produced in association with two heavy quarks, mainly top quarks, followed by bottom-quarks (ttH and bbH), as shown in Figures 1.6. Despite the significantly lower cross-sections, these channels present a distinctive signature due to the presence of b-quarks in the final state. The production in association with a top pair represents an important channel for the direct measurement of the Higgs couplings to top quarks.

1.4.2   Decay channels

The SM Higgs boson decays into pairs of bosons or fermions. In Figure 1.7 the decay branching ratios as a function of the Higgs mass are shown. The best channels to probe the properties of the Higgs boson at the LHC are: $H \rightarrow \gamma\gamma$, $H \rightarrow ZZ^*$, $H \rightarrow WW^*$, $H \rightarrow b\bar{b}$ and $H \rightarrow \tau\tau$. The Feynman diagrams for these decays are shown in Fig. 1.8. The decay into $b\bar{b}$ presents the largest branching ratio. However, this channel, as well as the other channels with hadronic content in the final state, such as $H \rightarrow \tau\tau$ decays, is harder to detect at LHC for the presence of a large multi-jets background. In order to distinguish signal from background events, it is necessary to look at production channels with a characteristic signature, such as VBF or VH.
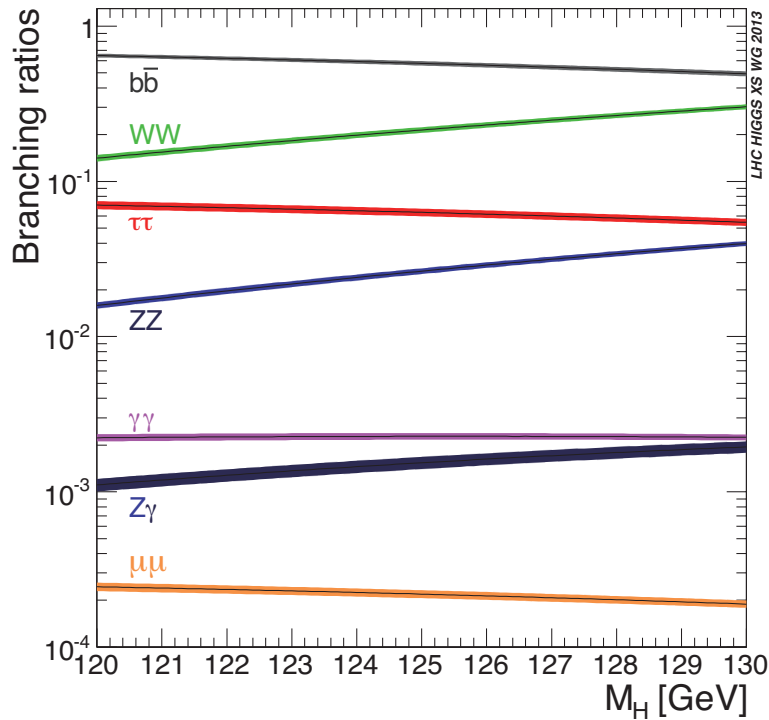
FIGURE 1.7: Decay branching ratios of the Standard Model
Higgs boson as a function of the Higgs boson mass. From [24].

The "golden" channels for the Higgs decays are $H \to ZZ \to 4\ell$ and $H \to \gamma\gamma$.
Despite a rather low branching fractions, they present a very clear experimental signature: it is indeed possible to fully reconstruct the event kinematic,
resulting in a clear Higgs mass peak over a smooth background.

This thesis will focus on the $H \to WW^* \to \ell\nu\ell\nu$ decay, whose characteristics
are described more in detail in the next section and in Chapter 7.

1.4.2.1 The $H \to WW^* \to \ell\nu\ell\nu$ decay channel

The decay of the Higgs boson into two W bosons presents the second largest
branching ratio (21%). Since the Higgs boson mass is $m_H = 125$ GeV, this decay
is kinematically allowed only if one of the two W bosons is off-shell (W^*).
The W bosons present a decay rate into hadrons of 67.6%. The branching ratio of $W \to \ell\nu$ is approximately 10.8% per lepton flavor. Therefore,
the possible final states for the $H \to WW^*$ channel can be fully hadronic
($qqqq$), semi-leptonic ($\ell\nu qq$) and fully leptonic ($\ell\nu\ell\nu$). The leptonic decays
present the highest experimental sensitivity thanks to its clear signature: two
opposite-sign leptons and the presence of missing energy due to neutrinos.
Thus, this channel is an excellent candidate to analyze the properties and
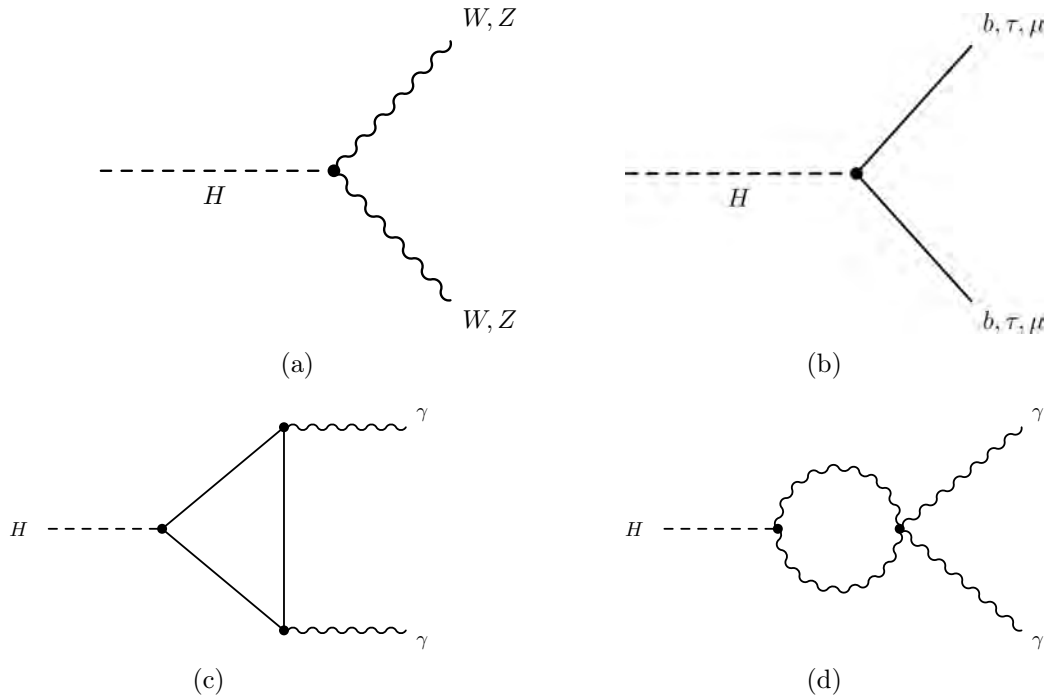
FIGURE 1.8: Feynman diagrams illustrating the Higgs boson
decays into vector bosons 1.8(a), into fermions 1.8(b), and into
photons 1.8(c)- 1.8(d).

the production cross-section of the Higgs boson. However, because of the
neutrinos, the Higgs boson invariant mass cannot be fully reconstructed and,
consequently, measured. Compared to $H \rightarrow ZZ \rightarrow 4\ell$ and $H \rightarrow \gamma\gamma$, this
channel is characterized by significantly larger statistics, due to the bigger
branching ratio. Despite this, it is more challenging to study because of the
poorer signal over background ratio, linked to the presence of large irreducible
backgrounds, that will be described more in detail in Section 7.2.

1.4.3   Higgs boson properties

The Higgs boson in the SM is a massive fundamental particle with spin-0,
with positive parity and electrically neutral. Its mass has been measured with
both Run 1 and Run 2 datasets in the $H \rightarrow ZZ \rightarrow 4\ell$ and $H \rightarrow \gamma\gamma$ channels.
A summary of these measurements results is given in Figure 1.9. In the Run
1 + Run 2 combination [25], the measured Higgs mass is:

$$m_H = 124.97 \pm 0.24 \text{ GeV}. \tag{1.35}$$
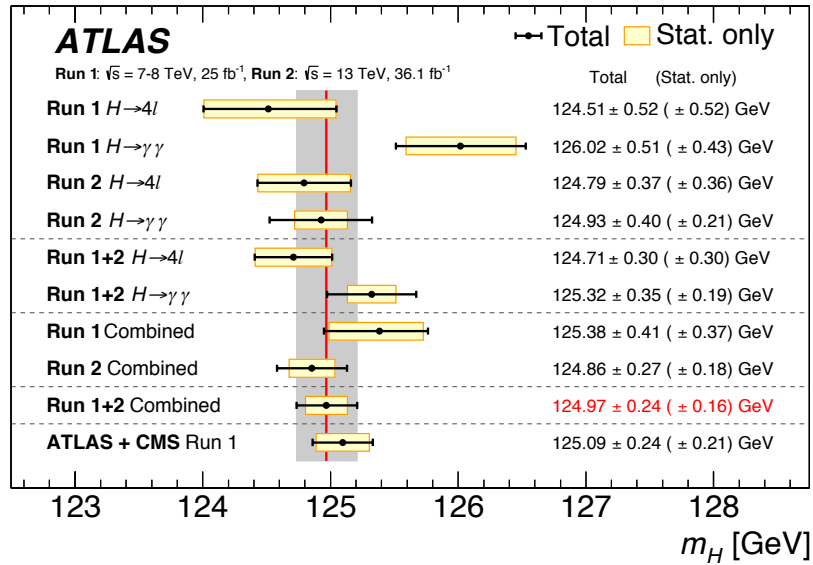
FIGURE 1.9: Summary of the Higgs boson mass measured in Run 1 and Run 2, for the individual $H \to ZZ$ and $H \to \gamma\gamma$ analyses and their combination. A comparison to the combined Run 1 measurement by ATLAS and CMS is also given. In the plot the systematic, statistical and total uncertainties are also shown. From [25].

After the first Higgs boson mass measurement, both ATLAS and CMS experiments started studying in detail some of the features of this new particle, such as spin and CP, in order to verify if its characteristics were conformed to the ones predicted by the SM. The SM predicts all the properties and quantum numbers of the Higgs boson, with the exception of the Higgs mass that is a free parameter in this theory.

In the Run 1 dataset, the quantum numbers for spin and parity have been studied and no divergences from the SM expectations has been found [26, 27]. The three diboson final states have been analyzed, testing the SM $J^{PC} = 0^+$ hypothesis against alternative BSM ones (such as 0^-, BSM 0^+ and 2^+). The non-SM spin hypotheses have been excluded at more than 99.9% CL in favor of the SM spin-0 one.

Higgs couplings to polarized vector bosons

This chapter outlines the motivations behind the measurement of the Higgs boson couplings to polarized vector bosons. At first, the definition of the gauge bosons polarization is stated. Then, the simple theoretical model that defines the Higgs couplings to the longitudinal and transverse parts of the vector bosons is described, following Reference [28]. At last, a translation of these coupling parameters into more general schemes, such as an effective field theories and the pseudo-observable framework, is given.

2.1 The gauge bosons polarization

In Quantum Field Theory (QFT), the equation of motion for a massive spin-1 particle is described by the Proca Lagrangian [3]:

$$\mathcal{L} = -\frac{1}{4}F^{\mu\nu}F_{\mu\nu} + \frac{1}{2}m^2 B^\mu B_\mu \,, \tag{2.1}$$

where $F_{\mu\nu}$ is the field-strength tensor, $F_{\mu\nu} = (\partial^\mu B^\nu - \partial^\nu B^\mu)$ for a vector field $B^\mu = (\phi, \mathbf{B})$. Imposing the Lorenz condition:

$$\partial_\mu B^\mu = 0, \tag{2.2}$$

B^μ can be expressed in terms of a wave-plane solution of the Klein-Gordon equation:

$$B^\mu(x) = C\epsilon^\mu(p)e^{-ipx} \,. \tag{2.3}$$

In this equation, p is the four-momentum of the particle, C is a normalization constant and ϵ^μ is the polarization vector corresponding to the plane wave. The Lorenz constraint 2.2 implies that the four-vector polarization meets

$$p_\mu \epsilon^\mu = 0. \tag{2.4}$$

For this condition, only three out of the four degrees of freedom of ϵ^μ are independent. Therefore, a massive spin-1 boson described by 2.3 presents three polarization states, as there is no further freedom to choose the gauge.

These three possible linear polarization states can be written in the boson rest frame

$$\epsilon_x^\mu = (0,1,0,0), \tag{2.5}$$

$$\epsilon_y^\mu = (0,0,1,0), \tag{2.6}$$

$$\epsilon_z^\mu = (0,0,0,1), \tag{2.7}$$

A Lorentz transformation can be applied in order to obtain an expression of ϵ_L^μ for a spin-1 boson traveling in the z-direction, with mass M, energy E and 3-momentum p_z. Two of the possible states can be seen as two circular polarization states:

$$\epsilon_+^\mu = \frac{1}{\sqrt{2}}(0,1,i,0), \tag{2.8}$$

$$\epsilon_-^\mu = \frac{1}{\sqrt{2}}(0,1,-i,0), \tag{2.9}$$

These quantities, ϵ_+^μ and ϵ_-^μ are the two degrees of freedom of polarization transverse to the boson direction. The longitudinal one, parallel to the z direction, ϵ_L^μ can be written as:

$$\epsilon_L^\mu = (a\frac{|\vec{p}|}{E}, a\frac{\vec{p}}{|\vec{p}|}) = (a\frac{p_z}{E},0,0,a), \tag{2.10}$$

where $a > 0$ and for the normalization condition a can be substituted with E/M, achieving:

$$\epsilon_+^\mu = \frac{1}{\sqrt{2}}(0,1,i,0), \tag{2.11}$$

$$\epsilon_-^\mu = \frac{1}{\sqrt{2}}(0,1,-i,0), \tag{2.12}$$

$$\epsilon_L^\mu = \frac{1}{M}(p_z,0,0,E). \tag{2.13}$$

The above expressions indeed satisfy the Lorenz condition, resulting in Eq. 2.4. Defining the helicity, as the projection of the boson's spin onto its direction of motion,

$$h = \frac{\mathbf{s} \cdot \mathbf{p}}{|p|}, \tag{2.14}$$

ϵ_+^μ, ϵ_L^μ and ϵ_-^μ correspond, respectively, to helicities +1, 0 and -1. In QFT, on-shell photons are purely transverse and more generically, any massless boson of spin J, can only have helicities $+J$ and $-J$.

Furthermore, as shown in Eq. 2.13, ϵ_L depends from the energy. At energies much larger than the boson mass, ϵ_L grows with E, leading, as described in the next section, to divergences of the unitarization of amplitudes in the scattering of two vector bosons.

Polarization for off-shell vector bosons The longitudinal and transverse polarization definitions 2.11-2.13 are valid for on-shell W and Z bosons. However, in a Higgs boson decay into two Ws, one of the two W bosons is close to the mass shell, but the other one is off-shell. Thus, the polarization has to be defined for the off-shell particles as well. The transverse and longitudinal parts of the W and Z-boson fields can be defined as:

$$V_T^\mu = \mathbb{P}_{T\nu}^\mu \, V^\nu \qquad \text{and} \qquad V_L^\mu = \mathbb{P}_{L\nu}^\mu \, V^\nu \,, \tag{2.15}$$

where $V = W, Z$ are the gauge boson fields in the unitary gauge and $\mathbb{P}_T^{\mu\nu}$ is the projection operator to the transverse plane, i.e. it projects the field onto the plane perpendicular to the direction of motion:

$$\mathbb{P}_T^{0\nu} = 0 = \mathbb{P}_T^{\mu 0} \qquad \text{and} \qquad \mathbb{P}_T^{ij} = \delta^{ij} - \frac{\vec{p}^i \vec{p}^j}{\vec{p}^2} \qquad (i,j = 1,2,3) \,, \tag{2.16}$$

where $\vec{p}$ is the three-momentum of the field. The projection operator to the longitudinal direction, $\mathbb{P}_L^{\mu\nu}$, is:

$$\mathbb{P}_{L\nu}^\mu = (\mathbb{1} - \mathbb{P})_\nu^\mu \tag{2.17}$$

The sum of the two projections gives the physical field V^μ. A characteristic of the projectors of V^μ is that they are not Lorentz invariant. Let's take the example of a W boson moving along the z-axis: the Lorentz matrix in this case commutes with the projection operators, but not in case of a boost orthogonal to the W boson direction. In case of such boost, a mixing of the longitudinal and transverse projections can happen: the bosons that are
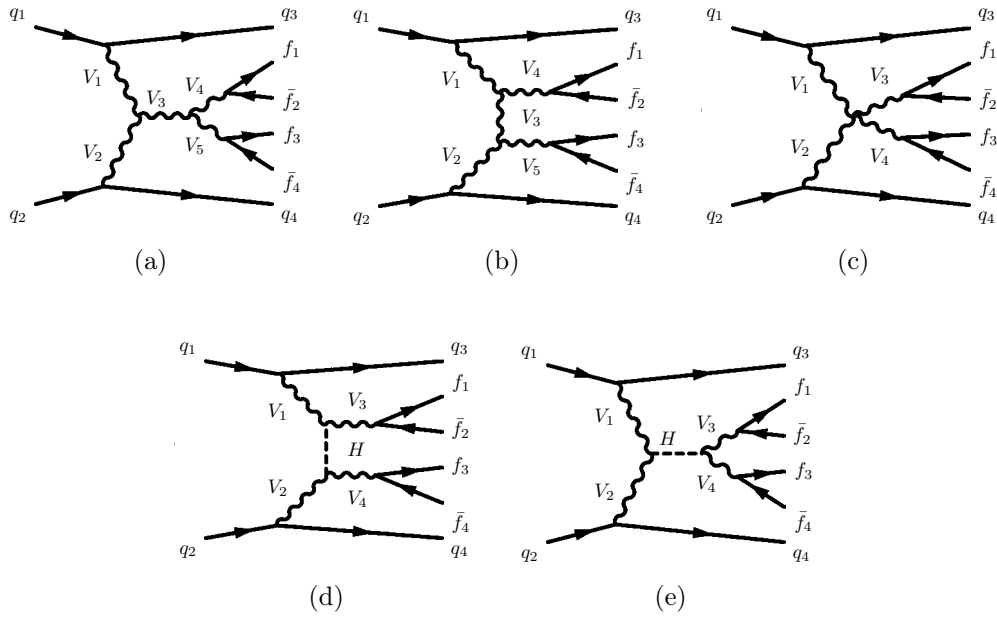
FIGURE 2.1: Leading order Feynman diagrams for $VVjj$-EW production. S-channel and t-channel triple gauge boson vertices are shown in the top left and in the top middle diagrams, respectively. Quartic gauge boson vertex is also illustrated in the top right diagram, together with the exchange of a Higgs boson through the s-channel (bottom left diagram) and t-channel (bottom right diagram).

transversally polarized in one frame may be longitudinal in the other frame and vice versa. The probability for a polarization change is proportional to the size of the boost.

2.2   Vector boson scattering

The nature of the electroweak symmetry breaking mechanism is directly probed by the scattering of two electroweak gauge bosons. These processes are usually referred to as vector boson scattering (VBS). The scattering of massive vector bosons W and Z is sensitive to EWSB. Processes involving photons are included in VBS, because of the experimental difficulties to fully separate Z and γ contributions. Both the ATLAS and CMS collaborations have been studying these processes, reaching the observation of a VBS signal in the channels $W^{\pm}W^{\pm}jj$ and $W^{\pm}Zjj$ [29–32].

As described in Chapter 1, thanks to the Higgs mechanism, a Higgs boson and three Goldstone modes are produced. The latter can be identified as the longitudinal massive modes of the weak gauge bosons. Since, as we can see

from Eq. 2.13, the polarization shows a dependency on the gauge boson momentum, in the scattering of gauge bosons at high energies the longitudinal amplitudes dominate. In this case, the longitudinal massive vector bosons can be replaced by the Goldstone bosons [4, 33].

The direct measurement of the properties of the Higgs boson is complementary to the VBS studies, as the presence of the Higgs unitarizes the VBS scattering amplitudes.

A vector boson scattering interaction at the LHC contains the processes illustrated in the Feynman diagrams in Figure 2.1. The scattering of $W_L^+ W_L^- \rightarrow W_L^+ W_L^-$ is characterized by the presence of a quartic boson vertex (Fig. 2.1(a)), triple gauge boson vertices (Fig. 2.1(b)- 2.1(c)) through the t- and s-channels of γ and Z exchanges and the s- and t-channels of Higgs exchange. As mentioned before, in the high-energy limit, the longitudinally polarized electroweak gauge bosons are originating from the Goldstone bosons. Therefore, the amplitude of the scattering of longitudinal bosons can be identified with the one of the would-be Goldstone scalars:

$$\mathcal{M}(W_L W_L \rightarrow W_L W_L) = \mathcal{M}(w_L w_L \rightarrow w_L w_L). \tag{2.18}$$

In the unitary gauge, i.e. if the Goldstone bosons are set to zero, and in the high energy limit, the amplitude for the scattering of two longitudinally polarized gauge bosons $W^\pm W^\pm \rightarrow W^\mp W^\mp$ in absence of an Higgs boson is described by[1]:

$$i\mathcal{M}^{\text{gauge}} = i\mathcal{M}_t^{\gamma+Z} + i\mathcal{M}_s^{\gamma+Z} + i\mathcal{M}_4 = -i\frac{g^2}{4m_W^2}u + O((E/m_W)^0) \ . \tag{2.19}$$

This term is proportional to the energy which causes unitarity violation. The latter is restored by including the s-channel and t-channel Higgs contributions (Fig.2.1(d) and 2.1(e)):

$$i\mathcal{M}^{\text{Higgs}} = -i\frac{g^2}{4m_W^2}\left[\frac{(s-2m_W^2)^2}{s-m_h^2} + \frac{(t-2m_W^2)^2}{t-m_h^2}\right] \ ,$$

that in the high energy limit becomes:

$$i\mathcal{M}^{\text{Higgs}} \simeq i\frac{g^2}{4m_W^2}u. \tag{2.20}$$

---

[1]with s, t, u in the following equations we represent the Mandelstam variables.

Therefore, the diverging terms cancel in the total calculation, leaving a constant term that does not violate unitarity. The latter, anyhow can still be violated if the coupling of the Higgs boson to the W boson diverges from the SM value. The HWW coupling can be expressed as a fraction $\sqrt{\delta}$ of its SM value:

$$\sqrt{\delta} \equiv \frac{g_{HWW}}{g_{HWW}^{\text{SM}}} \; . \tag{2.21}$$

In the limit of $s \gg m_h^2, m_W^2$, the contribution from the Higgs becomes:

$$i\mathcal{M}^{\text{Higgs}} \quad \simeq \quad i\frac{\delta^2 g^2}{4m_W^2} u \; , \tag{2.22}$$

If $\delta = 1$, as in the SM, there is a cancellation between the energy-raising terms of the gauge diagrams and the Higgs diagrams. In case of a deviation of δ, the total scattering amplitude, after the light Higgs pole at 125 GeV, would keep raising with $\sqrt{s}$. For example, a possible solution to restore unitarity can be found in the 2HDM, where the heavier neutral Higgs boson H couples to the weak gauge boson with a reduced strength g_{HWW}, unitarizing the amplitudes when $s_{WW} > m_H^2$. In Fig. 2.2, the scattering cross-sections for $W_L^+ W_L^- \to W_L^+ W_L^-$ versus the center-of-mass energy $\sqrt{s_{WW}}$ are shown. When $\delta = 1$, the sum of amplitudes converges to $O((E/m_W)^0)$ terms, as expected for the SM case, and the cross-section decreases with $1/s_{WW}$. As soon as $\delta \neq 1$, even for a small amount, the cross-section starts rising. This plot, taken from Ref. [34], assumes a Higgs boson mass of 200 GeV, but the same argument is still valid for a Higgs mass of 125 GeV.

2.3   Polarized couplings

There is a substantial difference between the longitudinal and the transverse modes of the gauge bosons. In the Higgs mechanism, when the Goldstone bosons are incorporated into the gauge bosons, the longitudinal modes are created: they correspond to the Goldstone bosons of electroweak symmetry breaking and they become dominant at large energies. As mentioned before, in Eq. 2.18, in the high energy limit ($E \geq M_W$), the longitudinal components can be exchanged with the Goldstone amplitudes ("Goldstone boson equivalence theorem") in the matrix element calculation for WW scattering. On the contrary, the transverse modes correspond to the original gauge bosons. This means that, in this limit, the two polarization modes can be distinctly divided: the longitudinal states correspond to the Goldstone bosons of the
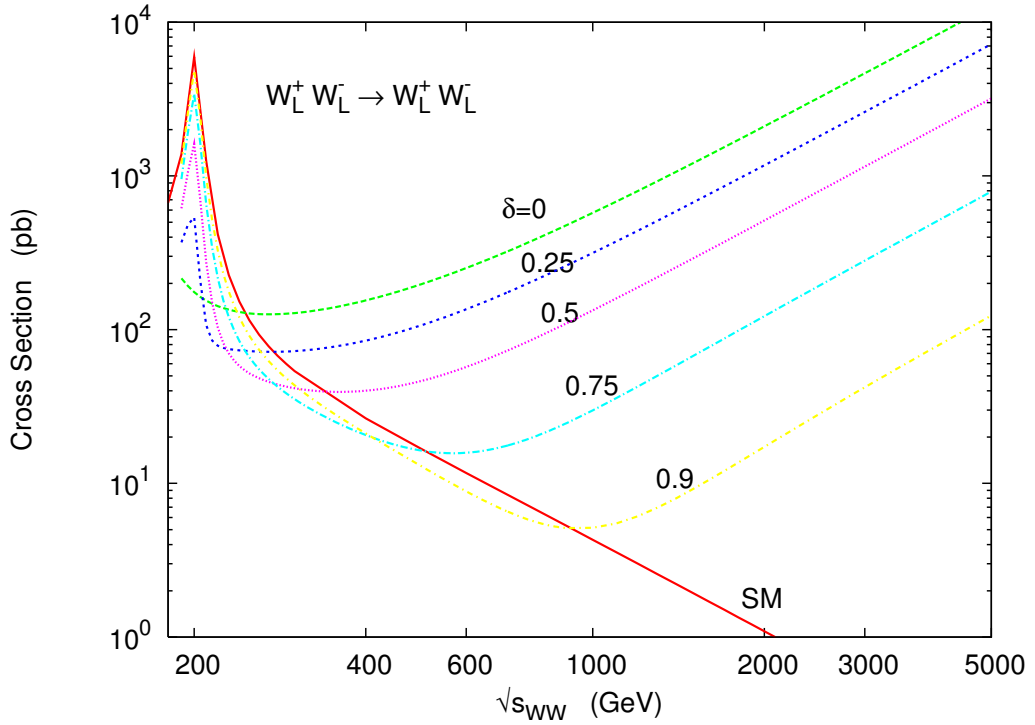
FIGURE 2.2: The $W_L^+ W_L^- \to W_L^+ W_L^-$ scattering cross-sections as a function of the center-of-mass energy $\sqrt{s_{WW}}$ for the SM case ($\delta = 1$) and deviations ($\delta \neq 1$). Here, δ describes the size of the Higgs amplitude relative to the SM one. From Ref. [34].

Higgs mechanism, whilst the transverse components are equivalent to the original electroweak gauge bosons. However, in a physical analysis, characterized by finite energies, it is necessary to take into account both on-shell and off-shell bosons, making the distinction between the two modes less neat, with a dependence on the reference frame.

Using the polarization definitions stated in the previous section, the Higgs-gauge interaction term can be divided into its longitudinal and transverse components, when this definition is applied to the Higgs rest frame. In this way, individual Higgs couplings to longitudinally and transversely polarized vector bosons $V = Z, W^\pm$ can be defined. Following the definition of polarization-dependent coupling strengths of Ref. [28], these couplings read:

$$a_L = \frac{g_{HV_L V_L}}{g_{HVV}}, \ a_T = \frac{g_{HV_T V_T}}{g_{HVV}}. \tag{2.23}$$

where g_{HVV} is the SM Higgs coupling to vector bosons. The choice of the Higgs rest frame is done so that the mixed-polarization couplings $g_{HV_L V_T}$ and $g_{HV_T V_L}$ are equal to zero.

This simple model is not gauge nor Lorentz invariant and cannot be described

in the Lagrangian framework. However, independent longitudinal and transverse Higgs-gauge couplings can be considered within valid models of new physics: as it will be shown in the next sections, these couplings, gaining a momentum-dependence, can be linked to effective field theory operators and pseudo-observables, that intrinsically account for Lorentz and gauge symmetries.

2.3.1 Sensitivity to polarized couplings

The VBF $H \rightarrow WW^*$ channel is investigated in this thesis. This channel, discussed in detail in Chapter 7, has the advantage of two HWW vertices being present, one for the Higgs production and another one for the decay. In the production vertex, given the impossibility to distinguish between the Z and the W bosons, also polarized Z bosons are considered.

2.3.1.1   Cross-section dependence

The cross-section for various values of the a_L and a_T couplings of the Higgs boson to longitudinal and transverse vector bosons is shown in Figure 2.3(a). The Standard Model is marked with a star at the point $a_L = a_T = 1$. From Figure 2.3(b) the cross-section deviations for a $\pm 30\%$ variation on a_L and a_T can be easily quantified: the cross-section increases to $2.6 \times \sigma_{SM}$ for a variation in a_L of +30%, while it decreases to $0.3 \times \sigma_{SM}$ for a modification of -30%. For small variations of a_T with respect to the SM coupling, the rate is not really sensitive: in the case where $a_T = 1.3$, the cross-section increases by 20%, while for $a_T = 0.7$, it decreases by -10%. The larger sensitivity to a_L is due to the fact that the longitudinal polarization vectors are proportional to energy and therefore dominant in the total cross-section.

2.3.1.2   The $\Delta\phi_{jj}$ angle

Modifications in the couplings, on the other hand, can be distinguished by shapes of kinematical distributions. The kinematic distributions of the two jets, formed by the quarks that characterize the VBF production, are related to the intrinsic structure of the production vertex and carry information about the polarization of the fusing gauge bosons. The distribution sensitive to vector boson polarizations in the initial state is the angle between the two leading jets in the plane perpendicular to the beam, $\Delta\phi_{jj}$, schematically shown
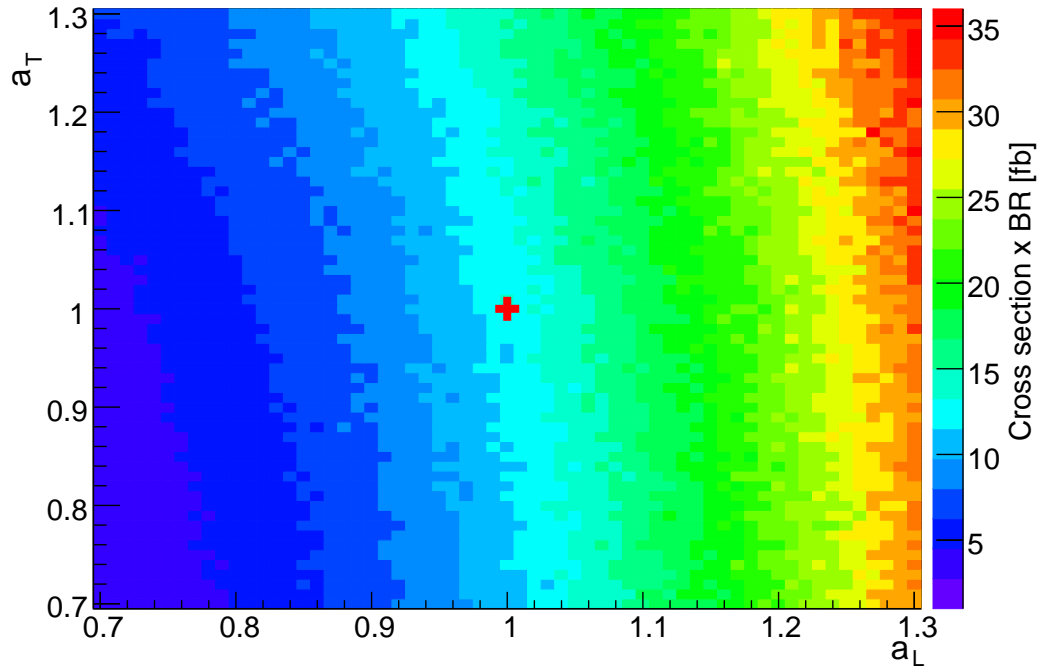
(a)
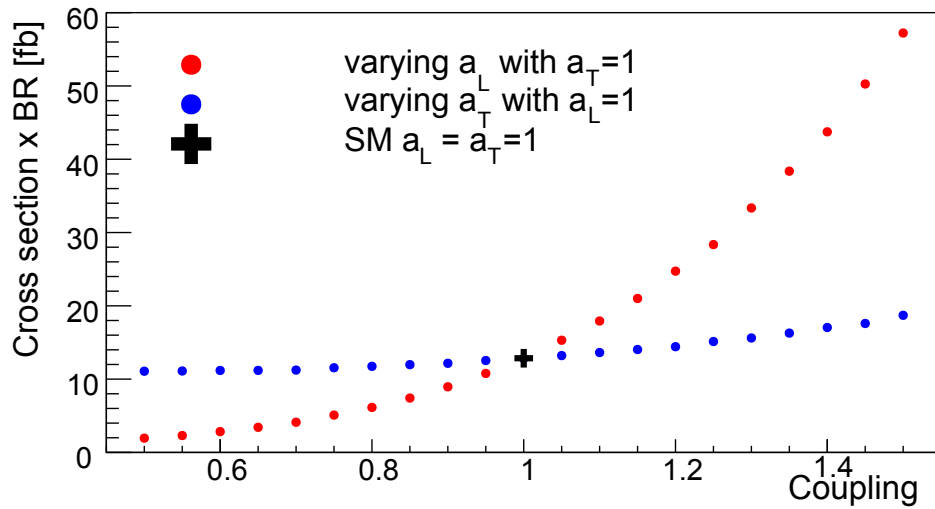
(b)

FIGURE 2.3: Cross-section dependence on a_L and a_T: 2.3(a) both couplings are varied simultaneously, 2.3(b) variation of a_L with $a_T = 1$ (red dots), variation of a_T with $a_L = 1$ (blue dots).

in Figure 2.4. This angle is defined as:

$$\Delta\phi_{jj} = \begin{cases} \phi_{j_1} - \phi_{j_2}, & \text{if } \eta_{j_1} > \eta_{j_2}. \\ \phi_{j_2} - \phi_{j_1}, & \text{if } \eta_{j_2} > \eta_{j_1}. \end{cases} \qquad (2.24)$$
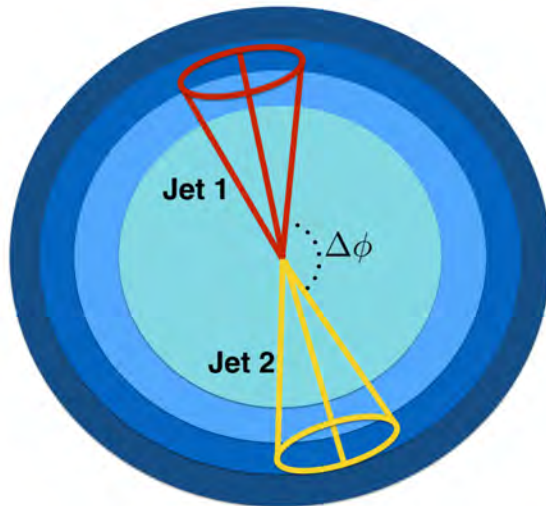
FIGURE 2.4: Illustration of the angle between two leading jets
$\Delta\phi_{jj}$ in the plane perpendicular to the beam.

The shape of this distribution differs with $a_L \neq a_T$ and is shown, at generator level, in Fig. 7.23. The cases where $a_L = a_T$ resemble the SM distribution, while changes in shape are clear when $a_L \neq a_T$.

 The leptonic observables are, on the other hand, sensitive to the decay vertex. Due to the presence of two neutrinos in the final state and one decaying W bosons being off-shell, some angular correlations between charged leptons cannot be reconstructed. Quantities such as the azimuthal angle between the two leptons $\Delta\phi_{\ell\ell}$, the η and the p_{T} of the leptons show much worse discriminating power or no discrimination at all, see Figures 2.6.

2.4   Re-interpretation of the simple model

With the a_L, a_T formalism, the Higgs-gauge sector has been parameterized in terms of independent longitudinal and transverse couplings. The downside of this simple method is that with the choice of a reference frame, the Lorentz invariance is broken, loosing as well gauge invariance. However, as a check of the validity of the model, this a_L, a_T parametrization can be mapped to a more generic approach based on effective field theories and pseudo-observables.

2.4.1   Effective field theories

The effective field theory [23, 35] approach is usually employed to parametrize deviations from the Standard Model in the Higgs-gauge sector, at energy scales (Λ) higher than the ones currently accessible by the experiments. The
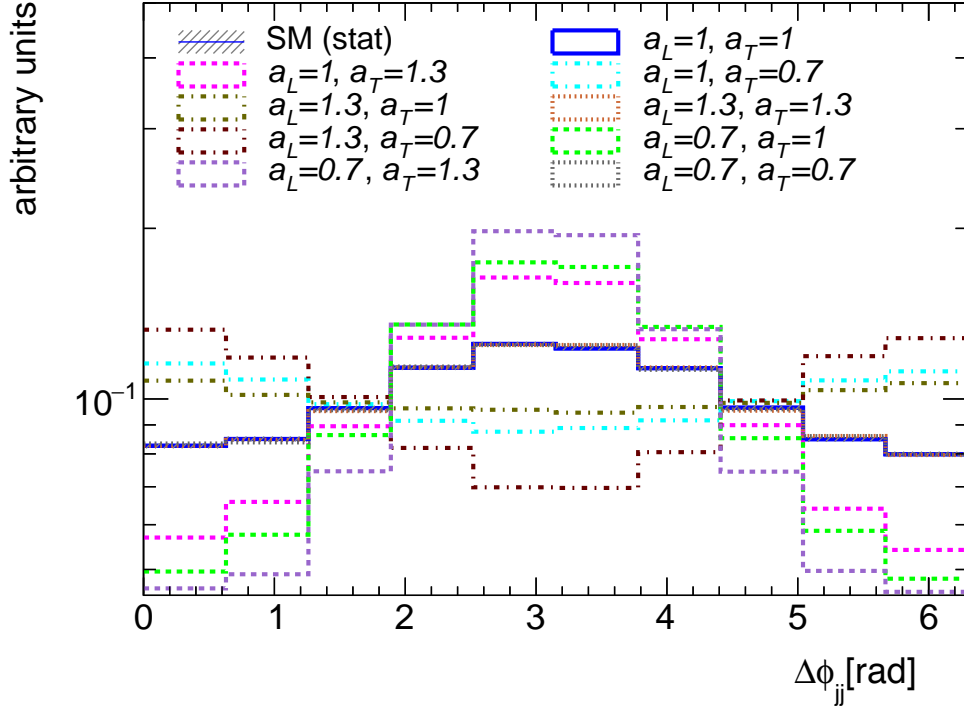
FIGURE 2.5: Truth-level $\Delta\phi_{jj}$ distribution for different pairs of a_L and a_T, in VBF $H \rightarrow WW^*$ events. The black solid line is the SM case ($a_L = a_T = 1$), while the colored dotted lines are 8 BSM cases with $\pm30\%$ variations. All distributions are normalized to unity.

SM Lagrangian is extended with new operators of dimension $D > 4$. The resulting effective Lagrangian has a linearly realized $SU(3)\times SU(2)\times U(1)$ local symmetry and has the same field content as the SM one. These operators are formulated in a ordered expansion with the dimension, where the successive term is suppressed by a larger power of the cutoff scale Λ.

The EFT Lagrangian is expressed as:

$$\mathcal{L}_{\mathrm{EFT}} = \mathcal{L}_{\mathrm{SM}} + \sum_{d>4} \sum_i \frac{c_i^d}{\Lambda^{d-4}} \mathcal{O}_i^d . \qquad (2.25)$$

where $\mathcal{O}_i^d$ is an operator of energy dimension d, and the terms c_i^d are called the *Wilson coefficients*. For a the Higgs field

$$\phi = \frac{1}{\sqrt{2}} \begin{pmatrix} 0 \\ h + v \end{pmatrix}, \qquad (2.26)$$
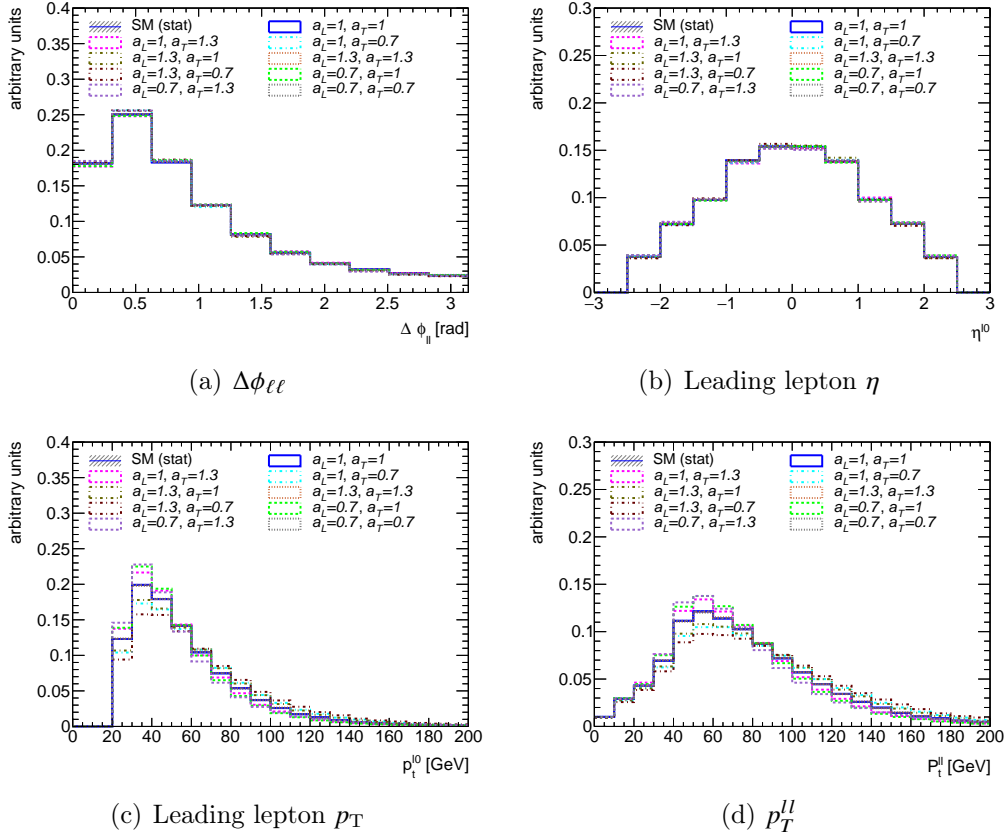
FIGURE 2.6: Truth-level lepton kinematical distributions, in VBF $H \to WW^*$ events, for different pairs of a_L and a_T. The black solid line is the SM case ($a_L = a_T = 1$), while the colored dotted lines are 8 BSM cases with ±30% variations. All distributions are normalized to unity.

and a vacuum expectation value v, the gauge fields related to $SU(2)_L$ and $U(1)_Y$ symmetries are:

$$
\begin{aligned}
\mathbf{W}^\mu &= W_i^\mu \frac{\tau_i}{2}, \\
\mathbf{B}^\mu &= \frac{Y}{2} B^\mu, \\
\mathbf{D}^\mu &= \partial^\mu - ig\mathbf{W}^\mu - ig'\mathbf{B}^\mu, \\
W_{\mu\nu} &= \partial_\mu W_\nu - \partial_\nu W_\mu - ig[W_\mu, W_\nu],
\end{aligned}
\tag{2.27}
$$

where Y is the weak hyper-charge, τ_i are Pauli matrices and g and g' are $SU(2)_L$ and $U(1)_Y$ couplings, respectively. Deviations of the Higgs couplings

described in the previous sections could arise from the following EFT dimension six operators [36, 37]:

$$\mathcal{O}_{\phi W} = -\frac{g^2 F_{\phi W}}{4}\left(\phi^\dagger \phi - \frac{v^2}{2}\right)\text{Tr}[\mathbf{W}_{\mu\nu}\mathbf{W}^{\mu\nu}], \quad \mathcal{O}_\phi = F_\phi\left(\phi^\dagger \phi - \frac{v^2}{2}\right)((\mathbf{D}_\mu\phi)^\dagger\mathbf{D}^\mu\phi),$$

(2.28)

where the coefficients $F_{\phi W}$ and F_ϕ are constant. The $\mathcal{O}_\phi$ operator is related to the renormalization of the Higgs wave function, and its effect is the rescaling of all Higgs boson couplings by a common factor. Instead, the $\mathcal{O}_{\phi W}$ operator directly affects the *HWW* vertex. The operators (2.28) are related to the coupling modifiers a_L and a_T through the following [38]:

$$a_L = 1 + \frac{v^2 F_\phi}{2} + F_{\phi W}q_1 \cdot q_2, \quad a_T = 1 + \frac{v^2 F_\phi}{2} + F_{\phi W}\frac{q_1^2 q_2^2}{q_1 \cdot q_2},$$

(2.29)

where q_1 and q_2 are the four-momenta of incoming *W* bosons. It follows from (2.29) that the proper mapping between coupling modifiers and EFT operators is momentum-dependent.

However, in VBF the four momenta are small in good approximation ($q_1 \cdot q_2 \rightarrow 0$), leading to:

$$a_L = a_T = 1 + \frac{v^2 F_\phi}{2}.$$

(2.30)

Thus, if dim-6 operators are considered, only the $\mathcal{O}_\phi$ operator is probed.

2.4.2 Pseudo-observables

The pseudo-observables framework [39, 40] (PO) defines a set of parameters, well distinct from a theoretical point of view and experimentally accessible, that can characterize possible deviations from the SM in Higgs processes. This framework is build in the same regime of validity of the effective field theories, without outlining a detailed underlying EFT, aiming to reach a more general approach. These pseudo-observables are defined from a decomposition of on-shell amplitudes involving the Higgs boson, under the assumption that there are no new particles lighter than the Higgs boson itself. The VBF production and the four-fermion Higgs decays can be described, neglecting the light fermion masses, by two fermion currents and a three-point correlation function of the Higgs:

$$\langle 0| \mathscr{T}\left\{J_f^\mu(x), J_{f'}^\nu(y), h(0)\right\}|0\rangle ,$$

(2.31)

where only on-shell states are involved. The $h \to 2\ell 2\nu$ decay is characterized by two leptonic currents and a fermionic final state. In VBF production, the quark states are off-shell, however, this "off-shellness", of order Λ_{QCD}, can be neglected, if compared to the EW scale that characterizes the hard process. The procedure to define the PO can be summarized as the following. An expansion around the physical poles is applied to the correlation function in Eq. (2.31), caused by the propagation of intermediate EW gauge bosons. The residues on the poles and the non resonant terms from the expansion define the PO.

For the $h \to \ell \bar{\nu}_\ell \bar{\ell}' \nu_{\ell'}$ process, the amplitude can be decomposed in the following way:

$$\mathscr{A}_{c.c.}\left[h \to \ell(p_1)\bar{\nu}_\ell(p_2)\nu_{\ell'}(p_3)\bar{\ell}'(p_4)\right] = i\frac{2m_W^2}{v_F}(\bar{\ell}_L\gamma_\mu\nu_{\ell L})(\bar{\nu}_{\ell' L}\gamma_\nu\ell'_L)\mathscr{T}^{\mu\nu}(q_1,q_2),$$
(2.32)

where $q_1 = p_1 - p_3$, $q_2 = p_2 - p_4$. Lorentz invariance allows only three possible tensor structures $\mathscr{T}^{\mu\nu}(q_1,q_2)$, to each of which a form factor G can be assigned:

$$\mathscr{T}^{\mu\nu}(q_1,q_2) = \tag{2.33}$$
$$G_L^{\ell\ell'}(q_1^2,q_2^2)g^{\mu\nu} \quad +G_T^{\ell\ell'}(q_1^2,q_2^2)\frac{q_1\cdot q_2\ g^{\mu\nu}-q_2^\mu q_1^\nu}{m_W^2} + G_{CP}^{\ell\ell'}(q_1^2,q_2^2)\frac{\varepsilon^{\mu\nu\rho\sigma}q_{2\rho}q_{1\sigma}}{m_W^2}.$$

In order to define the PO from the residues of the poles, it is necessary to apply a momentum expansion of the form factors around the poles, due to the presence of the gauge bosons. The final decomposition of the form factors can be written as:

$$G_L^{\ell\ell'}(q_1^2,q_2^2) \quad = \quad \kappa_{WW}\frac{(g_W^\ell)^* g_W^{\ell'}}{P_W(q_1^2)P_W(q_2^2)} + \tag{2.34}$$

$$+ \quad \frac{(\varepsilon_{W\ell})^*}{m_W^2}\frac{g_W^{\ell'}}{P_W(q_2^2)} + \frac{\varepsilon_{W\ell'}}{m_W^2}\frac{(g_W^\ell)^*}{P_W(q_1^2)},$$

$$G_T^{\ell\ell'}(q_1^2,q_2^2) \quad = \quad \varepsilon_{WW}\frac{(g_W^\ell)^* g_W^{\ell'}}{P_W(q_1^2)P_W(q_2^2)}, \tag{2.35}$$

$$G_{CP}^{\ell\ell'}(q_1^2,q_2^2) \quad = \quad \varepsilon_{WW}^{\text{CP}}\frac{(g_W^\ell)^* g_W^{\ell'}}{P_W(q_1^2)P_W(q_2^2)}, \tag{2.36}$$

where $P_W(q^2)$ is the W propagator and g_W^f are effective couplings determined from data using on-shell W decays. The resulting Pseudo Observables, that

can be extracted from physical observables, are: the fermion-independent POs associated to a double pole structure κ_{WW}, ε_{WW} and $\varepsilon_{WW}^{\mathrm{CP}}$, that are real couplings, and the fermion-dependent complex term $\varepsilon_{W\ell}$, that can point to new physics scenarios as flavor non-universality. In the SM at tree-level the values of these couplings are:

$$\kappa_{WW}^{\mathrm{SM-tree}} = 1 \ , \qquad \varepsilon_{WW}^{\mathrm{SM-tree}} = 0 \ . \tag{2.37}$$

The a_L and a_T couplings can be mapped into the above-defined pseudo-observables κ_{WW} and ε_{WW}, with the following relations [41]:

$$a_L = \kappa_{WW} + \Delta_L(q_1, q_2)\varepsilon_{WW}, \quad a_T = \kappa_{WW} + \Delta_T(q_1, q_2)\varepsilon_{WW}. \tag{2.38}$$

The functions $\Delta_L(q_1, q_2)$ and $\Delta_T(q_1, q_2)$ depend on the momenta of the W bosons, either in the Higgs production or in the decay.
In VBF $H \rightarrow WW^*$ the momenta of the W bosons are small to a good approximation and in the limit $q_1, q_2 \rightarrow 0$

$$\Delta_L(q_1, q_2) \rightarrow 0, \quad \Delta_T(q_1, q_2) \rightarrow \frac{m_H^2}{2m_W^2}. \tag{2.39}$$

From the Eq. 2.38 and 2.39 follows that

$$a_L \simeq \kappa_{WW} \ \text{ and } \ a_L - a_T \simeq -\frac{m_H^2}{2m_W^2}\varepsilon_{WW}. \tag{2.40}$$

The two interpretations in terms of EFT operators and in terms of pseudo-observables are equivalent, and, for the measurement of the polarized couplings a_L and a_T discussed in this thesis, the two coupling parameters have been also mapped into POs, as shown in Chapter 8.

The ATLAS detector

The data analyzed in this thesis have been collected by the ATLAS (*A Toroidal Lhc ApparatuS*) detector during 2015 and 2016. The ATLAS experiment[42, 43] is a general purpose detector and one of the four main Large Hadron Collider (LHC) experiments. ATLAS, in order to test the Standard Model and to search for new physics, precisely detects electrons, muons, photons and jets in broad kinematic regions. In this chapter, after a short description of the LHC accelerator, a general overview of the ATLAS main components is given, with particular emphasis to the sub-detectors and their characteristics relevant for the studies described in this thesis.

3.1 The Large Hadron Collider

The LHC is the largest and most powerful particle collider ever built. It is located at CERN (*European Organization for Nuclear Research*) in Geneva, Switzerland and it is placed in the 27 km long, 100 m underground, tunnel that previously was hosting the *Large Electron Positron Collider* (LEP) [44, 45].

The LHC is operative since 2010 and it has been designed to collide protons at a maximum center-of-mass energy of 14 TeV. It operated from 2010 to 2011 at $\sqrt{s}$ = 7 TeV, reaching $\sqrt{s}$ = 8 TeV in 2012. This activity period is usually referred to as Run 1. After a technical stop of two years, the Run 2 period took place from 2015 to 2018, with a raise of the center-of-mass energy up to 13 TeV. The LHC is also designed to collide heavy ions, such as lead nuclei with other Pb nuclei or with protons. For the studies discussed in this thesis only $p - p$ collisions are taken into account.

Before being injected in the LHC, the colliding protons pass through a chain of pre-accelerators. Protons are produced from ionized hydrogen atoms that

have their valence electron stripped off. They are afterwards accelerated to 50 MeV in the Linac-2 and then injected into a series of three accelerators, schematically shown in Figure 3.1: the Proton Synchrotron Booster (PSB), the Proton Synchrotron (PS) and the Super Proton Synchrotron (SPS). In the PSB, protons are accelerated to 1.4 GeV, while, in the PS and in the SPS, to 25 GeV and 450 GeV per beam, respectively. They are consequently injected in the LHC in bunches: the design number of protons in one bunch is 1.15×10^{11} and each beam is composed of up to 2808 bunches. The space between proton bunches in the beams can be lowered up to 25 ns. In order to reach the designated energy of 7 TeV per beam, each proton bunch is accelerated by eight super-conducting Radio Frequency cavities. The circular trajectory is maintained thanks to 1232 superconducting dipole magnets that operate at a temperature of 1.9 K, reaching a magnetic field of 8.3 T. In order to focus and stabilize the beam, a total of 392 quadrupole magnets are installed.

The two proton beams circulate in two beam pipes and collide in four interaction points, where the main LHC experiments are installed: ATLAS [42, 43], CMS (Compact Muon Solenoid) [46], LHCb (LHC beauty) [47] and ALICE (A Large Ion Collider Experiment) [48].
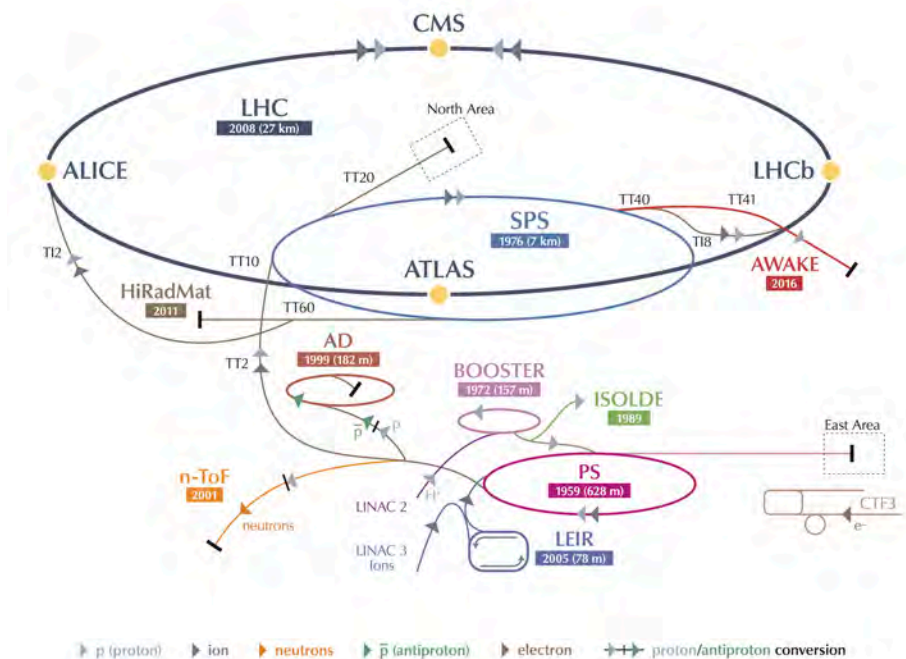
FIGURE 3.1:   The LHC accelerator complex, figure from Ref. [49].

(a) (b)
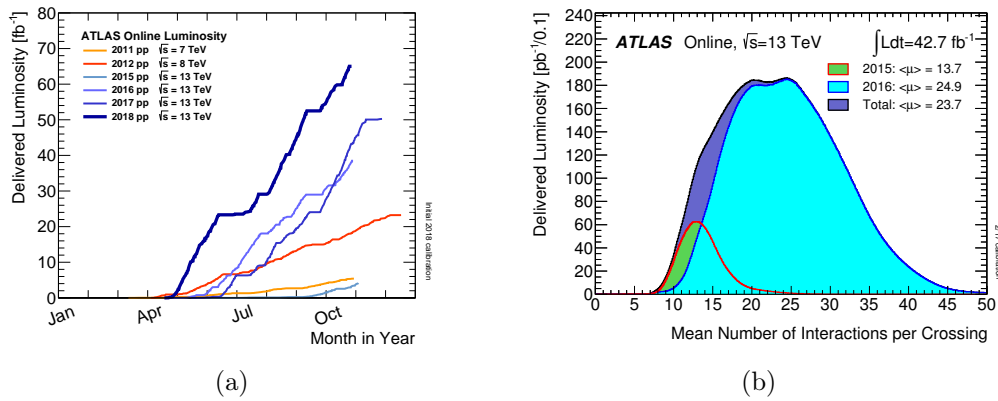
FIGURE 3.2: Fig. 3.2(a) shows the cumulative luminosity as a function of time delivered to ATLAS during stable beams for each year of Run 1 and Run 2 data taking periods. In Fig. 3.2(b) the luminosity-weighted distribution of the mean number of interactions per crossing for the 2015-2016 data at $\sqrt{s}$ =13 TeV is shown. The integrated luminosity and the mean *mu* value are shown for all the data delivered to ATLAS during stable beams. Figures from Ref. [50]

Luminosity and pile-up Luminosity is an important parameter of the LHC. It is defined as:

$$L = \frac{n_B N_p^2 f_{rev}}{4\pi\sigma_T^2} F. \tag{3.1}$$

In this equation N_p stands for the number of particles per bunch, while the number of bunches per beam is n_B; f_{rev} is the revolution frequency and σ_T is the transverse beam size at the interaction point. F is a parameter that takes into account of the luminosity reduction caused by the crossing angle at the interaction point.

The LHC has been designed to discover rare processes. The production rate of an event is given by $N = \sigma \cdot \mathcal{L}$, where σ is the cross section of the process (that depends on the center-of-mass-energy) and $\mathcal{L}$ is the integrated luminosity, that is measured in unit of inverse barn, $b^{-1} = 10^{24} cm^{-2}$, and is defined as:

$$\mathcal{L} = \int L \, dt \tag{3.2}$$

In Fig. 3.2(a) the cumulative luminosity is shown, delivered to ATLAS during stable beams, for each year of data taking time during Run 1 and Run 2. Since each bunch contains a large number of protons, in addition to the $p-p$ collision that triggers the event, several others $p-p$ collisions can happen. All the collisions that take place in addition to the one of interest are referred

to as *pile-up* collisions. In a bunch crossing, the number of $p - p$ interactions follows a Poisson distribution. The mean value of this distribution, referred to as μ, decreases during a fill with the beam intensity and with the increase of the emittance. In data μ is calculated as:

$$\mu = \frac{L \, \sigma_{inel}}{n_b \, f_{rev}} \qquad (3.3)$$

in this equation, L is the luminosity, σ_{inel} is the total inelastic cross-section, that has been estimated with PYTHIA to be 80 mb for 13 TeV collisions, n_b is the number bunches and f_{rev} is the LHC revolution frequency. The peak value, μ_{peak}, is the highest value of μ achieved in a single bunch crossing at the start of the stable beam period of the fill. The number of interactions in each bunch is not constant, but varies between bunches, and its average over all bunch crossings and over the luminosity is referred to as $< \mu >$. Fig. 3.2(b) shows the total delivered luminosity as a function of the mean number of interactions per crossing $< \mu >$ for the 2015-2016 data at $\sqrt{s} = 13$ TeV.

3.2   The ATLAS detector

The ATLAS detector is one of the main four experiments at the LHC; it has been designed to allow general purpose studies covering a broad range of physics processes, from BSM studies to precision SM measurements. It is the largest among all the others LHC detectors: it has a cylindrical shape, with a diameter of 25 m, length of 44 m and an overall weight of ~7000 tonnes. It is forward-backward symmetric with respect to the interaction point, covering the detection of particles in a solid angle of 4π thanks to the sub-detectors that are concentrically installed in layers around the interaction point.

A schematic illustration of the detector is given in Figure 3.3. Its main components are, starting from the sub-detector closer to the LHC beam pipe, the Inner Detector (ID), a solenoid magnet, the Electromagnetic Calorimeter (ECal), the Hadronic Calorimeter (HCal), the Muon Spectrometer (MS) and three toroidal magnets.

The origin of the ATLAS coordinate system is the nominal interaction point, while the z-axis is set along the beam direction and the $x - y$ plane is transverse to the beam direction. The positive part of the x-axis points from the interaction point to the center of the LHC ring, while the positive y-axis points upwards. Due to the cylindrical shape of the detector, a polar
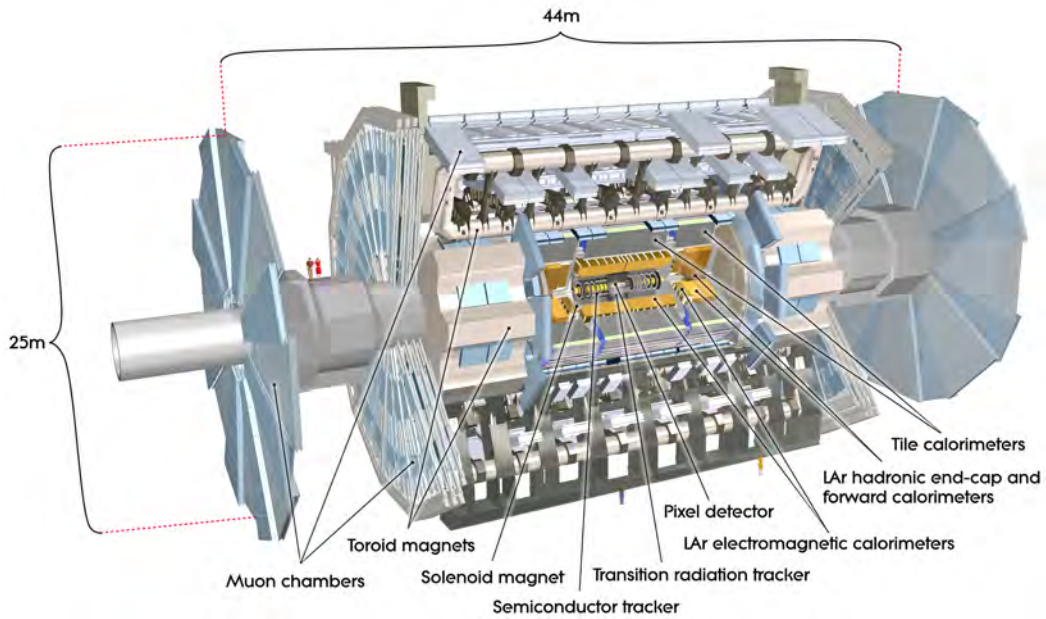
FIGURE 3.3: Illustration of the ATLAS detector, from Ref. [51].

coordinate system is used, with the azimuthal angle $\phi \in [-\pi, +\pi]$ measured around the beam axis, and the polar angle, $\theta \in [0, \pi]$, measured from the beam axis. To describe the position of a particle the pseudorapidity is also employed, defined as

$$\eta = -ln\,tan(\theta/2), \tag{3.4}$$

which in the massless assumption ($E >> m$) coincides with the rapidity

$$Y = \frac{1}{2}ln\frac{E + p_z}{E - p_z} \tag{3.5}$$

that is Lorentz boost invariant and used for massive objects. In the transverse plane $x - y$, a set of experimental quantities can be defined: the transverse momentum $p_T = p\,sin\theta$ and the transverse energy $E_T = E\,sin\theta$. The distance in the pseudorapidity-azimuthal angle space is $\Delta R = \sqrt{\Delta\eta^2 + \Delta\phi^2}$.

The ATLAS detector can be divided in three main sections: two *End-caps* and one *Barrel*. The last one is the cylindrically symmetrical part of the detector, with a pseudorapidity coverage of $|\eta| < 1.4$. The two *End-caps*, instead, are the two circular structures that are placed at the two sides of the *Barrel*. They cover a pseudorapidity range of $1.5 < |\eta| < 5$.

3.2.1   The Inner Detector

The ATLAS Inner Detector (ID) measures the tracks of the passing parti-
cles, providing a robust and hermetic pattern recognition and performing the
measurement of primary and secondary vertices with an excellent momentum
resolution (see Sec. 6.1). It is surrounded by the solenoid magnet that pro-
vides a magnetic field of 2T in the direction of the beam axis. This magnetic
field allows the measurement of the p_T of the charged particles thanks to the
trajectory curvature.
The ID is made up of three layers: closer to the beam there are two silicon-
based detectors, the Pixel detector and the Semiconductor Tracker (SCT),
while the outermost layer is the Transition Radiation Tracker (TRT). An
illustration of the barrel and endcap layers of the ID is given in Fig. 3.4

The Insertable b-layer   The Insertable b-layer [54] is a layer of the Pixel
detector that has been installed during the 2013-2014 shutdown. The increase
of luminosity from Run 1 to Run 2 caused a significant radiation damage to
the inner layers to the detector: this extra layer was inserted with the main
aim of avoiding losses of tracking efficiency, especially in tagging the decay of
the beauty quark. With its insertion, the distance between the first detector
subsystem and the interaction point is reduced from approximately 5 cm to
3.3 cm: this improves the determination of the track impact parameters and
also the capability of reconstructing secondary vertices (see Sec. 6.1). The
pixel size is $50{\times}250\mu m^2$ and provides a resolution of 47 μm in the longitudinal
direction and 8.5 μm in the transverse one. The pseudorapidity coverage of
the b-layer is up to $|\eta| < 3$.

The Pixel detector   The Pixel detector [55] is composed of 1744 modules,
with a total of 80.4 million readout channels and has a coverage of $|\eta| < 2.5$.
The modules are installed in three layers in the barrel and in three disks
in the end-caps. The innermost barrel layer is called Pixel B-Layer, while
the other two are referred to as Layer-1 and Layer-2. Each pixel module is
composed by 16 front-end (FE) electronics chips with 2880 channels and a
n-type pixel sensor with size of 50×400 μm^2 and thickness of 250 μm. The
hit resolution of each module is 115 μm in the longitudinal direction and 10
μm in the transverse one.

The Semiconductor Tracker   The Semiconductor Tracker (SCT) [56, 57]
is a silicon micro-strip tracker consisting of 4088 two-sided modules and over
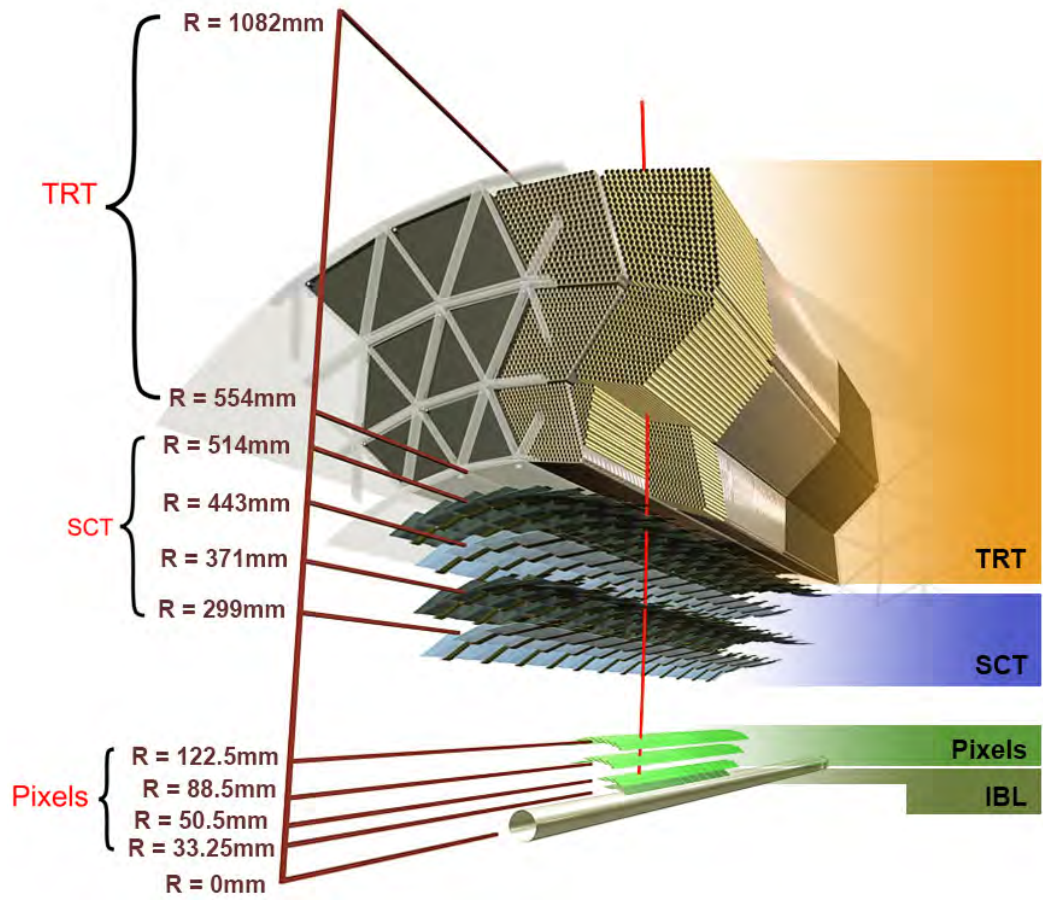
(a)
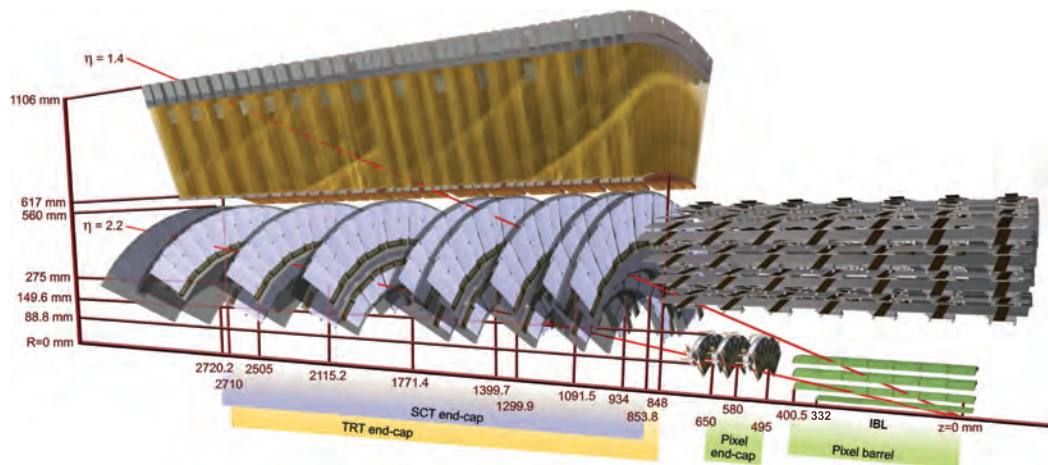
(b)

FIGURE 3.4: Illustrations of the ATLAS ID barrel 3.4(a) and endcap 3.4(b) with the Pixel, SCT and TRT sub-detectors. Figures adapted from [52, 53].

6 million implanted readout strips and covers a pseudorapidity region up to $|\eta| < 2.5$. Four cylinders with radius of respectively 30.0, 37.3, 44.7 and 52.0 cm form the SCT barrel. Each layer is constituted by several longitudinal staves on which the modules are installed.

The SCT end-caps are composed of nine disks, on which the modules are placed in the radial direction.

The basic unit of the SCT is a module: each module contains two single sided silicon microstrip sensors mounted back to back with a 40 mrad stereo-angle: this provides a measurement of the z coordinate along the strip length with a resolution of 580 $m\mu$. The azimuthal angle and the radial distance r from the beam axis, that are fundamental for the determination of the transverse momentum, are measured with high precision in the barrel and the end-caps, with a resulting resolution of 17 $m\mu$ in the r–ϕ coordinate. The barrel module sensors are rectangular, with an area of 64.0×63.6 mm^2, and their strips are nearly parallel to the beam axis, while the end-cap ones are fan-shaped with strips placed radially from the beam axis. The silicon sensors are of 285 μm thick n-type sensors with 768 micro-strips. The pitch of the barrel strips is 80 μm, while endcap one varies from 55 to 95 μm [58, 59]. The silicon sensors are read out by front-end ASICs called "ABCD3TA" [60]. Each one of the 128 channels in the chip have a preamplifier and a shaper with a time constant of 25 ns. All of the channels contain a comparator with an adjustable threshold and a digital pipeline that allows to store the data for about 3 ms while waiting for a trigger decision.

The Transition Radiation Tracker   The last part of the ID is the TRT [61], that has as main components drift tubes (straws) of 4 mm diameter filled with a gas mixture of Xe (70%)- CO_2 (27%) and O_2 (3%). As anode the tubes have installed a gold plated tungsten wire with a diameter of 31 μm. In the barrel the drift tubes are 144 cm long and are organized in 73 modules, such that the straws are interleaved with polypropylene fibers, serving as the transition radiation material, and are parallel to the beam line. In the end-caps they are installed radially in 160 layers interleaved with polypropylene foils. The TRT is characterized by less readout channels, only 351000, compared to the other two sub-detectors. It provides on average 36 hits per track in the region $|\eta| <$ 2, allowing the measurement of long trajectories. Each channel can measure one track hit coordinates, z in the end-cap and r–ϕ in the barrel, with a spatial resolution of 130 $m\mu$ per straw. The TRT is also designed to provide informations for electron identification, helping the discrimination between

electrons and charged hadrons with the detection of transition-radiation photons in the straw tubes. The transition radiation of a particle depends on E/m, therefore an electron will generate more radiation than, for example, a charged pion.

3.2.2 The Calorimetry System

The electromagnetic and the hadronic calorimeters form the ATLAS calorimetry system, that is represented in Fig 3.5. The system covers a pseudorapidity range of $|\eta| < 4.9$ and is symmetric in ϕ, providing a complete coverage around the beam axis. The ECAL, in the pseudorapidity region that is matched with the ID, presents a very fine segmentation for precision measurements of electrons and photons, while the hadronic and forward calorimeters have a lower granularity that is anyhow sufficient to perform jet reconstruction and E_T^{miss} measurements.

The ECAL thickness is 22 radiation length for electromagnetic interactions (X_0), while the HCal is deep 11 nuclear interaction lengths (λ). The thickness of the calorimeters is an important characteristic as it is directly linked to the containment of the showers created by the incident particles: if the absorbers are too thin, it can happen that some of the particles from the showers escape the calorimeters and penetrate into the muon spectrometer, where they are falsely detected as muons. These effects are usually referred to as *punch-through* and can result in lowered energy resolution in the calorimeters.

The electromagnetic calorimeter (ECAL) The ECAL [63] is a sampling calorimeter that uses as active material liquid argon (LAr) and lead plates as absorber. The liquid argon ensures homogeneity, a stable response over time and has a good resistance to radiation. The absorber plates have an accordion shape to prevent cracks in the azimuthal direction, providing good uniformity and a complete symmetric coverage over ϕ. The ECAL covers up to $|\eta| < 3.2$: it is formed by a barrel section, at $|\eta| < 1.475$, made of two half barrels joined at $\eta = 0$ and two end-caps, at $1.375 < |\eta| < 3.2$. A presampler is installed in the cryostat in front of the EM calorimeter for $|\eta| < 1.8$; this is a thin layer of argon with no lead absorber in front, with the purpose of correcting for the energy losses in the ID, in the solenoid and in the cryostat wall. The ECAL modules are formed by three layers in depth: the first layer is $4.3X_0$ thick and presents a good granularity $\Delta\eta \times \Delta\phi = 0.003 \times 0.1$. This layer ensures a precise measurement of the energy deposit of EM showers, energy that is afterwards absorbed by the second layer, with depth $16X_0$.
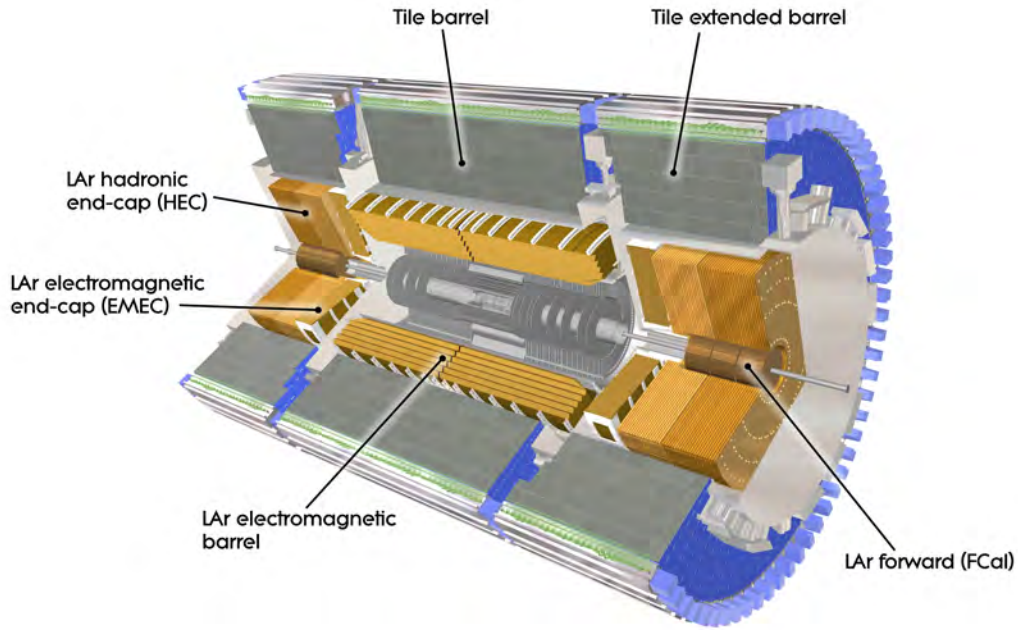
FIGURE 3.5: Illustration of the ATLAS calorimetry system,
from Ref. [62].

The last layer, since it is reached by only electrons with higher energy, is less segmented in η and thinner ($2X_0$). The total energy resolution of the ECAL is $\frac{\sigma_E}{E} = \frac{10\%}{\sqrt{E[GeV]}} \oplus 0.7\%$.

The hadronic calorimeter (HCAL) The ECAL is surrounded by the hadronic calorimeter HCAL [64], that measures the energy deposits of the hadronic showers. This sub-detector has three main constituents: the Tile calorimeter, the LAr hadronic endcap calorimeter (HEC) and the LAr forward one (FCal). The Tile calorimeter, that covers the range $0 < |\eta| < 1.7$, is a sampling calorimeter that employs steel as absorber and scintillating tiles as active material. It is extended to larger pseudo-rapidities ($1.5 < |\eta| < 3.2$) by the HEC, which uses copper as absorber and LAr as active material and is composed by two wheels per end-cap. The last part of the HCAL, the forward calorimeter ($3.1 < |\eta| < 4.9$), is composed by three modules in each end-cap and has a depth of 10 interaction lengths; the active medium is liquid argon and the first module, that is optimized for EM measurements, employs copper as absorber, while the remaining two, that measure the energy of hadronic interactions, use tungsten. The total energy resolution of the HCAL is $\frac{\sigma_E}{E} = \frac{50\%}{\sqrt{E[GeV]}} \oplus 3\%$ in the barrel and endcap ($|\eta| < 3.2$), and

$\frac{\sigma_E}{E} = \frac{100\%}{\sqrt{E[GeV]}} \oplus 10\%$ in the forward region.

3.2.3   The Muon spectrometer

Muons pass through the calorimeters unstopped, loosing only a small amount of energy. The Muon Spectrometer (MS) [65], placed right outside the calorimeters, is equipped with a system of high-precision tracking chambers and trigger for the measurement and identification of the muons in the pseudorapidity range $|\eta| < 2.7$ and p_T range 3 GeV - 1 TeV.

The toroid magnets provide an azimuthal magnetic filed that deflects the tracks of the muons allowing the measurement of the muon momentum. Muon tracks are bent thanks to the large barrel toroid, with a bending power of 1.5 to 5.5 Tm in the range $|\eta| < 1.4$, while in $1.6 < |\eta| < 2.7$, thanks to the end-cap magnets, with bending power from 1.0 to 7.5 Tm. A combination of the endcap and barrel fields ensures the magnetic deflection, with reduced bending power, for the transition region $1.4 < |\eta| < 1.6$.

An overview of the MS system is given in Fig 3.6: the MS is made of planar elements, referred to as stations or chambers, that are installed in the area covered by the toroids. These stations can be either precision tracking chambers, that mainly provide the track coordinate in the bending plane, or trigger chambers, that are characterized by a coarser spatial resolution but present a very fast response time ($< 25ns$). Their main aim is to provide trigger signals and timing information for the event. The MS provides a resolution of the muon p_T of $\frac{\sigma_{p_T}}{p_T} = 10\%$ at $p_T = 1$ TeV and 3.5% at $p_T = 200$ GeV.

Precision chambers   Precision-tracking chambers are high precision detectors with the aim of determining the muon tracks in the η bending plane $(r - z)$. An accurate determination of the muon p_T is achieved thanks to a precise measurement of the η position in the barrel region. This is done by the Monitored Drift Tube (MDT) chambers, that are placed between and on the eight coils of the barrel toroid magnets. The MDTs cover the up to $|\eta| < 2.7$, with the exception of the innermost end-cap layer that is limited to $|\eta|<2$. Each chamber is composed of three to eight layers of drift tubes, filled with a mixture of argon and CO_2 (93/7%) and, as anode, a tungsten-rhenium wire with 50 μm of diameter. An average resolution of 80 μm per tube can be achieved in the z-direction, resulting in a resolution of 35 μm per chamber. Cathode-Strip Chambers (CSC) are trapezium-shaped multi-wire proportional chambers that allow a simultaneous measurement of both η and ϕ

MDT chambers

Resistive plate chambers

Barrel toroid coils

End-cap toroid

Inner detector

Calorimeters

(a)

MDT chambers

Resistive plate chambers

Barrel toroid coil

Thin gap chambers

End-cap toroid

Cathode strip chambers

Radiation shield

12 m

10

8

6

4

2

0

20   18   16   14   12   10   8   6   4   2 m

(b)
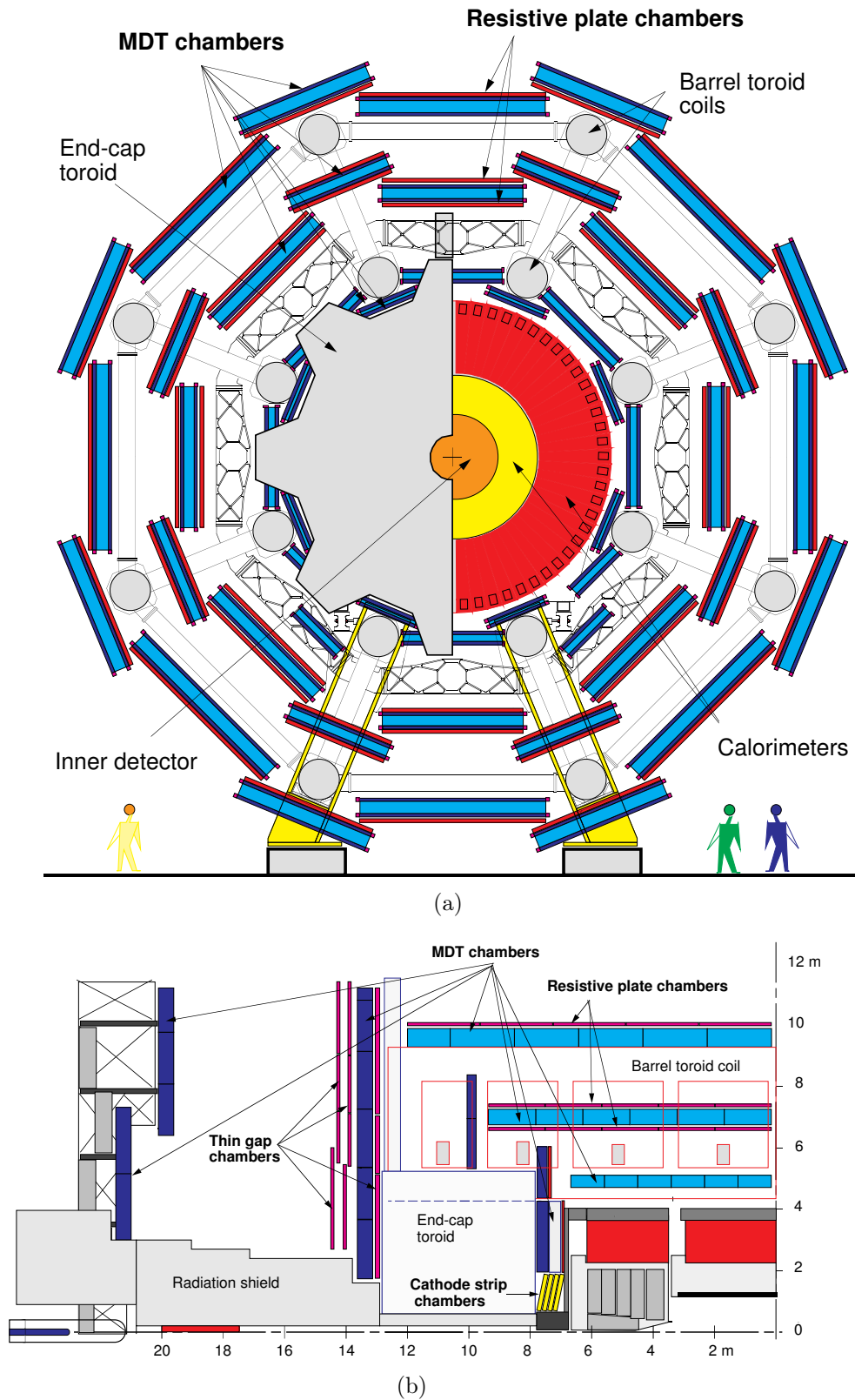
FIGURE 3.6: In Fig. 3.6(a) the cross-section of the barrel MS perpendicular to the beam axis is shown, while in Fig. 3.6(b) a quadrant of the MS in the $r-z$ plane parallel to the beam axis. Figures from [65].

track coordinates. The cathode strips are segmented in either the ϕ or η directions and are perpendicular to the wires that are oriented radially. The CSC are employed in the innermost tracking layer in the region $2 < |\eta| < 2.7$, for their better time resolution and their capability to sustain higher rates, thanks their reduced maximum drift time of 40 ns with respect to the MDTs (700 ns). The resolution of a chamber is 40 μm in the $r - z$ bending plane and about 5 mm in the plane transverse to the beam axis; this difference in the resolution is due to the fact that the azimuthal readout is parallel to the anode wires and due also to a different readout pitch.

Trigger chambers The trigger for the muons in the barrel region is provided by the Resistive Plate Chambers (RPC) in the region $|\eta| < 1.05$. Two RPC stations are installed on the middle barrel MDT chambers and one on the outer barrel chambers. They provide the second coordinate (ϕ) for the MDT measurements. Two measurements in η and ϕ are performed in each one of the RPC stations, for a total of six measurements per muon passing through the barrel spectrometer, with a resolution, in both the bending and the non-bending plane, of 10 mm and a time resolution of 1.5 ns. A RPC unit is composed by two Bakelite plates kept apart from each other by insulating spacers and filled with a drift gas, a mixture of $C_2H_2F_4/IsoC_4H_{10}/SF_6$ (94.7/5/0.3 %). The signal is read out via two orthogonal copper strips.
The Thin Gap Chambers (TGC) are multi-wire proportional chambers, that provide the trigger for the end-cap wheels, covering the forward region $1.05 < |\eta| < 2.7$. The TGC provides a measurement in both ϕ and η coordinates, with a spatial resolution of 3-7 mm in the bending plane and a timing resolution comparable to the RPC chambers. The TGCs are formed by four layers, one innermost and three in the end-cap. The chambers employ a gas mixture of CO_2/C_5H_{12} (55/45 %) and, for a fast collecting time, the distance between the wire and the cathode is smaller than the distance between two wires.

3.2.4 The Trigger and Data Acquisition System

The decision whether keeping or discarding a given event is taken by the ATLAS trigger system. The growth of the center-of-mass energy, of the luminosity and pile-up interactions during Run 2 resulted in an increase of a factor five of the rates with respect to Run 1. Therefore, during the LHC long shutdown, the trigger system went through some major upgrades. The Run 2 trigger system consists of an hardware-based first level trigger, referred to as Level-1 trigger, and a software-based high level trigger (HLT).

In Fig. 3.7 a schematic overview of the ATLAS trigger and data acquisition system is shown.
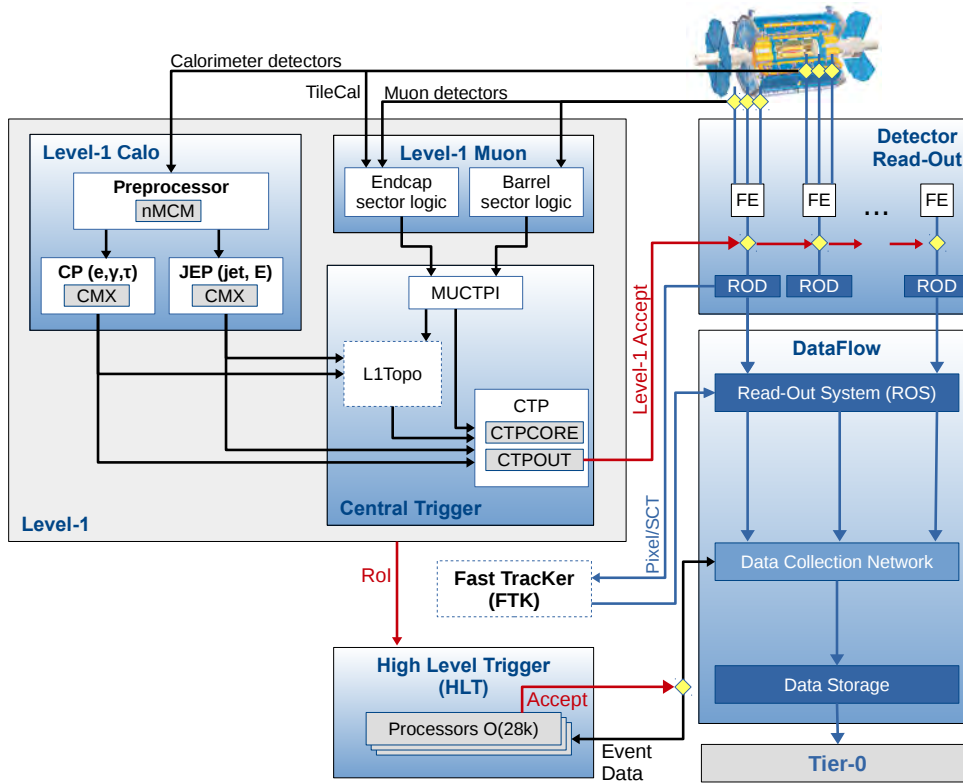
FIGURE 3.7: The ATLAS Trigger and Data Acquisition (TDAQ) system. FTK was installed in 2017 and not used for the data studied in this thesis. From Ref. [66].

Level-1 trigger   The L1 trigger is an hardware-based trigger that performs a fast selection of events with interesting signatures in a time window of about 2.5 μs. During this decision time, pipeline memories save the detector informations coming from the fast muon trigger chambers and the calorimeters. Three main components are part of the L1 trigger: the L1 calorimeter trigger (L1Calo), the L1 muon trigger (L1Muon) and the central trigger processor (CTP).

The L1 trigger analyzes informations coming from the MS trigger chambers and the energy deposits in the calorimeter trigger towers. L1Calo triggers on E_T^{miss}, taus, electrons or photons and jets, while L1Muon on muons. The CTP takes the trigger decision based on the information provided by the L1Calo and L1Muon, forming Regions-of-Interest (RoIs), that are defined as the $\eta - \phi$ detector regions where interesting activity has been found. These RoIs are

then passed to the HLT trigger. Thanks to the L1 trigger, the event rates are reduced from approximately 30 MHz to 100 kHz.

In 2017, a L1Topo trigger [67] has been added to obtain topological triggers that uses the combined kinematic informations from both calorimeter objects and muons, in order to trigger, for example, di-jet events from vector boson fusion or di-muon events originating from *b*-hadrons decays. For the data analyzed in this thesis the topological triggers have been not used.

HLT trigger The HLT is a software-based trigger that employs as input the RoIs provided by the Level-1 trigger. Thanks to sophisticated selection algorithms, the HLT studies in detail the informations coming from the different signatures, the energy and the coordinates in either the RoI or in the whole event. The reduction of the event rate, from Level-1 to HLT, is from 100 kHz to approximately 1 kHz, with a processing time of about 200 ms.

Starting from the 2017 data, the tracking algorithms will include a new fast hardware-based tracking, the Fast TracKer (FTK) [68], designed to perform a global track reconstruction receiving inputs from the ID after the Level-1 trigger, providing to the HLT a full-event track information. It improves trigger selections that require the full-event tracking information, as the b-jets reconstruction.

The Trigger Menu The trigger menu determine the list of L1 and HLT triggers. It consist of different kind of triggers, depending if used for physics analyses or for detector calibrations. A trigger is defined *unprescaled* if all the triggered events are saved. If a trigger object presents a high rate, due to looser selection (for example a loose cut on the p_T or on the energy), a *prescaling* is applied to adjust the overall output rate from the L1 and HLT triggers. A prescaling algorithm assigns a prescale factor to each item allowing the possibility to disable the triggers or to accept only a certain fraction of events. For example, if the prescale factor is equal to 3 every third triggered event is saved.

The trigger nomenclature in ATLAS is made by adding to the trigger level (L1 or HLT) different characteristics of the specific trigger, such as the particle type, the p_T threshold expressed in GeV or the isolation requirements. To each HLT trigger corresponds an L1 trigger as seed: if a HLT trigger has associated more than one L1 seeds, the seed is added in the suffix. For

example, HLT_mu20_L1MU15 requires a muon with p_T greater than 20 GeV, with L1_MU15 as seed.

Data processing   Each one of the sub-detectors contains a buffer pipeline, that allows the storage of the data while waiting for the L1 trigger decision. After this decision, the data is transmitted off the detector through readout links. The signals, after digitization, are sent to the data acquisition (TDAQ) system [69]. At first, the TDAQ stores the data in local buffers, while waiting for the HLT trigger. The selected events are then stored in the RAW data format. Furthermore, reconstruction algorithms and calibrations are applied to the data and the *Analysis Object Data* (AOD) are formed, that contain the informations necessary for the analyses (muons, electrons, jets...).
During stable beams, when all the ATLAS subsystems are ready, data taking can start. To a single LHC fill correspond one or more runs that are labeled with an unique number. Each run usually covers a data taking a period in the range of hours up to a day and is divided into luminosity blocks. A block corresponds to a data taking time of the order of a minute, where the luminosity can be approximated as constant. The physics analyses refer to the so-called *Good Runs List*, that contains the list of all the luminosity blocks in which no issue in the sub-detectors has been registered.

Test beams for ITk

High Luminosity LHC (HL-LHC) is the upgrade project for LHC that will be operative from 2026. It will provide an increase of instantaneous luminosity of $7.5 \times 10^{34} cm^{-2} s^{-1}$, corresponding to approximately 200 inelastic p-p collisions per bunch crossing. In around ten years, ATLAS will aim to reach the record integrated luminosity of 3000 fb^{-1}.

HL-LHC will help studying BSM physics at the TeV scale and also will lead to a better precision on the measurement of the Higgs boson properties.

As shown in Figure 4.1, a maximum center-of-mass energy of $13-14$ TeV can be achieved during Run 2, with an expected reach of the design luminosity of $10^{34} cm^{-2} s^{-1}$. However, LHC exceeded this target reaching $2.06 \times 10^{34} cm^{-2} s^{-1}$, twice the nominal value. Between 2015 and 2018, this yielded to a total integrated luminosity of 13 TeV p-p data of about $150 fb^{-1}$. After 2020, without a sizable increase in luminosity, the statistical gain in running the accelerator will become minimal: ten years of run would be needed to reduce by fifty percent the statistical error in the measurements [70]. Starting form the Long Shutdown 2 (2019-2020) but especially during the Long Shutdown 3 (2024-2026), some modifications will be realized to increase the luminosity, including upgrades in the hardware components and the replacement of the LHC inner triplet magnets.

In order to face this high luminosity challenge and improve the detector performances, ATLAS will have to deal with structural modifications and technical improvements [71]. Development and characterization studies of the new detector components are therefore extremely important. For this purpose, test beams represent a very practical and complete way to test the prototypes behavior and measure their physical properties.
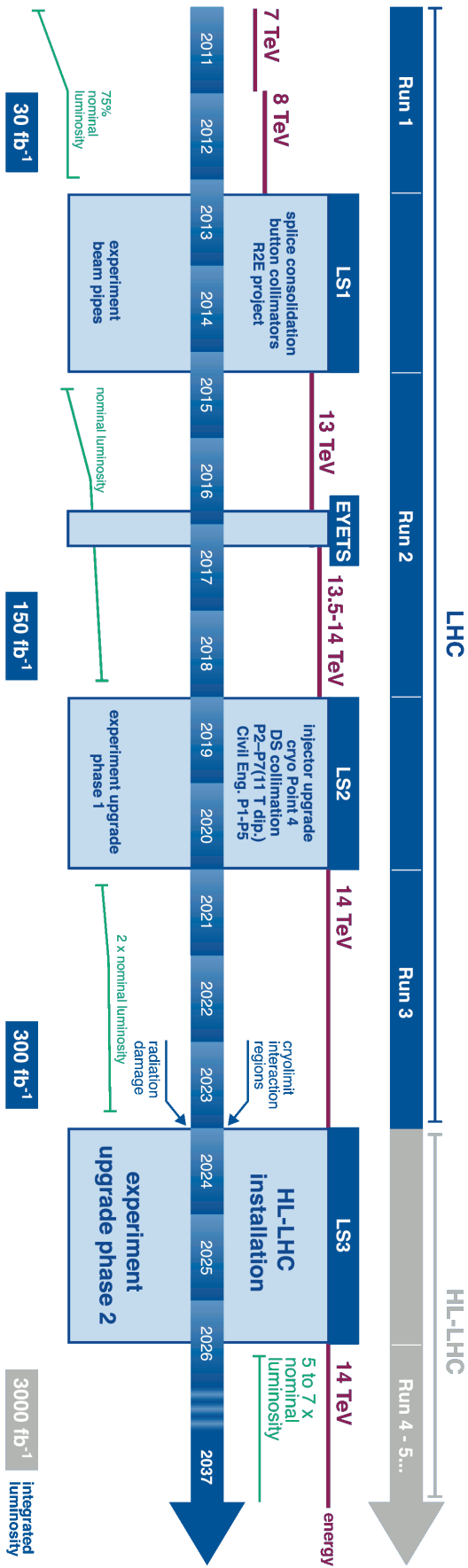
FIGURE 4.1: Status of the LHC baseline plan [1].

4.1 The ATLAS Inner Tracking System (ITk)

As described in Section 3.2.1, the current ATLAS inner detector consists of four layers of pixels, four layers of silicon micro-strips and as outermost component the Transition Radiation Tracker, that is a combination of a straw tracker and a transition radiation detector. The survival time for the inner detector was planned to be 10 years at luminosity of $10^{34}\ cm^{-2}s^{-1}$, therefore it was not designed to sustain the expected increase on beam luminosity at the HL-LHC.

The baseline layout of the proposed new inner detector is called *Inner Tracker* or *ITk*. The ITk will entirely be a silicon detector, with an innermost part of pixel detector surrounded by micro-strip sensors.

Several issues have to be taken into account for the upgrade. Due to the higher luminosity, the detector will need to manage higher particle densities. This will lead to an increase in the detector occupancies and in the levels of radiation damage. Due to the higher rates, the front-end electronics need larger bandwidth to buffer the data and avoid bandwidth saturation, reaching a maximum data rate per link of be 5.6 Gbits/s for the pixel detector and 4.16 Gbits/s for the strips one.

ITk will have to withstand a radiation level that will exceed, in the innermost region (Pixel detector), $2 \cdot 10^{16} neq/cm^2$ and of 1.7 GRad. The Strip part of ITK one will face a lower radiation, of about $1.2 \cdot 10^{15} neq/cm2$ and 50 MRad, that is a factor 10 higher than the radiation level of the current ATLAS SCT.

In the barrel of the ITk, sensors will be installed cylindrically around the beam axis. Starting from the innermost part, there will be five layers of pixel detector, surrounded by two short-strip and two long-strip layers of paired stereo modules. The end-caps will be formed by six strip disks and by several pixel rings, with number that varies with the layer and with the η position [72].

The schematic layout of the ITk is shown in Figure 4.2. The strip detector would provide a coverage in pseudorapidity of $|\eta| < 2.5$, while the coverage for the pixel one is up to $|\eta| < 4$. Several important physics analyses for the HL-LHC, such as vector boson fusion and vector boson scattering processes, including the studies presented in this thesis, will largely benefit from the extended η coverage, as was discussed in [73], with clear benefits in the forward jet reconstruction, E_T^{miss} resolution and pile-up jet rejection.
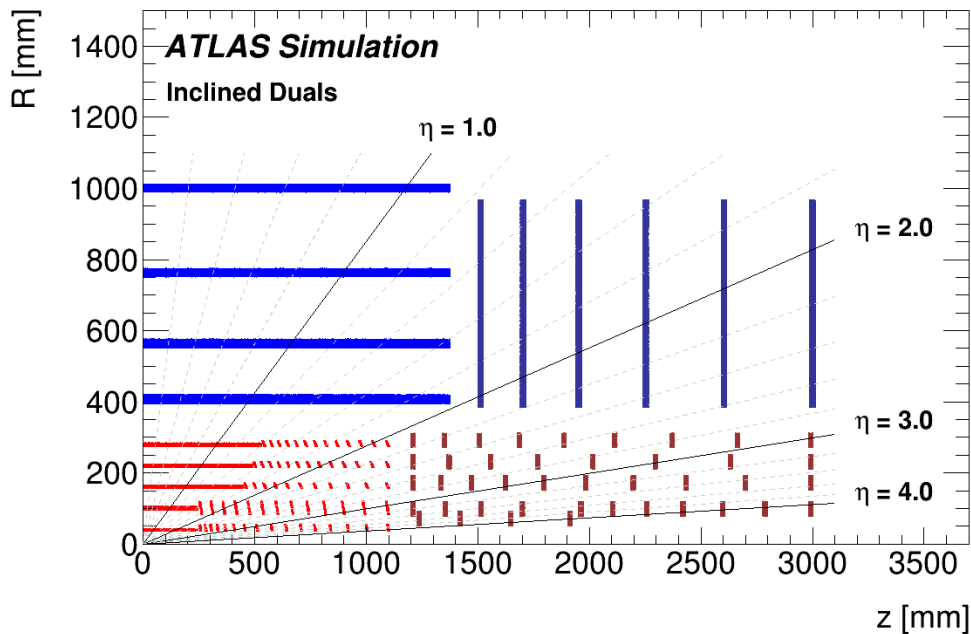
FIGURE 4.2: The baseline layout proposed in [72] for the AT-
LAS inner tracker (ITk). The pixel detector is shown in red,
while the strip one in blue.

4.1.0.1   Expected performances

Several simulations on the ITk expected performances have been done [1, 72–74]. The resolution on the transverse impact parameter $\sigma(d_0)$ and the longitudinal one $\sigma(z_0)$, compared to the ones of the Run 2 ID, are shown in Table 4.1. At $|\eta| = 3.5$ ITk is expected to present similar or even better res-

Track parameter ($|\eta| < 0.5$)	Existing ID with IBL no pile-up $\sigma_x(p_T \to \infty)$	Phase-II tracker 200 events pile-up $\sigma_x(p_T \to \infty)$
Longitudinal impact parameter (z_0) [μm]	65	50
Transverse impact parameter (d_0) [μm]	8	8
Inverse transverse momentum (q/p_T) [/TeV]	0.3	0.2

TABLE 4.1: Comparison of the performances of the Run 2
ATLAS ID with the expected ones of the Phase-II tracker.
The resolutions are shown for the transverse momentum and
impact parameters. The numbers are for $p_T \to \infty$ to remove
the contribution due to the material. Table adapted from [73].

olution performances than the Run 2 at $|\eta| = 2.5$, revealing the big potential of the tracker extension [74].

Furthermore, the expected performances for *b*-quark tagging algorithms (see Section 6.2.1 for further details) have been studied [75] at the operating points that correspond to b-tagging efficiencies of 70% and 85%. An improvement of 30% in the rejection of fake b-tags caused by light-jets is achieved by ITk with respect to Run 2, with pile-up $< \mu >$=140. A similar level of improvement is maintained in conditions with higher pile-up ($< \mu >$=200).

4.1.1 The strip system

This chapter will focus on the characterization prototypes of the ITk strip detector. For a more detailed description of the Pixel detector see Reference [72].

As previously mentioned, the upgraded strip detector will have a pseudorapidity coverage of $|\eta| < 2.5$ and will surround the pixel detector. It will consist in a barrel region composed by four cylinders, 2.8 m long, that surround the beam-line. The end-caps are formed by six disks on each side (*end-cap A* and *end-cap C*). Both the barrel and the end-caps are double-sided to have a two-dimensional space information.

The barrel mechanical design consists of *staves*; these are long rows of sensor modules integrated within the structure with the electronic components. The barrel layers are made of of 392 staves with modules installed on both sides. A stave is composed by 28 modules (14 per side). The barrel will contain two short-strip (24.1 mm) layers and two long-strip (48.2 mm) layers, with pitch of 75.5 μm. On each stave side, the strips are mounted rotated with respect to the *z*-axis of ±26 mrad, resulting in a relative rotation between the strips on each side of 52 mrad (stereo angle).

The end-caps consist in six disks of strips, and their basic modular mechanical structure is called *petal stave*. There are 32 identical petals on each disk and every petal is double sided (with a total stereo angle of 40 mrad) with nine modules placed in six rings, that present different sensor geometries in order to adapt to a wedge-shaped area. The pitch of the strips also varies with the geometry, with an average value of 75.5 μm.

Figure 4.3 shows the barrel and petal stave components. The basic electrical unit of a petal or a stave is a silicon-strip module. A module is formed by one sensor and one or two *hybrids*, that are low-mass printed circuit boards (PCBs). The hybrid readout electronic is composed by two different kind of chips: the front-end chips (ATLAS Binary Chip *ABCStar* [76]) and the Hybrid Controller Chips (HCCStar). The charged particles, that pass through the silicon sensors, generate a signal charge in the sensor diode. A wired
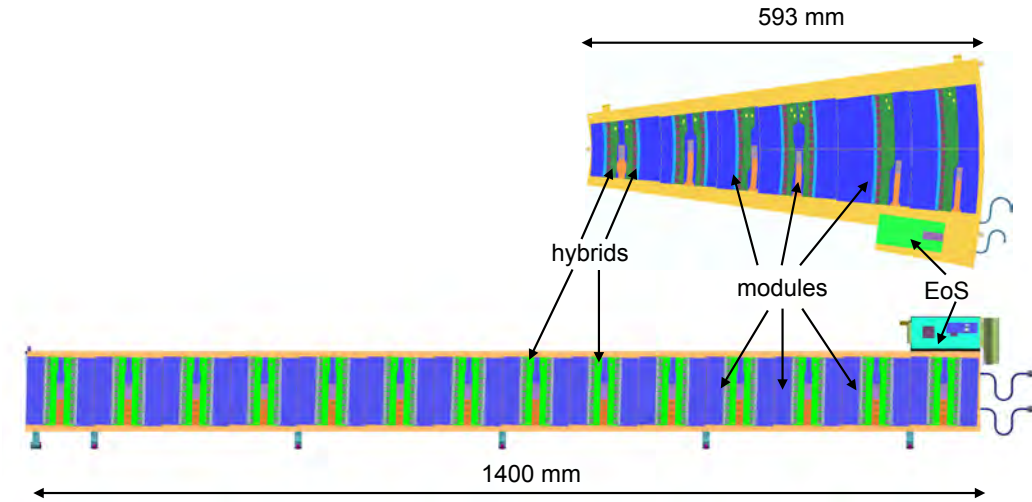
FIGURE 4.3: Barrel stave components (below) and petal stave
components (above). From [1].

connection transmit this signal to the ABCStar front-end chip. This chip
presents 256 analogue preamplifier-shapers and discriminators, that can indi-
vidually perform threshold trimming. The binary output of the discriminator
is stored in the event buffer and consequently compressed by a cluster algo-
rithm. The data is then directly transferred to the HCCStar chip. This chip
has the role of collecting the data from the ABCs and send them to the End-
of-Substructure Card (EoS). The EoS allows the communication among the
stave or petal with the off-detector electronics. Furthermore, it connects the
stave or petal with the power supplies for low voltage and high voltage from
the power supplies. Each stave or pedal presents two EoS cards, one per side.
Several modules geometries will be built, according to the location in the de-
tector. Two different kind of modules will form the barrel, depending on the
length of the strips: a long-strip module and short-strip one. The first will
be mainly employed for the regions at larger radii (i.e. the two outermost
layers), while the short ones in the two innermost layers. A schematic view of
the short-strip module is given in Figure 4.4. The short-(long-)strip module
will host two (one) hybrids, that will contain up to twelve ABCStar read-out
chips.

The petal modules present a much complex geometry. As previously men-
tioned, the modules are arranged in six rings: the three innermost ones present
one module each with one or two hybrids, while the outer three ones two mod-
ules placed side-by-side, each with one hybrid crossing over the two neigh-
boring modules. In total six different geometries and thirteen hybrids are
foreseen.

Silicon sensors as well present different shapes accordingly to their installa-
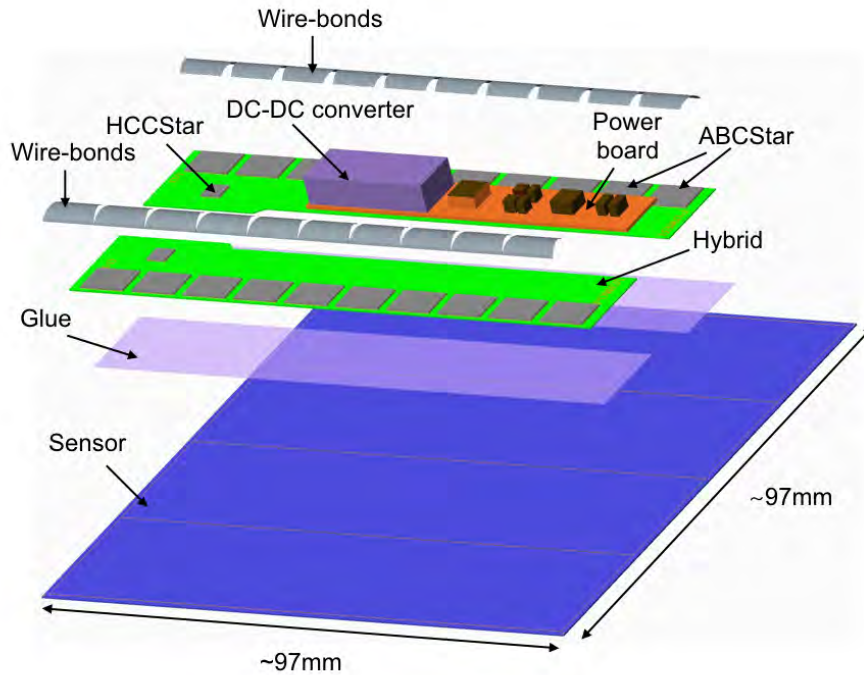
FIGURE 4.4: Representation of a short-strip barrel module.
Both the long-strip modules and end-cap modules present the
same components. From [1].

tion position: the barrel ones are squared, while end-cap ones have a trape-
zoidal shape with two curvy edges. The sensors are AC-coupled with a n^+-
strip on p-bulk design, with 1280 AC-coupled readout strips. This sensor
does not present any radiation induced type inversion. With respect to the
ATLAS SCT, that operates with p-in-n sensors, the n^+-in-p implants have
been chosen because of their resistance to radiation: the sensors have to sur-
vive to the expected maximum fluence of $8.1 \cdot 10^{14} neq/cm^2$, an ionizing dose
of 33.3 MRad, while operating at a depletion voltage up to 700 V. In these
conditions, the n^+-in-p sensors supply a factor of two more charge.

4.2   Test beam at DESY

Before installation, the new detectors have to be properly tested in conditions
similar to the ones they will find once they will be installed in the ATLAS
detector. Test beams are performed to achieve this goal, by irradiating the
detectors with a beam of high energetic particles. According to the nature of
the beam, the kind of particles passing through the device and their energy

are well known. However, the exact position of the incident particle is difficult to determine. To achieve this, beam telescopes are used: telescopes allow to track the charged particles during an off-line reconstruction to evaluate, for example, the efficiency and the charge sharing performances of the device as a function of the bias voltage, the threshold and the particle position.

Test beam measurements were performed at the Deutsches Elektronen-Synchrotron (DESY) in Hamburg with the DATURA and DURANTA telescopes [77, 78] using the beam facilities of the DESY II synchrotron.
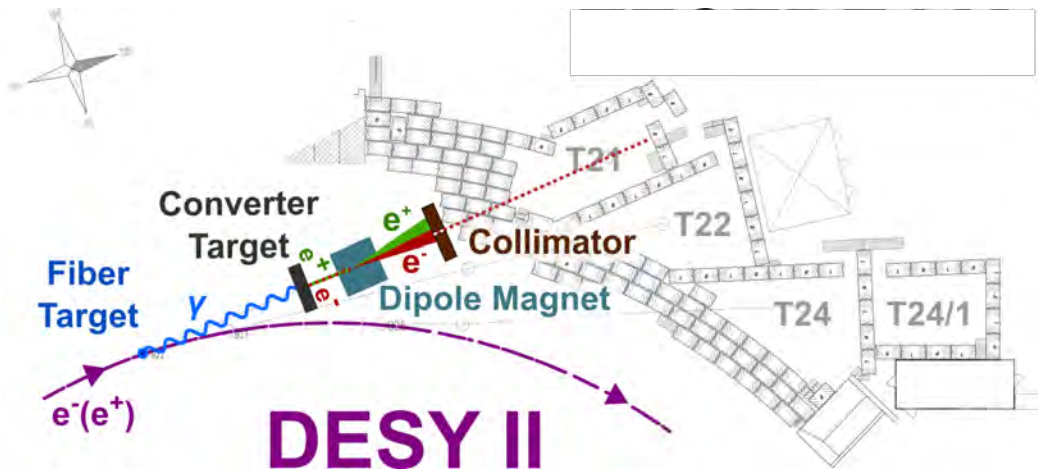
FIGURE 4.5: Schematic figure illustrating the beam production for test beams at DESY

4.2.1   The DESY II Electron Beam

The DESY II Electron Beam synchrotron operates as source for the DORIS and PETRA accelerators, but is also used as beam for test beam users. The DESY II magnet cycle is around 80 ms, since the e^+/e^- beam is accelerated and decelerated in a sinusoidal mode with a frequency of 12.5 Hz.

Figure 4.5 illustrates how the electron or positron beam is set up for test beams at DESY. Electron and positrons are accelerated in the synchrotron and then converted through bremsstrahlung radiation into photons by a $7\,\mu m$ carbon fiber placed in the beam. Afterwards, a metal plate converts these photons into pairs of e^+/e^-. The beam is spread out as a function of the sign and energy by a dipole magnet, and a collimator produces the desired beam of minimum ionizing particles (MIPs) within an energy range of 1-6 GeV. The so-formed beam is consequently directed into one of the three test beam areas (T21, T22, T24).

4.2.2 The test beam setup

The test beam set up is shown in Figure 4.6. The telescope allows to extract the track of a particle passing through the sensors very precisely. It is formed by six reference planes placed usually three in front and three behind the Device Under Test (DUT). The pointing resolution is usually better than the expected intrinsic resolution of the DUT. The coincidence of two pairs of crossed scintillators (Fig. 4.7), that are placed upstream and downstream the telescope, provides the trigger. These triggers are then passed to a Trigger Logic Unit (TLU). The set up also includes a FEI4 device placed in front of the last plane (see Sec. 4.2.2.2).
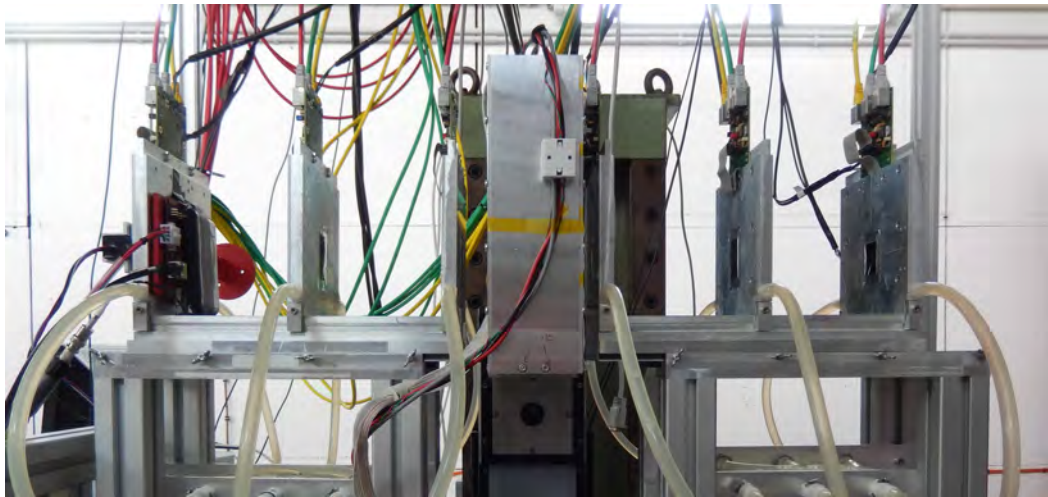
FIGURE 4.6: The Datura telescope with a DUT placed in the
middle. The beam passes through the setup from right to left.
The FEI4 device is placed before the last plane.

4.2.2.1 The Mimosa telescopes

There is a whole family of Mimosa pixel telescopes [77] originated from the EUDET project in 2010. The first telescope, EUDET, has been the prototype for many copies. At DESY two of them are present: DATURA in the test beam area 21 and DURANTA in the test beam area 22. A Mimosa telescope is made from six identical planes of Mimosa-256 pixel detectors, each with a active sensor area of 21.2 mm by 10.6 mm, with pixels arranged in a 1152×576 matrix and with pitch of 18.4 μm. The telescope has a spatial resolution of $2\mu m$ and an integration time of $115.2\mu s$ [78].

The optimal configuration of the distance between the six planes and the planes with the DUT has been chosen optimizing the resolution [79]: the best configuration is obtained with equidistant planes and minimizing the distance
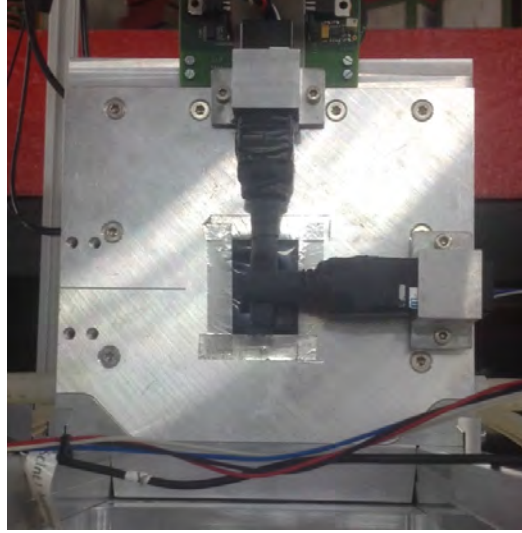
FIGURE 4.7: Two pairs of crossed scintillators are placed up-
stream and downstream the telescope. They provide trigger
informations.

between the planes and the DUT. In Table 4.2 the chosen configuration is
shown.

plane	0	1	2	DUT	3	4	FEI4	5
z [mm]	0	150	305	375	458	608	~ 750	759

TABLE 4.2: Distance relations between the planes and DUT.

4.2.2.2   The FEI4

The FEI4 [80] is a pixel readout integrated circuit that has been placed in front
of the last plane. It is characterized by an integration time of $\sim 25ns$, that
is more than three orders of magnitude smaller than the telescope one, but
presents a larger spatial resolution, due to the larger pixel size ($14 \times 72 \mu m^2$).
The combination of the two allows to time-stamp the individual tracks with
the FEI4 time resolution, while tracking them with the good spatial resolution
of the telescope planes.

4.2.2.3   The Data Acquisition System

Figure 4.8 gives an overview of how the DAQ process works. It consists of
two steps: an hardware-based one and a software-based. In the first one, the
Trigger Logic Unit (TLU) plays a fundamental role, receiving the triggers
from the coincidence of the scintillators and consequentially giving the green
light for data acquisition to the FEI4, the telescope and the DUT. The data

acquisition framework is called EUDAQ [81]. It is a C++ software that uses different processors to communicate between the various hardware devices that are easily accessible for the user with a graphical interface (*Run Control*). The data is collected as RAW files and contains the informations coming from each telescope plane, DUT and FEI4.
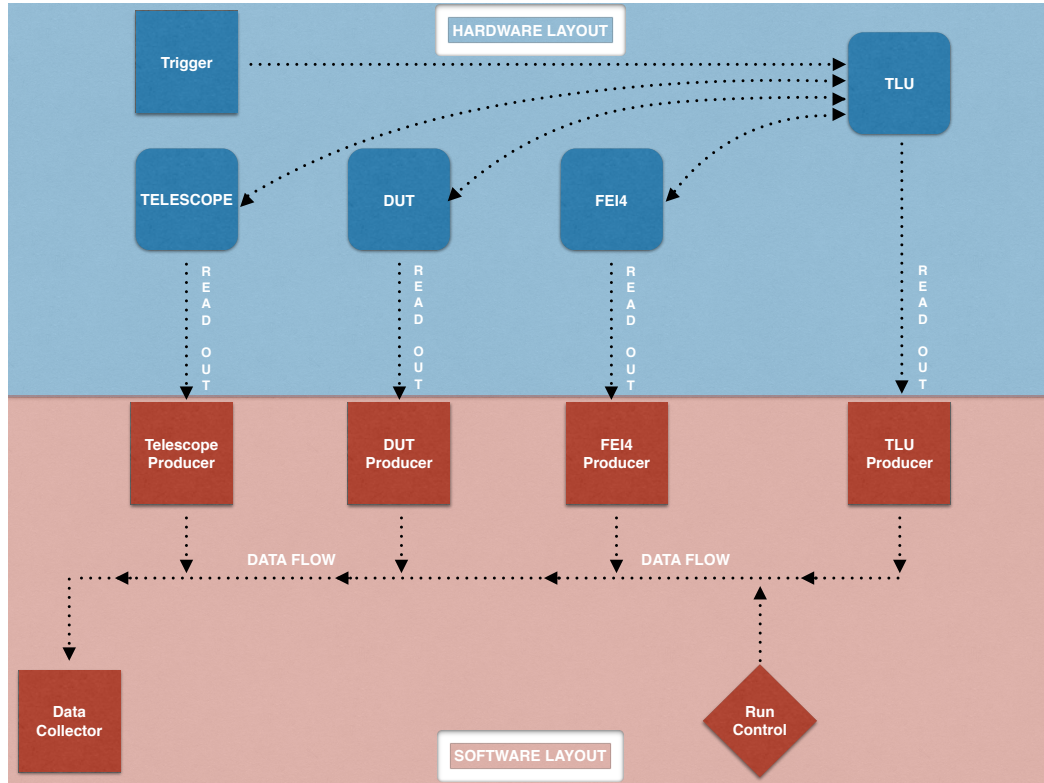
FIGURE 4.8: Schematic overview of the DAQ system.

4.3 Tested devices

In 2015 two test beam campaigns took place at DESY: the first one in May 2015, the second one during October 2015. Since both the ABCStar and HCC-Star chips were not yet available during 2015, the precursor chips ABC130 and HCC130 were instead used [82, 83]. After the production and the initial tests on the ABC130 chip, the ATLAS trigger rates were increased to 1 MHz. The ABC130 and HCC130 readout architecture could not withstand to this higher rate level. Therefore, a design change was necessary that lead to the production of the ABCStar and HCCStar chips. The main change, with respect to the 130 chips, is in the interface from ABCs to the HCC: the ABC130 presented a serial transfer of data to the HCC, and this connection was replaced with a direct communication from all ABCs to the HCC.

To allow this, the HCCStar chip faced a complete re-design: with this new configuration, the HCC builds the events in parallel from fragments coming from all the ABCStar, considerably simplifying the system architecture, by removing the bandwidth "congestion" in the transfer of the data from the ABC to the HCC.

During the over-mentioned test beam campaigns, non-irradiated prototypes have been tested and analyzed. More precisely:

- *Mini-sensors hybrids*: two identical n^+-in-p silicon strips barrel hybrids with two ABC130s wire bonded to miniature strip sensors of dimensions $1 \times 1 cm^2$. The sensors have 100 channels and a pitch of 74.5 μm [84]. The two hybrids are referred to as *Device 1* and *Device 2*. The picture of one of the devices is given in Fig 4.9(a).

- *Long-strip module*: a full barrel module with ten ABC130, short and long n^+-in-p silicon strips. The long-strip barrel module is bonded up to have three different configurations, as shown in Figure 4.10. A short-strip section with strips 2.5 cm long (called *position 1*), that is the best case scenario for noise. A long-strip section obtained stitching together two short strips 2.5 cm long, for a total of 5 cm. The long part of the stitched section, that represents the worse case scenario for noise, is referred to as *position 2*, while the long-strip short segment as *position 3*. Figure 4.9(b) shows the picture of the module.

Thanks to the DESY II synchrotron facilities, the beam energy has been modulated in order to achieve the rate of particle desired: 4.6 GeV for May test beam and 3.4 GeV for the October one.

With these beam energies, scans at 16 different binary read-out thresholds, from 20 mV to 240 mV, have been performed at different bias voltages: 150V, 250V, 350V and 400V. Approximately 200000 events each run have been collected. For the long-strip barrel module data were gathered only for high voltages of 250 V and 395 V.

Furthermore noise measurements have been done, performing scans at lower threshold values (from 2 mV to 40 mV) and switching off the beam.

4.4   Tracks reconstruction

The first crucial part of the analysis of the data collected during test beams, is the reconstruction of the particle tracks through the telescope planes and the devices under test. For all the data collected during both test beam
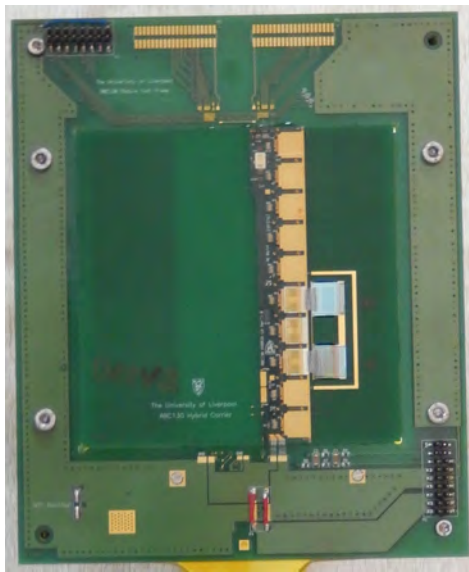
(a) Mini-sensors barrel hybrid with ABC130s
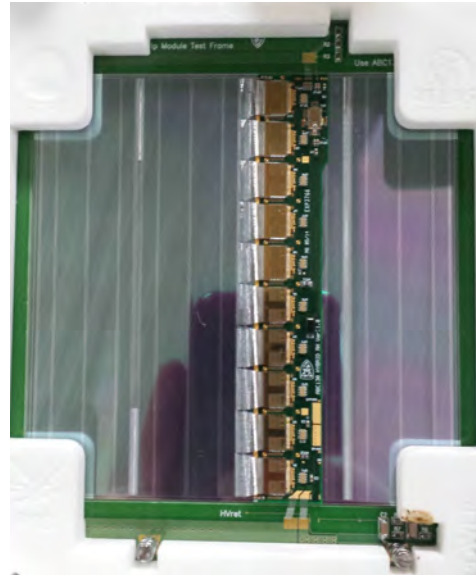
(b) Long-strip barrel module with ABC130s

FIGURE 4.9: Pictures of two of the devices tested: the mini-sensors barrel hybrid (Fig. 4.9(a)) and the long-strip barrel module (Fig. 4.9(b)).

campaigns, the reconstruction has been performed using the *EUTelescope* software [85]. This software can produce, in several steps, fitted tracks in 3-dim global reference frame as a ROOT file. A schematic overview is given in Figure 4.11. At first, there is the conversion from RAW data format to Linear Collider In/Out (LCIO) data format (step called *Converter*). After this, there is the *Clustering* step: due to charge sharing, the collected charge, that comes from a single particle track, is recorded by multiple cells in the same
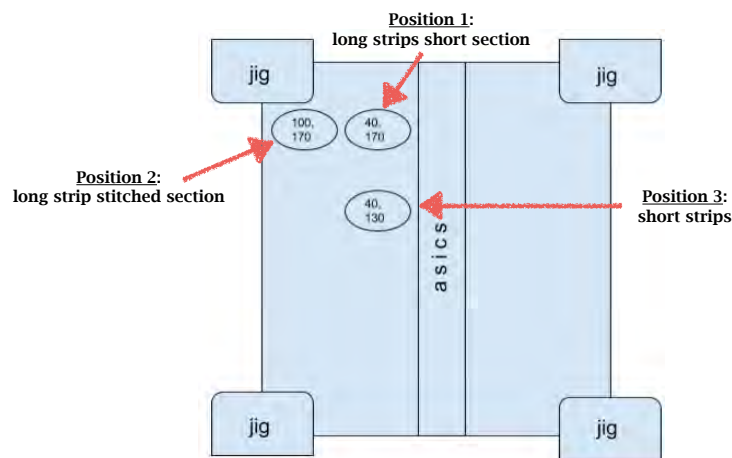
FIGURE 4.10: Schematic overview of the long-strip barrel module.
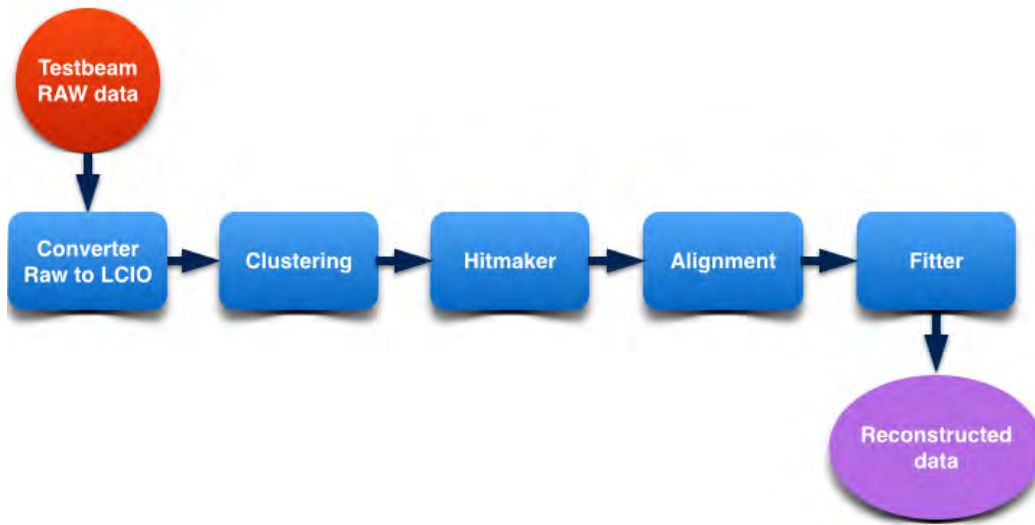
FIGURE 4.11: Schematic overview of the EUTelescope soft-
ware.

device. Those hits must be collected together as a cluster. Subsequently,
there is the *HitMaker* step, where a coordinate transformation from the local
coordinates of the sensor into the telescope global coordinate frame is per-
formed. The new coordinates are x, y, z, where z is the beam direction and is
always perpendicular to the telescope planes and centered in $x = y = 0$. At
this point, the user must provide to EUTelescope a file, called GEAR-file, that
contains all the geometrical informations about the test beam setup, such as
positions, thickness and dimension of each detector. Furthermore, the user
has to provide the radiation length of each sensor, in order to perform an
accurate track fitting, taking into account multiple scattering. Those global
coordinates provide pre-alignment values in the $x - y$ directions for the next
stage that is the *Alignment*: this step uses the MillepedeII [86] software to
determine the alignment constants.

This processor corrects the position of the telescope planes using track
fitting algorithms in such a way that the fitted tracks are in compliance with
the actual hits. The alignment constants of the sensor planes are determined
with a linear least squares fit of the local and global parameters of the track.
The main parameters are the three shift coordinates dX, dY, dZ and the
three rotation angles that are defined in the GEAR-file. The last step is the
Fitter: after the alignment, it is necessary to reconstruct the tracks along
the telescope, and this has been done using a processor based on the General
Broken Lines (GBL) algorithm [87].
Before forming a track, it is necessary to understand which hits make up the
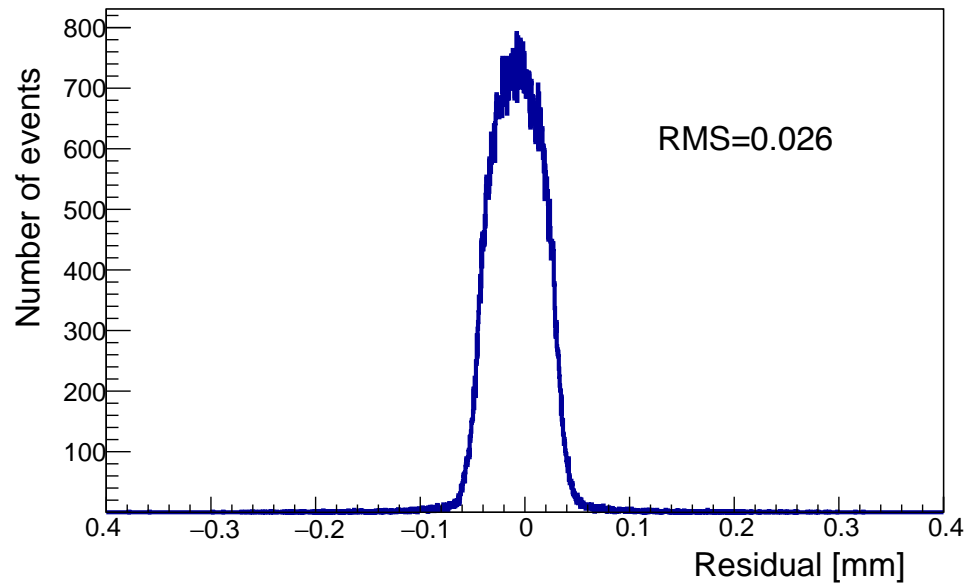
(a)
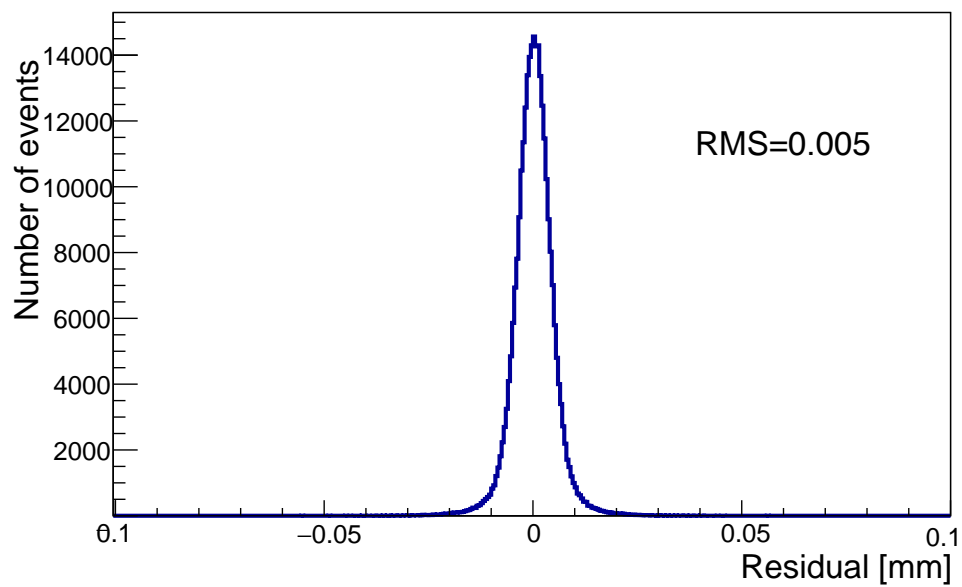
(b)

FIGURE 4.12: Figure 4.12(a) shows an example of residual distribution for the mini-sensors barrel hybrid, while Figure 4.12(b) for the telescope planes.
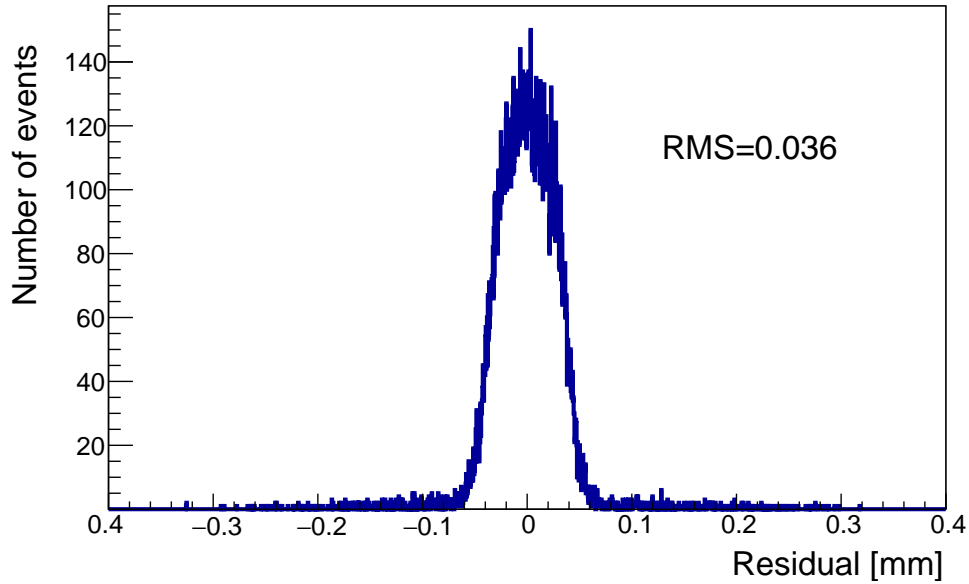
(a)
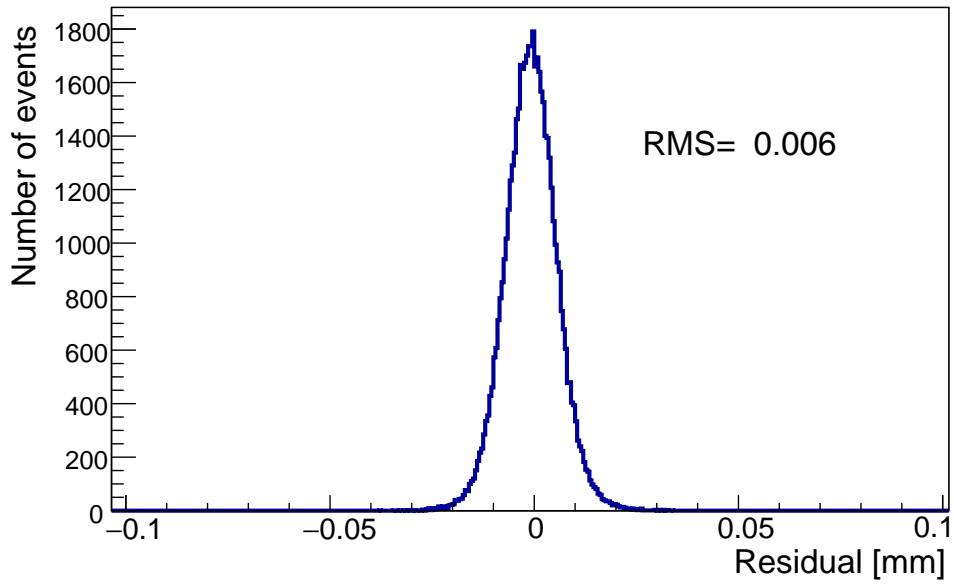
(b)

FIGURE 4.13: Figure 4.13(a) shows an example of residual distribution for the long-strip barrel module (on position 1), while Figure 4.13(b) for the telescope planes. Similar results are obtained for position 3.

track (*Pattern Recognition*). Some planes are chosen as *seed planes*: the hits on these are used to extrapolate the closest hits on the next plane, storing the so formed track until the last plane. A selection is then applied on these tracks: the ones with few hits and as well with too many shared hits are rejected. Also tracks in which the hit has a distance larger than some value known as *window size* to the seed hit are discarded. The output of this software is then stored in a root file to be easily analyzed with ROOT.

The spatial resolution is given by the width (RMS) of the distribution obtained taking the difference between the extrapolated track position and the actual hit of the particle, called *residual*. For the track reconstruction of May 2015 test beam, the residual distribution of the mini-sensors barrel hybrid is shown in Figure 4.12(a), while in Figure 4.12(b) for the telescope planes. The resolution achieved is around 25-35 μm for the DUT and ~ 5 μm for the telescope planes.

Similarly, for the October 2015 campaign, in Figures 4.13(a) and 4.13(b), the residual distributions of the DUT at position 1 and one of the telescope planes are shown. The residuals achieved with GBL are around 35-40 μm for the DUT and $\sim 5-6$ μm for the telescope planes. For the long strip stitched section (i.e. position 2), some not fully understood issues have been experienced during reconstruction: the residuals achieved are ~ 100 μm for the DUT and around 10-30 μm for the telescope planes. This could be due to a misalignment of the beam, hitting partially a dead area (stitching bonds) of the sensor. Therefore, this part of the module was not analyzed further.

4.5 Results on the long-strip barrel module

In this Section are reported the results achieved for the two short positions of the long-strip barrel module tested during the October 2015 test beam. For the analysis of the mini-sensors barrel hybrid see reference [88].

After tracks reconstruction, before a complete data analysis, a useful check is to see if everything is properly aligned. Since the clusters along a particle track are spatially correlated between the different planes in the setup, the alignment can be checked by looking to the correlations separately in the x- and y-directions for the telescope planes and the devices, These correlations and the hit maps for the DUT are shown in Figures 4.14. As expected with a good aligned setup, the $x - x$ plots show a clear correlation between the telescope and the DUT, while the $x - y$ plots shows the hit map with no correlations.

The same check has been performed to verify the alignment of the FEI4 and the telescope planes. Figures 4.15 show the $x-x$ and $y-y$ correlations between the FEI4 and the telescopes. Also in this case, the devices are properly aligned between each other.
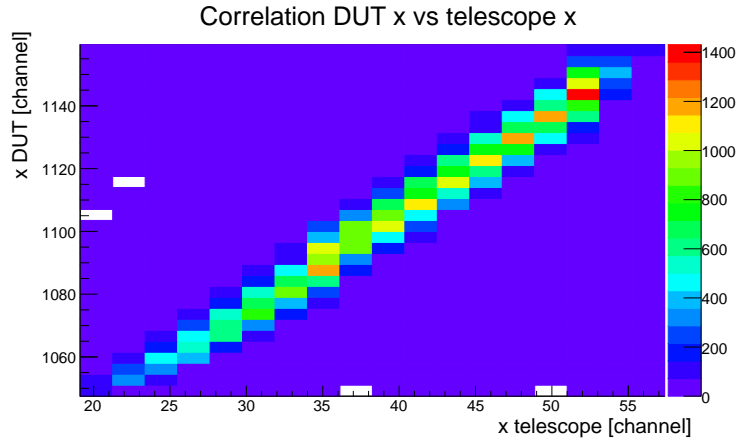
(a)
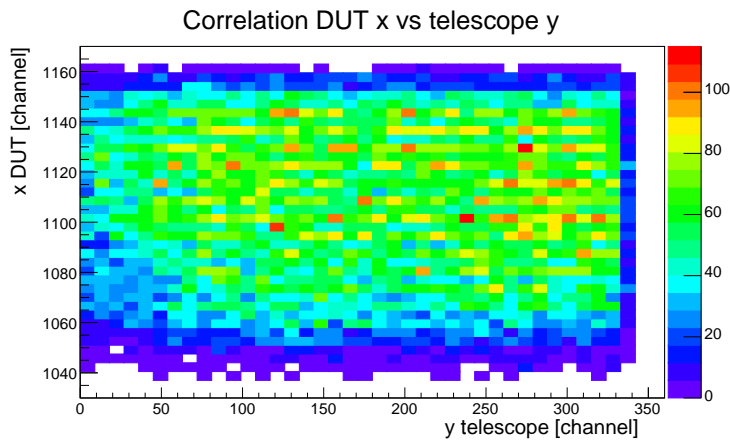
(b)

FIGURE 4.14: Correlations between $x - x$ coordinates and $x - y$ (hit maps) for the DUT and the telescope for position 1. Analogous distributions are obtained for position 3.

During the reconstruction, FEI4 tracks were not included in the track reconstruction fit. The information coming from this device has been inserted at a later stage, during data analysis. Therefore, in the analysis the tracks are selected if they present a corresponding hit on the FEI4. In this way, the residual distributions, shown in the previous section in Figure 4.13, get a slight improvement: from 35-36 μm, 25 μm are reached for the short-strip positions, as shown in Figure 4.16. Here, the x axis is expressed in strip units and, to have the resolution expressed in μm, it is necessary to multiply the RMS by the pitch size (74.5 μm).

(a)

(b)
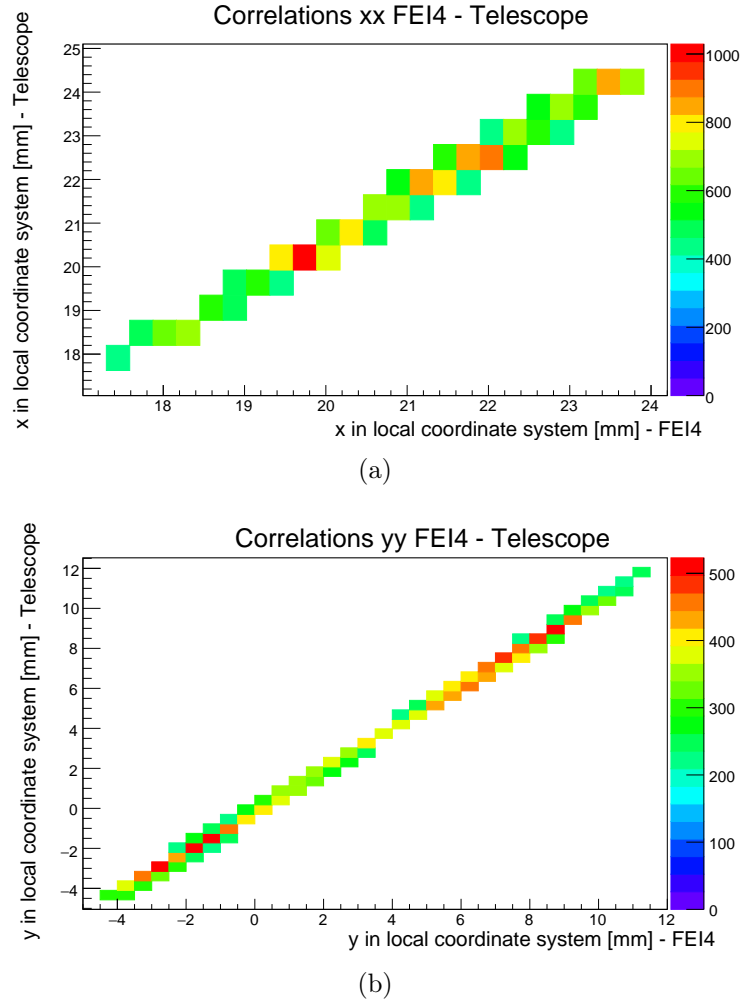
FIGURE 4.15: Correlations between $x - x$ coordinates and $y - y$ for the FEI4 and the telescope for position 1. Analogous distributions are obtained for position 3.

These residual values for the two short strip positions lead to a total pointing resolution of:

$$\text{Pointing resolution} = \sqrt{res^2 - (\frac{pitch}{\sqrt{12}})^2} \sim 12 \ \mu m \ ^{[1]} \tag{4.1}$$

As it will be shown later, this good pointing resolution will allow to perform inter-strip studies.

One of the goals of the analysis is to measure the detection efficiency of the device and its noise occupancy at the operating threshold.

The efficiency is calculated as the ratio between the number of hits seen by the DUT and the total hits, which are obtained selecting the tracks on the

---

[1]The spatial resolution of a DUT, with a binary system of cluster size one and pitch p, is given by $\sigma_{DUT}^2 = \frac{1}{p} \int_{-p/2}^{+p/2} x^2 dx = \frac{p^2}{12}$
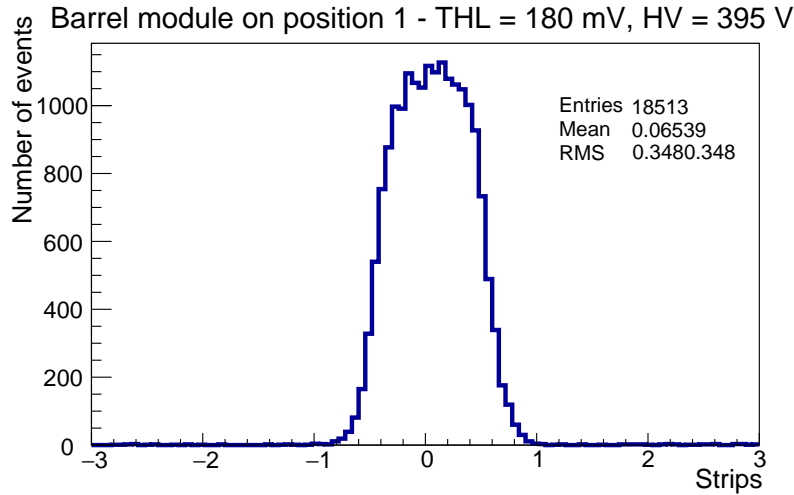
FIGURE 4.16: Residual for position 1 on the long strip barrel
module after requiring a corresponding hit on the FEI4.

telescope that have a corresponding hit on the FEI4:

$$\epsilon = \frac{DUT_{hits}}{Total_{hits}}. \tag{4.2}$$

The spectrum of the deposited charge is Landau-distributed, while the noise
due to the electronic readout is Gaussian-distributed. A convolution of these
two distributions can properly describe the signal readout. It is interesting to
study the so called *S-Curve*, that is the cumulative distribution of the proba-
bility density function (PDF) of a convoluted Landau and Gaussian function.
To obtain an S-Curve, as illustrated in Figure 4.17, the efficiency has been
expressed as a function of the increasing threshold. The most probable value
(MPV) can be extracted with a fit, performed with a convoluted Landau-
Gaussian function. The MPV is the position of the maximum of the Landau
distribution. The extracted MPVs are shown in Table 4.3 for positions 1 and
3 at two different high voltages. As it will be shown later, the extracted MPVs
will be used to estimate the gain of the ABC130 pre-amplifier. Another im-
portant benchmark is to get the pedestal and the noise occupancy of the DUT.
This has been done performing threshold scans at 20 different low thresholds
values from 0 to 40 mV, switching off the beam. The pedestal is a constant
offset of the output from each strip obtained in absence of any input signal.
It is measured by taking the MPV value of threshold scans performed with
no beam. The strips present a full occupancy below the pedestal value, while
zero occupancy above. Its variation around the mean value is referred to as
input noise. In Figure 4.18(a) the pedestals for each strip are shown, while
in Figure 4.18(b) the input noise at 395 V for the long strips barrel module.
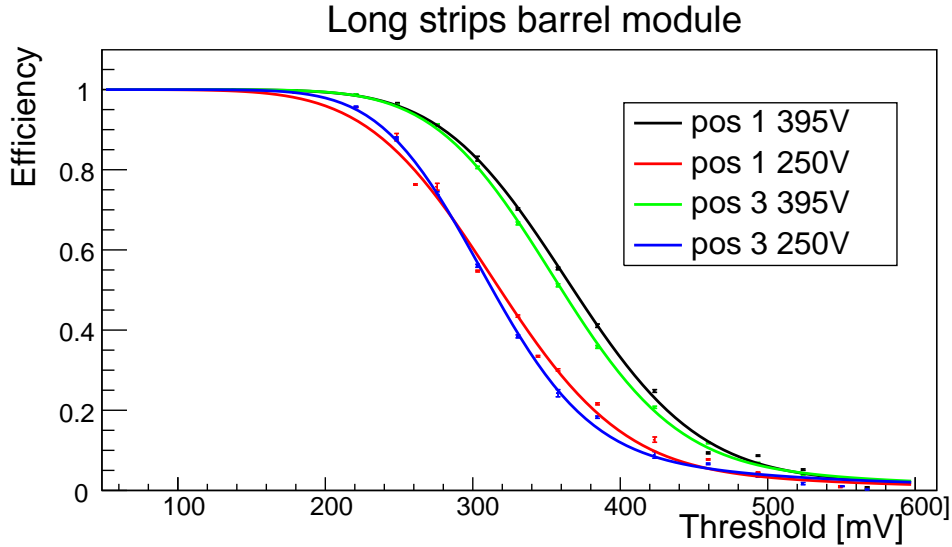
FIGURE 4.17: S-Curves for the two different positions on the
long strips barrel module and two high voltages. The efficiency
is calculated as in equation (4.2) and it is shown as a function
of the increasing threshold. The error bars of each scan point
are estimated from the the binomial distribution variance.

Similar results are obtained for the 250V scans. The pedestal obtained is
around 51 mV, while the input noise around 8 mV.

Once the MPV and the pedestals at different high voltages are calculated,
the gain calculation is performed. At first, the pedestal is subtracted from
the MPV: $MPV - pedestal = MPV_r$.
Then, the gain is defined as follows:

$$gain = \frac{MPV_r}{q_{max}}, \tag{4.3}$$

where q_{max} is the charge deposition. The values of the charge for the two
high voltages considered are taken from previous studies with ALiBaVa read-
out [89, 90] and are $q_{max} = 2.81 \pm 0.10 \ fC$ for 395V and $q_{max} = 2.42 \pm 0.08 \ fC$
for 250 V.

	MPV at 250 V	MPV at 395 V
Position 1	(302.0 ± 3.7) mV	(352.3 ± 1.9) mV
Position 3	(295.4 ± 1.2) mV	(342.7 ±1.4) mV

TABLE 4.3: Table of the most probable values obtained from
the fit of the S-Curve with a convoluted Landau - Gaussian
distribution for the two short strips positions of the barrel
module at HV= 250 V and 395 V.
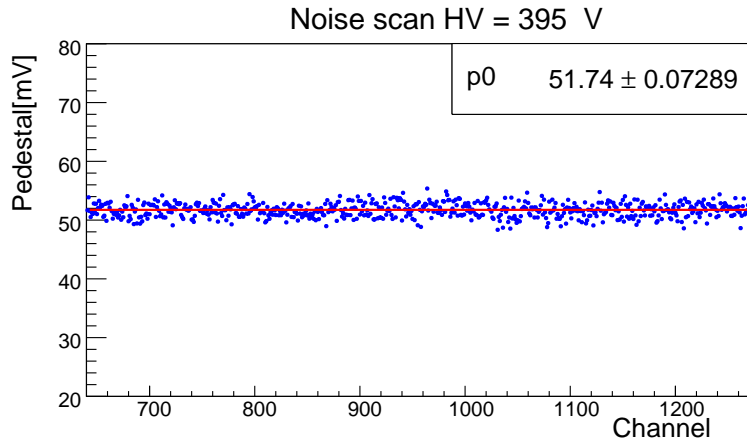
(a)
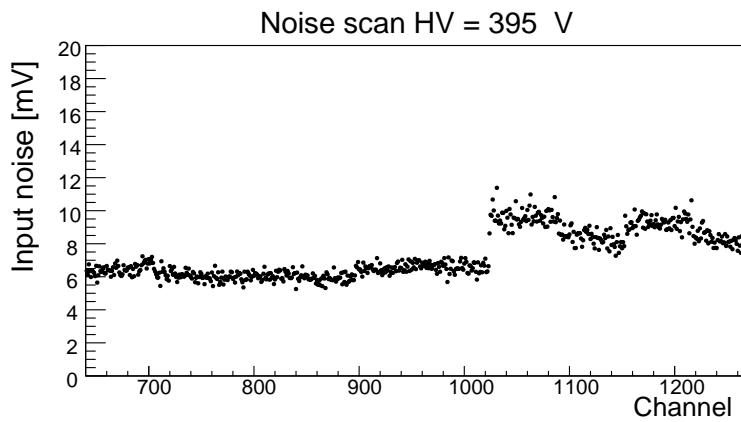
(b)

FIGURE 4.18:   Pedestal in Figure 4.18(a) and input noise
in Figures 4.18(b) as a function of the different channels at
HV=395V for the long strips barrel module. The long-strip
channels correspond to the areas with higher noise.

In Table 4.5 the average gains at the MPV obtained with formula 4.3 are

	250 V	395 V
Position 1	$103.2 \pm 3.5 \; \frac{mV}{fC}$	$107.0 \pm 3.8 \; \frac{mV}{fC}$
Position 3	$100.4 \pm 3.3 \; \frac{mV}{fC}$	$103.3 \pm 3.7 \; \frac{mV}{fC}$

TABLE 4.4:   Average gain at the MPV for HV = 250 V and
395 V

listed. A very similar performance is observed between the two positions.
The values obtained are slightly higher than what indicated in the specifica-
tion document of the ABC130 [82], that reports a gain of 95 mV/fC. This is

probably due to non linearity of the ABC130 ASIC response[2].

Thanks to the very good pointing resolution given in Equation 4.1, it is possible to see where in the strip the electron passed. Subdividing each strip in smaller bins, the hit efficiency, the MPV and the cluster size as a function of the inter-strip position can be studied. This can allow to study charge-sharing effects among strips. In Figure 4.19 the hit efficiency as a function of the inter-strip position for different thresholds is shown. Following the expectations, the efficiency is maximal at the center of the strip and decreases at the edges due to charge sharing effects and efficiency losses caused by the low field in those regions. Charge sharing among the strips is due to the capacitive coupling of the neighboring strips: a small fraction of the signal of a charge that drifts into a single strip can be shared with the neighboring one. In this way the total charge deposited Q is given by

$$Q = \sum_i Q_i, \tag{4.4}$$

where Q_i is the charge collected on the strip i . Therefore the charge that is not seen in one strip has to be measured in the very next one. Another important effect to point out from this plot is that, when increasing the threshold, the charge sharing effects become less evident; instead, for lower thresholds, the strips are coupled and the charge which is not detected in one strip is detected in the neighboring.

From these hit efficiencies, the S-Curves can be built and the MPVs can be extracted as a function of the inter-strip position, as shown in Figure 4.20. The MPV present a broad range of values depending on the inter-strip position: the MPV has a maximum in the center of the strip and decreases at the edges.

The cluster size behavior in between the strips can also be analyzed, as is shown in the plot in Figure 4.21 for a threshold of 96 mV and a fully depleted sensor. At this threshold, clusters with size 1 and 2 are obtained: the cluster size decreases in the center of the strip and increases at the edges because of charge sharing effects.

---

[2]Comparisons with the ALiBaVa studies performed with a β source suggest that the gain is not constant with the threshold. However, this study has been performed making the assumption of a constant gain, since we want to calculate only the gain at the MPV.
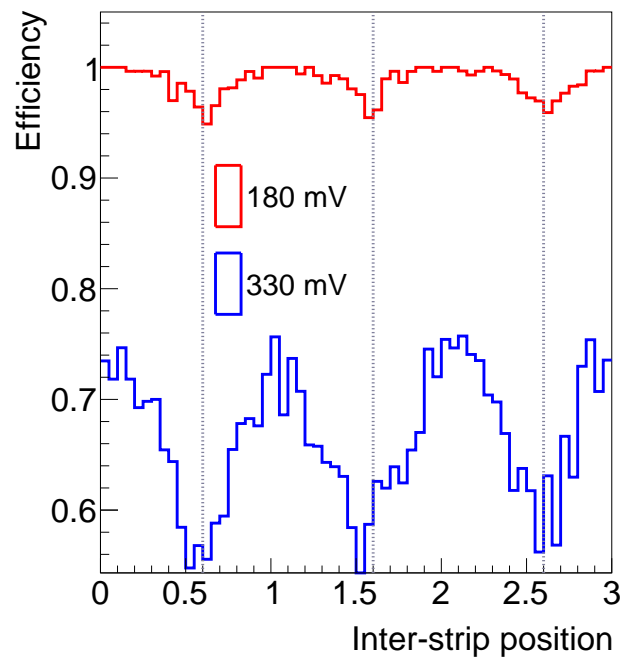
FIGURE 4.19: Efficiency as a function of the inter-strip position for HV = 395 V (fully depleted) and different thresholds. The vertical lines indicate the middle position between two strips.
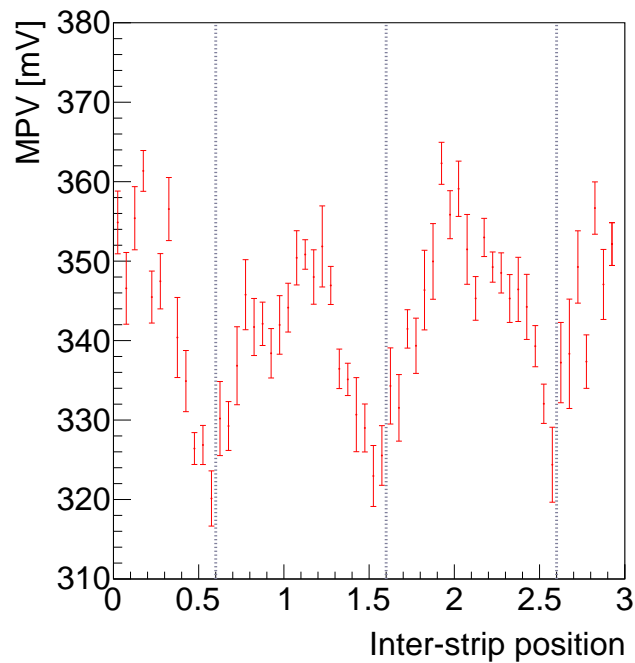
FIGURE 4.20: MPV as a function of the inter-strip position at HV = 395 V (fully depleted). The vertical lines indicate the middle position between two strips, while the error bars the statistical errors.
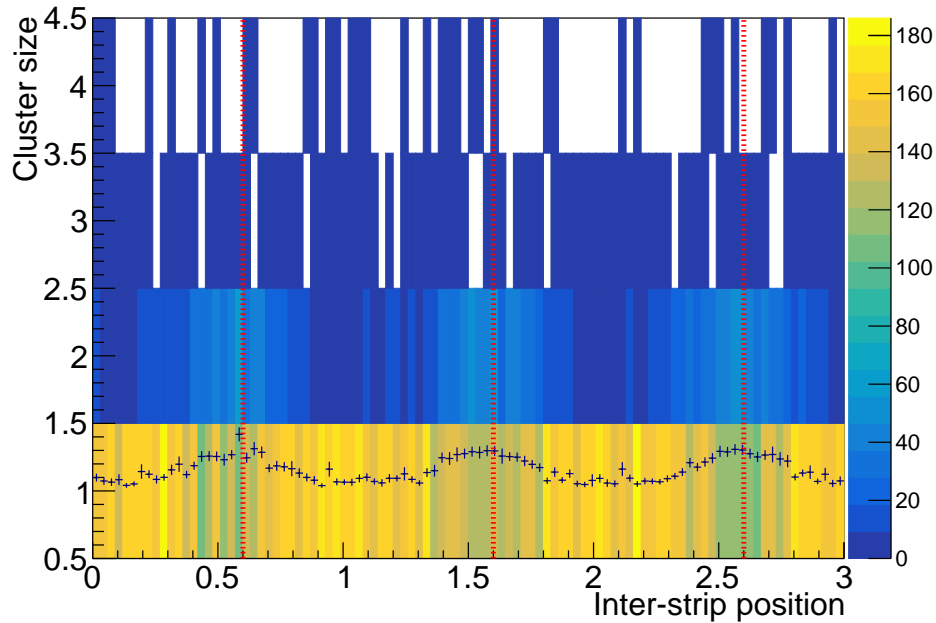
FIGURE 4.21: Cluster size as function of the inter-strip position for position 3 at threshold equal to 96 mV and high voltage 395 V (fully depleted). The z-axis shows the number hits with a given cluster size at a given inter-strip position. The profile plot shows the average value of the cluster size at a given inter-strip position with its statistical error. The vertical lines indicate the middle position between two strips.

4.6 Simulation studies

A simulation has been developed with the aim to reproduce the test beam efficiency results.

This simulation reproduces the behavior of a binary readout and a silicon sensor of 100 strips with pitch 74.5 μm.

The hit position has been generated with a random uniform distribution, as is shown in Figure 4.22(a); instead the deposited charge has been randomly generated with a convoluted Gaussian-Landau function. In Figure 4.22 the red distribution is the charge spectrum obtained from ALiBaVa measurements on ATLAS12 endcap sensors at 400 V, from [89] . This distribution has been used as input for the simulated events (in blue).

Once the deposited charge is generated, the fraction of the charge collected in each strip is simulated. For this, the assumption that the collected charge follows a Gaussian distribution centered in the hit position is made. Thereby, to have the fraction of charge collected by each strip, the generated charge value is multiplied by the difference between two cumulative distribution functions

of the standard normal distribution, as:

$$F(x_{i+i}) - F(x_i) = \frac{1}{2}[1 + erf(\frac{x_{i+1} - \mu}{\sigma \sqrt{2}})] - \frac{1}{2}[1 + erf(\frac{x_i - \mu}{\sigma \sqrt{2}})], \qquad (4.5)$$

where x_i and x_{i+1} are the positions of the strip i and $i+1$, μ is the hit position and σ is the gaussian standard deviation, given as input parameter in the simulation.

The following step is to add a processor that models the response of the digitizer. Since the program aims to simulate a binary readout, the threshold, above which everything is considered as a hit, has to be set as input from the user. This processor also contains a pre-amplifier, that performs the conversion from fC to mV.

(a)   (b)
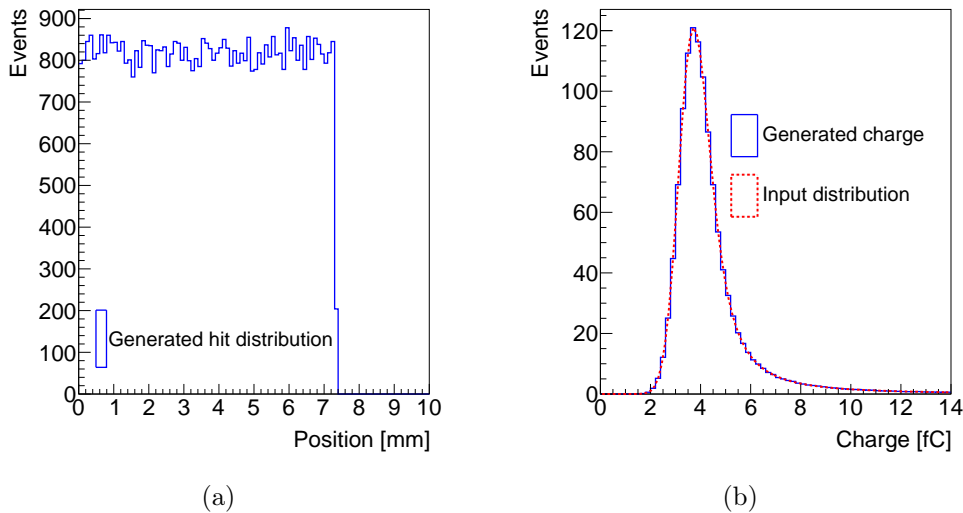
FIGURE 4.22: Generated hit position and charge distribution. The latter is taken from AliBaVa measurements on a ATLAS12 endcap sensor at HV=400V [89] (red distribution).

Other features added to the simulation are the resolution and crosstalk effects. The first ones are simulated randomly modifying the hit position following a Gaussian distribution. The crosstalk among the strips instead is simulated with a processor that finds the leading strip and redistributes a 10% of its charge to the other strips of the cluster.[3]

Finally, in order to be consistent with the data, pedestals are added to the simulated signal. The value for the pedestal is 51 mV, chosen to be consistent with the test beam results, presented in Figure 4.18.

---

[3]This 10% crosstalk is the average value seen on characterization studies of the mini-sensor barrel hybrid.

A crucial point in the simulation is to set a plausible σ of the Gaussian distribution for the collected charge, since this parameter has a strong dependency with the cluster size. This is clearly shown in Figure 4.23, where a strong correlation between the cluster size and the σ-parameter is visible.

In order to find the correct value that best simulates the data, the simulation
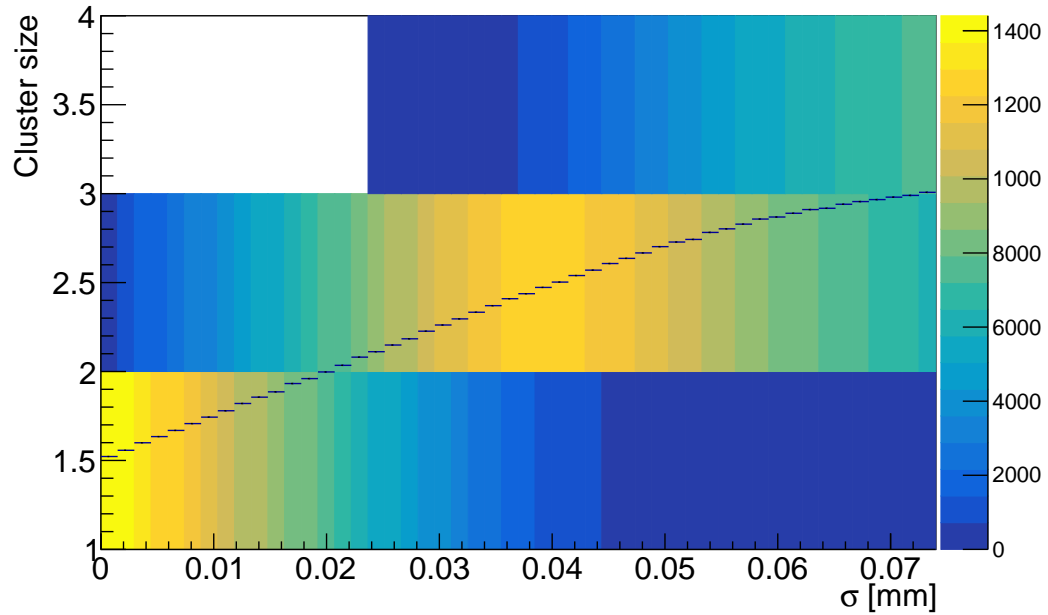
FIGURE 4.23: Custer size as a function of σ-parameter. There is a strong correlation them.

has been trained on the data from May test beam. The optimal value for σ has been found by taking the σ value that minimizes the χ^2 function:

$$\chi^2 = \sum_i (x_i - y_i)^2, \tag{4.6}$$

where x_i is the cluster size for position i taken from the data, while y_i is the simulated cluster size for position i. The value of σ that minimizes the χ^2 is found to be at $\sigma = 11 \ \mu m$.

The simulated cluster size as function of the inter-strip position has been compared with the data, as shown in Figure 4.24: a very good agreement is obtained between the data and the simulation.

Given that the simulation describes well the data and the inter-strip effects, the hit efficiency has been computed as

$$\epsilon = 1 - \left(\frac{n_{nullclusters}}{n_{events}}\right), \tag{4.7}$$
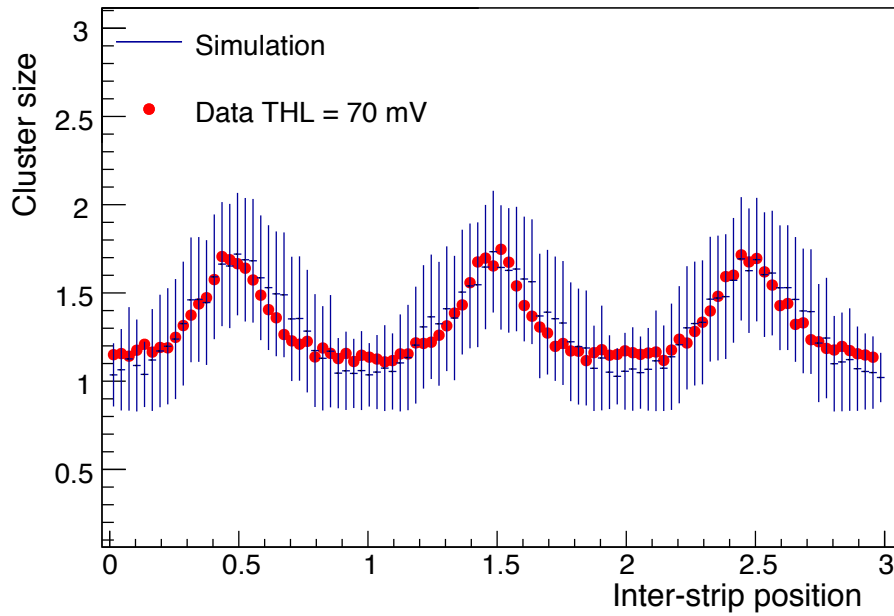
FIGURE 4.24: Comparison between the data from the barrel hybrid of May 2015 test beam at THL = 70 mV and HV=350V and simulated cluster size as function of the inter-strip position. The error bars represent the statistical error.

where $n_{nullclusters}$ is the number of simulated clusters with size 0 and n_{events} is the total number of simulated events.

Once the efficiency is calculated as function of the threshold, the S-Curves
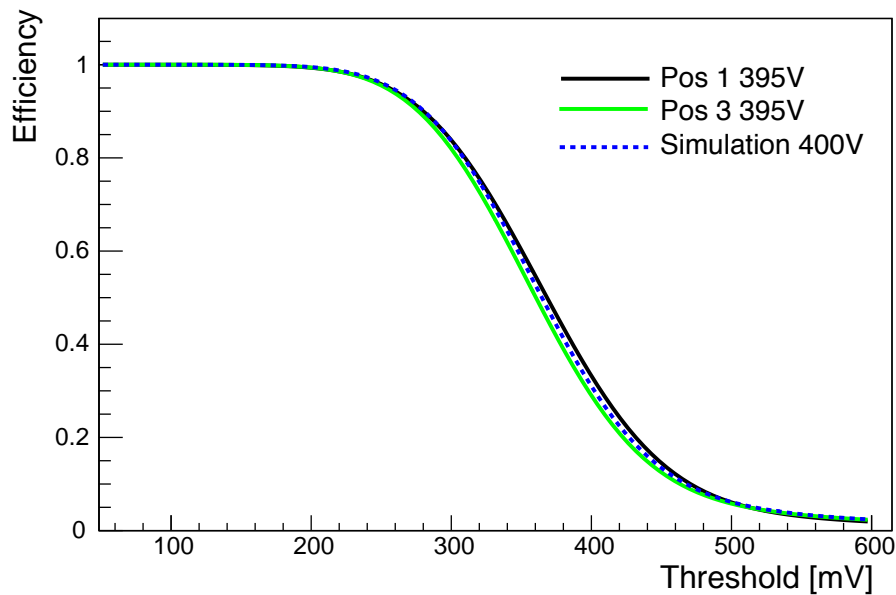
FIGURE 4.25: Comparison between the S-Curves from the long strips barrel module data and the simulation.

can be built. Figure 4.25 shows the fitted S-Curves from the barrel module data compared with the one obtained with the simulation: a good agreement between the simulation and the data is achieved. As reported in Table 4.5, the gain in the critical region around MPV is compatible with the measurements within the errors.

Sample	HV [V]	MPV [mV]	Gain at MPV [$\frac{mV}{fC}$]
Data - position 1	395	352.3 ± 1.9	107.0 ± 3.8
Data - position 3	395	342.0 ± 1.4	103.3 ± 3.7
Simulation	400	347.0 ± 1.4	104.3 ± 3.7

TABLE 4.5: MPV and gain for the barrel module and from simulation obtained with different input gains and gain degradation parameters.

Monte Carlo generation

A Monte Carlo (MC) generator is a software that produces hypothetical events with distributions based on theoretical predictions. Its aim is to describe, as closely as possible, the $p - p$ collisions that take place inside the detector. By repeating the modeling programs, an infinite number of pseudo-experimental data, that can provide an estimation of the real data composition, can be produced.

In this chapter, the phenomenology behind a proton - proton collision at LHC and its implementation in a Monte Carlo generator are described. A very good understanding of this process is a fundamental ingredient for data analysis in high energy physics.

5.1 Phenomenology of $p - p$ collisions

The complex phenomenology of a $p - p$ collision is behind any Monte Carlo generator. It is composed by different steps, illustrated in Figure 5.1, that will be delineated in detail in the next sections. The hard scatterer, described by the partonic cross-section, see Section 5.1.2, is the starting point for the creation of new particles in a $p - p$ collision: two partons inside the protons interact with each other with high momentum transfer. Several other ingredients describe a $p - p$ collision: the parton densities functions (Section 5.1.1), the parton shower (PS) (Section 5.1.3), the hadronization and decay (Section 5.1.4) and the underlying event (Section 5.1.5).

5.1.1 Parton Distribution Functions

A $p - p$ collision is a very tangled process that involves hundreds of hadrons in its final state. An accurate simulation of this process is necessary in order
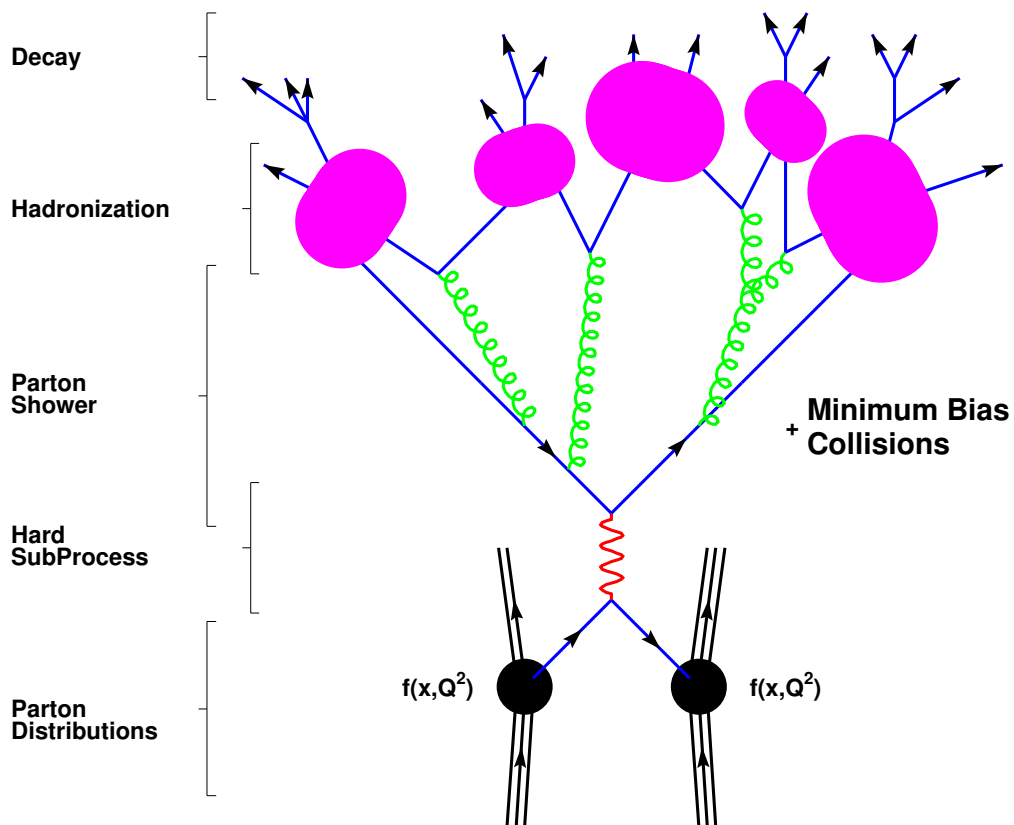
FIGURE 5.1: Schematic overview of the structure of a Monte
Carlo event. From Ref. [91].

to analyze its final states.

Every proton is composed by three valence quark, surrounded by a sea of quark-antiquark pairs, that are produced by virtual gluons. With the increase of the proton energy the partons move independently and freely in the proton (asymptotic freedom). Therefore, each one of them carries a fraction $x_i = 0, ...1$ of the proton total momentum $p_i = x_i p$: the probability of a parton carrying this momentum fraction x_i at a given energy scale Q^2 is described by a so called parton distribution function (PDF) $f(x, Q^2)$. The behavior of the PDF with the energy scale is quantitatively predicted by QCD from the DGLAP equation [92–94], while its dependence from x has to be determined experimentally. This is done in several well-known processes as in deep inelastic scattering, in Drell-Yann and $pp \rightarrow jets$ processes. Thanks to the DGLAP equation, the PDF is evolved at different Q^2 values and the parameters are constrained through a fit of the predictions to the measured data.

Those fits are performed by different groups of theorists that provide the PDF sets for the proton, like the CTEQ [95], HERAPDF [96], MSTW [97], and NNPDF [98, 99].

In Fig. 5.2 the PDFs for quark and gluons inside the proton as a function of the momentum fraction x for different momentum transfer scales are shown: on the left-hand side for $Q^2 = 10 \ GeV^2$ and on the right-hand side for $Q^2 = 10^4 \ GeV^2$. In the low x regions gluons are predominant and for high Q^2 the contributions from sea quarks are more relevant.

5.1.2 Hard scattering cross-section

Scattering processes at high energy hadron colliders are described by Quantum Chronodynamics (QCD) and they can be divided in two main components: hard and soft processes. The first ones, like for example Higgs boson or high p_T jet productions, are characterized by large momentum transfer and are well described by a perturbation theory. The second ones, soft processes, such as the underlying event, present a small momentum transfer and are less understood since they are dominated by non-perturbative QCD effects.

In Figure 5.3 a general hard-scattering process for two hadrons A and B is shown. The two partons a, b inside the incoming hadrons undergo the hard scattering process (HS) described by the cross-section $\hat{\sigma}$ [100]. The PDFs $f_{a/A}(x_a, \mu_F^2)$ and $f_{b/B}(x_b, \mu_F^2)$ are the probability to find the parton a/b in hadron A/B with a momentum fraction respectively x_a and x_b at the energy scale μ_F^2. In this way, integrating over all the momentum fractions and

MSTW 2008 NLO PDFs (68% C.L.)
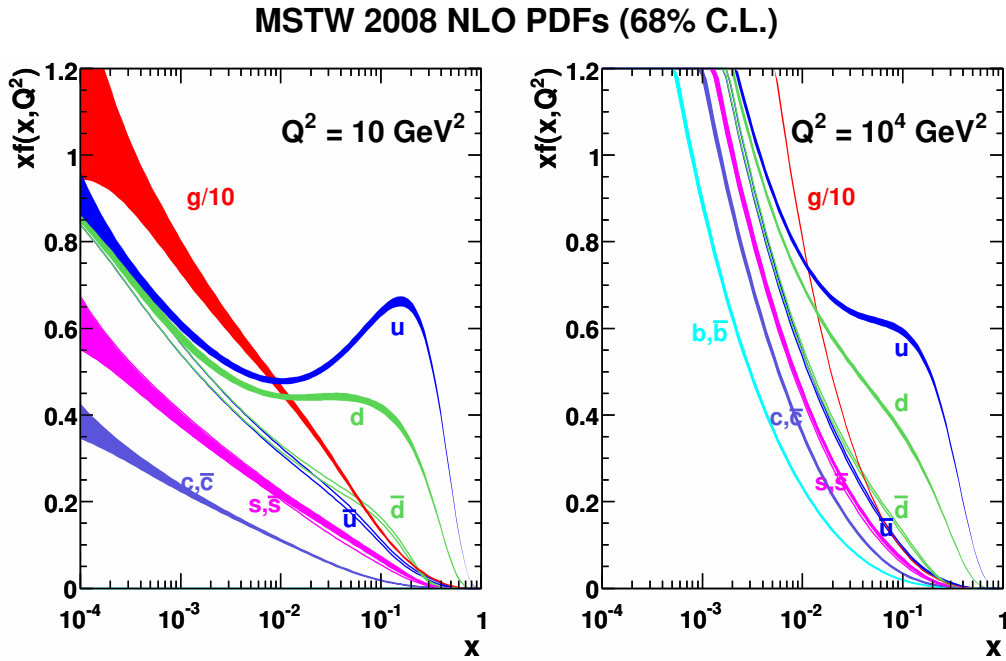
FIGURE 5.2: MSTW 2008 NLO PDFs for quark and gluons that are inside the proton as a function of the momentum fraction x, for (left) $Q^2 = 10\ GeV^2$ and (right) $Q^2 = 10^4\ GeV^2$. The bands are the uncertainties at the 68% confidence level.
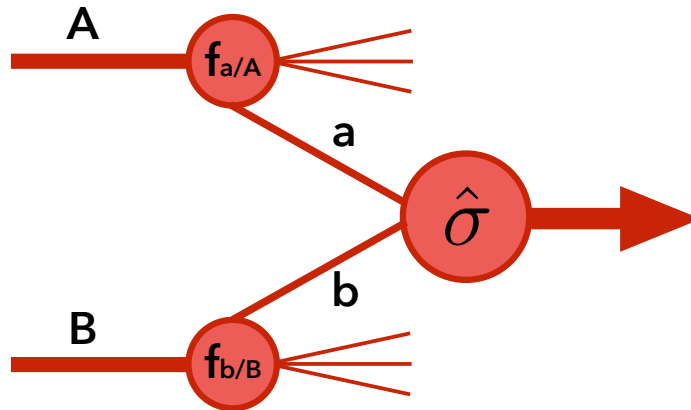
FIGURE 5.3: An example of hard scattering process.

summing over all the possible parton-parton scattering processes, the total hadron-hadron cross-section can be calculated:

$$\sigma_{AB} = \sum_{a,b} \int dx_a dx_b f_{a/A}(x_a, \mu_F^2) f_{b/B}(x_b, \mu_F^2) \hat{\sigma}_{ab \to X}(x_a, x_b, \alpha_s(\mu_R^2)). \quad (5.1)$$

In formula 5.1 μ_F is the factorization scale that can be seen as the scale that disjoints short and long distance processes, α_s is the running coupling

that is a function of the non-physical renormalization scale μ_R; if, for a given process, μ_R is chosen to be close to the scale of the momentum transfer Q, then $\alpha_S(\mu_R^2 \approx Q^2)$ gives an indication of the effective strength of the strong interaction in the considered process [101].

Real and virtual gluon corrections to the lowest order process, that are responsible of collinear singularities, can be assimilated into renormalized scale dependent parton distributions. A general feature of the inclusive hard scattering process is that all collinear divergences, that show up in the process corrections, can be factorized into renormalized parton distributions (*factorization theorem*). Thus, Equation 5.1 can be rewritten taking into account the finite contributions left behind after the singularities have been factorized into the PDF [102]:

$$\sigma_{AB} = \sum_{a,b} \int dx_a dx_b f_{a/A}(x_a, \mu_F^2) f_{b/B}(x_b, \mu_F^2)[\hat{\sigma}_0 + a\hat{\sigma}_1 + a^2\hat{\sigma}_2 + ...]_{ab \to X} \quad (5.2)$$

where $a = \alpha_s(\mu_R^2)/2\pi$.

In equation 5.2 $\hat{\sigma}_0$ is the leading order (LO) cross-section and $\hat{\sigma}_1$, $\hat{\sigma}_2$ are the cross-sections at higher orders, respectively the next to leading (NLO) and the next-next to leading order (NNLO). The cross-sections at higher orders are usually parametrized as total k-factors:

$$\hat{\sigma}_n = \hat{\sigma}_0 \cdot K^n, \quad (5.3)$$

where K^n is the ratio of the cross-section at the order n normalized to the LO cross-section.

In order to avoid another reappearance of the over-mentioned divergences in the perturbation series, it is a good choice to set the μ_F and μ_R values at about the order of the momentum scales of the hard scattering process. Furthermore, a common choice is to assume $\mu_R = \mu_F$. As an example, for the Drell-Yan process, the conventional choice is the mass of the lepton pair $\mu_R = \mu_F = m_{\ell\ell}$.

In the behavior of the strong coupling constant can also be found an explanation of why only the hard scatterer can be described with a perturbation theory, while the soft processes can not. Indeed, $\alpha_S(Q^2)$ decreases with increasing Q^2, therefore processes with high momentum transfer can be described with a series expansion, neglecting higher order terms that become more and more small. On the contrary, in processes with low momentum transfer, higher order terms turn progressively larger and can not be expressed in a series

expansion.

5.1.3   Parton Shower

In the previous section, the generation of an hard process has been described according to the lowest order matrix elements. However, although this can give a good description of the outgoing jets momenta, a fixed order description is not enough to give a complete picture of the process.

A *parton shower* algorithm helps to simulate the effect of all higher orders: it reproduces a series of emissions from the incoming and outgoing partons. The momentum transfer evolution from the scales associated with the hard process down to low scales of the order of a few GeV is simulated. A succession of simple parton branchings is the base of the evolution of a multi-parton final state. This series is regulated by timing constraints that ensure that the successive emission takes place with lowered energy. It can happen that one of the incoming colliding partons or one of the final state ones emit radiation: the first scenario is usually referred to as *initial state radiation* (ISR), while the second one *final state radiation* (FSR).

5.1.4   Hadronization and decay

The process referred to as *hadronization* starts when the particles momenta reach the scale of QCD (Λ_{QCD}). At this stage, with the combination of gluons and quarks into colorless states, hadrons are formed. Afterwards, the hadrons decay into stable particles. The hadronization process regulates the transformation from partons into a cone of hadrons, called *jet* (see Section. 6.2). The final jets are evaluated by reconstruction algorithms, with the aim of analyzing the features of the original partons. Soft and collinear emissions can take place during parton shower and as well during hadronization processes. These emissions are included in the reconstruction algorithms (*infrared and collinear safety*) to guarantee a correct definition of the hadronic final state observables.

5.1.5   Underlying event

All those processes that do not come from the hard scattering are referred to as *underlying event*. An example is given by the interactions coming from the remaining partons in the colliding protons. The characterization of an underlying event is usually given in terms of p_{T} of the partons. The physics of

soft processes (meaning with low p_T values) is very complicated and it cannot be fully described in perturbative QCD: soft models have to be introduced and their description has to be tuned to the data.

5.2 Monte Carlo generators

There are several Monte Carlo generators available to model background and signal processes or provide estimates of theoretical uncertainties. In general, these can be divided in two groups: matrix element and general purpose generators. The first ones only simulate the HS processes: the parton shower is applied in a second step using a dedicated generator. For the general purpose ones, instead, the full $p - p$ collision with parton showering and hadronisation is simulated. In the following, the main generators employed in this thesis are briefly outlined.

MADGRAPH5_AMC@NLO [103] generates parton-level events for a broad range of processes at the leading order and next-to-leading order in QCD. The output, in form of a "Les Houches" file [104], can consequently be processed by a general purpose Monte Carlo for showering and hadronization.

POWHEG [105] is a matrix element Monte Carlo that can simulate the HS at NLO QCD, and can be interfaced with parton shower generators.

Sherpa [106] is a general purpose Monte Carlo used to model the hard process at NLO, the initial and the final state radiation, the underlying event and showering. One of its main goals is to describe final states with more than two partons.

PYTHIA [107] is a multi-purpose simulator that can model two-to-two processes at LO but it is mainly employed for parton showering, including the the underlying event, hadronization and pile-up events (for the definition of pile-up events see Sec 6.1).

HERWIG [108] is a LO general purpose Monte Carlo that simulates the HS, with two initial particles going into two final particles. The parton shower simulates the final states with higher multiplicity, with initial and final state radiation, the underlying event and hadronisation. This generator is mainly employed for its parton-shower algorithms.

5.3   Signal samples production

The VBF $H{\to}WW^*{\to}\ell\nu\ell\nu$ samples for different values of the coupling parameters a_L and a_T, described in Chapter 2, have been simulated with MAD-GRAPH5_AMC@NLO at the leading order and then showered with PYTHIA 8. A total of nine samples have been produced, corresponding to the following (a_L,a_T) pairs: (1,1), (1,1.3), (1,0.7), (1.3,1), (1.3,1.3), (1.3,0.7), (0.7,1), (0.7,1.3) and (0.7,0.7). Other points in the a_L and a_T phase-space have been simulated using the analytical Lagrangian morphing method, as described in Section 8.2.

A necessary ingredient for the matrix element calculation is the Lagrangian with its parameters, and this is implemented in FEYNRULES [109], while the generation of the corresponding helicity amplitude subroutines is performed thanks to the ALOHA package [110]. To produce the polarized samples, the helicity amplitudes, used in the matrix element generation of the Higgs production and decay, are modified to account for deviations in the Higgs coupling strengths in the Higgs rest frame, following the prescription given by the authors of Reference [28].

The polarized coupling definition in both decay and production vertices is only possible to implement at LO. Therefore, some precautions have been taken to minimize the difference between the LO and NLO SM predictions.

LO is characterized by a larger dependence on the choice of renormalization and factorization scales with respect to a NLO calculation. In general, an advantageous scale choice is to set a scale proportional to the momentum transfer of intermediate vector bosons. If a fixed scale is chosen, a straightforward choice would be to set the scales to the mass of the W boson: $\sqrt{Q_1Q_2} = \sqrt{M_W M_W} = M_W$, since the contribution to the cross-section comes from virtualities that are of the order of the W boson propagator mass or smaller. However, a fixed scale is not ideal. Considering higher order in α_S, additional initial state radiation can happen at energies different than the W boson mass. Therefore, a more appropriate choice is to set a dynamic scale as the sum of all the p_T of the final state partons:

$$\mu_R = \mu_F = \sum p_T^{partons}. \tag{5.4}$$

The main shape differences between LO and NLO predictions are affecting jet distributions. Therefore, the shower evolution scale and its link to the hard process scale has been studied. To correct LO predictions and make it

more similar to NLO, the value of the parameter `ptMaxFudge` in the PYTHIA 8 settings has been changed. If the final state of the hard process contains at least one quark, gluon or photon, then the maximum p_T for the shower evolution scale is chosen to be at the level of the factorization scale. `ptMaxFudge` regulates $p_T^{max} = p_T^{factorization}$ introducing a multiplicative factor f such that $p_T^{max} = f \times p_T^{factorization}$. This applies only to the hardest and the second-hardest jet in an event. Tuning this parameter by a factor f, the hardest and the second hardest jets are limited to be less powerful if $f < 1$ or more powerful if $f > 1$.

In Figures 5.4- 5.6 the comparisons at pre-selection level between some truth level jet quantities at NLO and LO are shown. The LO prediction is given for different settings of `ptMaxFudge`. This parameter has been changed from its default value of 1 (yellow dots) to 0.5 (green dots) and 0.25 (red dots). The overall best agreement between LO and NLO is obtained for `pTmaxFudge` equal to 0.25.

Several distributions have benefited from this tuning. In Fig. 5.4(a) the p_T of the sub-leading jet is shown. The best agreement between NLO and LO is achieved when `pTmaxFudge` = 0.25. A similar agreement is also obtained for the leading-jet. The invariant mass of the two jets is shown in Fig. 5.4(b). Low values of the m_{jj} distribution do not present the best agreement at `pTmaxFudge` = 0.25. However, at m_{jj} values between 200 and 1200 GeV, a better accordance is on average visible between NLO and `pTmaxFudge` = 0.25. A good correspondence is also visible for the central values of the η distributions of the two jets (Fig. 5.5(a)-5.5(b)) at `pTmaxFudge` = 0.25. Instead, the ϕ distributions of the two jets are not significantly affected by this parameter modification, as shown in Fig. 5.6(a)-5.6(b).

To compensate for this parameter tuning, a systematic uncertainty has been evaluated, see Section 7.8.2 for more details.
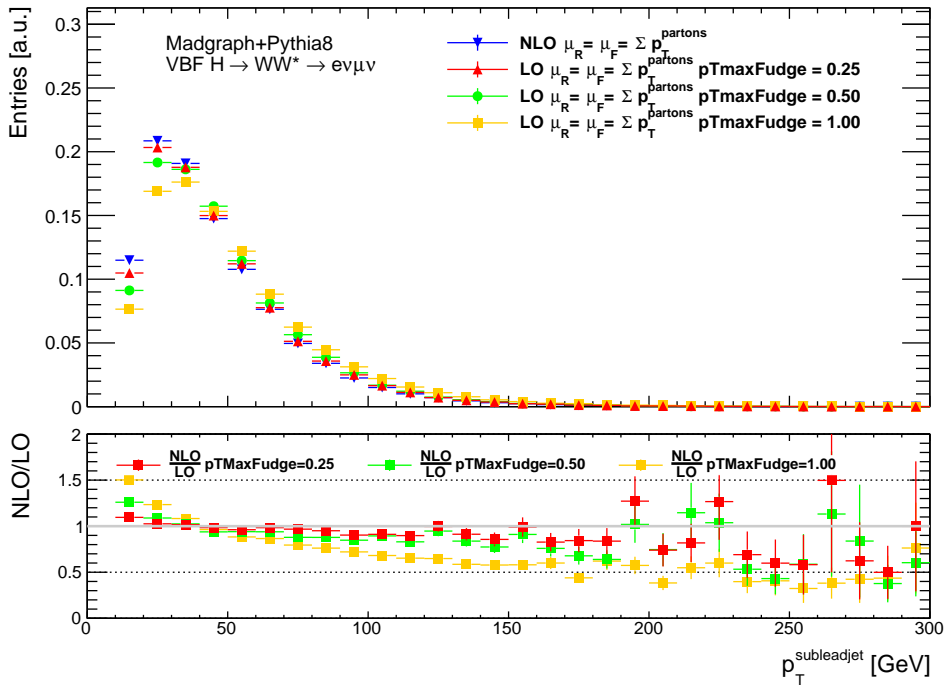
(a)
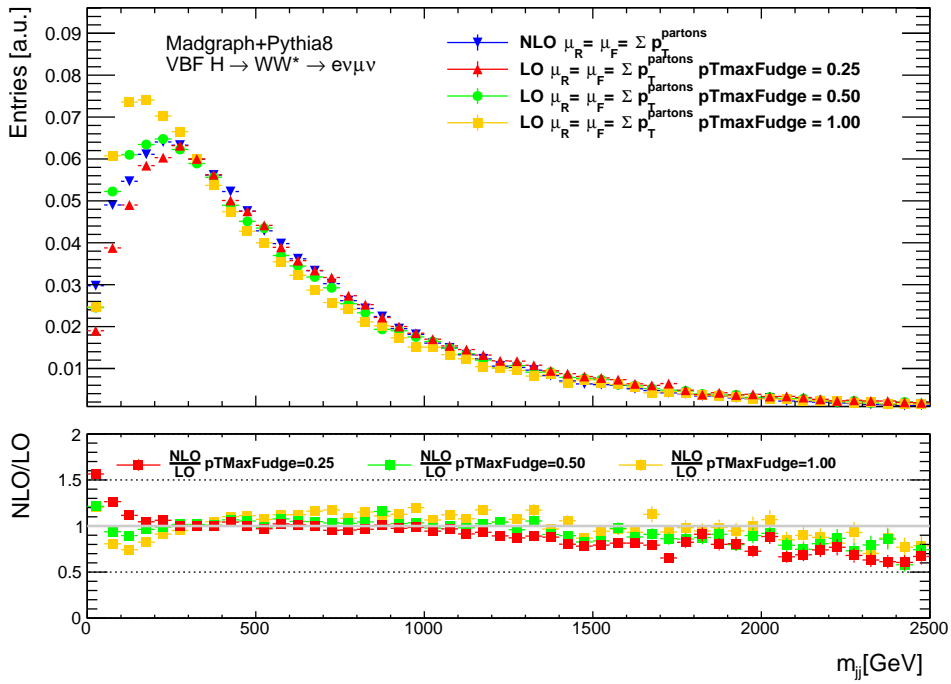
(b)

FIGURE 5.4: Comparison between truth-level p_T of the sub-leading jet and m_{jj} at NLO and LO with different `ptMaxFudge` settings (1, 0.5 0.25). The plots are at pre-selection level, described in Section 7.5. On the bottom plot, the ratio between the NLO prediction and each one of the LO cases is shown. The errors show the statistical uncertainty.
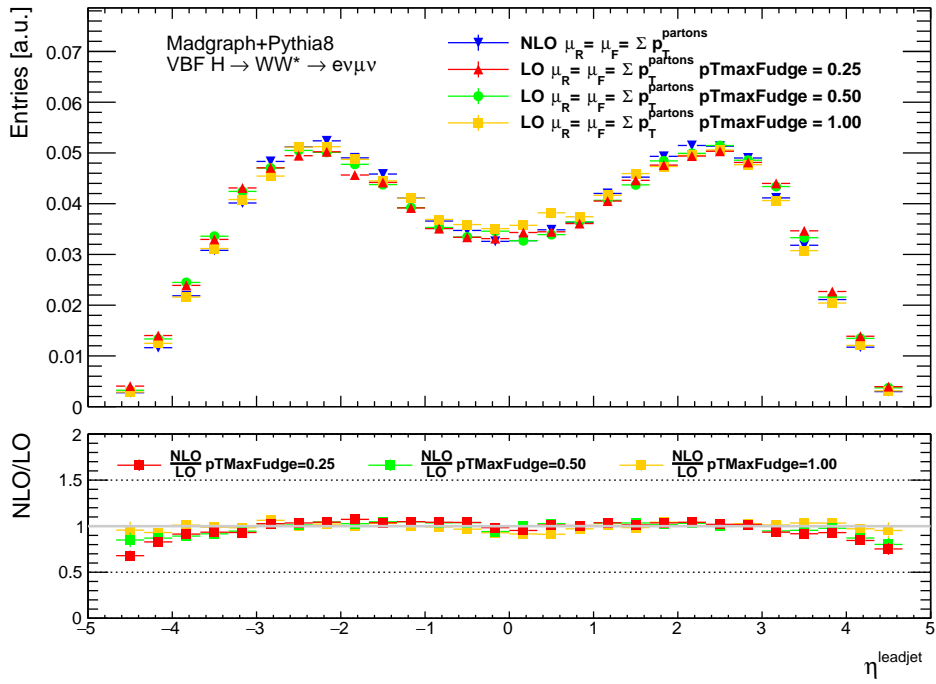
(a)
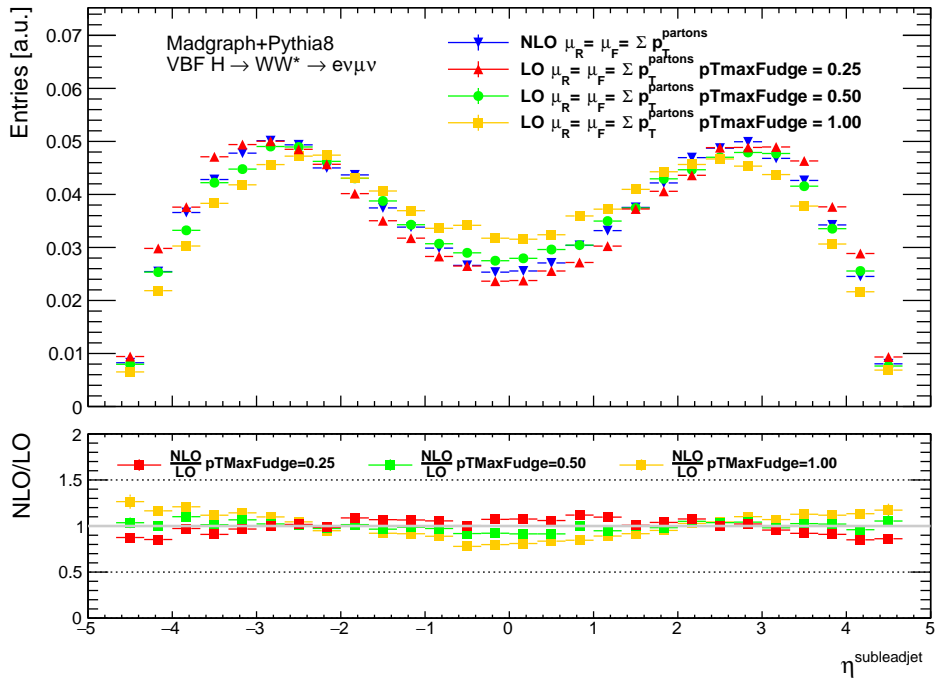
(b)

FIGURE 5.5: Comparison between truth-level η distributions of the leading and sub-leading jet at NLO and LO with different `ptMaxFudge` settings (1, 0.5 0.25). The plots are at pre-selection level, described in Section 7.5. On the bottom plot, the ratio between the NLO prediction and each one of the LO cases is shown. The errors show the statistical uncertainty.
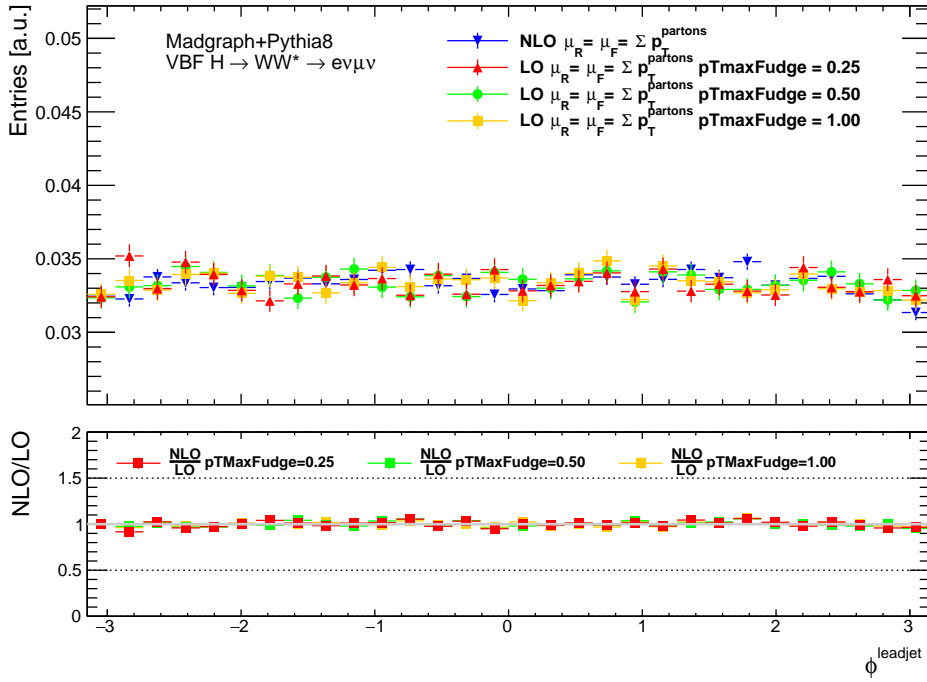
(a)
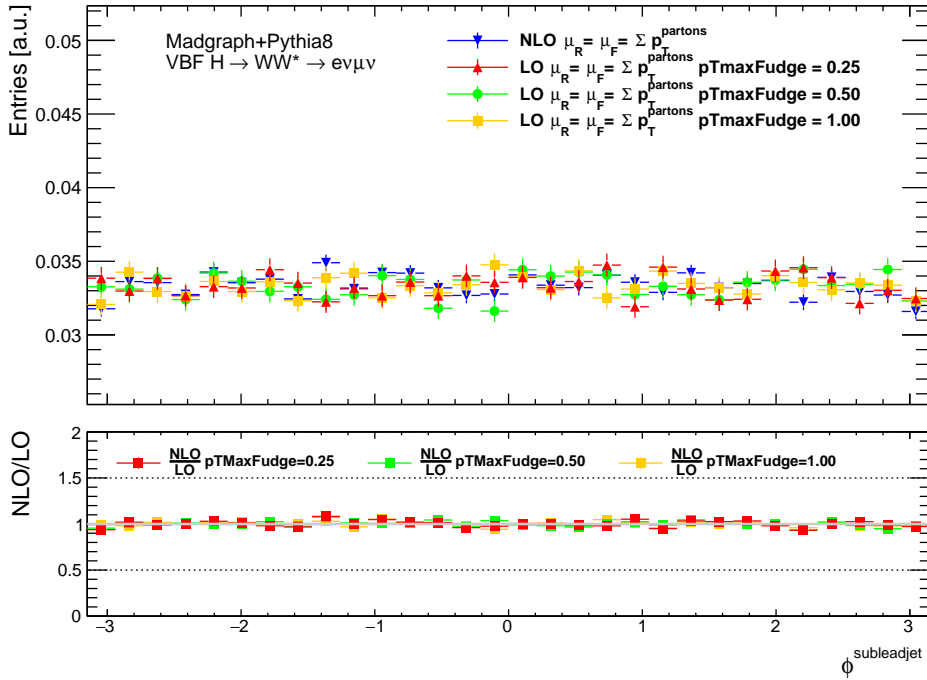
(b)

FIGURE 5.6: Comparison between truth-level ϕ distributions of the leading and sub-leading jet at NLO and LO with different `ptMaxFudge` settings (1, 0.5 0.25). The plots are at preselection level, described in Section 7.5. On the bottom plot, the ratio between the NLO prediction and each one of the LO cases is shown. The errors show the statistical uncertainty.

Event reconstruction

The final state for the $H \rightarrow WW^* \rightarrow \ell\nu\ell\nu$ analysis consists in two leptons, an electron and a muon, two neutrinos and two high-energetic jets. All these particles need to be properly reconstructed and identified. Each object produced in a $p - p$ collision travels through the detector and interacts with each sub-part of it according to its own characteristics. By combining the sub-detector responses, the final state objects can be correctly identified and their physical properties can be defined. The reconstruction of tracks and particles is usually referred to as *event reconstruction*. This chapter aims to outline the reconstruction algorithms and techniques used to identify the final state objects relevant for the analysis discussed in this thesis.

6.1 Tracks and vertices

The reconstructed particles are not only the result of the hard-scatter process, but can be due to additional collisions that accompany the signal. These low p_{T} $p - p$ collisions are called *pile-up interactions*. There are two kinds of pile-up interactions: an *in-time pile-up*, where the interactions originate from additional $p - p$ interactions in the current bunch-crossing, and *out-of-time pile-up*, that arises from energy deposits in the ATLAS calorimeter from bunch crossings that happened right before or after the triggered event. The Inner Detector is particularly affected by the increase of particle multiplicity with pile-up. In an high pile-up environment, the increase of the per-event occupancy, meaning the fraction of channels that are read out from each sub-detector, becomes a challenge for the read-out electronics of the sub-detectors. The Pixel detector, that is closest to the interaction point, sees the highest particle flux but, because of his high granularity, has the lowest occupancy. In the SCT, since the strips are larger than the pixels, the highest occupancies

are in the first layer of the silicon detectors. The TRT, that presents smaller granularity, has even higher occupancy. Due to the increased detector occupancy, track reconstruction gets more challenging. A bad hit reconstruction can result in a degraded track parameter resolution, fake tracks arising from random hit combinations and decreased efficiency. Vertex resolution is also affected by the increased density of collisions; for example, this happens when a track is included in a vertex or when two nearby vertices are merged into a single one. Algorithms for both track and vertex reconstruction are therefore designed to minimize the impact of these effects arising from high density environments.

6.1.1   Tracks reconstruction

Tracks are described by the following parameters:

$$(d_0, z_0, \phi, \theta, \frac{q}{p}). \tag{6.1}$$

z_0 and d_0 indicate the minimum distance, respectively, in the longitudinal direction and in the transverse plane to the center of the detector. The angles ϕ and θ are the azimuthal and polar angle of the track at its perigee. At last, q/p is the ratio of the charge over the momentum. During track reconstruction, quality requirements are applied to the over-mentioned parameters and to the number of hits in the ID. Different track reconstruction algorithms are employed for primary and secondary particles [111]. A particle is defined primary if its life time is longer than 3×10^{-11} s and if it has been produced at the interaction point or if it is the result of the decay of another particle with shorter lifetime. To track this kind of particles, an *inside-out* algorithm is used, that iteratively builds the track starting from the innermost layers of the detector. A three point seed in the silicon detectors (Pixel and SCT) is the starting point of the algorithm that consequently adds hits moving away from the interaction point, employing a combinatorial Kalman filter [112]. Dedicated algorithms resolve the ambiguities in the track candidates encountered in the Pixel and SCT, allowing to extend the tracks into the TRT [113]. For secondary tracks, an opposite strategy is instead applied, using *outside-in* algorithms, also called "back-tracking". This sequence includes the hits not considered by the inside-out algorithm; the seed is located in the TRT and the track is consequently reconstructed inwards in the silicon detectors. The reconstruction algorithm selects tracks with $p_\mathrm{T} > 400$ MeV and $|\eta| < 2.5$.

Further requirements are then imposed: the *Loose* selection, that is the default track requirement applied during the inside-out reconstruction, requires at least 7 silicon hits, zero or one shared modules and pixel holes and two or less silicon holes. Holes are missing hits on a track: more precisely, a hole is defined as crossings of the track with a detector component which does not present a hit. Instead, a shared module for the Pixel detector consists in a hit associated to more than one track, while, for the SCT, in two shared hits in the same SCT layer. The *Loose* track selection presents a highly efficient charged particle reconstruction with a non-negligible fraction of fake tracks. On top of this, more strict requirements can be added with the *Tight Primary* selection. As its name reflects, it selects primary tracks, with a high rejection of fake tracks, but with a reduced track reconstruction efficiency. It requires tracks with at least 9 or 11 silicon hits (if $|\eta| \leq 1.65$ or $|\eta| \geq 1.65$), the presence of at least one hit in one of the two innermost pixel layers and zero pixel holes.

The fraction of primary particles, with $p_\mathrm{T} > 400$ MeV and $|\eta| < 2.5$, associated to a reconstructed track, defines the reconstruction efficiency, shown in Fig. 6.1 for both the *Loose* and the *Tight Primary* selections. The track reconstruction efficiency for *Tight Primary* is overall lower than for *Loose* tracks, as a consequence of the more strict requirements. However, the fake rejection improves with the *Tight Primary* selection, as shown in Figure 6.2. In Figure 6.2(a) the average number of tracks passing the *Loose* and *Tight Primary* selections as a function of the average number of collisions per bunch crossing μ is shown. The fake rate is approximated, assuming a proportionality between the number of non-fake tracks and the number of pile-up interactions. Deviations from linearity are considered caused by the fakes. A linear fit is performed in the region $10 \leq \mu \leq 15$ where simulation and data present a linear behavior. The fake rate is then estimated as the deviation from the linear fit as a function of μ (see Figure 6.2(b)). Consequently, the *Tight Primary* selection has a smaller fake rate than the *Loose* one.

6.1.2 Primary vertex reconstruction

When all tracks are fitted, they are assigned to their vertices thanks to dedicated algorithms.

Iterative vertex finding algorithms ([111]) are employed to reconstruct primary vertices. The tracks selected for the primary vertex reconstruction must fulfill the *Tight Primary* selection criteria. Selected events have to present at least one vertex to be reconstructed using at least two good quality tracks.
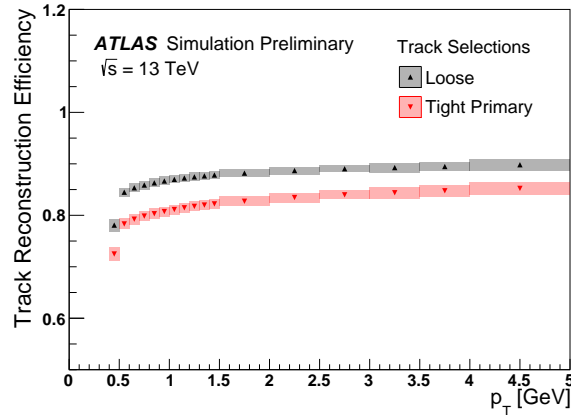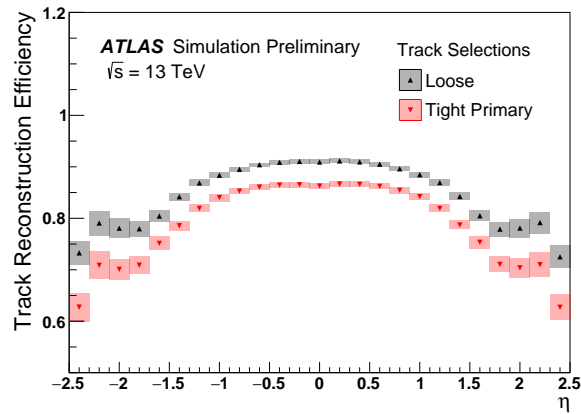
FIGURE 6.1: Track reconstruction efficiency as a function of track p_T and η, evaluated with simulated events, for *Loose* and *Tight Primary* track selections. The bands show the total systematic uncertainty. From Ref. [114]

The seed of the vertex can be derived from the z-position at the beam-line of the reconstructed track. After having found the seed, the nearby tracks are studied with an iterative χ^2 fit: a weight is assigned to each track, based on the χ^2 of the fit, in order to measure the track compatibility with the fitted vertex. If a track is found to be away by more than 7σ from the vertex is discarded and the procedure is iterated until no additional vertices are found. The position of the proton beam, usually called *beam-spot*, is identified thanks to a three-dimension spatial distribution of the reconstructed vertices: it is determined by monitoring the primary vertex position in a certain time window. The mean of the corresponding Gaussian distribution is taken as the resulting beam position. Consequently, a second reconstruction of the vertices

(a)

(b)
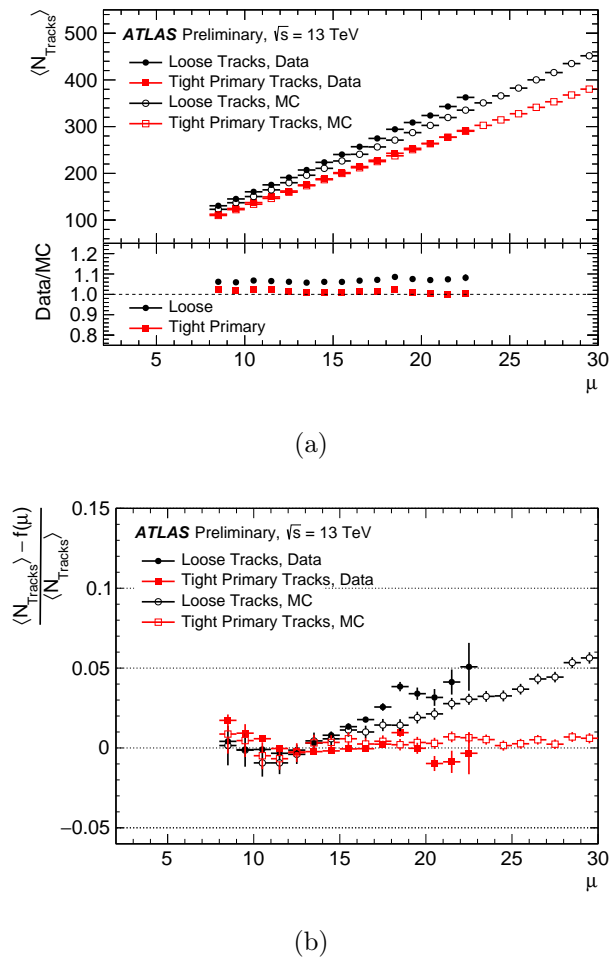
FIGURE 6.2: In 6.2(a) the average number of reconstructed tracks N_{trk} as a function of the average number of collisions per bunch crossing μ is shown for *Loose* and *Tight Primary* selections. The statistical errors are reported but too small to be seen. The plot in the lower box shows the data/MC ratio. In 6.2(b) is shown the estimation of the tracking fake rate, derived from the deviation from linearity of a fit to the number of tracks as a function of μ. Figures from Ref. [114]

is performed adding the derived beam spot as an additional measurement. The resolution on the vertex position increases with the number of tracks and with the square sum of the transverse momenta. The primary vertex is defined as the vertex with the largest squared sum of the tracks transverse momenta: $\Sigma_i^{N^{trk}} p_{T,i}^2$.

The remaining reconstructed vertices are then associated to pile-up ones. The vertex reconstruction efficiency, shown in Fig. 6.3(a), is calculated from data by taking the ratio between events with a vertex that has been reconstructed and events that present at least two reconstructed tracks. At least four tracks

are needed in order to have an efficiency greater than 99%. Fig. 6.3(b) shows
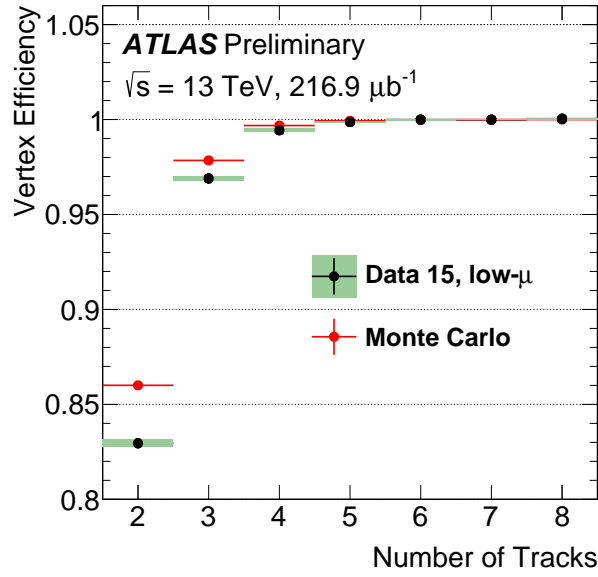
(a)
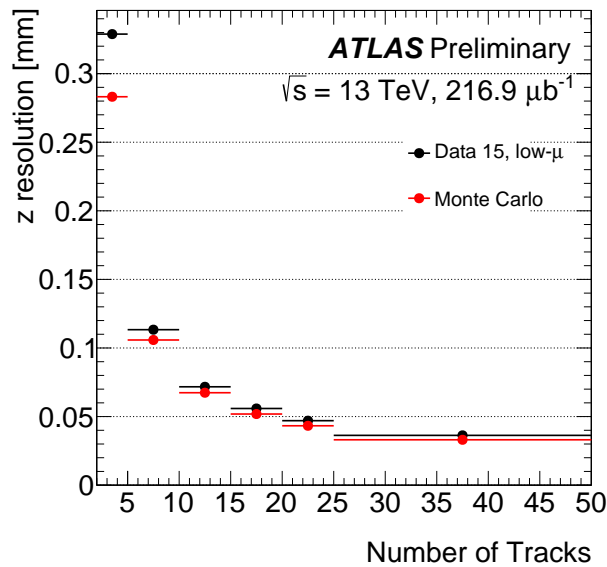
(b)

FIGURE 6.3: In Figure 6.3(a) the vertex reconstruction efficiency as a function of the number of tracks is shown. Figure 6.3(b) shows, instead, the data-Montecarlo comparison for the resolution on the z vertex coordinate as a function of the number of associated tracks, N^{trk}. Figures from Ref. [115].

the data/MC simulation comparison for the resolution on the z vertex coordinate as a function of the number of associated tracks, N^{trk}.

6.2   Jets

Each parton, coming from the hard process, goes through an hadronization process, generating a collimated bundle of hadrons, with null color charge. The energy of this *jet*, that has approximately the same direction of the original parton, is deposited into the calorimeters and is mainly measured in the hadronic calorimeter. The topological calorimeter cells that contain a high signal over noise ratio are used to build clusters of energy deposits, called *topo-clusters* [116, 117]. These energy clusters are given as input for jet finding algorithms. In ATLAS the main jet finding algorithm is the anti-kt algorithm [118]. Its main characteristics are that it is collinear and infrared safe: its results are not sensitive in case of a collinear splitting or in case of an emission of a low energy gluon. The algorithm studies the distances between an object i with another object j or the beam B. The objects i and j are combined if their distance, d_{ij}, is the smallest, otherwise, if the distance d_{iB} results to be the smallest, i is considered as a jet and removed from the list of considered objects. This procedure is iterated until no more objects are left. The distances are defined as following:

$$d_{ij} = min(k_{T_i}^{2p}, k_{T_j}^{2p}) \frac{\Delta R_{ij}}{R} \tag{6.2}$$

and the distance to the beam axis:

$$d_{iB} = k_{T_i}^{2p} \tag{6.3}$$

where, in Formula 6.2, $\Delta R_{ij} = (\eta_i - \eta_j)^2 + (\phi_i - \phi_j)^2$ and k_{T_i}, η_i and ϕ_i are respectively the transverse momentum, the rapidity and the azimuthal angle of the particle i. The two constants, R, that defines the size of the jet cone, and p, that ensures that energy deposits caused by soft radiation are clustered together into the hard object, are set respectively to 0.4 and to -1.

Jet calibration   The measured jet energy needs to be calibrated [119] to take into account several detector effects, like, for example, energy losses in non-sensitive areas of the detector or calorimeter non compensation. This calibration is performed at different stages, summarized in Figure 6.5. The calorimeter energy measured at the electromagnetic energy scale, that evaluates the energy of the showers of electrons and photons, is used as starting point. Afterwards, the four-momentum of jets is re-calculated such that they
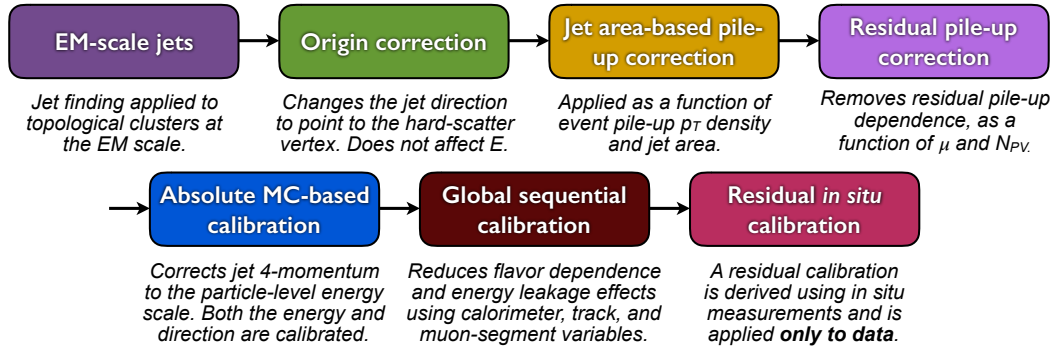
FIGURE 6.4: Different stages of the calibration procedure for
EM-scale jets. Excluding the origin correction, all the other
stages of the calibration are applied to the four-momentum of
the jet. From [119].

point towards the hard-scatter vertex rather than towards the center of the
detector. This correction improves the η-resolution of jets from roughly 0.06
to 0.045 for jet p_T =20 GeV and from 0.03 to below 0.006 above 200 GeV.
At this stage, corrections on the the pile-up are applied to remove the excess
energy due to in-time and out-of-time pile-up. At first, an area-based method
subtracts to the p_T of each jet the per-event pile-up contribution according
to its area; then, a residual correction is derived from simulation.

In the next step, the absolute jet energy scale (JES) calibration and η cali-
bration are applied. The reconstructed jet four-momentum are corrected to
the particle-level energy scale, taking into account for biases in the jet η re-
construction.

A global sequential calibration, that uses information from the calorimeter,
MS and track-based variables, is then performed to improve the reconstructed
energy and related uncertainties.

Finally, in the last stages, a residual *in situ* calibration is applied to account
for discrepancies in the jet response between data and simulation. The latter
one can indeed present some imperfections in each one of its steps, from the
simulation of the hard process to the simulation of the detector response. The
quantification of these differences is done by comparing the p_T of a jet with
an other well-measured reference objects.

Jet energy scale uncertainty   A set of eighty JES systematic uncertainty
terms are propagated from each single calibration to the final one. Most of
these uncertainties arise from in situ calibrations, and take into account all
the assumptions made for the event topology, the MC simulation, and the

sample statistics. Furthermore, all the propagated uncertainties of the electron, muon, and photon energy scales are considered. The JES uncertainty shown in Figure 6.5, is found to be at a level of 4.5% at 20 GeV, 1% at 200 GeV, and 2% at 2 TeV.
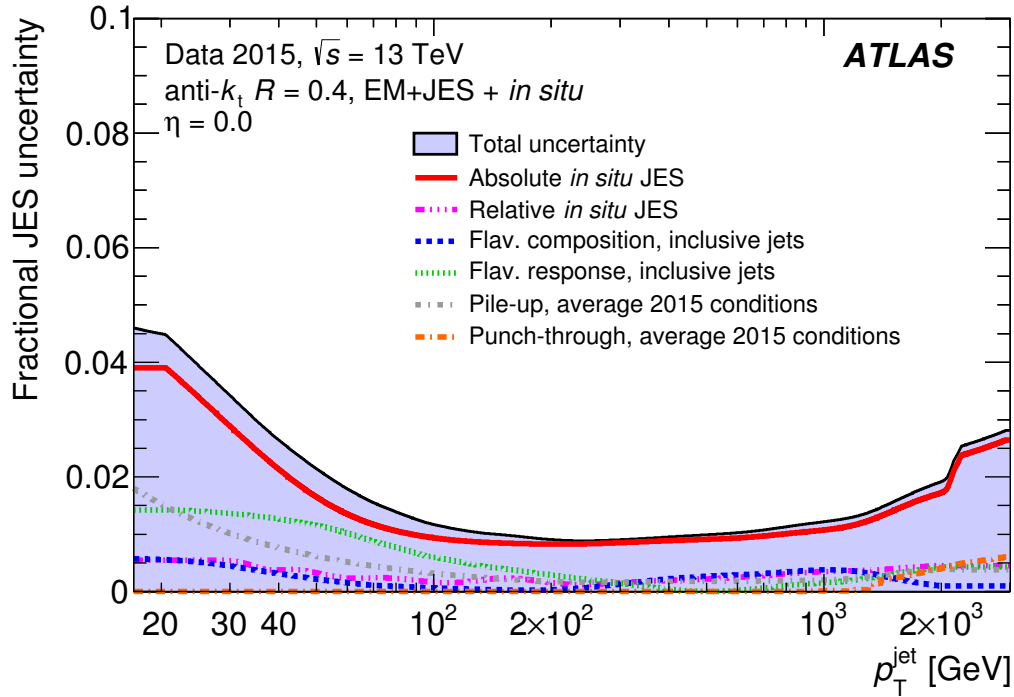
FIGURE 6.5: Fractional JES uncertainty as a function of the jet p_T. The systematic uncertainty includes the pile-up and punch-through components, and as well the uncertainties propagated from the Z/γ-jet and the absolute and the relative *in situ* JES. Figure from [119]

Pile-up jets and the Jet Vertex Tagger   The pile-up contribution is usually estimated and subtracted from the signal interaction of interest. However, spurious pile-up jets can come from local fluctuations in the pile-up activity. These additional jets can be classified into two categories. In the first one, the jet particles come from a single QCD process that took place in a single pile-up interaction (*QCD pile-up jets*). In the second one, the jet particles come from different interactions (*stochastic jets*). The majority of the particles matched to the hard-scatter jet come from the primary interaction, while for QCD pile-up jets the majority of the particles derive from a single pile-up interaction. In the stochastic pile-up jet, the particles do not have a prevalent origin and are matched with both pile-up interactions in the event. In Figure 6.6 an event with a stochastic pile-up jet, a QCD pile-up jet and a

hard-scatter jet are shown.

In order to suppress this pile-up contribution, a discriminant, called Jet Vertex Tagger (JVT) is built [120]. This discriminant is constructed by defining
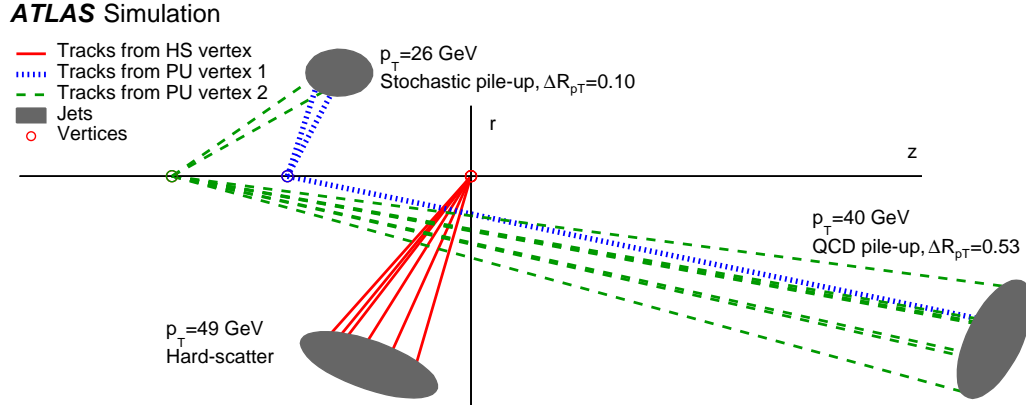
FIGURE 6.6: Illustration of an event containing a hard-scatter, a stochastic and a QCD pile-up jets in the $r - z$ plane. Figure from[121].

a 2-dimensional likelihood based on a k-nearest neighbor algorithm (kNN) [122]. It uses two quantities: the first one is defined as the sum of the scalar transverse momentum of the tracks coming from the hard-scatter vertex associated with the jet, divided by the scalar p_T sum of all associated tracks:

$$corrJVF = \frac{\sum p_T^{\text{trk}}(\text{PV}_0)}{\sum p_T^{\text{trk}}(\text{PV}_0) + \frac{\sum_{i \geq 1} \sum p_T^{\text{trk}}(\text{PV}_i)}{(k \cdot n_{trk}^{PU})}}, \tag{6.4}$$

where $\sum p_T^{\text{trk}}(\text{PV}_0)$ is the scalar p_T sum of the tracks that are associated with the jet from the hard-scatter vertex, while term $p_T^{PU} = \sum_{i \geq 1} \sum p_T^{\text{trk}}(\text{PV}_i)$ is the scalar p_T sum of the associated tracks from the pile-up interactions. To correct for the linear increase of $< p_T^{PU} >$ with the total number of pile-up tracks per event (n_{trk}^{PU}), p_T^{PU} has been corrected with a factor $(k \cdot n_{trk}^{PU})$ with $k = 0.01$[1]. All tracks associated with vertices other than the hard-scatter vertex define the total number of pile-up tracks per event. This variable can have values between 0 and 1, but for jets with no associated tracks a value of -1 is assigned. The mean of the JVF distribution shifts to smaller values when the denominator of JVF increases, because the latter one grows with the number of pile-up tracks associated with the jet and consequently, with the number of reconstructed primary vertices in the event.

---

[1]The parameter k does not affect performance and is chosen to ensure that the corrJVF distribution stretches over the full range between 0 and 1.

The second variable used by the JVT discriminant, R^0_{pT}, is defined as the ratio between the scalar p_T sum of the tracks, matched to the jet coming from the hard-scatter vertex, and the fully calibrated jet p_T after pile-up subtraction:

$$R^0_{pT} = \frac{\sum p_\text{T}^\text{trk}(\text{PV}_0)}{p_\text{T}^\text{jet}}. \tag{6.5}$$

This quantity assess the compatibility between the jet p_T and the total p_T of the hard-scatter charged particles within the jet. It helps discriminating between stochastic pile-up jets and the QCD ones in the central region. The tracks that correspond to QCD pile-up jets mostly originate from a vertex PV_i matched to a pile-up interaction ($i \neq 0$), resulting in $R^i_{pT} > R^0_{pT}$ for a given jet. These jets present large values of R^i_{pT} with respect to the pile-up vertex i from which they came from, while the tracks that correspond to stochastic pile-up jets rarely originate from the same interaction, resulting in small R^i_{pT} values with respect to any vertex i. Therefore, to classify the pile-up jets, ΔR_{pT} can be used, defined as the difference between the leading and median values of R^i_{pT} .
The signature of a VBF Higgs event, that is characterized by two high energy forward-backward jets, raises the probability to pick up pile-up jets. For jets with $p_\text{T} < 60$ GeV and $|\eta| < 2.4$, a cut is applied on the JVT discriminant, requiring that JVT>0.59. The optimal working point has been chosen with dedicated studies on a $Z \to \tau\tau+$ jet sample and it is robust against the increase of the pile-up. Figure 6.7(a) shows the average number of jets with $p_\text{T} > 20$ GeV as a function of the number of interactions per bunch crossing, before and after applying the JVT cut in data and in MC simulations. In Figure 6.7(b) the jet selection efficiency for the JVT as a function of the leading jet p_T is given: the overall efficiency is greater than 90%.

Furthermore, for the VBF topology, it is crucial to reduce pile-up in the forward region ($|\eta| > 2.5$), no tracking information is available. A variation of the JVT algorithm is exploited for jets with large pseudorapidity, called Forward-JVT (fJVT) [121, 124, 125]. The fJVT algorithm requires a maximum JVT value, JVT_{max}, to reject the central hard-scatter jets. It also requires a minimum ΔR_{p_T} to ensure that the selected pile-up jets are QCD pile-up jets and to remove the stochastic ones. The selected jets are afterwards matched to the vertex PV_i that corresponds to the highest $R^i_{p_\text{T}}$ value.

For a given forward jet, the fJVT discriminant is defined as the normalized projection of the missing transverse momentum for a pile-up vertex i on the
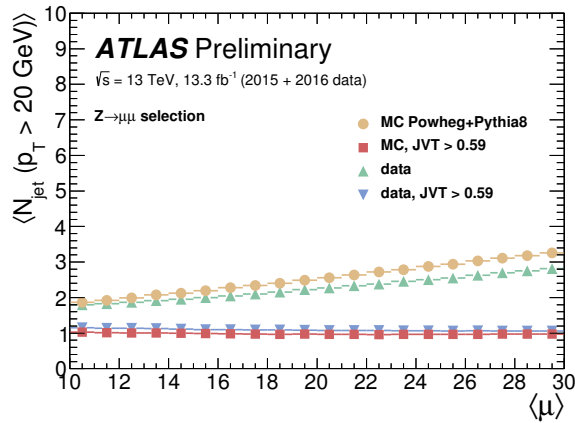
(a)
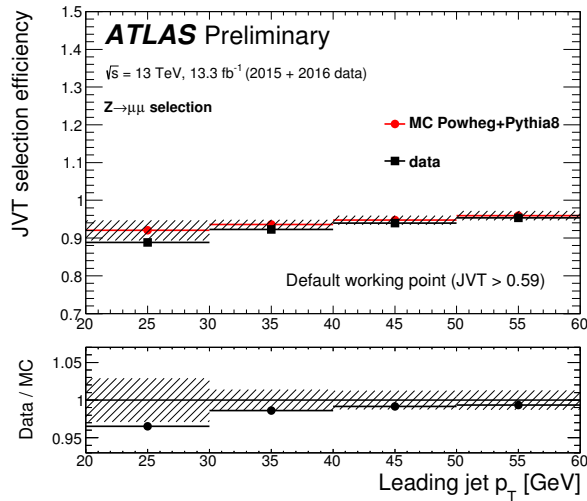
(b)

FIGURE 6.7: Figure 6.7(a) shows the average number of jets
with $p_T > 20$ GeV as a function of the number of interactions
per bunch crossing before and after requiring JVT > 0.59, for
$Z \to \tau\tau$+jets MC simulation and 2015+2016 data. Instead, in
Figure 6.7(b) the jet selection efficiency of a JVT > 0.59 cut
as a function of the leading jet p_T is shown. The bottom plot
shows the data/MC ratio. The error band corresponds to the
statistical and systematic uncertainties, the last one evaluated
by varying the residual contamination from pileup jets of 20%.
Figures from Ref. [123].

forward jet's transverse momentum $\boldsymbol{p}_T^{\mathrm{fj}}$:

$$\mathrm{fJVT}_i = \frac{\langle \boldsymbol{p}_{\mathrm{T}i}^{\mathrm{miss}} \rangle \cdot \boldsymbol{p}_{\mathrm{T}}^{\mathrm{fj}}}{|\boldsymbol{p}_{\mathrm{T}}^{\mathrm{fj}}|^2}, \qquad (6.6)$$

where $\langle \boldsymbol{p}_{\mathrm{T},i}^{\mathrm{miss}} \rangle$ is defined as as the weighted vector sum of the jet ($\boldsymbol{p}_{\mathrm{T}}^{\mathrm{jet}}$) and track ($\boldsymbol{p}_{\mathrm{T}}^{\mathrm{track}}$) transverse momenta:

$$\langle \boldsymbol{p}_{\mathrm{T},i}^{\mathrm{miss}} \rangle = -\frac{1}{2} \left(\sum_{\mathrm{tracks} \in \mathrm{PV}_i} k \boldsymbol{p}_{\mathrm{T}}^{\mathrm{track}} + \sum_{\mathrm{jets} \in \mathrm{PV}_i} \boldsymbol{p}_{\mathrm{T}}^{\mathrm{jet}} \right). \tag{6.7}$$

In this equation, k is a factor that takes into account of the intrinsic differences between the jet and track terms[2]. The contribution from neutral particles is not included int the track component, and $\boldsymbol{p}_{\mathrm{T}}^{\mathrm{jet}}$ is not sensitive to soft emissions below 20 GeV.

The fJVT efficiency for hard-scatter jets is calculated in $Z + \mu\mu$ data events,
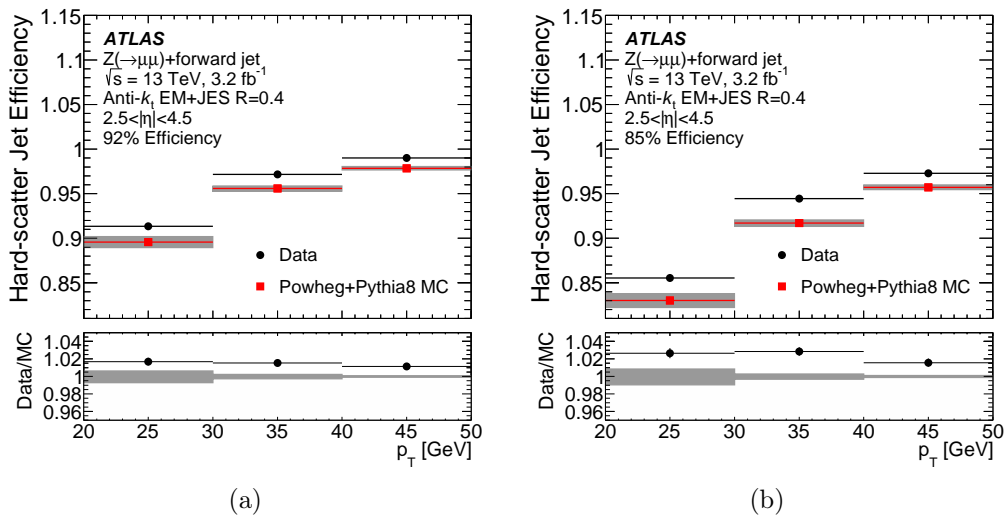
FIGURE 6.8: Efficiency for hard-scatter jets to pass fJVT requirements in $Z \rightarrow \mu\mu$ events as a function of p_{T} for the 92% and 85% hard-scatter efficiency operating points. Black circles represent the data, while red squares the MC simulation. In the lower plot the ratio data/MC is shown. The gray bands take into account statistical and systematic uncertainties. Figures from [125]

with the tag-and-probe procedure. Two operation points are defined: *loose* and *tight*. The *loose* corresponds to a maximum fJVT of 0.5 and the *tight* to 0.4, achieving respectively hard-scatter efficiencies of 92% and 85% and pile-up fake rate efficiencies between 60% and 50%, for jets with $20 < p_{\mathrm{T}} < 50$ GeV. Figure 6.8 shows the hard-scatter efficiency evaluated in simulation and data as a function of the jet p_{T} for both the *loose* 6.8(a) and a *tight* 6.8(b) working points. This efficiency is underestimated in the simulation, with a

---

[2]Its value is set to $k = 2.5$ to optimize the overall rejection of forward pile-up jets.

disagreement that at low jet p_T and high $|\eta|$ is around 3%. The evaluated efficiencies are employed to prescribe a calibration procedure that takes into account this discrepancy. In the $H \to WW^* \to \ell\nu\ell\nu$ analysis, the *loose* working point fJVT has been used: the fJVT rejects 56% of events in which pile-up jet are taken as leading VBF jets, and 50% of events which pile-up jets are taken as subleading VBF jets. The VBF signal efficiency for the fJVT selection is about 96%.

6.2.1 Identification of b-jets

In order to identify the hadrons containing b quarks, dedicated algorithm are built. These techniques, called "b-tagging", take mainly advantage of the long life time of hadrons containing b quarks, that is of the order of 1.5ps.
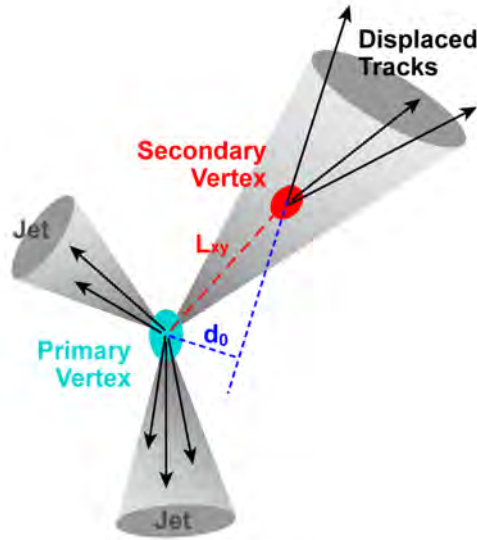
FIGURE 6.9: Sketch of an event with two light jets coming from the primary vertex and a b-jet from a secondary vertex. The displaced vertex and the impact parameter d_0 of one of the tracks are also shown.

A B-hadron with $p_T = 50$ GeV, thanks to his mean flight path length $(l = \beta\gamma c\tau)$, before decaying will approximately travel 3 mm in the transverse direction. As a consequence, at least one vertex displaced from the primary vertex will be generated. Different algorithms have been developed to detect b quarks, and all of them exploit the over-mentioned characteristic of B-hadron decays, sketched in Fig. 6.5.

Jets containing b-hadrons are identified, in the analysis discussed in this thesis, using the MV2C10 b-tagging algorithm [126]. This uses a gradient-
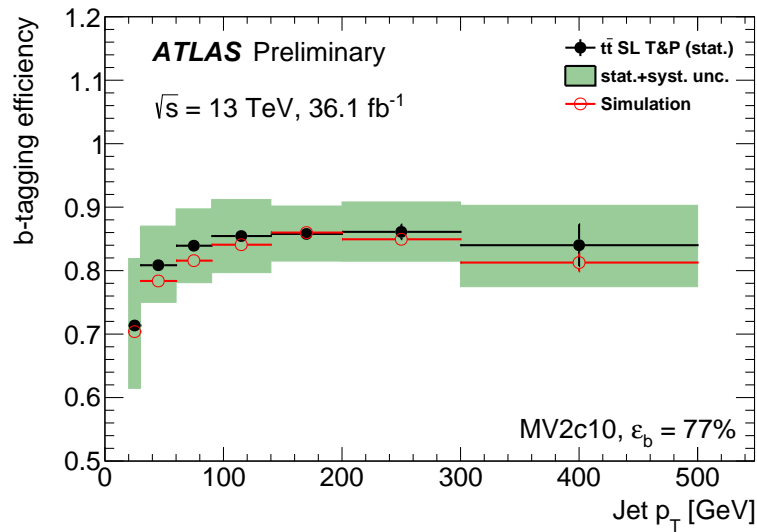
FIGURE 6.10: *b*-tagging efficiencies for the MV2c10 algorithm
at the 77% working point as a function of the p_{T} of the probe
jet obtained selecting $t\bar{t}$ single lepton events. The *b*-tagging
efficiencies from simulation are shown in red. The efficien-
cies measured in data through the tag-and-probe method are
shown as black dots [127]. The total statistical and systematic
uncertainties on the measurement are shown in the green bars.
Figure from [128]

boosted decision tree algorithm, which combines the information coming from
the impact parameter d_0 and the displaced vertices. Depending on the needs
of each analysis, the MV2C10 algorithm can be adapted, deciding if invest
on higher efficiency or on higher purity. According to the chosen cut on the
discriminant distribution, that is the output of the algorithm, a working point
corresponding to a certain efficiency and rejection can be selected. In Fig. 6.10
the *b*-tagging efficiencies for the MV2c10 algorithm at the 77% working point
as a function of the p_{T} of the probe jet obtained selecting $t\bar{t}$ single lepton
events are shown.

The working point chosen for the analysis discussed in this thesis corresponds
to an efficiency of 85%, determined from $t\bar{t}$ simulated events. The rejection
efficiency for selecting jets originating from a light quark or gluon is 33.53%
and for jets that contain *c*-hadrons is approximately 3.1%.

6.3   Lepton identification and reconstruction

6.3.1   Electrons

Electron Reconstruction   Electrons are reconstructed in the central region of the detector ($|\eta| < 2.47$) from energy deposits (also called *clusters)* in the electromagnetic calorimeter matched to tracks in the ID [129].

To search for such clusters, a *sliding-window algorithm* [116] is used, that needs as input calorimetric towers of size $\Delta\eta \times \Delta\phi = 0.025 \times 0.025$. The size of the window is 3×5 towers. Cluster seeds are produced if the towers transverse energy inside the window is above 2.5 GeV. This last requirement defines a Region of Interest (RoI) in the Inner Detector. Then, a track reconstruction algorithm is used. As first step, the ATLAS Global χ^2 [130] fit is performed. This searches for tracks matching the EM clusters. The reconstructed tracks are then re-fitted using the Gaussian Sum Filter [131]. This is an optimized track fitter specifically designed for electrons, that takes into account non-linear energy losses due to bremsstrahlung. The track that best matches the calorimeter cluster, among all the successfully fitted tracks, is selected and the electron candidate finally is built.

Electron identification   Not all the reconstructed electrons are real electrons coming from the hard scattering. There is a large contamination of falsely reconstructed, that are mainly jets faking an electron. In order to reject as many fake electrons as possible, without loosing too many prompt electrons, an identification method based on a likelihood approach (LH) [132] is used. Different features of the electron candidates are simultaneously evaluated with multivariate analysis techniques. Probability density functions (PDFs) of the discriminating variables for signal and background events are exploited. Based on these PDFs, the event is categorized as signal-like or background-like.

Three different levels of identification are applied: *loose, medium* and *tight.* These three operating points are constructed so that the tighter selections include the looser ones. The background rejection increases with the strictness of the requirements. The ID operating points have been optimized in bins of $|\eta|$ and E_{T} to take into account the dependency of the electron shower shape distributions from the material encountered by the electrons traversing the detector. Furthermore, with the increase of the energy, significant changes

(a)

(b)

(c)
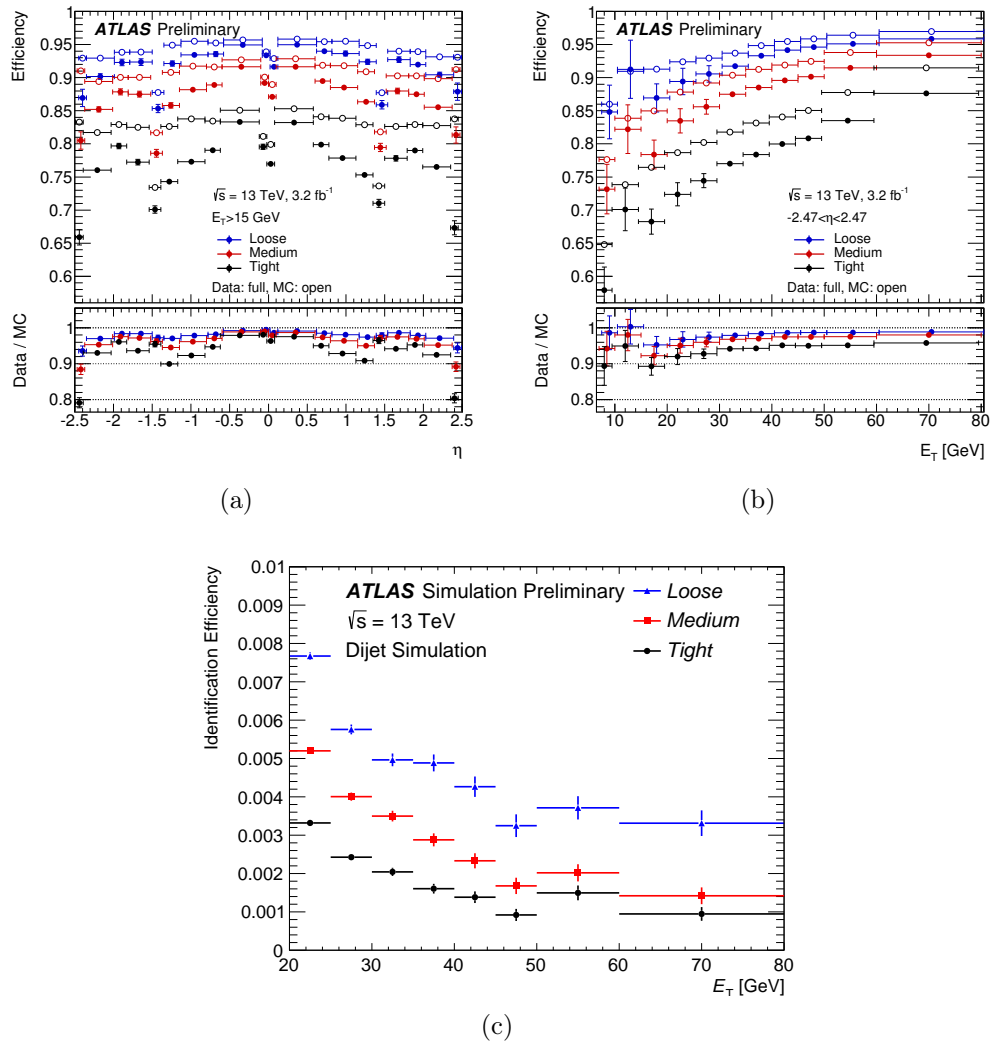
FIGURE 6.11: Electron identification efficiencies in $Z \rightarrow ee$ events as a function of the pseudo-rapidity η (for $15 < E_T < 50$ GeV) on the left 6.11(a), and, on the right 6.11(b), of the transverse energy E_T. The data efficiencies are derived with data-to-MC efficiency ratios, calculated in $J/\psi \rightarrow ee$ or $Z \rightarrow ee$ decays for data and on on $Z \rightarrow ee$ decays for the MC prediction (POWHEG +PYTHIA 8). The error bars show the statistical uncertainties. A mis-modeling of calorimetric shower shapes in the GEANT detector simulation is the cause of the lower efficiency in data than in MC. Figure 6.11(c) shows the efficiency to identify hadrons as electrons estimated using simulated dijet samples. The efficiencies are obtained using Monte Carlo simulations, and are measured with respect to reconstructed electrons. Figures 6.11(a)- 6.11(b) are from Ref [133], while Fig 6.11(c) from [132].

into the shower shape and track properties are expected. In Fig. 6.11(a)- 6.11(b), the efficiencies on the electron identification as a function of η and

E_T are shown, while in Fig. 6.11(c) the efficiency to identify hadrons as electrons is given. The efficiencies on the signal for electron candidates vary in the range from 65 to 95% and increase with E_T. Depending on the operating point, background efficiencies for electron candidates with $E_T = 25$ GeV are in the range from 0.3 to 0.8%. Both the reconstruction and the identification efficiencies are measured with the *tag and probe* method, defined as follows. A strict identification criteria is applied on the first electron coming from $Z \rightarrow ee$ or $J/\psi \rightarrow ee$ decays (*tag* electron), while the second one (*probe* electron) is identified with a looser selection and is used for the efficiency calculation. Results on the efficiency for MC and data can slightly differ to each other. This effect can be corrected introducing a multiplicative *scale factor* (SF), that is defined as the ratio between the efficiency measured in data and the one measured in the simulation.

Electron isolation   The electrons treated in this analysis must also fulfill isolation requirements, to achieve an optimal signal and background discrimination. Isolation variables allow to distinguish prompt electrons (like from the W or Z boson decays) from electrons originating from converted photons produced in hadron decays or electrons from heavy flavor hadron decays or from light hadrons mis-identified as electrons. This is done quantifying the energy of the particles produced nearby the electron, using mainly two discriminating variables: $E_T^{cone0.2}$, the calorimetric isolation energy, defined as the sum of the E_T of topological clusters, and a track isolation variable, $p_T^{varcone0.2}$, defined as the sum of the p_T of all tracks. For the isolation, different working points are defined. The *Loose* and *Tight* requirements provide, respectively, isolation efficiencies of 99% and 95% independently of the lepton p_T. *Gradient* and *GradientLoose* isolation, instead, are isolation efficiencies characterized by a linear dependence with the electron p_T. The *Gradient* (*GradientLoose*) working point gives an efficiency of 90% (95%) for electrons with p_T of 25 GeV, reaching 99% at 60 GeV. Both track and calorimeter isolation are requested to be smaller than the electron-p_T dependent efficiency function: $\epsilon = 0.1143 \times p_T + 92.14$ for *Gradient* and $\epsilon = 0.057 \times p_T + 95.57$ for *GradientLoose*. Another isolation point is called *LooseTrackOnly* isolation: as the name suggests, it applies for track based isolation only. It is independent from the lepton p_T and provides an efficiency of 99%.

Selected electrons   The electrons selected in the $H \rightarrow WW^* \rightarrow \ell\nu\ell\nu$ analysis are required to have $E_T > 15$ GeV. They should pass the *medium* (*tight*)

selection, if their E_T is greater (smaller) than 25 GeV. The pseudorapidity of electrons is required to be within the range of $|\eta| < 2.47$, excluding the transition region between the barrel and endcaps in the liquid argon calorimeter ($1.37 < |\eta| < 1.52$).

The absolute value of the longitudinal impact parameter of each electron track, calculated with respect to the primary vertex, is required to fulfill $|z_0 sin\theta| < 0.5$ mm and it is also requested that the transverse impact parameter significance satisfies $|d_0|/\sigma_{d_0} < 5$.

Furthermore, objects that have been reconstructed as both an electron candidate and as a converted photon are rejected. This is requested in order to reduce the $W\gamma$ background (more than 40% of reduction) with a small signal loss (around 1%).

The isolation selection has been optimized by taking into account the signal and the background efficiency. Different isolation requirements have been applied to electrons with $E_\mathrm{T} < 25\,GeV$ and $E_\mathrm{T} > 25\,GeV$. The efficiency-targeted working points, like the *Gradient* one, present a lower background rejection at low p_T with respect to the working points that use a simple cut on the isolation variables. A new working point, called *FixedCutTrackCone40*, has therefore been introduced to maximize the signal efficiency at low p_T, optimized for the $ggF + 0$ jet channel [134]. For the μe final state, if the electron $p_\mathrm{T} < 25$ GeV, the fake contribution from electrons is around 23%, while much lower, around 4%, for electrons with $p_\mathrm{T} > 25$ GeV. The optimization of the isolation cut is crucial to reduce the fake contribution, since, if this background is too large, it is not possible to model it with reasonably small uncertainties.

The *FixedCutTrackCone40* working point has been defined as follows: for the energy sum within a radius of $\Delta R = 0.2$ in the calorimeter system around the electron cluster, it is required that $E_\mathrm{T}^{0.2} < 0.11 \cdot p_\mathrm{T}$. Moreover, the transverse momentum sum around the electron track in a radius $\Delta R = 0.4$ in the ID is required to be smaller than 0.06 times the electron p_T, $p_\mathrm{T}^{0.4} < 0.06 \cdot p_\mathrm{T}$. With the new working point *FixedCutTrackCone40*, the analysis sensitivity and as well the modeling of the final state are improved, as shown in Table 6.1. Here, the yields of signal and fake-leptons for the *FixedCutTrackCone40* working point are compared to the yields of the *Gradient* one. The significance and the rejection of the fake background are improved with respect to the *Gradient* criteria, especially for $p_\mathrm{T}^{\mathrm{sublead}} < 20\mathrm{GeV}$.

Instead, for candidates with $E_\mathrm{T} > 25\,GeV$, the E_T and η dependent *Gradient* isolation criterion described before has been applied.

Isolation	ggf	*e*-Fake	*μ*-Fake	Total bkg	Signal loss	*W*+jets loss	Significance
	0-jet SR, *μe*, $p_{\mathrm{T}}^{\mathrm{sublead}} < 20$GeV						
Gradient	75	203	24	675			0.72
FixedCutTrackCone40	59	90	12	447	-21.5%	-55.6%	1.02
	0-jet SR, *μe*, 20GeV $< p_{\mathrm{T}}^{\mathrm{sublead}} < 25$GeV						
Gradient	60	72	19	508			1.00
FixedCutTrackCone40	54	49	15	426	-10.9%	-31.9%	1.09

TABLE 6.1: Comparison of the expected yields for different isolation criteria in the *μe* channel of the ggF $H \to WW^* \to \ell\nu\ell\nu$ final state. The W+jet background is estimated with a fake factor method as shown in Section 7.2.1. The total significance takes into account a 40% uncertainty on the W+jets background yields and a 10% on the non-W+jets background yields. Table adapted from [134].

The comparison between the different values of the cuts applied on the $E_{\mathrm{T}}^{cone0.2}$ and $p_{\mathrm{T}}^{varcone0.2}$ variables as a function of the electron p_{T} are shown in Fig 6.12 for different isolation requirements. When applying the *Gradient* criteria, the cut becomes looser at smaller electron p_{T} values, while with the *FixedCutTrackCone40* the cut is tighter.

(a) $E_{\mathrm{T}}^{cone0.2}$ (b) $p_{\mathrm{T}}^{varcone0.2}$
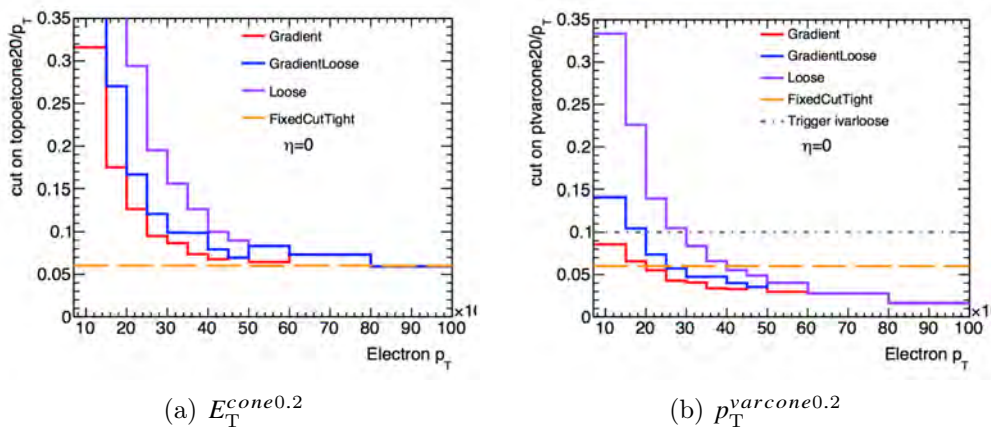
FIGURE 6.12: Illustration of the cuts applied on both $E_{\mathrm{T}}^{cone0.2}$ and $p_{\mathrm{T}}^{varcone0.2}$ when requiring different isolation criteria as a function of the electron p_{T}. Figures from [134].

6.3.2   Muons

Muon Reconstruction   Muons are at first reconstructed separately in the inner detector and in the muon spectrometer. However the informations from the sub-detectors are combined to form the muon tracks [135]. Four different muon types are built:

- **Combined muons (CB)**: after an independent track reconstruction in both the ID and MS, the tracks are combined thanks to a global refit that uses the hits from both the ID and MS sub-detectors. In this refitting procedure, the hits from the MS can be removed or added to increase the fit quality. An outside-in pattern recognition is used for most muons: muons are at first reconstructed in the MS and then the tracks are built inward and matched to an ID track. The mirrored strategy, where tracks are reconstructed with an inside-out technique, is used as a complementary approach.

- **Segment-tagged (ST) muons**: a candidate is built if a muon is reconstructed in the ID and it is associated with at least one local track segment in the MDT or CSC chambers in the MS. ST muons generally hit only one layer of the MS chambers, because of their for low p_{T} or because they interact with regions with lower MS acceptance.

- **Calorimeter-tagged (CT) muons**: it combines a muon track in the ID with an energy deposit in the calorimeter that is compatible with a minimum-ionizing particle. Optimal for muons in the region ($|\eta| < 0.1$) and a momentum range of $15 < p_{\mathrm{T}} < 100$ GeV: they are characterized by lower purity among all the muon types but these muons recover the acceptance in the region where the ATLAS muon spectrometer is only partially instrumented.

- **Extrapolated (ME) muons**: for muons with tracks in the muon spectrometer only that do not match any track in the ID. ME muons are primarily used to extend the acceptance for muon reconstruction into the forward region $2.5 < |\eta| < 2.7$, that is not covered by the ID.

Muon Identification Muon identification is performed to select prompt muons with high efficiency and to suppress background, that comes mainly from pion and kaon decays. Prompt and background muon candidates are studied thanks to several discriminating variables for CB tracks, like the normalized χ^2 of the track fit in simulated $t\bar{t}$ events (where the muons from the W decays are taken as signal , while as background the muons from light-hadron decays). Another observable is the q/p significance, that is the absolute value of the difference between the ratio of the charge and momentum of the muons measured in the muon spectrometer and inner detector divided by the sum in quadrature of the corresponding uncertainties. A similar quantity is ρ', that is the absolute value of the difference between the transverse momentum

measurements in the ID and MS divided by the p_T of the combined track. For a good track quality, the number of hits in the ID and MS must fulfill specific requirements. A muon candidate must present at least one Pixel hit, five SCT hits, and that 10% of the TRT hits originally matched to the track are included in the final fit.

The ATLAS muon performance group provides four different muon identification selections: *loose*, *medium*, *tight* and *high-p_T*. The *medium* quality identification is used by default in ATLAS. This selection uses only CB and ME tracks and it is the one that minimizes the reconstruction and calibration systematic uncertainties.

The *loose* identification criteria is built to maximize the reconstruction efficiency while providing good-quality muon tracks. It uses all types of muons: *loose* muons are specifically optimized for reconstructing Higgs boson candidates in the four-lepton final state. The CB and ME muons that satisfy the *medium* requirements are also included in the *loose* selection.

The muons that satisfy the *tight* criteria are only CB muons with hits in at least two stations of the MS that also fulfill the *medium* requirements. They are optimized to maximize the purity at the cost of the loss of some efficiency.

The *high-p_T* identification level maximizes the momentum resolution for muons with $p_T > 100$ GeV. The muon identification efficiencies for prompt muons and hadrons faking a muon, computed with a $t\bar{t}$ POWHEG +PYTHIA 8 semileptonic sample, for the different working points are shown in Table 6.2, separately for low ($4 < p_T < 20$ GeV) and high ($20 < p_T < 100$ GeV) momentum and $|\eta| < 2.5$.

Selection	$4 < p_T < 20$ GeV		$20 < p_T < 100$ GeV	
	ϵ_μ^{MC} [%]	$\epsilon_{Hadrons}^{MC}$ [%]	ϵ_μ^{MC} [%]	$\epsilon_{Hadrons}^{MC}$ [%]
Loose	96.7	0.53	98.1	0.76
Medium	95.5	0.38	96.1	0.17
Tight	89.9	0.19	91.8	0.11
High-p_T	78.1	0.26	80.4	0.13

TABLE 6.2: Identification efficiencies for prompt and non-prompt muons computed using a $t\bar{t}$ MC sample, for the four identification selection criteria. The numbers are given for low ($4 < p_T < 20$ GeV) and high ($20 < p_T < 100$ GeV) momentum muons separately for candidates with $|\eta| < 2.5$. Numbers from [135]

The muon reconstruction efficiency is estimated employing a *tag-and-probe* method. Decays such as $Z \rightarrow \mu\mu$ and $J/\psi \rightarrow \mu\mu$, that cover a broad muon p_T

spectrum, are exploited. The tag is a muon, reconstructed in the ID or in the MS, that is used to test the other muon. Scale factors take into account the differences in the measured reconstruction efficiency in data and in simulation. The muon reconstruction efficiency as a function of η in $Z \rightarrow \mu\mu$ events for *medium* muons with $p_T >10$ GeV is shown in Fig. 6.13(a). Also *loose* muons, in the region $|\eta| < 0.1$ where the *loose* and *medium* selections differ significantly, are shown. The reconstruction efficiency for *medium* muons is above 95%. In Figure 6.13(b) instead is shown the reconstruction efficiency as a function of the muon p_T, in the region $0.1< |\eta| < 2.5$, obtained with $Z \rightarrow \mu\mu$ and $J/\psi \rightarrow \mu\mu$ events. The efficiency is slightly above 99% for $p_T > 6$ GeV and has a stable trend. Both values from $Z \rightarrow \mu\mu$ and $J/\psi \rightarrow \mu\mu$ events are in agreement in the overlap region between 10 and 20 GeV.

Muon Isolation   Non prompt muons can be accompanied by another particle contained in a jet: to avoid this, an isolation requirement can be imposed. To discriminate between non-prompt muons from jet and prompt muons, like from W or Z decays, two kind of isolation variables can be used: a track-based one and a calorimeter based one. The first one, $p_T^{varcone30}$, is the scalar sum of the transverse momenta of the tracks (excluding the muon track itself) with $p_T >1$ GeV in a cone of size $\Delta R = 0.3$ around the muon of transverse momentum p_T. Instead, the calorimeter-based isolation variable, E_T^{cone20} is defined as the sum of the transverse energies of topological clusters in a cone of size $\Delta R = 0.2$ around the muon. The contribution from the energy deposit of the muon itself is subtracted and corrections for pile-up effects are also applied. As for the electron, the default isolation recommended in Run 2 is the so-called *Gradient* isolation, that is tuned to produce a nominal efficiency of 90% (99%) for leptons with p_T of 25 (60) GeV, requiring both track and calorimeter isolation variables to satisfy $\epsilon = 0.1143 \times p_T + 92.14$.

Muon selection   In the $H \rightarrow WW^* \rightarrow \ell\nu\ell\nu$ analysis muon candidates must have pseudorapidity lower than 2.5, while the transverse momentum has to exceed 15 GeV. Furthermore, it is requested that muons must satisfy the *tight* quality criteria.
The requirements on the longitudinal and transverse impact parameters are, respectively, $|z_0 sin\theta| < 0.5$ mm and $|d_0|/\sigma_{d_0} < 3$.
Both track-based and calorimeter-based isolation criteria are also applied on the selected muons. The isolation working point has been optimized, as for the electrons, on ggF + 0 jets events [134]. An important contribution of the
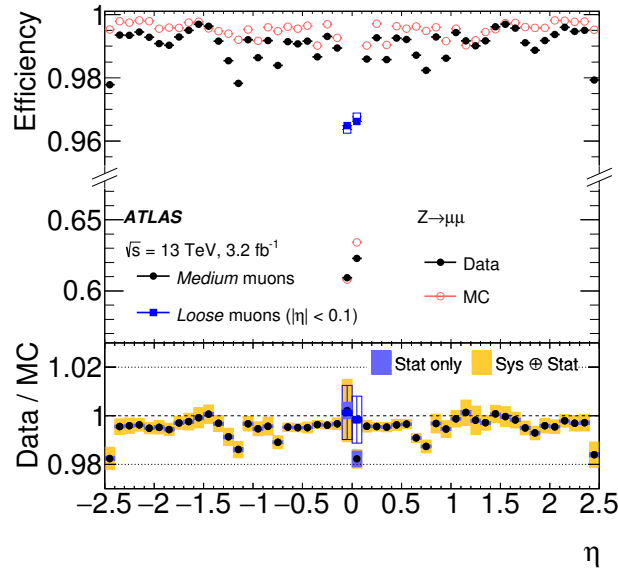
(a)
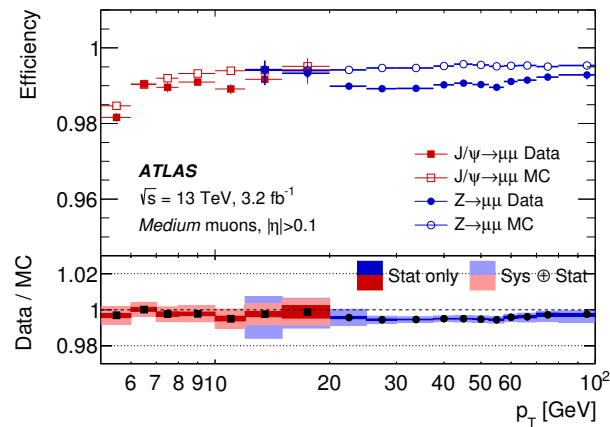
(b)

FIGURE 6.13: Figure 6.13(b) shows the muon reconstruction efficiency as a function of η in $Z \to \mu\mu$ events for muons with $p_\mathrm{T} > 10$ GeV shown for the *medium* muon selection and the *loose* selection (in squares) in the region $|\eta| < 0.1$ where the *loose* and *medium* selections differ significantly. Instead, in Figure 6.13(b) the reconstruction efficiency as a function of the muon p_T is shown, in the region $0.1 < |\eta| < 2.5$, obtained with $Z \to \mu\mu$ and $J/\psi \to \mu\mu$ events. For both figures, the statistical uncertainty is shown in the error bars on the efficiencies and the bottom panel shows the ratio of the measured to predicted efficiencies, with systematic and statistical uncertainties. $Z \to \mu\mu$ events are simulated with POWHEG +PYTHIA 8 generators, while $J/\psi \to \mu\mu$ events with POWHEG complemented with PHOTOS to simulate the effects of final-state radiation. Figures from Ref. [135].

signal sensitivity comes from the muons with low p_T, therefore the isolation has to maximize the efficiency for muons with $p_T < 25GeV$, which represents the region with the largest fake contribution.

A set of working points has been studied to find an optimal selection for the $H \to WW^* \to \ell\nu\ell\nu$ analysis. All the studied working points present a tighter selection for low p_T muons than the *Gradient* isolation. Figure 6.14 shows the comparison between the values of the different cuts applied on the $E_T^{cone0.2}$ and $p_T^{varcone0.3}$ variables as a function of the muon p_T, for different isolation requirements: for low p_T values, the *Gradient* isolation presents looser cuts with respect to a fixed cut point, such as, for example, *FixedCutTightTrack-Only*. The customized working point (referred to as *WP3*) has been chosen,

(a) $E_T^{cone0.2}$ (b) $p_T^{varcone0.3}$
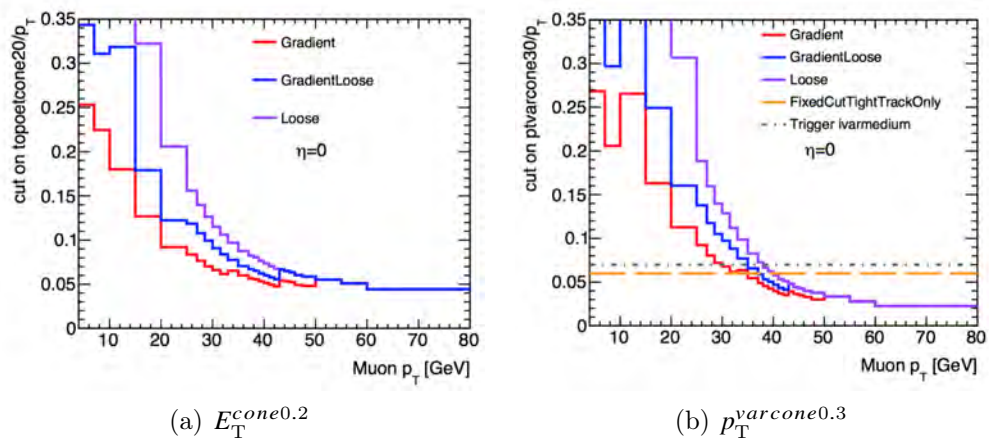
FIGURE 6.14: Illustration of the cuts applied on both $E_T^{cone0.2}$ and $p_T^{varcone0.3}$ when requiring different isolation criteria as a function of the muon p_T. Figure from [134].

after a 2D scan over $E_T^{cone0.2}$ and $p_T^{varcone0.3}$, selecting the point that presented the highest rejection of the W+jets background, without loosing too much signal. The selected point is defined as follows: the energy sum within a radius $\Delta R = 0.2$ in the calorimeter system around the combined track has to be smaller than 0.09 times the transverse muon momentum, $E_T^{cone20}/p_T < 0.09$. In addition, the transverse momentum sum around the muon track in a radius $\Delta R = 0.3$ in the ID is required to be smaller than 0.06 times the muon p_T: $p_T^{varcone30}/p_T < 0.06$. From Tab. 6.3 a reduction of the W+jets contamination with the new working point is visible. A tighter isolation criteria, with respect to the *Gradient* one, can indeed help to decrease the fake contribution in the analysis. For muons with 15 GeV $< p_T < 20$ GeV, *WP3* provides a very good performance achieving a reduction of W+jets of 25%, with a signal loss of 12%. Instead, for muons with 20 GeV $< p_T < 25$ GeV, the performances

are affected by low statistic causing non negligible fluctuations of the W+jets estimation. However, even in this case, the performances of *WP3* lead to a reduction of W+jets of 19%, with a signal loss of 5%.

Isolation	ggF	*e*-fake	*μ*-fake	Signal loss	W+jets loss	W+jets Fraction	Significance
0-jet SR, *eμ*, 15GeV < p_T^μ < 20GeV							
Gradient	87.36	49.30	84.90	–	–	19.55	1.307
WP3	77.13	39.31	60.89	-11.71	-25.33	16.90	1.358
0-jet SR, *eμ*, 20GeV < p_T^μ < 25GeV							
Gradient	75.96	12.59	22.93	–	–	5.88	1.356
WP3	71.88	8.67	20.13	-5.37	-18.92	5.09	1.357

TABLE 6.3: Performance of the new customized muon isolation working points for ggF 0 jet signal region in the *eμ* channel. The W+jet background is estimated with a fake factor method as shown in Section 7.2.1. Table adapted from [134]

6.4   Missing transverse energy

Neutrinos, because of their very low interaction cross section, pass through the ATLAS detector without any interaction. This makes a direct reconstruction impossible. However, an indirect measurement can be performed by studying the transverse momentum imbalance of the identified particles. The initial state transverse momentum of the colliding particles is equal to zero. Therefore, because of energy conservation, an imbalance in the total measured transverse momentum in the final state could hint to the presence of undetected particles. This missing transverse energy (E_T^miss) consists of two parts. The first one is related to signal particles from the hard event, while the second part is related to the "soft event", meaning all those reconstructed tracks not associated with the physics objects from the hard scatter. It is defined as the negative sum of the momenta of the hard and soft particles in a collision [136]:

$$\boldsymbol{E}_\mathrm{T}^\mathrm{miss} = -\sum_\mathrm{e} \boldsymbol{p}_\mathrm{T}^e - \sum_\gamma \boldsymbol{p}_\mathrm{T}^\gamma - \sum_\tau \boldsymbol{p}_\mathrm{T}^\tau - \sum_\mu \boldsymbol{p}_\mathrm{T}^\mu - \sum_\mathrm{jets} \boldsymbol{p}_\mathrm{T}^\mathrm{jet} - \sum_\mathrm{unusedtracks} \boldsymbol{p}_\mathrm{T}^\mathrm{tracks}.$$

(6.8)

For the $H \to WW^* \to \ell\nu\ell\nu$ analysis, the photon and τ-lepton terms are not in the final state, therefore they are not used in the E_T^miss recalculation.

There are three main methods to quantify the missing transverse momentum: the so-called CST E_T^miss, the Track E_T^miss and TST E_T^miss. The first one is based on energy deposits in the ATLAS calorimeters: the soft term is calorimeter-based (CST) and is built from the energy deposits in
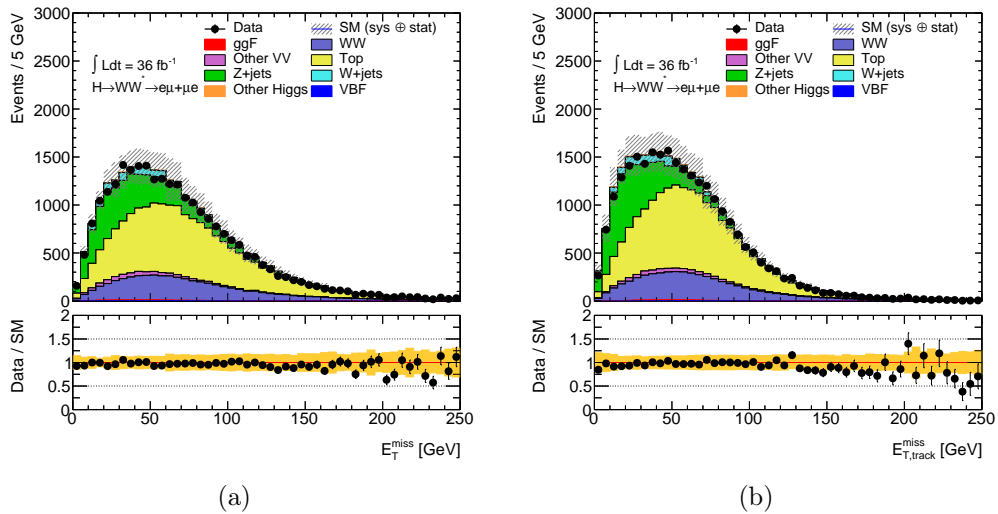
FIGURE 6.15: The $E_T^{miss,TST}$ 6.15(a) and $E_T^{miss,Track}$ 6.15(b) at the pre-selection cut stage of the VBF $H \to WW^* \to \ell\nu\ell\nu$ analysis. The yellow band represents the MC statistic and the main source of detector systematics. The lower plot shows the data/MC ratio.

the calorimeter that are not associated with any hard objects. The main contributions to the soft term come from the soft radiation from the hard event and the underlying event activity. The major issue of this method is that is vulnerable to pile-up interactions, that give an extra contribution to the CST E_T^{miss}. The second method, Track E_T^{miss}, as its name suggests, is a track-based method that gives a E_T^{miss} definition based on the momenta of ID tracks. This method is largely independent from the pile-up but has two limitations: the acceptance is limited to $|\eta| < 2.5$ and it is insensitive to neutral particles that leave no tracks in the ID. The last definition is the one used in the VBF $H \to WW^* \to \ell\nu\ell\nu$ analysis: the TST E_T^{miss} employs a track-based soft term combined this with calorimeter-based measurements for the hard objects, resulting in a good compromise between the track and calorimeter based methods. The TST is quite insensitive to pile-up interactions, since the tracks can be matched to a primary vertex, but, as the Track E_T^{miss}, does not include contributions from soft neutral particles. In Figures 6.15(a) and 6.15(b) are shown respectively the data/MC comparison for VBF $H \to WW^* \to \ell\nu\ell\nu$ events for $E_T^{miss,TST}$ and $E_T^{miss,Track}$ at pre-selection stage for the VBF analysis (see Section 7.5). A better agreement between data and MC predictions for the TST calculation with respect to the Track one is obtained.

The VBF $H \rightarrow WW^* \rightarrow \ell\nu\ell\nu$ channel

One of the best channels suited to the study of the properties of the Higgs boson is $H \rightarrow WW^* \rightarrow \ell\nu\ell\nu$, because of its high production cross-section, via ggF and VBF production, and its large branching ratio.

During Run 1 data taking, thanks to the 25 fb^{-1} of data taken at $\sqrt{s} =$ 8 and 7 TeV, searches for the Standard Model Higgs boson decaying into two W bosons were performed in the ggF, VBF and VH production modes. This resulted in the observation of the Higgs boson with a significance of 6.5 standard deviations. The ratios between the measured value and the expected value of the total production cross-section times branching fraction (*signal strength*) were

$$\mu_{ggF+VBF+VH} = 1.16^{+0.16}_{-0.15}(stat)^{+0.18}_{-0.15}(sys),$$

corresponding to a total production cross-sections of [137, 138]:

$$\sigma_{ggF} = 4.6 \pm 0.9(stat)^{+0.8}_{-0.7}(sys)pb \text{ and } \sigma_{VBF} = 0.51^{+0.17}_{-0.5}(stat)^{+0.13}_{-0.08}(sys)pb.$$

At 13 TeV, a first measurement of the Higgs boson production cross-section via Vector Boson Fusion (VBF) and associated WH production was performed, using $5.8 fb^{-1}$ of data [139]. This resulted in the measured total production cross-sections:

$$\sigma_{VBF} \times B_{H \rightarrow WW^*} = 1.4^{+1.9}_{-0.7}pb \text{ and } \sigma_{WH} \times B_{H \rightarrow WW} = 0.9^{+1.3}_{-1.2}pb.$$

In terms of signal strength:

$$\mu_{VBF} = 1.7^{+1.1}_{-0.9} \text{ and } \mu_{WH} = 3.2^{+4.4}_{-4.2}.$$

In Chapter 6, the physics objects reconstruction and a first event selection were discussed. This chapter, after a description of the signal topology and of the main backgrounds, will focus on the full selection of the events to maximize the sensitivity to VBF, in order to measure both the cross-section and the polarized couplings a_L and a_T. Finally, the main sources of uncertainties are outlined.

7.1   The signal topology

The signature of this analysis is characterized by the presence of two isolated, charged, opposite-sign and different flavor leptons ($e\mu$, μe) and the presence of missing transverse energy due to two neutrinos in the final state. In the analysis, the kinematic properties of the di-lepton system are investigated. The Higgs boson is a spin zero particle, while, as already discussed in Section 2.1, the W bosons have helicity states 1,0 and -1. For the conservation of the angular momentum, three possible combinations of the spin projection of the W bosons are allowed. Due to the V-A structure of the weak interactions the neutrinos have negative helicity, while the anti-neutrinos positive helicity. As shown in illustration 7.1, the charged leptons are preferably emitted in the same direction, while the two neutrinos travel in opposite directions with respect to the leptons, resulting in a large missing E_T.

As a result of this spin correlation, the opening angle between the charged leptons $\Delta\phi_{\ell\ell}$ tends to be small. Consequently, their invariant mass, defined as

$$m_{\ell\ell} \simeq \sqrt{E_{\ell_1} E_{\ell_2}(1 - cos(\Delta\phi_{\ell\ell}))}, \tag{7.1}$$

is also small. Among the final state particles, there are also two neutrinos, therefore, a large missing transverse energy, that balances the transverse momenta of the two leptons, is expected.

The presence of the neutrinos in the final state prevents the full reconstruction of the Higgs boson invariant mass. However, the transverse mass m_{T} of the Higgs boson can be approximated via:
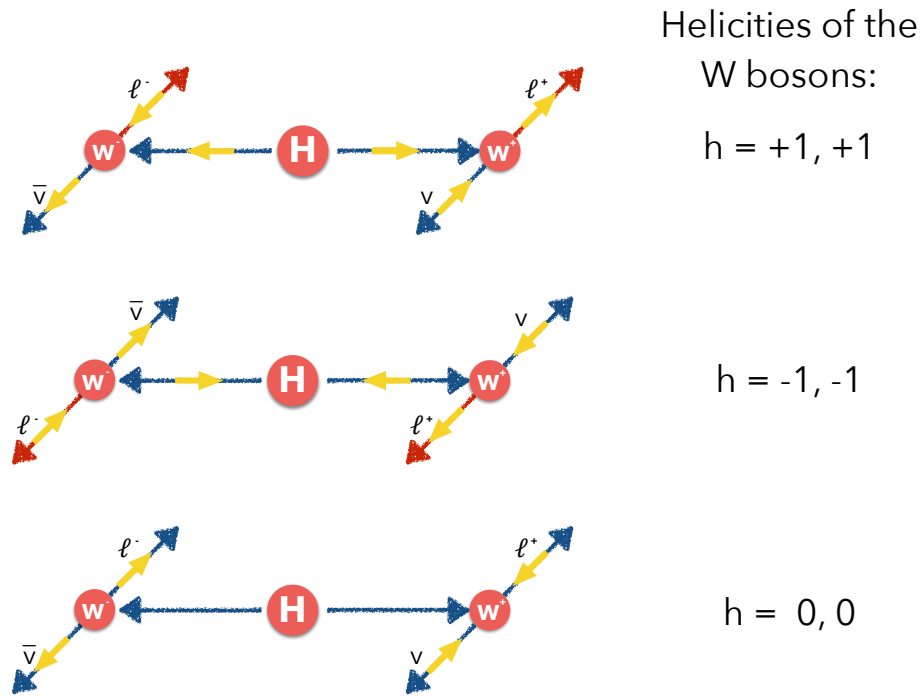
FIGURE 7.1: Illustration of the $H \rightarrow WW^* \rightarrow \ell\nu\ell\nu$ decay.
The direction of motion of the particles is indicated by the
small arrows, while their spin projections by the large yellow
arrows. The three possible decays, allowed by spin conser-
vation, are shown: on top, positive helicity of the W boson,
negative helicity in the middle and helicity zero at the bottom.
As shown by the red arrows, the two charged leptons follow
the same direction for helicity states of W bosons equal to 1
and -1. In this sketch, both the H and W decays are shown in
the decaying particle's rest frame.

$$m_{\mathrm{T}} = \sqrt{\left(E_{\ell\ell} + E_{\mathrm{T}}^{miss}\right)^2 - |p_{\mathrm{T},\ell\ell} + E_{\mathrm{T}}^{miss}|^2}, \qquad (7.2)$$

with $E_{\ell\ell} = \sqrt{|p_{\mathrm{T},\ell\ell}|^2 + m_{\ell\ell}^2}$ and $p_{\mathrm{T},\ell\ell}$ the combined dilepton four-vector
in the transverse plane. The Higgs boson mass represents an upper bound
to the m_T distribution, therefore this variable helps to distinguish between
Higgs boson production modes and some of the backgrounds (such as the
non-resonant WW and top-quark production, see Section 7.2).
The VBF production presents a peculiar signature, as shown in the Feynman
diagram in Fig. 7.2. Two virtual vector bosons are radiated by two scattering
quarks coming from the initial proton. These bosons annihilate producing

a Higgs boson that consequently decays into two Ws. The final state is also characterized by two highly energetic forward jets, usually referred to as *tagging jets*. These arise from the hadronization of the original quarks, and present a high invariant mass m_{jj} and a large rapidity gap: $\Delta y_{jj} = |y_{jet_1} - y_{jet_2}|$. Another feature is the absence of color exchange between the two scattering quarks, since this process is purely electroweak. Therefore, there are no additional jets in the rapidity gap between the two tagging jets. Furthermore, since the Higgs boson is produced centrally, its decay products must lay in between the two tagging jets. All the over-mentioned features are employed to discriminate between the signal and the various backgrounds, as show in the next sections.
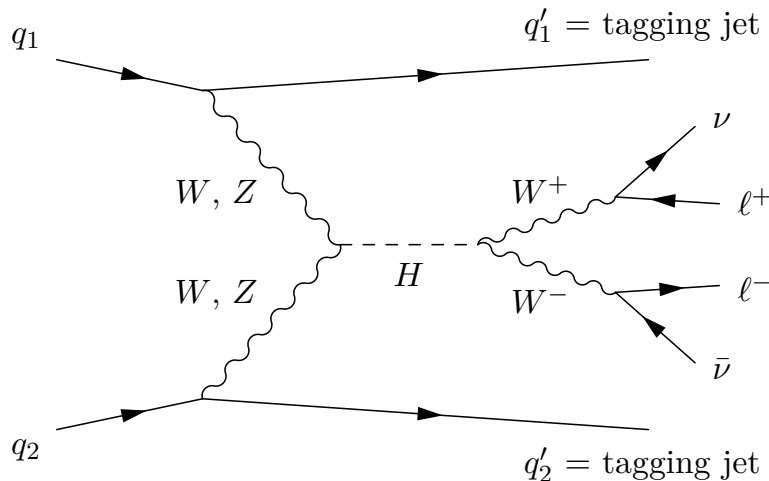
FIGURE 7.2: Feynman diagram of the VBF $H \rightarrow WW^* \rightarrow \ell\nu\ell\nu$ channel.

In the following, $e\mu$ channel will designate the final state where the leading lepton (i.e. the lepton with higher p_T) is the electron, whilst μe the final state where the leading lepton is a muon. The generic case, where the leading lepton can be either a muon or an electron, is referred to as $e\mu + \mu e$.

7.2   Main backgrounds

As mentioned before, the $H \rightarrow WW^* \rightarrow \ell\nu\ell\nu$ channel presents one of the largest branching ratios, but is affected by the presence of large backgrounds. Indeed, there are several processes that can mimic the signal. In general, there are two kinds of background processes: the *irreducible backgrounds* are processes that have the same final state as the signal. Instead, the *reducible backgrounds* are

processes that present similar but not exactly equal final state as the signal. The backgrounds are usually estimated either through data-driven techniques (see Section 7.2.1) or from MC simulation. It is fundamental that the MC models the data in a proper way. To check this, background-enriched regions, called *control regions* (CRs), are built. These are usually defined in an orthogonal way with respect to the signal-enriched region (SR). The MC predictions are corrected in these CRs from a comparison with the data: normalization factors are extracted and then applied to the predictions in the SR. A summary of all backgrounds and their estimation is given in Table 7.1.

Process	Estimation	Generator
Higgs Signals		
Polarized couplings analysis		
VBF $H \to WW \to \ell\nu\ell\nu$	MC	MadGraph5_aMC@NLO + Pythia 8
ggF $H \to WW \to \ell\nu\ell\nu$	MC	MadGraph5_aMC@NLO + Pythia 8
Cross-section analysis		
VBF $H \to WW \to \ell\nu\ell\nu$	MC	Powheg-Box+Pythia 8
ggF $H \to WW \to \ell\nu\ell\nu$	MC	Powheg-Box+Pythia 8
VH $H \to WW \to \ell\nu\ell\nu$	MC	Powheg-Box+Pythia 8
VBF, ggF $H \to \tau\tau \to \ell\nu\nu\ell\nu\nu$	MC	Powheg-Box+Pythia 8
Top background		
$t\bar{t}$ fully-leptonic	Data+MC	Powheg-Box+Pythia 8
Wt fully-leptonic	Data+MC	Powheg-Box+Pythia 6
Diboson background		
WW	MC	Sherpa v2.2.2
EW WW	MC	Sherpa v2.1.1
WZ, ZZ, $V\gamma$, $V\gamma^*$	MC	Sherpa v2.1.1 & Sherpa v2.2.2
Z+jets background		
$Z(\to \tau\tau)$+jets	Data+MC	Sherpa v2.2.1
EW $Z(\to \tau\tau)$+jets	Data+MC	Sherpa v2.1.1
$Z(\to ee/\mu\mu)$+jets	MC	Sherpa v2.2.1
W+jets background		
W+jets	Data-Driven	-

TABLE 7.1: Summary of Monte-Carlo generators used to produce nominal samples of various signal and background processes.

Top-quark background   The largest background in the VBF $H \to WW^* \to \ell\nu\ell\nu$ channel arises from decays of the top-quark, in processes like $t\bar{t}$ production and single-top, Wt. The top-quark decays into a b-jet and a W boson $t \to Wb$. This background produces the same final state as the signal, if the W boson decays leptonically, with the exception of the presence of b-jets. To reduce it,

a veto on the presence of the b-quarks is applied. However, due to inefficiencies in the b-jet identification, this background is not strongly suppressed. It is estimated by MC, but its prediction are corrected in a dedicated control region, as described in Section 7.6.1.

WW background   The second largest background is due to the irreducible continuum $WW \to \ell\nu\ell\nu$ production in association with two jets. This background can be reduced requiring a small opening angle and invariant mass of the final state leptons, considering the spin correlations discussed in the previous section. The WW background is divided in processes containing only electroweak vertices (EW WW) and those containing a QCD vertex (QCD WW). Despite the fact that the cross-section of the QCD processes is more than 20 times larger than the EW one, the two contributions are comparable in the VBF phase space. The WW prediction relies totally on the MC estimation, but, as a check, a validation region is built, see Sec. 7.6.3.

Z+jets background   The Drell-Yan (DY) processes $Z/\gamma^* \to \ell\ell$, produced in association with jets, are important backgrounds for this analysis. Considering a different flavor final state ($e\mu + \mu e$), the dominant DY process is $Z/\gamma^* \to \tau\tau \to \ell\nu\nu\ell\nu\nu$, while $Z/\gamma^* \to ee/\mu\mu$ is prevailing for same flavor final states, $ee/\mu\mu$, that are not considered in this analysis. The final state of $Z/\gamma^* \to \tau\tau$ presents two leptons and neutrinos from the tau-lepton decays, making it very similar to the signal signature. Anyhow, the two DY leptons tend to be oppositely aligned, resulting in a lower momentum, which makes possible to reduce this background with kinematic selections. This background is estimated by MC, but its prediction are corrected in a dedicated control region, as described in Section 7.6.2.

W+jets and multi-jet backgrounds   W bosons produced in association with one or more jets, usually referred to as W+jets, mimic the signal topology with two identified leptons, when a jet is misidentified as a prompt lepton. The same can happen for multi-jet production accompanied by mis-measured missing energy. There are two kinds of misidentified leptons: *non prompt leptons* that arise from leptonic decays of heavy quarks and *fake leptons* from hadronic showers that simulate electromagnetic showers. A more detail description of this background and of its evaluation method is given in Section 7.2.1.

Other diboson background A smaller contribution to the total background is given by other diboson backgrounds such as $W\gamma, W\gamma^*$, WZ and ZZ. For $W\gamma$, a photon can fake an electron due to the photon converting to an electron-positron pair and the higher p_T lepton of the pair tends to be reconstructed as a lepton candidate. The $W\gamma^*$ background comes from the associated production of a W boson and a virtual γ; the photon then converts into a pair of charged leptons. Differently from the $W\gamma$ case, the photon can decay also in a pair of $\mu\mu$ and $\tau\tau$. For the WZ, ZZ backgrounds there can be two, three or four leptons: the signal region can be contaminated if the additional leptons are lost or misidentified. However, their contribution is rather low, and they can be reduced vetoing additional leptons. The effect of these processes in the VBF SR is rather low, and they are all estimated using MC predictions.

Other Higgs production and decay modes The Higgs production via gluon-gluon fusion and associated production are considered as a background for the VBF studies. Requirements on jet multiplicity and on other kinematic variables help to distinguish between the different production modes. In ggF the jets are produced via the parton radiation from the initial state partons, while the VBF production mode is characterized by two highly energetic jets coming from the initial state quarks. The contribution of VH in the VBF SR is almost null, instead the ggF one is of the same order as the signal. The contributions from ggF and VBF productions in $H \to \tau\tau$ decays are also considered as backgrounds, while the ttH and bbH production modes are neglected due to their small cross-sections. All the Higgs production and decay modes are estimated via Monte Carlo simulation.

7.2.1   Fakes estimation

Fake leptons originate from either non-prompt leptons, that mainly come from the decay of hadrons containing a heavy quark, or from light jets faking a lepton. The misidentification is not properly described by the simulation, therefore a data-driven fake-factor-based method is used to estimate the normalization and the kinematics of this background: this is evaluated in data, using a W+jets data control sample, in which there are two leptons, one that satisfies the same selection criteria of the SR (*identified lepton*), while the other fails the signal region selection but passes looser identification and isolation criteria (*anti-identified lepton*). Anti-id electrons are required to pass the *Loose* identification and anti-id muons are required to pass the *Medium*

identification. Moreover, the anti-id muons have the impact parameter definition changed to $d_0/\sigma(d_0) < 15$.

The normalization of the W+jets background is estimated thanks to extrapolation factors, called *fake factors*, that scale the events in the data control sample. The fake factors are calculated in jet enriched regions such as in Z+jets and di-jet data samples and are defined as the ratio of identified to anti-identified leptons, estimated in bins of the anti-identified lepton p_T and η:

$$F.F. = \frac{N_{\rm id}}{N_{\rm anti-id}}. \tag{7.3}$$

A separate F.F. measurement is performed for electrons and muons. Possible contaminations from other backgrounds are subtracted before the fake factor definition. In this analysis, for the W+jets estimation, the Z+jets fake factors are used, in which the Z decayed in either ee or $\mu\mu$ pairs, while di-jet fake factors are employed for the W+jets events in which the fake lepton is the only object that fires the trigger.

There are two kinds of backgrounds from mis-identified leptons: the *single-fake* ones present one real lepton plus a mis-identified one, like for W+jets processes; in the *double-fake* backgrounds, instead, both leptons are mis-identified, like for QCD processes. Therefore, in the signal sample the number of id pairs can be defined as:

$$N_{id+id} = N_{id+id}^{EW} + N_{id+id}^{W+jets} + N_{id+id}^{QCD}, \tag{7.4}$$

where $N_{\rm id+id}^{W+\rm jets}$ represent the single-fake W+jets contribution in the SR, $N_{\rm id+id}^{\rm QCD}$ indicate the double-fake background (QCD) in the SR, while $N_{\rm id+id}^{\rm EW}$ is the sum of all other processes with two real leptons in the signal sample (including the signal). As previously mentioned, the W+jets control sample, aimed at evaluating the fake background, is determined requiring one identified and an anti-identified leptons. Consequently:

$$N_{id+anti-id} = N_{id+anti-id}^{W+jets} + N_{id+anti-id}^{EWMC} + N_{id+anti-id}^{QCD}. \tag{7.5}$$

The term $N_{\rm id+anti-id}^{W+\rm jets}$ is the contribution from W+jets, while $N_{\rm id+anti-id}^{\rm EW}$ refers to all other backgrounds in the W+jets control sample. This term is subtracted from the control sample when predicting the W+jets background in the signal region. At last, $N_{\rm id+anti-id}^{\rm QCD}$ is the QCD contribution, that has generally a smaller effect compared to W+jets. This term is typically incorporated in the evaluation as it is included in the W+jets control sample (see Eq. 7.5).

To avoid double counting, the numbers of QCD events has to be subtracted from the W+jets control sample.

Since the calculation of the F.F. is performed in a Z+jets data sample, but applied on a W+jets one, possible differences in the fake composition in those two samples have to be estimated: a correction of the F.F., denoted as *correction factor*, defined as the ratio of the F.F from Z+jets to the opposite charge W+jets, is computed on MC predictions, separately for muons and electrons and for low-p_T (< 25 GeV) and high-p_T (> 25 GeV).

The fake factor is estimated in bins of p_T for both muons and electrons. Electrons are also binned in two $|\eta|$ bins; instead, for the muons, since no statistically significant difference between low and high pseudorapidity has been observed, the fake factor is integrated over $|\eta|$ to gain statistical precision. The central value and the statistical error of the FF for each p_T and η bins is presented in Table 7.2.

p_T range [GeV]	electron $|\eta| < 1.5$	electron $|\eta| > 1.5$	muon
15.0 − 20.0	0.030 ± 0.008	0.046 ± 0.012	0.108 ± 0.012
20.0 − 25.0	0.080 ± 0.020	0.058 ± 0.031	0.125 ± 0.030
25.0 − 35.0	0.170 ± 0.039	0.224 ± 0.060	0.112 ± 0.085
35.0 − 1000.0	0.284 ± 0.073	0.259 ± 0.084	

TABLE 7.2: Table summarizing the estimated fake factors from the Z+jets data sample. The uncertainties shown are statistical only.

7.3 Objects selection

The selection of the object candidates has been discussed in Chapter 6. A summary of this selection for electrons and muons is given in Table 7.3.

An overlap removal procedure, based on the angular separation ΔR in the $\eta\phi$-plane between two reconstructed objects, is applied in order to avoid multiple counting of physics objects.

Events with jets are discarded from the analyses if their ΔR with respect to a charged lepton is smaller than 0.2. On the other hand, in case the charged lepton is a muon, a different criterion is applied. The jet is removed if it has less than three associated tracks with $p_T > 500$ MeV or if the p_T ratio of the muon and jet is larger than 0.5 ($p_T^\mu/p_T^{jet} > 0.5$) and, at the same time, the ratio of the muon p_T to the sum of p_T of tracks with $p_T > 500$ MeV associated to the jet is larger than 0.7.

Both electron and muon candidates are removed, if they are within $0.2 <$

$\Delta R < \min(0.4, 0.04 + 10\ \text{GeV}/p_\text{T})$ to any jet passing the previously stated overlap removal procedures.

Furthermore, electron candidates are removed if they share an ID track with a muon. Instead, a muon is removed if an ID track is shared between a calorimeter-tagged muon and an electron.

Electrons		Muons	
15 GeV < p_T < 25 GeV	p_T > 25 GeV	15 GeV < p_T < 25 GeV	p_T > 25 GeV
$z_0 \sin\theta < 0.5\,\text{mm}$		$z_0 \sin\theta < 0.5\,\text{mm}$	
$d_0/\sigma(d_0) < 5$		$d_0/\sigma(d_0) < 3$	
$|\eta| < 2.47$ excluding $1.37 < |\eta| < 1.52$		$|\eta| < 2.5$	
TightLH	*MediumLH*	*Tight*	
$E_\text{T}^{\Delta R=0.2} < 0.11 \cdot E_\text{T}$ $p_\text{T}^{\Delta R=0.4} < 0.06 \cdot E_\text{T}$	Gradient isolation	$E_\text{T}^{\Delta R=0.3} < 0.09 \cdot p_\text{T}$ $p_\text{T}^{\Delta R=0.2} < 0.06 \cdot p_\text{T}$	

TABLE 7.3: Object definition requirements for electron and muon candidates.

Furthermore, in order to avoid overlaps between the simulated V+jet and $V + \gamma$ samples, events from the V+jets samples are removed if an additional photon is found at a distance $\Delta R > 0.1$ from the leptons originating from the V boson decay.

7.4   Trigger selection

As mentioned in Chapter 3.2.4, where the ATLAS trigger and DAQ systems have been introduced, the collected events fire given triggers and are accordingly stored. After the primary object reconstruction selection, described in Chapter 6, specific trigger requirements are solicited and the reconstructed objects are matched to the triggered ones (*trigger matching*). In the early Run-2 studies of $H \to WW^* \to \ell\nu\ell\nu$, only single-lepton triggers where used. For this studies, instead, both single- and di-lepton triggers were employed in order to maximize the total trigger efficiency. The increase in efficiency is mostly relevant for low values of the leading lepton p_T, allowing, in this way, to lower the cut on the leading lepton p_T from 25 GeV to 22 GeV, thus increasing as well the signal statistics. In Table 7.4 are reported the single lepton trigger configurations for different data-taking periods of 2015 and 2016, while the available di-lepton triggers are instead listed in Table 7.5 (for the nomenclature of the trigger configuration see Section 3.2.4).

Lepton Type	Periods	Un-prescaled Single Lepton Triggers
Electron 2015	All year	`HLT_e24_lhmedium_L1EM20VH ‖`
		`HLT_e60_lhmedium ‖`
		`HLT_e120_lhloose`
Electron 2016	A-D3	`HLT_e24_lhtight_nod0_ivarloose`
		`HLT_e60_lhmedium_nod0 ‖`
		`‖ HLT_e140_lhloose_nod0`
Electron 2016	D4-L	`HLT_e26_lhtight_nod0_ivarloose`
		`HLT_e60_lhmedium_nod0 ‖`
		`‖ HLT_e140_lhloose_nod0`
Muon 2015	All year	`HLT_mu20_iloose_L1MU15 ‖ HLT_mu50`
Muon 2016	A-D3	`HLT_mu24_ivarmedium ‖ HLT_mu50`
Muon 2016	D4-L	`HLT_mu26_ivarmedium ‖ HLT_mu50`

TABLE 7.4: Configuration of the OR among single lepton triggers for 2015-2016 data

Di-lepton Triggers	Periods
`e17_lhloose_mu14`	2015-2016
`e7_lhmedium_mu24`	2015-2016

TABLE 7.5: List of the available di-lepton triggers for the data taking periods 2015 and 2016.

7.4.0.1 OR-ing di-lepton and single lepton triggers

Scale factors are applied on the trigger efficiency in order to correct the Monte Carlo simulation description of the data. A per-event scale factor is defined as follows:

$$SF = \frac{\varepsilon_{data}}{\varepsilon_{MC}} \tag{7.6}$$

where ε_{data} is the efficiency obtained from real data and ε_{MC} from MC simulation, respectively on $Z \to \mu\mu$ and $Z \to ee$ data and simulated events. In both cases, muon and electron trigger efficiencies are obtained by means of the tag & probe method (see Section 6.3). Event-level trigger scale factors for events with multiple lepton triggers in logical OR have to be calculated. Trigger efficiencies and scale factors measured per individual lepton and single trigger legs are used as an input for this computation. The efficiency for the OR between the di- and single-lepton triggers is estimated as follows. Calling S_e and S_μ the unions of the single-electron/muon triggers, and by D_e^2/D_μ^2 the

legs of the $e\mu$ trigger:

$$
\begin{aligned}
P(T_{n_e+n_\mu}) &= P((D_e^2 \wedge D_\mu^2) \vee S_e \vee S_\mu) \\
&= P(S_e \vee S_\mu) + [P(D_e^2) - P(D_e^2 \wedge S_e)][P(D_\mu^2) - P(D_\mu^2 \wedge S_\mu)] \\
&= P(S_e \vee S_\mu) + [P(S_e \vee D_e^2) - P(S_e)][P(S_\mu \vee D_\mu^2) - P(S_\mu)] \\
&= 1 - [1 - P(S_e)][1 - P(S_\mu)] + [P(S_e \vee D_e^2) - P(S_e)][P(S_\mu \vee D_\mu^2) - P(S_\mu)].
\end{aligned}
\tag{7.7}
$$

The trigger legs hierarchization is one of the crucial points in the computation of the event-level efficiencies. A lepton firing a given trigger leg has to fire all looser legs, such that if $L1 < L2$, $\mathcal{P}(L1|L2) = 1$. The on-line p_T thresholds and particle identification requirements (PID) are the basis of the hierarchy, which indeed can vary with the leptons p_T.

With the trigger configuration shown in Tables 7.4 and 7.5, an example of trigger hierarchy can be found in the comparison between the electron leg of the di-lepton trigger `e7_lhmedium` and the OR among the triggers `e24_lhmedium`, `e60_lhmedium` and `e120_lhloose`: the PID of the `e7` branch is greater or equal than `e24`/`e60`, but tighter than `e120`. In Figure 7.3(a) the efficiencies of the two aforementioned trigger legs are shown. These have been calculated as the ratio between the events with one lepton with p_T above the threshold that matched the given trigger and the events that have a lepton above the trigger p_T threshold. In Figure 7.3(b), the probability for an electron to be matched to `e7_lhmedium` when it is already matched to the OR between `e24_lhmedium`, `e60_lhmedium` and `e120_lhloose` is shown. Instead, in Figure 7.3(c), the probability for an electron to be matched to the OR among `e24_lhmedium`, `e60_lhmedium` and `e120_lhloose` when it is already matched to `e7_lhmedium` is given. As shown in Figure 7.3(b), for high electron p_T values, the hierarchy can be reversed due to the looser PID of `e120`, giving `e7`<`e24_OR_e60_OR_e120` below 120 GeV, and the contrary above.

Following the same logic as for the electrons, in Figure 7.4(a) the muon trigger efficiencies for legs `mu14` and `mu20_ivarloose_OR_mu50`, are shown, while their conditional efficiencies, $\mathcal{P}($ `mu14`| `mu20_ivarloose_OR_mu50`), is given in Figure 7.4(b). As expected, the conditional efficiency for the trigger leg `mu14` is 100%.
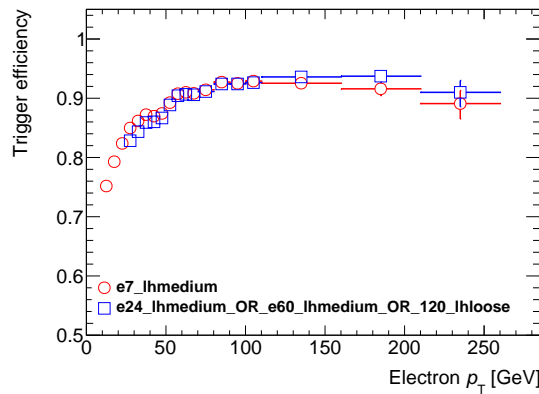
(a)
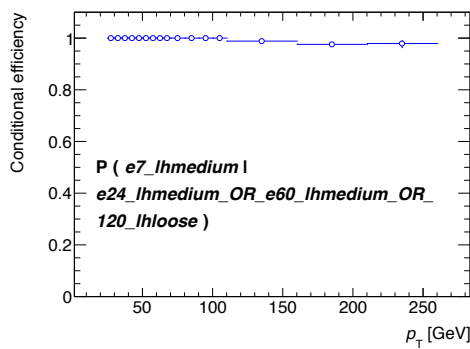
(b)
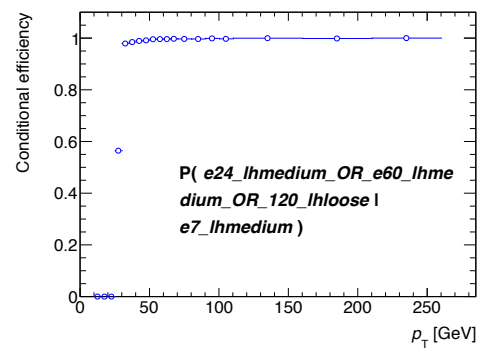
(c)

FIGURE 7.3: Figure 7.3(a) shows the matching efficiency as a function of the electron p_T for the trigger leg `e7_lhmedium` (red curve) and the OR among `e24_lhmedium`, `e60_lhmedium` and `e120_lhloose` (blue curve). In Figure 7.3(b) is given, instead, the probability for an electron to be matched to `e7_lhmedium` when it is already matched to the OR among `e24_lhmedium`, `e60_lhmedium` and `e120_lhloose`, while in Figure 7.3(c), the probability for an electron to be matched to the OR between `e24_lhmedium`, `e60_lhmedium` and `e120_lhloose` when it is already matched to `e7_lhmedium`. The uncertainties in the plots are statistical only.

7.4.0.2 Efficiency gain

As mentioned before, OR-ing single and di-lepton triggers can increase the total efficiency, especially for low lepton p_T values. Table 7.6 shows the efficiency gains with respect to the single lepton trigger, expressed in percentage, obtained OR-ing single-lepton triggers with the `e17_lhloose_mu14` trigger only or with both di-lepton triggers listed in Table 7.5.

These efficiency gains are calculated after the pre-selection, described in the next Section, and applying different cuts on the leading lepton p_T.
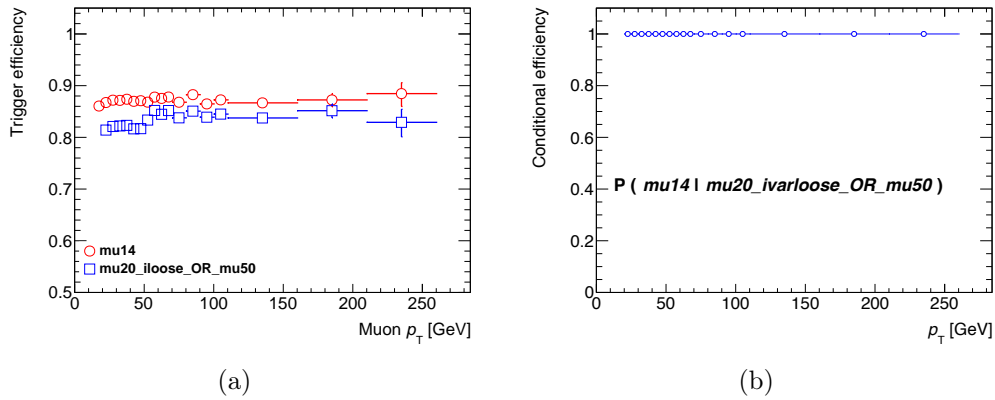
FIGURE 7.4: Figure 7.4(a) shows the matching efficiency as a function of the muon p_T for the trigger leg `mu14` (red curve) and the OR among the triggers `mu20_iloose` and `mu50` (blue curve). In Figure 7.4(b) is instead shown the probability for a muon to be matched to `mu14` when it is already matched to `mu20_iloose_OR_mu50`. The uncertainties in the plots are statistical only.

The efficiency calculation for the ggF signal is split in three different jet regions: 0 jets, 1 jet and 2 or more jets. The efficiencies for VBF are shown only for ≥ 2 region. The plots in Figure 7.5 show the trigger efficiency as a function of the leading lepton p_T for the ggF signal in the 0-1 jet categories, while in Figure 7.6 for the ggF and VBF ≥ 2 jets categories.

As shown in the tables and the figures, the efficiency gain decreases requesting more jets and the $e\mu$ channel presents a larger gain when the `e17_lhloose_mu14` trigger is added: for $p_T^{lead} > 22GeV$ there is an increase of efficiency of 22.1% for ggF 0-jet, 15.6% for ggF 1-jet, 10.5% for ggf 2-jets and 8.0% for VBF 2-jets, as can be seen from Table 7.6. The effect of the di-lepton trigger on the μe channel is less pronounced, more precisely is about a factor ~ 2 smaller than for the $e\mu$ channel.

The effect when adding also the `e7_lhmedium_mu24` trigger is on average relatively small: it doesn't affect at all the $e\mu$ channel, but increases only the efficiency of the μe channel by a few percentage points. Therefore, for the analyses, it was adopted only the `e17_lhloose_mu14` di-lepton trigger. The effects on the total $e\mu + \mu e$ channel are visible in Figures 7.5(e), 7.5(f), 7.6(e) and 7.6(f): the resulting increase of efficiency in the $e\mu + \mu e$ channel is of 17.0% for ggF 0-jet, 12.1% for ggF 1-jet, 8.0% for ggf 2-jets and 6.0% for VBF.

As mentioned before, the addition of the di-lepton trigger allowed to lower the cut on the leading lepton p_T from 25 GeV to 22 GeV, thus increasing
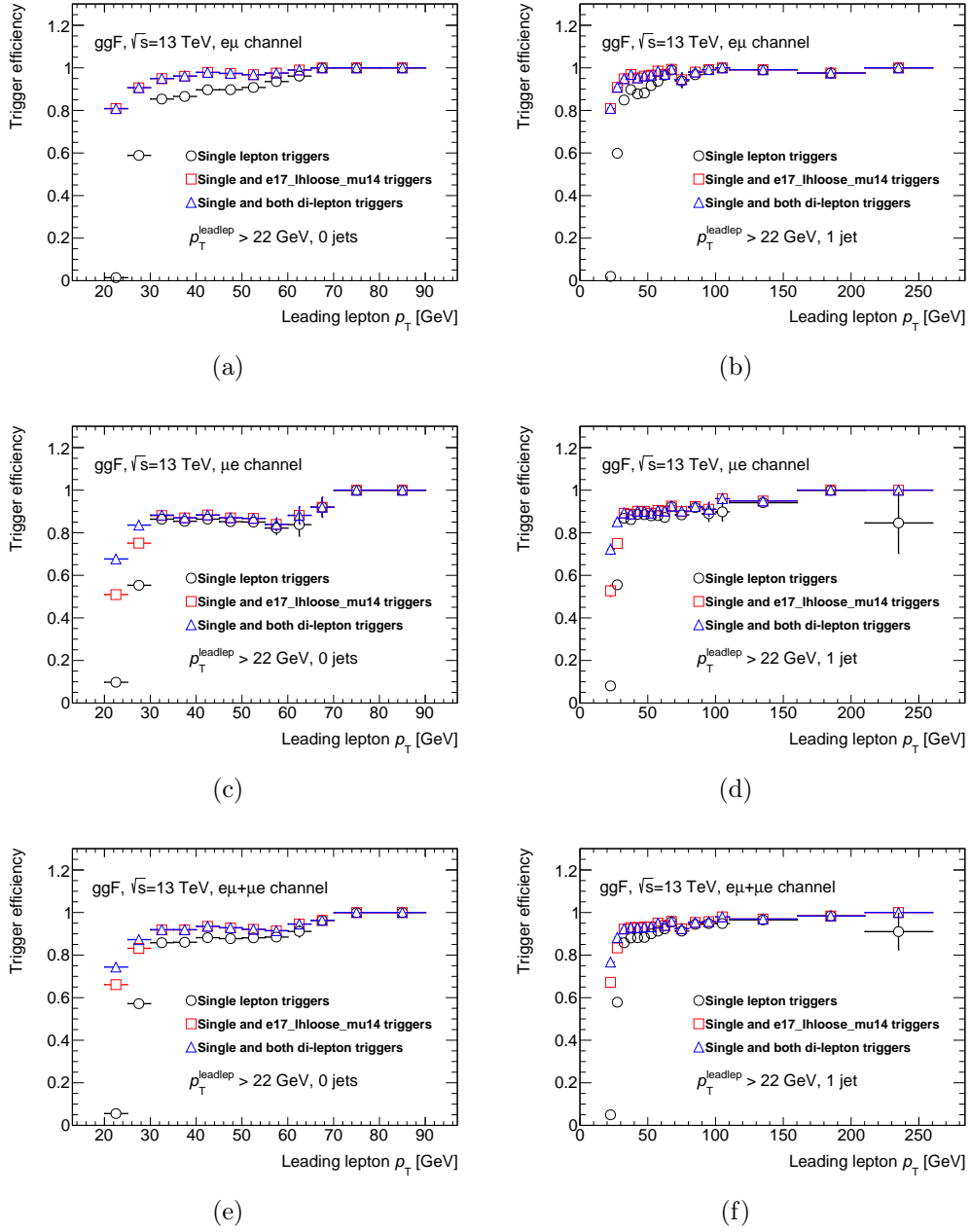
FIGURE 7.5: Efficiency plots for ggF $e\mu$, μe and $e\mu + \mu e$ channels requiring, respectively, 0 jets (Fig 7.5(a), 7.5(c), 7.5(e)) and 1 jet (Fig 7.5(b), 7.5(d), 7.5(f)) and requesting leading lepton $p_T > 22$ GeV. The uncertainties in the plots are statistical only.

the signal statistics without affecting the backgrounds. The distributions of the computed scale factors are shown in Figures 7.7 for the ggF and VBF samples, respectively, after the pre-selection for the $e\mu + \mu e$ channel.
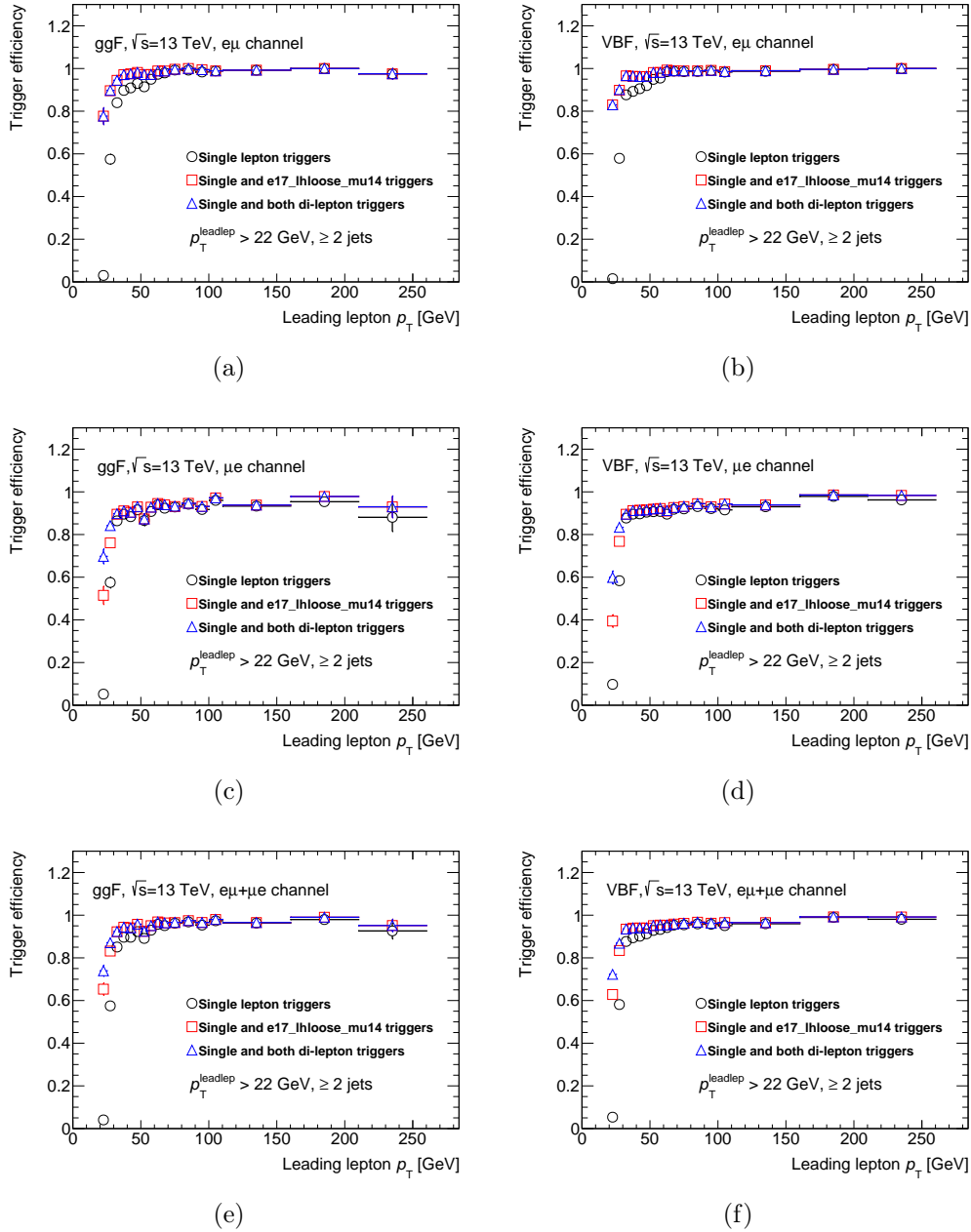
FIGURE 7.6: Efficiency plots for ggF + 2 jets (Fig 7.6(a), 7.6(c), 7.6(e)) and VBF + 2 jets (Fig 7.6(b), 7.6(d), 7.6(f)) in the $e\mu$, μe and $e\mu + \mu e$ channels and requesting leading lepton $p_T > 22$ GeV. The uncertainties in the plots are statistical only.

(a)   (b)
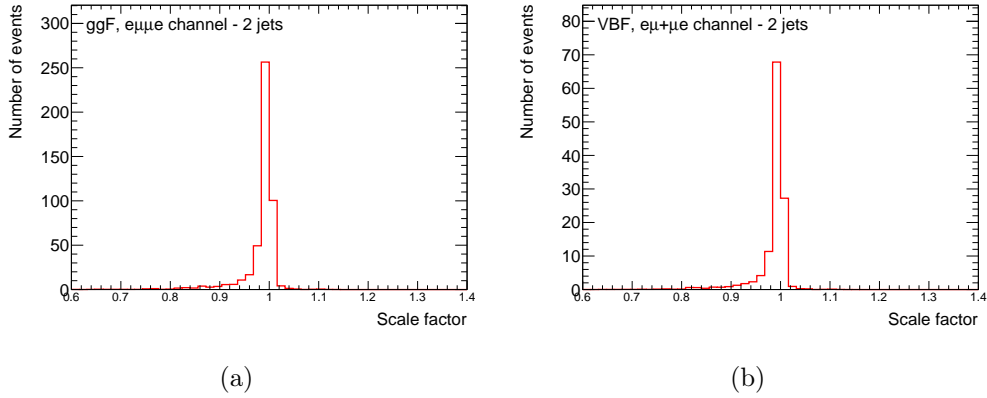
FIGURE 7.7: Computed overall trigger scale factors for ggF
and VBF at pre-selection level in the $e\mu + \mu e$ channel.

	ggF 0-jets [%]	ggF 1-jet [%]	ggF $\geq$ 2 jets [%]	VBF $\geq$ 2 jets [%]
$p_T^{lead} > 25 GeV$				
Single + `e17_lhloose_mu14`				
$e\mu$	15.8	11.1	7.5	5.3
μe	6.9	5.2	3.3	2.8
$e\mu + \mu e$	11.8	8.4	5.6	4.2
Single + both di-lepton triggers				
$e\mu$	15.8	11.1	7.5	5.4
μe	9.2	6.9	4.2	3.4
$e\mu + \mu e$	12.9	9.2	6.0	4.5
$p_T^{lead} > 22 GeV$				
Single + `e17_lhloose_mu14`				
$e\mu$	22.1	15.6	10.5	8.0
μe	10.7	8.0	5.2	3.8
$e\mu + \mu e$	17.0	12.1	8.0	6.0
Single + both di-lepton triggers				
$e\mu$	22.2	15.7	10.5	8.0
μe	14.6	11.0	6.8	5.0
$e\mu + \mu e$	18.8	13.5	8.8	6.6

TABLE 7.6: Efficiency gain with respect to the single lepton
efficiency, expressed in percentage, after pre-selection for ggF
and VBF and applying the requirement $p_T^{lead} > 25/22 GeV$ in
different jet bins.

7.5   Pre-selection and topological variables

Apart from object definitions and the trigger requirements, a VBF $H \to WW^* \to \ell\nu\ell\nu$ candidate is selected by requiring:

- exactly two opposite sign and different flavour leptons ($e\mu + \mu e$);

- $p_{\mathrm{T}}^{lead} > 22$ GeV, $p_{\mathrm{T}}^{sublead} > 15$ GeV;

- $m_{ll} > 10$ GeV in order to remove low mass meson resonances and DY events;

- at least two jets with a p_{T} above 30 GeV,

- no jet tagged as a b-jet (*b-jet veto*).

This selection defines the *pre-selection* stage. After the previous to the last cut, different requirements must be fulfilled in order to define the signal-enriched region and the control regions. The event yields for the preselection are given in Table 7.7. A further reduction of the backgrounds can be achieved using the so called *topological* variables, that can help enhancing the Higgs decay topology and the VBF production mode. These topological variables are listed below.

- $p_{\mathrm{T}}^{\mathrm{tot}}$: is the total transverse momentum of the event, defined as:

$$p_{\mathrm{T}}^{\mathrm{tot}} = \boldsymbol{p}_{\mathrm{T}}{}^{l1} + \boldsymbol{p}_{\mathrm{T}}{}^{l2} + MET + \sum \boldsymbol{p}_{\mathrm{T}}{}^{\mathrm{jets}}, \qquad (7.8)$$

  where the sum over jets runs over all jets which pass the good-jet definition criteria. This variable helps distinguishing events with significant soft gluon radiation that recoils against the $\ell\ell + 2j$ system with no high-p_{T} jets. The missing transverse energy employed is the $E_{\mathrm{T}}^{\mathrm{miss}}$ with Track Soft Term, which is the default missing transverse energy, as described in Section 6.4.

- $m_{\tau\tau}$: is the mass of the τ lepton pair, defined under the assumptions of the Collinear Approximation Method [140]. In this approximation the charged leptons are the products of the decay of a pair of τ leptons, and the neutrinos emitted in these decays are collinear with the charged leptons and are the only source of the observed E_{T}^{miss} in the event, making possible to compute the energy fractions of the neutrinos. Also in this case, the TST missing transverse energy is used in the $m_{\tau\tau}$ calculation. This cut is imposed to suppress also $H \to \tau\tau$ decays

- Δy_{jj}: the VBF signal is characterized by big separation between the two tagging jets in rapidity, therefore a gap in Δy_{jj} is a useful quantity to separate this production mode from the backgrounds.

- m_{jj}: a high invariant mass of the tag jets is a characteristic signature of the VBF signal.

- η_{lep} centrality: this quantity returns the exact positions of the leptons with respect to the two tag jets in the η-plane:

$$\mathrm{OLV}_{l_1} = 2 \cdot |\frac{\eta_{l_1} - \bar{\eta}}{\eta_{j_1} - \eta_{j_2}}|$$

$$\mathrm{OLV}_{l_2} = 2 \cdot |\frac{\eta_{l_2} - \bar{\eta}}{\eta_{j_1} - \eta_{j_2}}|$$

$$\eta_{\mathrm{lep}} \text{ centrality} = \mathrm{OLV}_{l_1} + \mathrm{OLV}_{l_2} \tag{7.9}$$

where $\bar{\eta} = (\eta_{j_1} + \eta_{j_2})/2$ is the average η of the two tag jets. For each lepton,

$$\mathrm{OLV}_l \begin{cases} = 0 & \text{the lepton is right in the middle of the jets rapidity gap.} \\ < 1 & \text{the lepton lies within the jets rapidity gap.} \\ > 1 & \text{the lepton is outside the jets rapidity gap.} \end{cases}$$
$$\tag{7.10}$$

- $\sum_{\mathrm{l,j}} \mathrm{M_{lj}}$ is defined as the sum of the invariant masses of all four possible lepton-jet pairs. For the VBF signal it peaks at higher values than for the backgrounds: the leptons tend to be in the central region, while the jets in the forward one, resulting in large opening angles between the jets and the leptons.

$\sqrt{s} = 13\,TeV$, $\mathscr{L} = 36\,fb^{-1}$,

Cut	VBF	ggF	Other Higgs	WW	Other diboson	Top	Z+jets	W+jets	Total MC	Data
2-leptons	226.27 ± 0.57	986.99 ± 7.53	908.36 ± 2.59	46587.47 ± 81.99	102677.01 ± 474.32	429561.91 ± 289.99	1668627.37 ± 2950.43	176106.04 ± 704.15	2425681.44 ± 3084.91	1227411
$p_T^{lead} > 22$ GeV	226.27 ± 0.57	986.99 ± 7.53	908.36 ± 2.59	46587.47 ± 81.99	102677.01 ± 474.32	429561.91 ± 289.99	1668627.37 ± 2950.43	176106.04 ± 704.15	2425681.44 ± 3084.91	1227411
$p_T^{sublead} > 15$	189.41 ± 0.52	811.39 ± 6.84	740.85 ± 2.34	43230.33 ± 78.95	76292.11 ± 428.95	393952.30 ± 278.41	1115960.74 ± 2311.31	131982.17 ± 547.38	1763159.28 ± 2430.96	936471
OS Leptons	187.95 ± 0.52	805.91 ± 6.82	672.78 ± 2.31	42545.05 ± 78.13	39653.40 ± 213.24	388929.91 ± 278.66	761006.99 ± 1871.94	123274.73 ± 455.23	1357076.72 ± 1959.48	785243
$M_{\ell\ell} > 12/10$ GeV	178.33 ± 0.51	764.48 ± 6.65	666.76 ± 2.29	42269.93 ± 77.91	34100.81 ± 193.82	386135.12 ± 275.70	531940.13 ± 1710.08	122002.26 ± 435.59	1118057.82 ± 1798.28	719525
2-jets	96.67 ± 0.37	229.23 ± 3.08	130.05 ± 0.95	6200.86 ± 17.11	1300.78 ± 25.78	246060.41 ± 220.49	7180.72 ± 71.84	5492.60 ± 94.94	266691.32 ± 252.51	264515
b-veto	85.74 ± 0.35	187.09 ± 2.74	103.24 ± 0.83	5170.06 ± 15.76	1045.84 ± 22.86	13982.22 ± 50.03	5751.73 ± 66.29	1209.19 ± 39.10	27535.11 ± 95.95	26229

TABLE 7.7: Event yields at pre-selection level. The errors shown in the table are from statistics only. No pre-fit normalization factors are applied.

Cut	VBF	ggF	Other Higgs	WW	Other diboson	Top	Z+jets	W+jets	Total MC	Data
1 b-jet	10.26 ± 0.14	35.93 ± 1.34	22.07 ± 0.43	910.15 ± 6.46	216.93 ± 10.13	87076.79 ± 128.27	1193.09 ± 26.88	2156.13 ± 55.71	91621.36 ± 142.92	92007
CJV < 20 GeV	6.58 ± 0.11	23.40 ± 1.07	15.49 ± 0.35	572.71 ± 5.40	132.00 ± 7.63	58458.79 ± 105.07	788.72 ± 24.00	1404.42 ± 45.44	61402.11 ± 117.34	61802
OJV	5.02 ± 0.09	4.58 ± 0.46	3.88 ± 0.17	86.63 ± 2.02	24.28 ± 3.24	11255.88 ± 46.45	240.55 ± 20.38	140.54 ± 15.68	11761.35 ± 53.23	11722
$Z \to \tau\tau$ veto	4.31 ± 0.09	3.95 ± 0.44	1.46 ± 0.12	52.36 ± 1.68	13.36 ± 2.43	7372.03 ± 37.57	176.27 ± 16.45	52.44 ± 5.36	7676.19 ± 41.47	7668

TABLE 7.8: Event yields in the Top control region. The errors shown in the table are from statistics only. Pre-fit normalization factors are applied.

Cut	VBF	ggF	Other Higgs	WW	Other diboson	Top	Z+jets	W+jets	Total MC	Data
$|m_{\tau\tau} - m_Z| < 25$	7.30 ± 0.10	15.98 ± 0.78	24.59 ± 0.39	445.49 ± 4.48	213.86 ± 12.03	1197.22 ± 14.21	2505.00 ± 46.29	157.19 ± 17.55	4566.61 ± 53.09	4223
$M_{ll} < 80$ GeV	7.13 ± 0.10	15.66 ± 0.77	20.81 ± 0.36	154.39 ± 2.61	156.63 ± 11.43	381.00 ± 7.96	2455.54 ± 45.83	101.20 ± 15.62	3292.36 ± 50.46	2970
CJV < 20 GeV	5.07 ± 0.08	10.87 ± 0.65	15.81 ± 0.31	109.12 ± 2.21	109.04 ± 9.33	246.66 ± 6.20	1838.07 ± 43.67	74.31 ± 13.63	2408.96 ± 47.15	2194
OJV	3.97 ± 0.08	2.37 ± 0.31	5.78 ± 0.16	21.98 ± 1.04	23.95 ± 3.56	56.81 ± 3.05	387.97 ± 15.68	23.45 ± 7.54	526.29 ± 18.05	501

TABLE 7.9: Event yields $Z \to \tau\tau$ CR. The errors shown in the table are from statistics only. Pre-fit normalization factors are applied to both Top and $Z \to \tau\tau$ backgrounds.

Cut	VBF	ggF	Other Higgs	WW	Other diboson	Top	Z+jets	W+jets	Total MC	Data
$m_T > 130$ GeV	7.29 ± 0.10	21.82 ± 0.96	11.55 ± 0.23	3894.52 ± 13.49	457.72 ± 10.92	10831.98 ± 44.51	168.38 ± 12.13	516.58 ± 25.26	15909.83 ± 55.39	15549
$m_{T2} > 160$ GeV	2.01 ± 0.06	3.74 ± 0.39	1.04 ± 0.08	614.40 ± 4.77	58.66 ± 3.25	504.69 ± 9.62	19.45 ± 2.42	39.19 ± 9.66	1243.19 ± 15.00	1114
CJV < 20 GeV	1.19 ± 0.04	2.53 ± 0.33	0.78 ± 0.08	393.29 ± 4.06	36.28 ± 2.89	281.23 ± 7.32	14.01 ± 2.18	32.10 ± 9.07	761.42 ± 12.86	686

TABLE 7.10: Event yields WW VR. The errors shown in the table are from statistics only. Pre-fit normalization factors are applied to both Top and $Z \to \tau\tau$ backgrounds.

Cut	VBF	ggF	Other Higgs	WW	Other diboson	Top	Z+jets	W+jets	Total MC	Data
CJV < 20 GeV	61.92 ± 0.29	135.95 ± 2.33	77.97 ± 0.73	3694.62 ± 13.76	717.56 ± 19.27	9342.96 ± 40.92	4216.98 ± 61.11	883.06 ± 33.37	19131.01 ± 84.19	18301
OJV	50.68 ± 0.27	34.98 ± 1.12	23.97 ± 0.34	641.06 ± 6.21	157.69 ± 10.43	2005.07 ± 19.05	906.38 ± 25.74	194.95 ± 15.91	4014.79 ± 37.78	3813
$Z \to \tau\tau$ veto	43.73 ± 0.25	31.05 ± 1.05	6.30 ± 0.20	399.53 ± 5.24	87.46 ± 8.46	1304.54 ± 15.14	308.50 ± 16.73	107.13 ± 10.90	2288.23 ± 26.98	2164

TABLE 7.11: Event yields in the signal region. The errors shown in the table are from statistics only. Pre-fit normalization factors are applied to both Top and $Z \to \tau\tau$ backgrounds.

7.6   Modeling of the backgrounds

Among the main backgrounds there are top-quark, WW and $Z \to \tau\tau$ backgrounds. In this section, the control regions for the top-quark and $Z \to \tau\tau$ backgrounds and the WW validation region are described. A signal region (SR) is defined as a phase-space region enriched in signal events. A proper estimation of the background events in the SR is a crucial step for measuring the signal. To be sure that the Monte Carlo properly simulates a given background process, a control region is defined, enriched of background events, with a negligible contribution from the signal ones. Given the number of observed events in the CR, N_{CR}^{data}, and the corresponding number of background events, N_{CR}^{MC}, from MC simulation, the *normalization factor* (NF) can be defined as:

$$NF = \frac{N_{CR}^{data}}{N_{CR}^{bkg,MC}}. \tag{7.11}$$

This NF can be applied to the signal region events. The resulting number of background events in the signal region, can be estimated as follows:

$$N_{SR}^{bkg} = NF \cdot N_{SR}^{bkg,MC}. \tag{7.12}$$

The obtained normalization factor is a correction that affects only the total normalization, without adjusting any possible kinematic mis-modeling in the SR. Therefore it is important to avoid big differences in the kinematic properties between the SR and the CR, that has to be similar enough to the SR to make justifiable this extrapolation.

In case of multiple control regions, the most simple approach is to calculate the NF of the purer CR with Eq. 7.11, apply it to the second-purer CR and extract its NF. This procedure can be propagated to all the defined CRs. However, this method does not take into account correlations among the control regions. To avoid this, the *Matrix Inversion* method is instead used. In this method, a matrix of samples and regions is built for Monte Carlo. In the case of two control regions, one obtains:

$$\begin{pmatrix} N_{CR_1}^{data} \\ N_{CR_2}^{data} \end{pmatrix} = \begin{pmatrix} N_{CR_1}^{bkg1,MC} & n_{CR_1}^{bkg2,MC} \\ N_{CR_2}^{bkg1,MC} & n_{CR_2}^{bkg2,MC} \end{pmatrix} \cdot \begin{pmatrix} NF_1 \\ NF_2 \end{pmatrix}, \tag{7.13}$$

The NFs can be extracted by inverting the matrix:

$$\begin{pmatrix} NF_1 \\ NF_2 \end{pmatrix} = \begin{pmatrix} N^{bkg1,MC}_{CR_1} & n^{bkg2,MC}_{CR_1} \\ N^{bkg1,MC}_{CR_2} & n^{bkg2,MC}_{CR_2} \end{pmatrix}^{-1} \cdot \begin{pmatrix} N^{data}_{CR_1} \\ N^{data}_{CR_2} \end{pmatrix}. \tag{7.14}$$

Therefore, the total number of background events in the SR can be written as:

$$N^{bkg}_{SR} = \begin{pmatrix} N^{bkg1,MC}_{SR} & N^{bkg2,MC}_{SR} \end{pmatrix} \cdot \begin{pmatrix} NF_1 \\ NF_2 \end{pmatrix}. \tag{7.15}$$

The method described above is used to calculate normalization factors that are employed only to optimize the analysis before the the statistical treatment (referred to as *pre-fit NFs*). The backgrounds, for which a control region has been built, have their final normalization estimated in the maximum likelihood fit, discussed in more detail in Chapter 8: in the fit a free normalization parameter is included for these backgrounds as an unconstrained nuisance parameter. In this way, since SR and CRs are fitted simultaneously, the estimated *post-fit NFs* are consequently coherent in all regions.

7.6.1   Top Control Region

The top-quark control region definition follows the pre-selection, but inverting the b-jet veto. Therefore, the presence of one b-tagged jet, $N_{b-jet} = 1$ is requested. The choice of requiring just one b-tagged jet, instead of an inclusive b-tagged region, is determined by the fact that, in this way, the flavor composition of the tagged jets gets closer to the one in the b-vetoed SR. Afterwards three more cuts are applied. All the events with jets with $p_T > 20$ GeV which lie between the tagging jets in pseudo-rapidity are rejected. This requirement, usually referred to as *central-jet veto* (CJV), is a cut on events with additional jets that quantifies the hadronic activity between the leading jets. Afterwards, the outside lepton veto (OLV) is imposed in order to reduce the $Z \to \tau\tau$ background. Events that are around the Z mass pole are also removed, specifically requiring $m_{\tau\tau} < m_Z - 25$ GeV. The extracted pre-fit normalization factor is found to be $NF = 1.00 \pm 0.01(stat)$.

In Table 7.8 the event yields for the Top CR can be found, while Figures 7.8 and 7.9 show the p_T and η respectively of the leading and subleading leptons and jets. An overall good agreement between data and Monte Carlo predictions is visible. Both uncertainties coming from MC statistics and experimental systematics sources are shown. The experimental uncertainties

are fully described in Section 7.8.1. This region is found to be rather pure in top-quark background, with an estimated purity of 96%.

7.6.2 $Z \to \tau\tau$ Control Region

The $Z \to \tau\tau$ control region definition differs from the signal region by the inversion of the $Z \to \tau\tau$ veto: $|m_{\tau\tau} - m_Z| \leq 25$ GeV. Furthermore, a cut is requested on the invariant mass of the two leptons, $m_{ll} < 80$ GeV. OLV and CJV vetos are applied. The pre-fit normalization factor, extracted at the OLV cut, is found to be 0.92 ± 0.07 (stat). In Figures 7.10 and 7.11 the quality of modeling of the leptons and jets p_T and η distributions is shown. The agreement between data and MC is within the uncertainties, coming from statistics and experimental systematics.

In Table 7.9, instead, the yields for the main backgrounds and signal in the $Z \to \tau\tau$ CR are reported. This region is found to be less pure than the top-quark CR, with an estimated purity of 74%.

7.6.3 WW Validation Region

Due to the high $t\bar{t}$ contamination in this region, it was not possible to build a control region, leaving the estimation of this background to the MC predictions only. However, to assure that the predictions are reliable, a validation region has been studied. This region is defined after the VBF pre-selection, requiring two cuts on the transverse mass. The first cut is applied on the transverse mass defined in Equation 7.2: $m_T > 130$ GeV. The m_T distribution at pre-selection level is shown in Figure 7.12(a). A cut at 130 GeV significantly removes Z+jets events. To further improve the separation against the $t\bar{t}$ background the information on the kinematical differences between W bosons produced from heavy top quarks decays and other EW and QCD processes has been used, in particular studying the m_{T2} distribution (see [141]). This quantity represents a lower bound on the parent particle's mass and it is defined by minimizing over all neutrinos transverse momenta, $p_T^{\nu_1}$ and $p_T^{\nu_2}$, that sum up to the observed missing momentum E_T^{miss}. The m_{T2} transverse mass is therefore defined as:

$$m_{T2} = min_{p_T^{\nu_1}+p_T^{\nu_2}=E_T^{\mathrm{miss}}}(max(m_\mathrm{T}^2(p_T^{\nu_1},p_T^{l_1}),m_\mathrm{T}^2(p_T^{\nu_2},p_T^{l_2}))) \qquad (7.16)$$

In the $t\bar{t}$ events, the upper limit of m_{T2} is around the value of top quark mass and it is lower for WW events. The cut applied on this variable is $m_{T2} > 160$
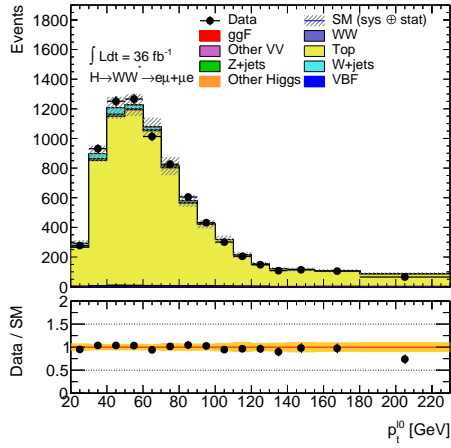
(a) Leading lepton p_T
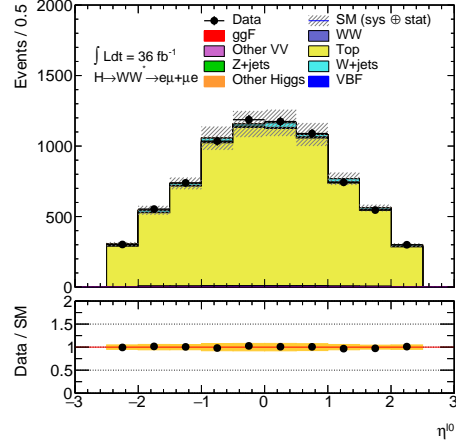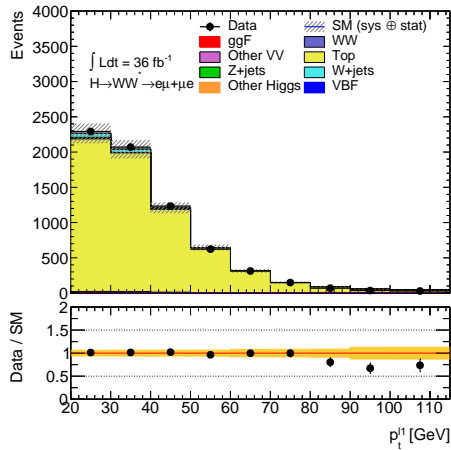
(b) Leading lepton η

(c) Subleading lepton p_T
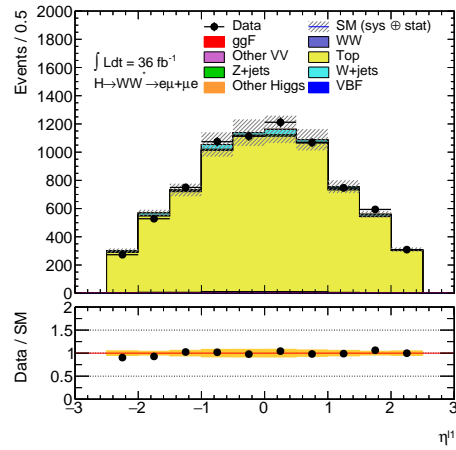
(d) Subleading lepton η

FIGURE 7.8: Pre-fit distributions for the leading and subleading lepton in the top control region. The top and $Z \rightarrow \tau\tau$ backgrounds are re-scaled with pre-fit normalization factors. The bottom plots show the ratio between the data and the MC. In both plots the error bands include both statistic and experimental systematic uncertainties.

(a) Leading jet p_T

(b) Leading jet η

(c) Subleading jet p_T
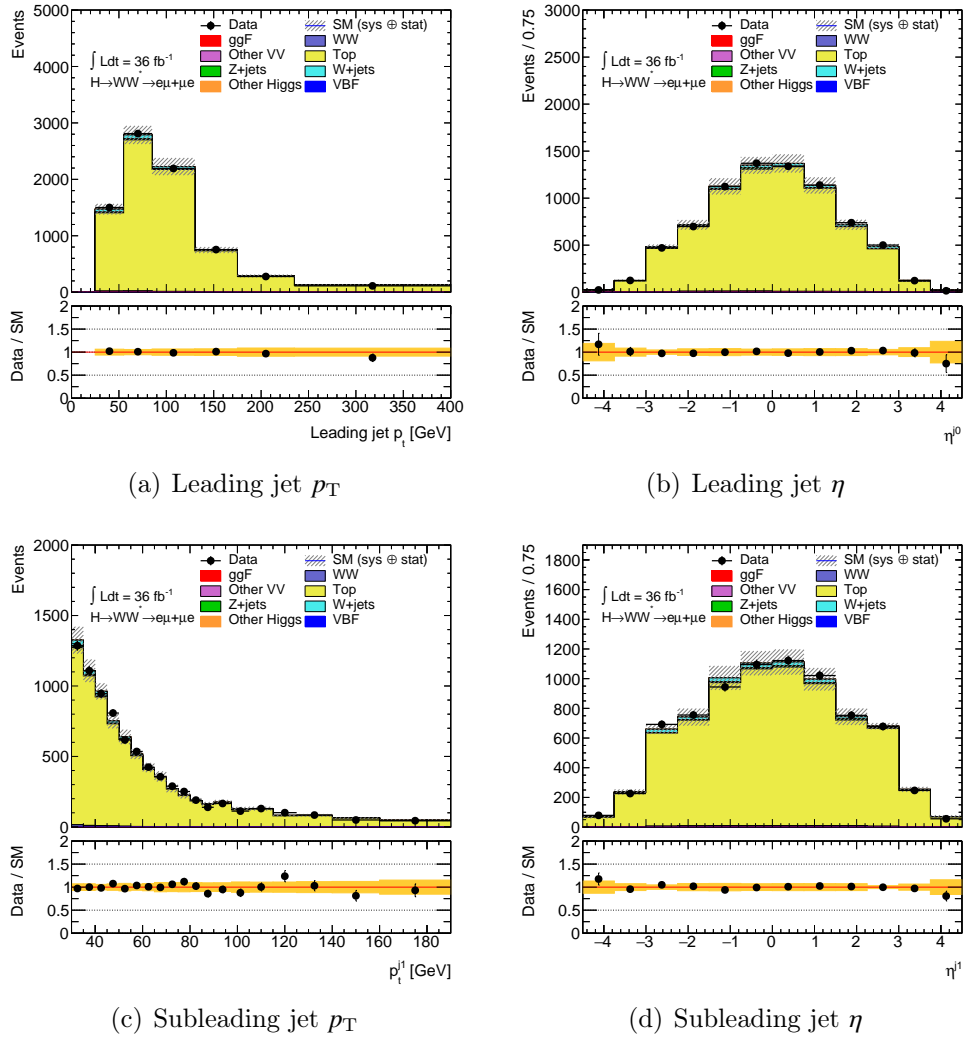
(d) Subleading jet η

FIGURE 7.9: Pre-fit distributions for the leading and sub-leading jet in the top control region. The top and $Z \to \tau\tau$ backgrounds are re-scaled with pre-fit normalization factors. The bottom plots show the ratio between the data and the MC. In both plots the error bands include both statistic and experimental systematic uncertainties.

(a) Leading lepton p_T

(b) Leading lepton η

(c) Subleading lepton p_T

(d) Subleading lepton η
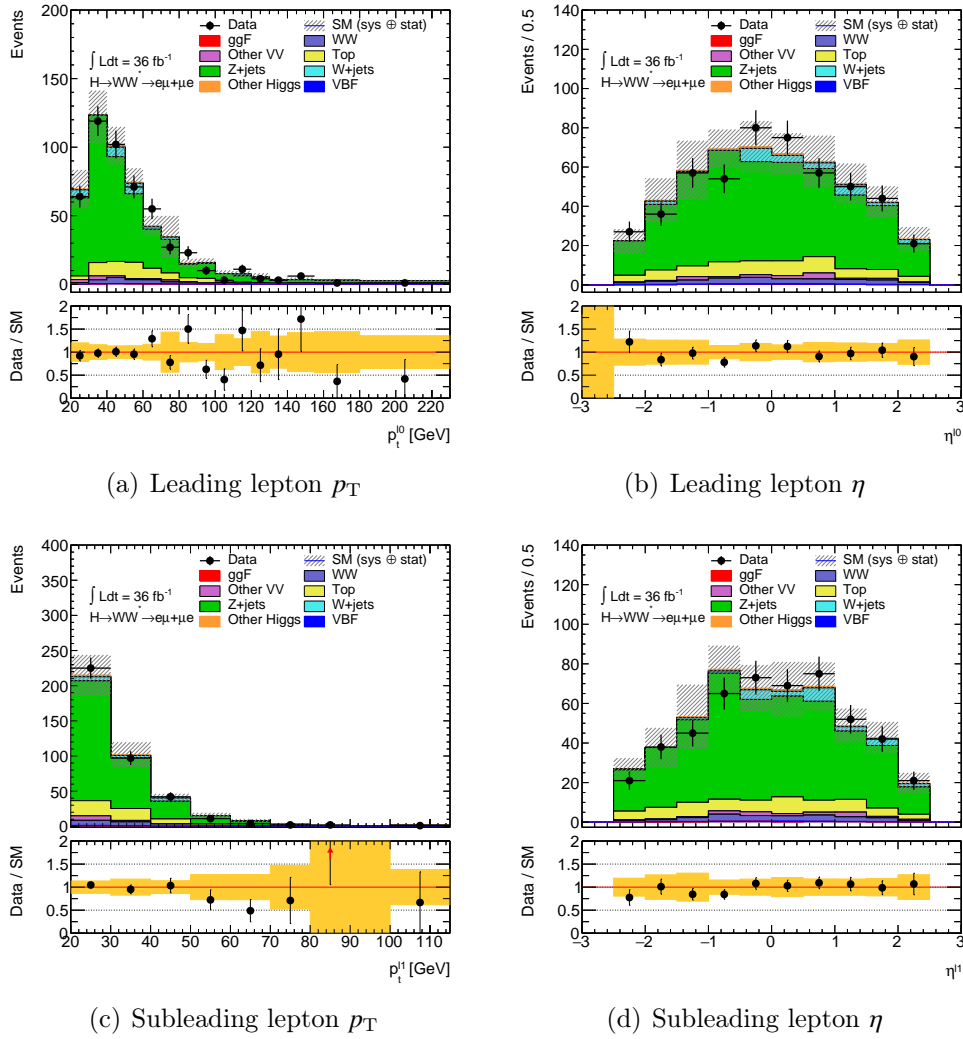
FIGURE 7.10: Pre-fit distributions for the leading and sub-leading lepton in the $Z \to \tau\tau$ control region. The top and $Z \to \tau\tau$ backgrounds are re-scaled with pre-fit normalization factors. The bottom plots show the ratio between the data and the MC. In all plots the error bands include statistic and experimental systematic uncertainties.

(a) Leading jet p_T

(b) Leading jet η

(c) Subleading jet p_T
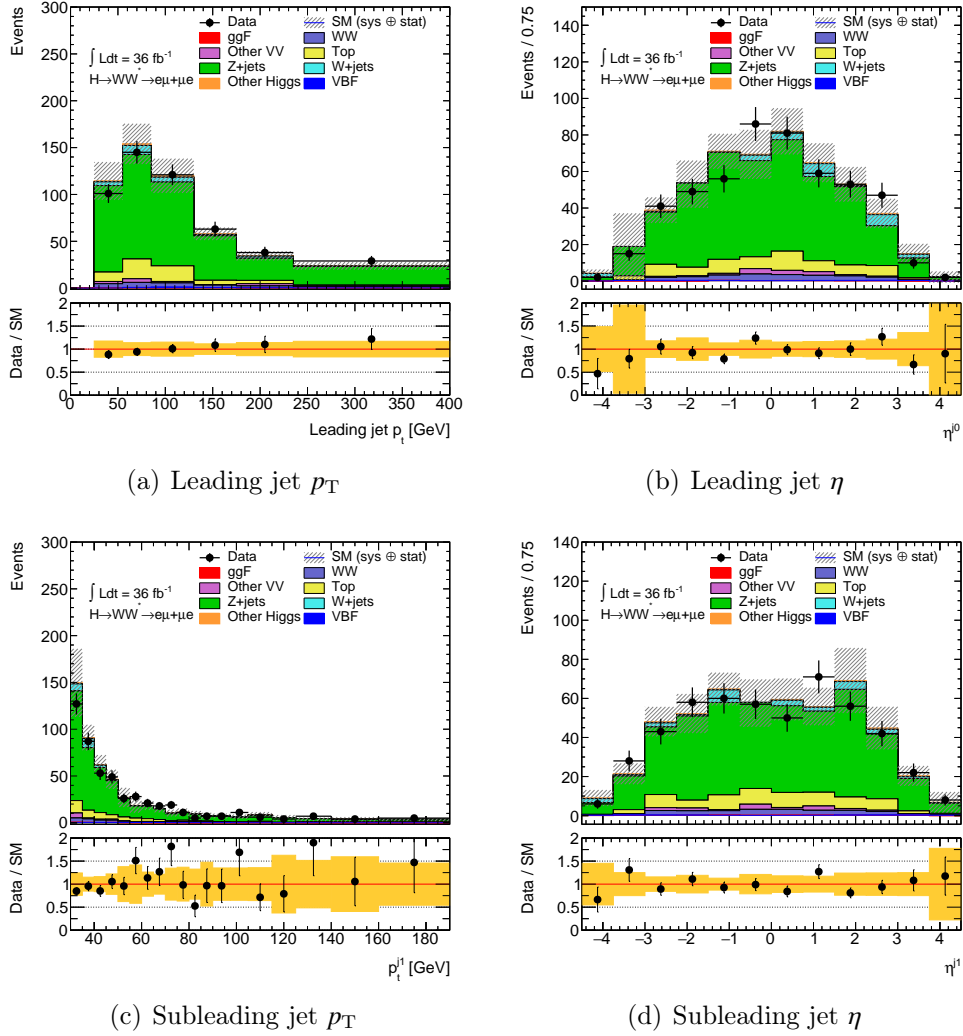
(d) Subleading jet η

FIGURE 7.11: Pre-fit distributions for the leading and subleading jet in the $Z \to \tau\tau$ control region. The top and $Z \to \tau\tau$ backgrounds are re-scaled with pre-fit normalization factors. The bottom plots show the ratio between the data and the MC. In all plots the error bands include statistic and experimental systematic uncertainties.

GeV. Figure 7.12(b) shows the m_{T2} distribution in the WW VR after the m_T cut: cutting at $m_{T2} > 160$ GeV significantly removes $t\bar{t}$ events.

Figures 7.13 and 7.14 present quality of modeling of p_T and η of leading and subleading leptons and jets. The event yields are given in Table 7.10: as might be seen, the purity of the validation region is approximately 50%.

(a) m_T

(b) m_{T2}
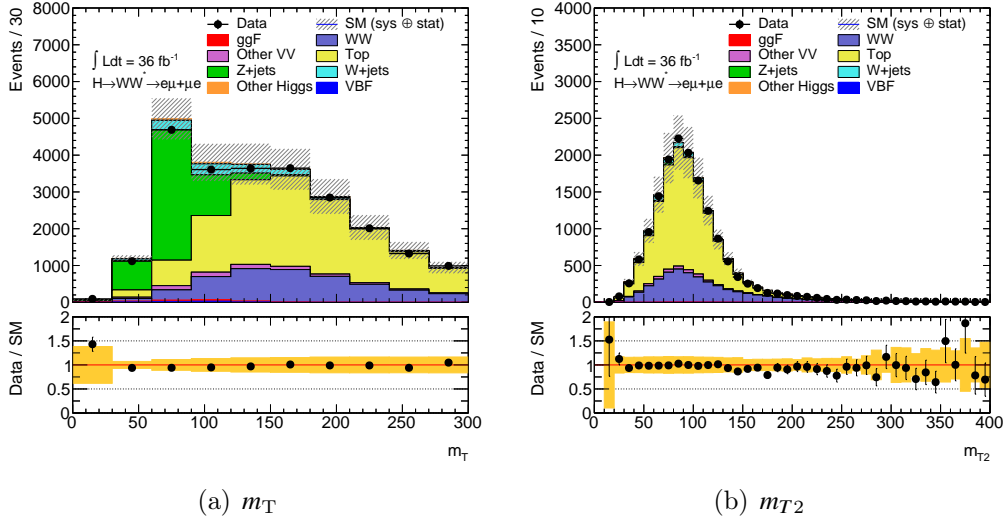
FIGURE 7.12: Pre-fit distributions of m_T at pre-selection and m_{T2} in the WW VR after the m_T cut. The bottom plot shows the ratio between the data and the Monte Carlo, and the yellow band shows the statistics and experimental systematics uncertainties.

(a) Leading lepton p_T

(b) Leading lepton η

(c) Subleading lepton p_T

(d) Subleading lepton η
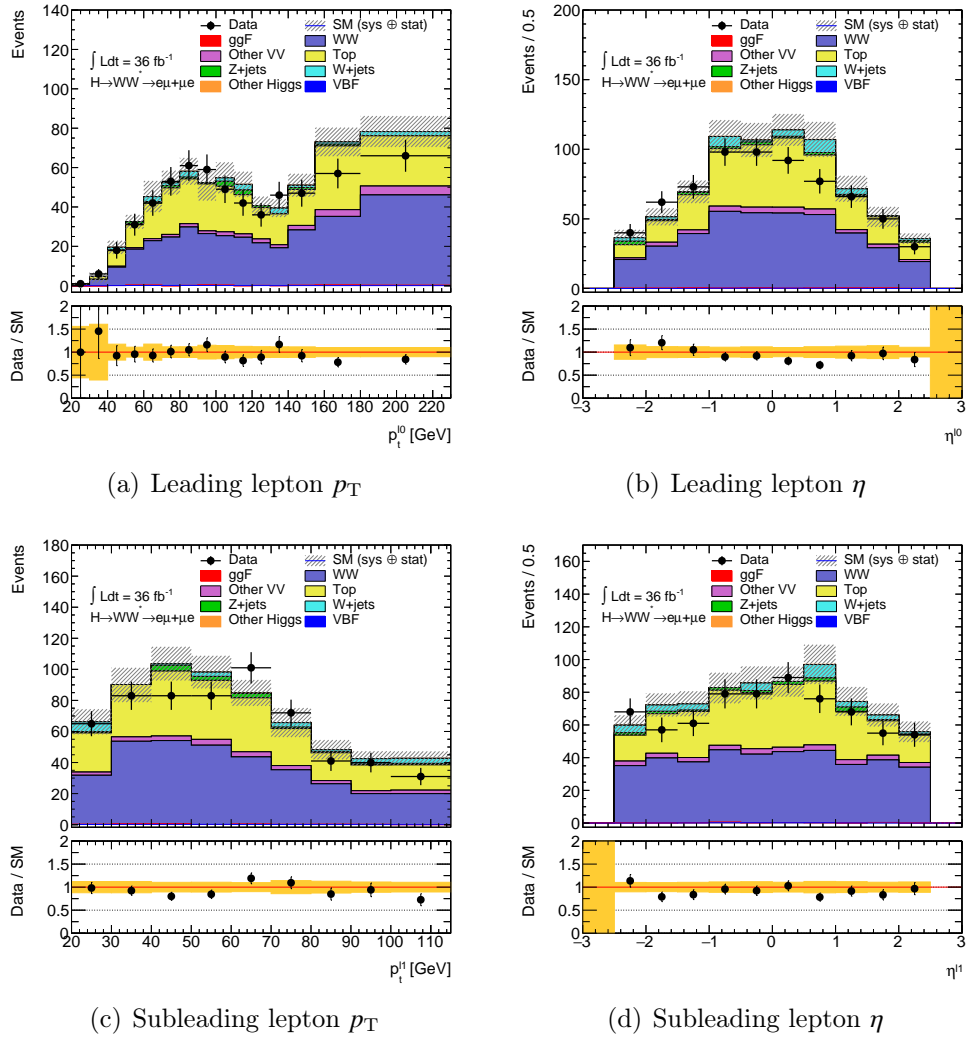
FIGURE 7.13: Pre-fit distributions for the leading and sub-leading lepton in the WW validation region. The top and $Z \to \tau\tau$ backgrounds are re-scaled with pre-fit normalization factors. The bottom plots show the ratio between the data and the MC. In all plots the error bands include statistic and experimental systematic uncertainties.

(a) Leading jet p_{T}

(b) Leading jet η

(c) Subleading jet p_{T}
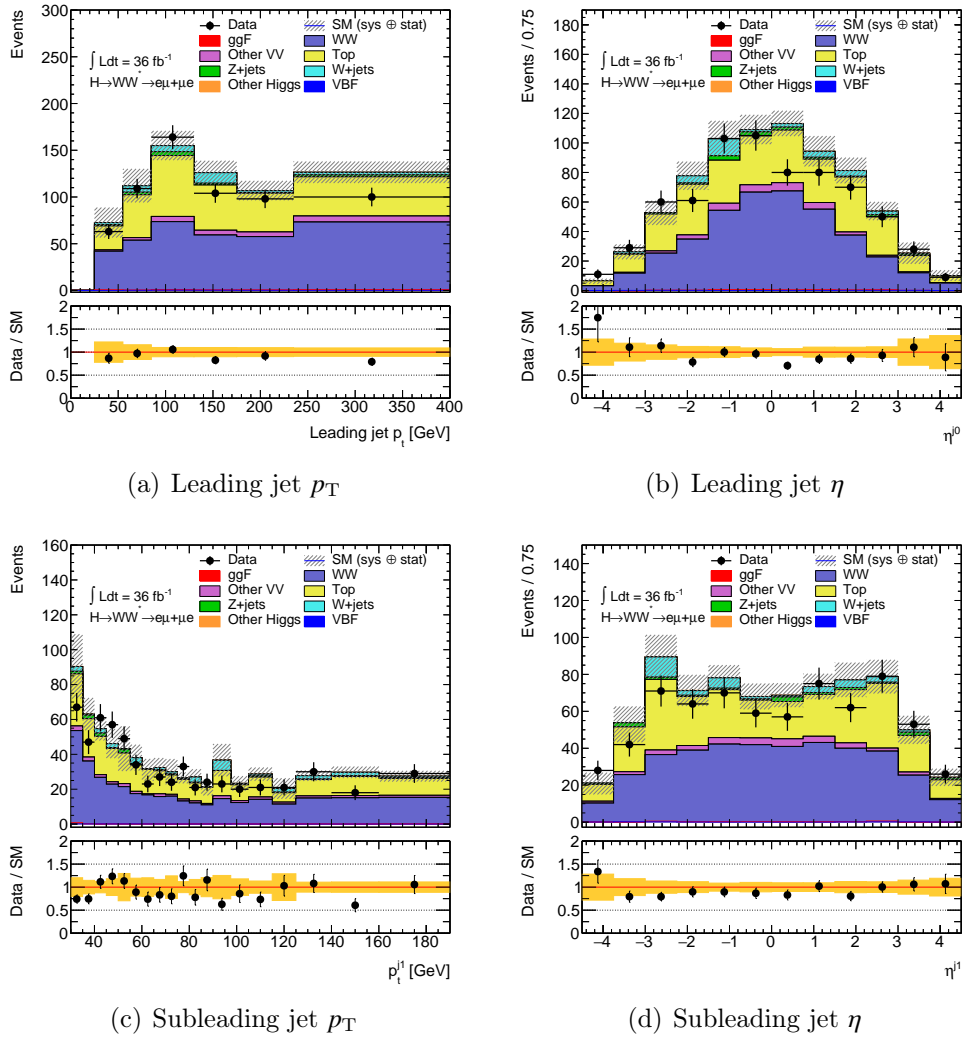
(d) Subleading jet η

FIGURE 7.14: Pre-fit distributions for the leading and sub-leading jet in the WW validation region. The top and $Z \to \tau\tau$ backgrounds are re-scaled with pre-fit normalization factors. The bottom plots show the ratio between the data and the MC. In all plots the error bands include statistic and experimental systematic uncertainties.

|	Signal region	$Z \to \tau\tau$ CR	Top-quark CR
Preselection	Two isolated leptons ($\ell = e, \mu$) with opposite charge $p_T^{\text{lead}} > 22$ GeV , $p_T^{\text{sublead}} > 15$ GeV $m_{\ell\ell} > 10$ GeV, $N_{\text{jet}} \geq 2$		
	$n_{b-jets} = 0$	$n_{b-jets} = 0$	$n_{b-jets} = 1$
A BDT is trained at this level. Eight discriminant variables are used: $\Delta\phi_{\ell\ell}$, $m_{\ell\ell}$, m_T, Δy_{jj}, m_{jj}, p_T^{tot}, $\sum_{\ell,j} m_{\ell j}$, and $\eta_\ell^{\text{centrality}}$			
Selection	$m_{\tau\tau} < 66.2$ GeV $-$	$|m_{\tau\tau} - m_Z| < 25$ GeV $m_{\ell\ell} < 80$ GeV OLV applied CJV applied	$-$ $-$

TABLE 7.12: Event selection criteria used to define the signal and control regions in the VBF analysis. Definitions including the p_T thresholds for jet counting are given in the text.

7.7 Signal Region optimization

The event selection that defines the final signal region includes:

- the VBF pre-selection, see Section 7.5;

- CJV (Central Jet Veto): Events with jets with $p_T > 20$ GeV which lie between the tagging jets in pseudo-rapidity are rejected.

- OLV (Outside Lepton Veto): The two charged leptons must have rapidity that are between the tag jets' rapidity gap, the so-called outside-lepton veto (OLV).

- $Z \to \tau\tau$-veto: In order to reduce the $Z \to \tau\tau$ background a cut that removes events around the Z mass pole is applied: $m_{\tau\tau} < m_Z - 25$GeV.

In Table 7.12 a summary of the selection in the signal and control regions is given, while the SR event yields are summarized in 7.11.

7.7.1 The Boosted Decision Tree

In order to maximize the signal over background ratio in the signal-enriched region, *boosted decision trees* (BDT's) are employed. A BDT is a set of *decisions* that aims to classify events as signal-like or background-like; it has a binary-tree structure, illustrated in Figure 7.15. A succession of positive and negative decisions, that starts from a *root node*, is completed on each single variable, until certain criteria are met. The variable that, in a given *leaf node*, gives the best separation between signal and background is employed;
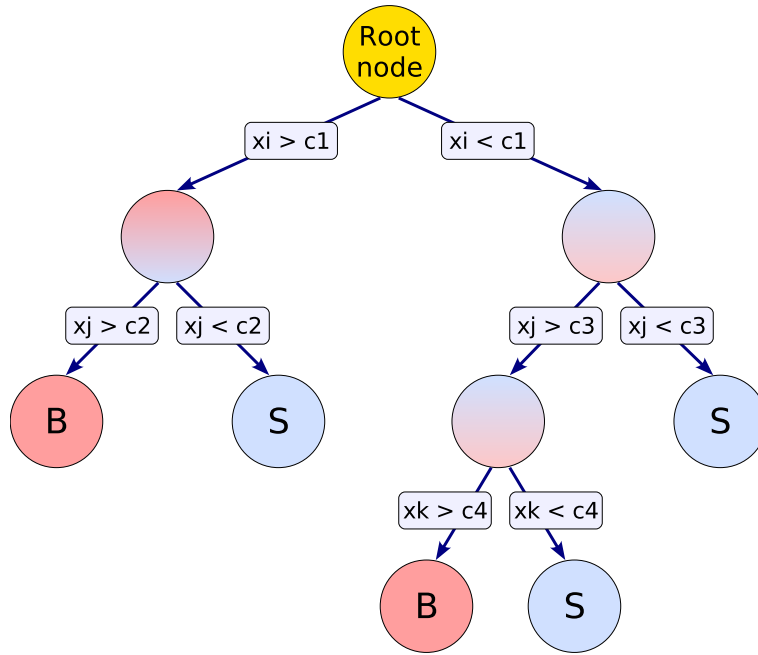
FIGURE 7.15: Sketch of a decision tree. From [122].

the same variable can be used for several splits or not used at all. The final decisions, that are at the bottom of the tree, are categorized as background or signal depending on the majority of events that they contain: therefore, an event is considered a signal event if it is in a signal-enriched leaf, and the other way around for the background ones. The procedure that extends this sequence from one tree to several trees, forming a *forest*, on re-weighted (or *boosted*) versions of the training data is called *boosting*. The boosting is used to optimize the performances of the MVA and to ensure a statistical stability of the response. The BDT output variable is built then from the weighted average of all the trees. This variable, that has a range between -1 and 1, gives the probability of an event to be signal- or background-like: a signal event would tend to be in the higher BDT bins, while a background ones in the low BDT bins.

To train a multivariate classifier, two subsamples are needed: one to perform the MVA training (*training sample*) and another one to test the classifier (*testing sample*). In order to make sure that the BDT has no dependence on the statistical fluctuations of the training sample (effect known as *over-training*), the splitting of the training and testing samples is performed on two statistically independent subsets, A and B: sample A contains all the events with even number, while sample B with odd number. Two BDTs are trained independently on A and B, respectively BDT_A and BDT_B. Afterwards, BDT_A

is tested on B and vice-versa. This procedure is usually referred to as *k-fold cross-validation*. The final BDT output discriminant is defined as:

$$\text{BDT} = \begin{cases} \text{BDT}_A & \text{for event} \in B \\ \text{BDT}_B & \text{for event} \in A \end{cases} \tag{7.17}$$

The BDT for the VBF $H \rightarrow WW^* \rightarrow \ell\nu\ell\nu$ analysis is trained using $e\mu + \mu e$ events after the VBF pre-selection. The most relevant background processes, such as top-quark, ggF, WW and $Z \rightarrow \tau\tau$ backgrounds, are included in the training, while the other backgrounds that present a smaller contribution in the SR are neglected. In the training, as signal samples, the SM $a_L = a_T = 1$ sample together with all the eight BSM samples are employed.

(a) $\Delta\phi_{\ell\ell}$ (b) $m_{\ell\ell}$

(c) Δy_{jj} (d) m_{jj}
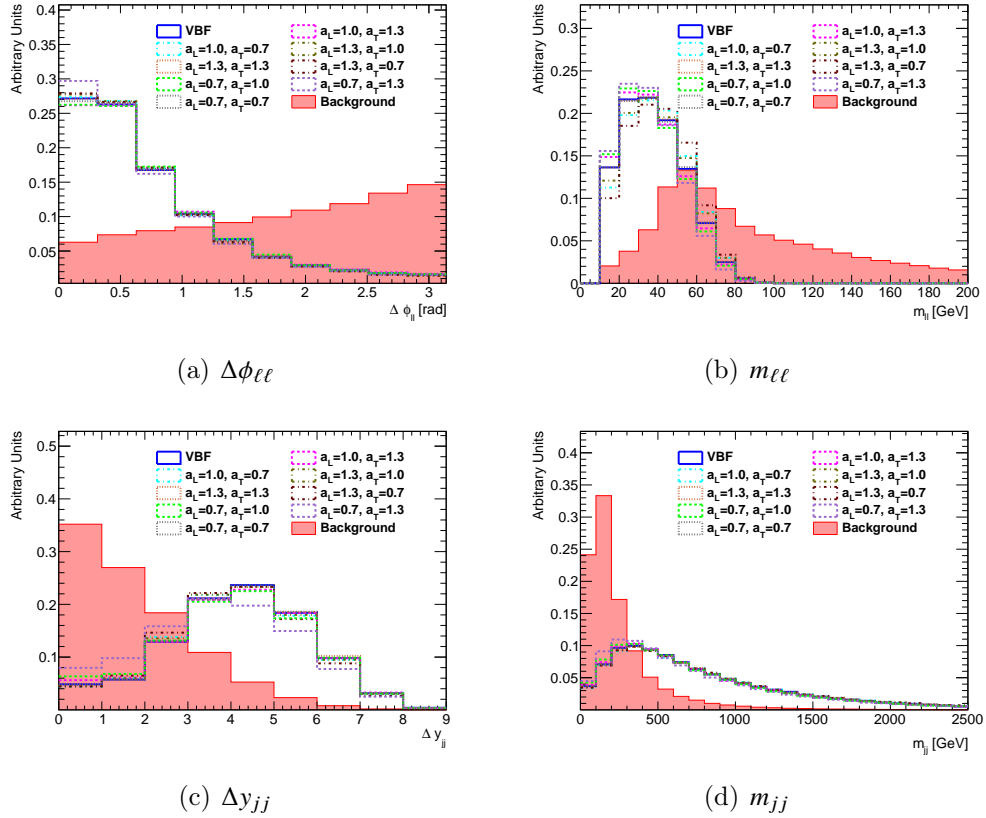
FIGURE 7.16: Normalized distributions of $\Delta\phi_{\ell\ell}$, $m_{\ell\ell}$, Δy_{jj} and m_{jj} after pre-selection, in blue for the VBF signal and in red for the total background.

BDT training The input variables (also called *features*) employed for the BDT training are: $\Delta\phi_{\ell\ell}$, $m_{\ell\ell}$, Δy_{jj}, m_{jj}, p_T^tot, m_T, lepton centrality $\eta_\ell^\text{centrality}$ and sum of invariant masses of lepton and jet $\sum_{\ell,j} m_{\ell j}$. The description of

(a) m_T

(b) $p_\mathrm{T}^\mathrm{tot}$
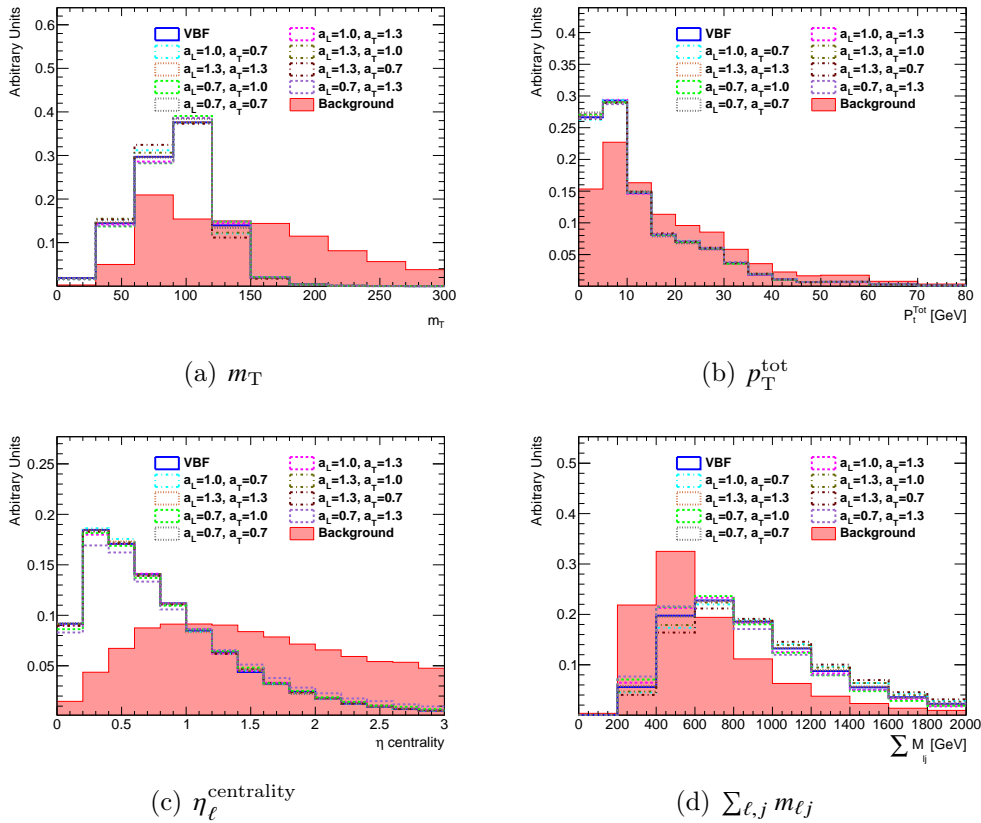
(c) $\eta_\ell^\mathrm{centrality}$

(d) $\sum_{\ell,j} m_{\ell j}$

FIGURE 7.17: Normalized distributions of m_T, $p_\mathrm{T}^\mathrm{tot}$, $\eta_\ell^\mathrm{centrality}$ and $\sum_{\ell,j} m_{\ell j}$ after pre-selection, in blue for the VBF signal and in red for the total background.

these variables has been given in the previous section. The comparison between the signal and the background distributions for each of them is given in Figures 7.16 and 7.17 after pre-selection level, where the BDT is trained. Their linear correlation is instead shown in Figures 7.18(a) for the signal samples and 7.18(b) for the background ones. As it is evident from the plots, the most correlated quantities are Δy_{jj} and m_{jj}, and smaller correlations are also present in variables related to the leptons (such as $\Delta\phi_{\ell\ell}$, $m_{\ell\ell}$ and m_T).

In order to optimize the multivariate analysis, several machine learning tools have been tested: TMVA [122], that is the default algorithm used in the HWW analysis framework [142], scikit-learn [143] and XGBoost [144]. In all these classifiers, the values of parameters of the MVA (*hyper-parameters*) are not directly learned within the estimation, but they are given as arguments to the constructor of the estimator class. To tune them, grid searches have been performed. This grid search compares the performances of classifiers trained with different hyper-parameters configurations. These performances can be estimated by studying the *Receiver Operating Characteristic*
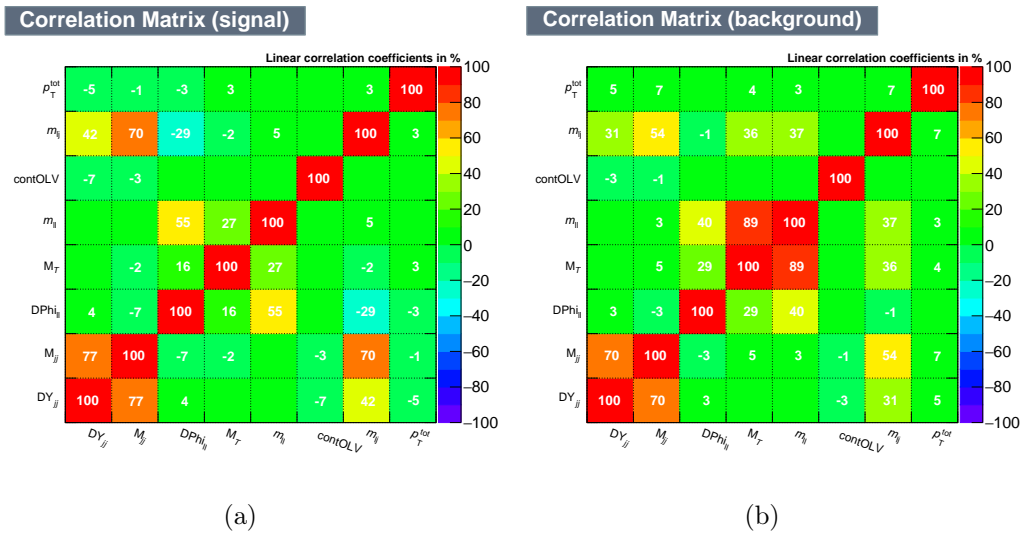
FIGURE 7.18: Features correlations for the signal and background processes.

curve, also called *ROC* curve. This distribution gives the relation between the background rejection and the signal efficiency. The area under the curve of a ROC distribution, shortened to *AUC*, defines the probability that a classifier will rank a randomly chosen signal event higher than a randomly chosen background. The grid scan compares the ROC AUC obtained with different parameters settings, returning the combination that achieve the higher AUC: the closest to 1 AUC it gets, the better discrimination is obtained with the given classifier.

For the TMVA implementation, the classifier used is the BDT with gradient boosting. The hyper-parameters studied are the number of trees (`NTrees`), the maximum depth of the decision tree allowed before further splitting is stopped (`MaxDepth`), the minimum percentage of training events in a leaf node (`MinNodeSize`), the number of steps in the optimization of the cut for a node (`nCuts`) and the learning rate for GradBoost algorithm (`Shrinkage`). The grid search spanned in the range `NTrees` in [100-800], `MaxDepth` in [2,5], `MinNodeSize` in [0.1%, 5%], `NCuts` in [10, 40] and `Shrinkage` in [0.1, 1]. A scan over 50 random combinations of these parameters has been performed, for both BDT_A and BDT_B. The optimal points resulted for `NTrees=500`, `MinNodeSize=0.3`, `Shrinkage=0.4`, `NCuts=35`, `MaxDepth=4`.

The output discriminant from TMVA is shown in Figure 7.19 for both BDT_A and BDT_B, in red for the background and in blue for signal events. With full histograms the distributions for the training data are shown, while with dotted histograms for the testing ones. An overall good agreement is observed

between the two samples: the result of the Kolmogorov-Smirnov test [145] of the equality of the two distributions is also shown. The agreement of the training and testing distributions, reinforced by the reasonable value of the KS test, indicates that there is no significant over-training.

(a) BDT distribution for BDT_A (b) BDT distribution for BDT_B
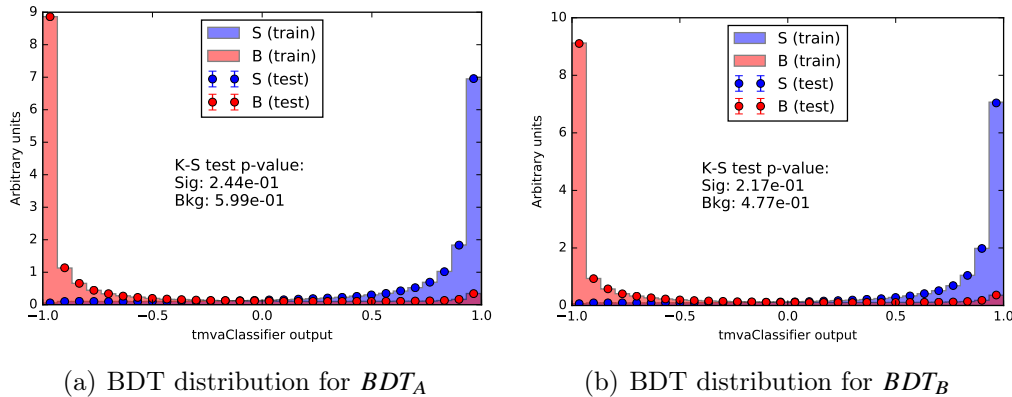
FIGURE 7.19: BDT scores for the training (histogram) and the testing (points) samples as points and as histograms, respectively for signal (blue) and background (red), for BDTs *A* (Fig 7.19(b)) and *B* (Fig 7.19(a)).

As mentioned before, the performances of TMVA have been compared to those of scikit-learn and XGBoost. For both scikit-learn and XGBoost, a grid scan over 20 combinations of the hyper-parameters have been performed, to achieve the best combination of the number of estimators, of the learning rate and of the max depth of the decision tree. Also in this case, for both scikit-learn and XGBoost the gradient boosting has been used.

The comparison of the ROC curves for these three algorithms is given in Figure 7.20. Evidently, the three MVA classifiers behave in a similar way, presenting no differences in the discrimination power, with a ROC AUC of 0.97. However, a remarkable difference is seen in the training execution time of the computation, that sees TMVA at least a factor five slower than XGBoost and scikit-learn.

The rankings of the importance of each feature are shown, as an example, for XGBoost and scikit-learn, in Figure 7.21. Usually, this scoring is performed by counting in how many nodes the variable was employed (like for the XGBoost ranking). To score Scikit-learn a weight for each utilization is assigned, that takes into account the gain in separation and the number of events in each node.

Final discriminant and binning optimization   The final BDT used in the analysis is the BDT trained for the cross-section measurement in VBF.
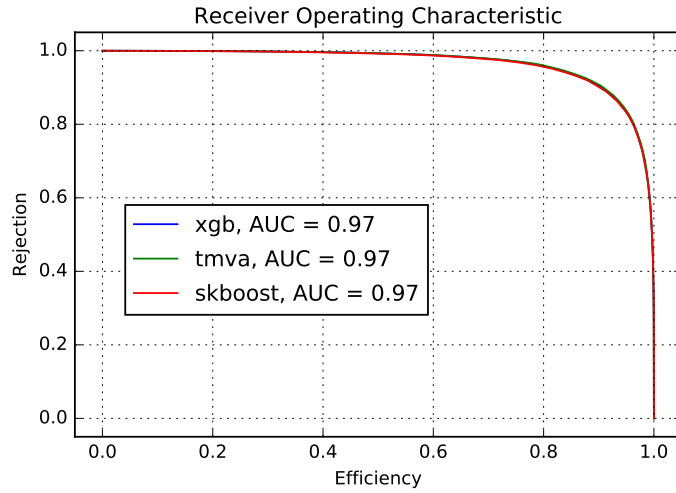
FIGURE 7.20: Comparison of the ROC curves for the three different algorithms studied, TMVA (in green), scikit-learn (in red) and XGBoost (in blue).
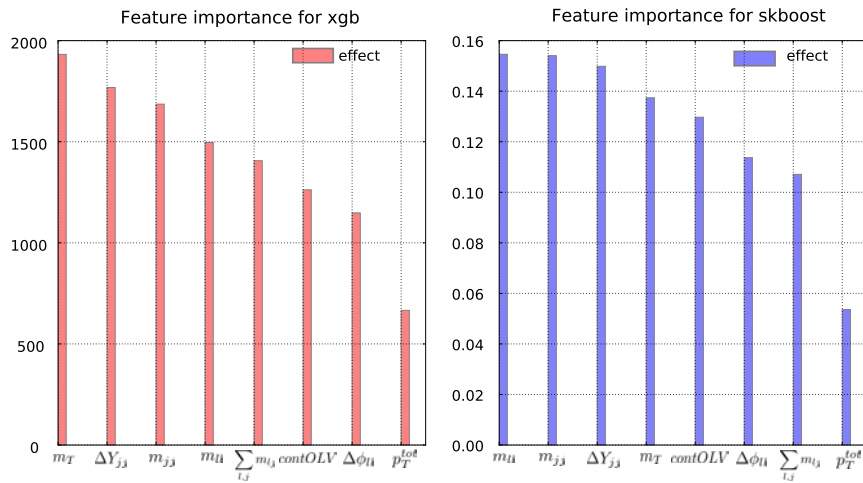
FIGURE 7.21: Ranking of the feature importances for scikit-learn and XGBoost. The higher, the more important is the feature.

The main difference, with respect to the training described in the previous section, is that this training is performed employing a POWHEG +PYTHIA 8 VBF NLO sample as signal sample. The scikit-learn tool is used to build the BDT distribution. Also in this case, the boosting algorithm is employed, while the hyper-parameters chosen are summarized in Table 7.13. This BDT shows a slightly lower, but overall very similar, discrimination efficiency with respect of the previously discussed training, presenting a ROC AUC of 0.96.

Parameter	Value
Boosting algorithm	Gradient
Maximum tree depth	5
Number of trees	200
Minimum number of events required per node	5%
Learning rate	0.1

TABLE 7.13: BDT hyper-parameters used for the scikit-learn training.

The BDT output distribution is shown in Figure 7.22(a) in the VBF signal region for all the background processes and the VBF signal one.

In order to optimize the binning of the BDT output distribution, the following procedure has been followed. A scan is performed on the BDT to find the boundaries that provide the best significance; once the first boundary is found, the procedure is iterated starting from the first boundary to get a second one. This is repeated iteratively until no additional gain is achieved in the significance. The significance used for the scan is defined in the following way [146]:

$$Sig = \frac{N_S}{\sqrt{N_S + N_B + \Delta N_B^2}} \tag{7.18}$$

where N_S is the signal yield, N_B is the total background yield and ΔN_B is the statistical uncertainty of the sum of the backgrounds. This is considered in the definition of the significance because the analysis is highly affected by the MC statistic uncertainty. The optimal binning configuration found is the following: [-1,0.26,0.61,0.86,1] and the distribution is shown in Figure 7.22(b).
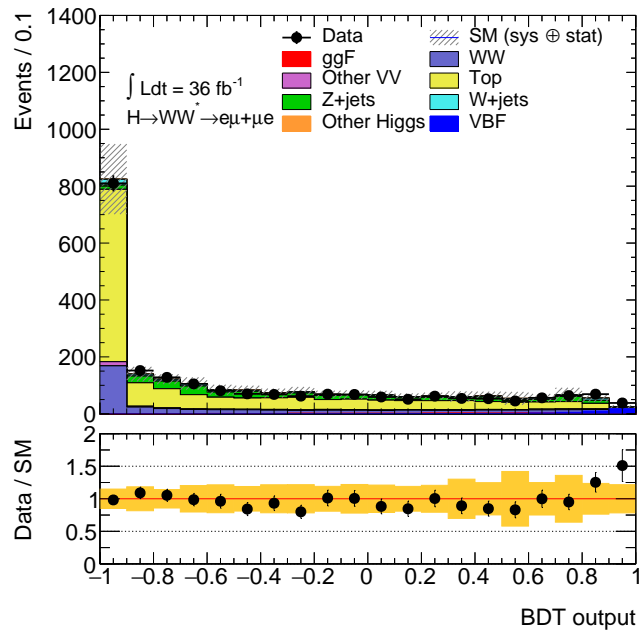
(a)
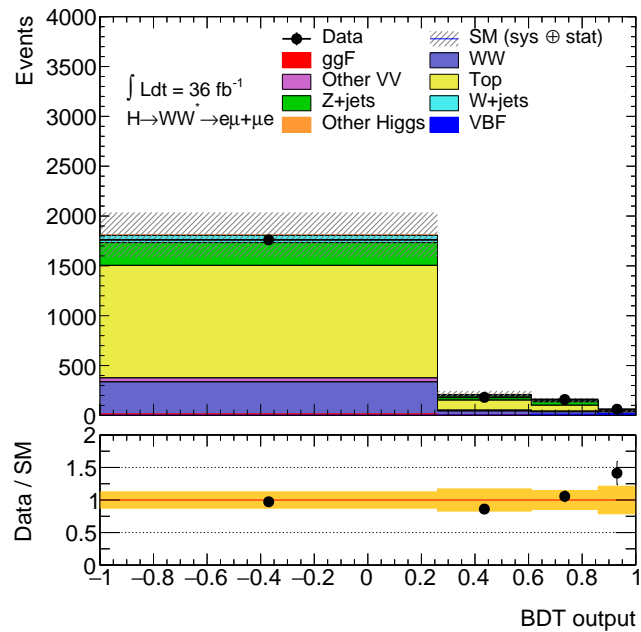
(b)

FIGURE 7.22: Pre-fit distribution of the BDT output in the VBF SR, before 7.22(a) and after 7.22(b) the optimal binning scan. The top and $Z \to \tau\tau$ backgrounds are re-scaled with pre-fit normalization factors. The bottom plots show the ratio between the data and the MC. In all plots the error bands include statistic and experimental systematic uncertainties.

7.7.2   The discriminating variable

After the BDT training and the signal region selection, the discriminating power of $\Delta\phi_{jj}$ with respect to different BSM signals is verified. In Figures 7.23(a) and 7.23(b) the $\Delta\phi_{jj}$ distributions for different a_L and a_T pairs in the VBF signal region, after the $Z \to \tau\tau$ veto, are shown. On the left hand side, the distributions are normalized to the number of events, while on the right hand side to unity. Even after the VBF selection, the BSM coupling parameters still leave a clear signature in the shape of the distribution, especially for the cases where $a_L \neq a_T$. The modeling of the $\Delta\phi_{jj}$ distribution in
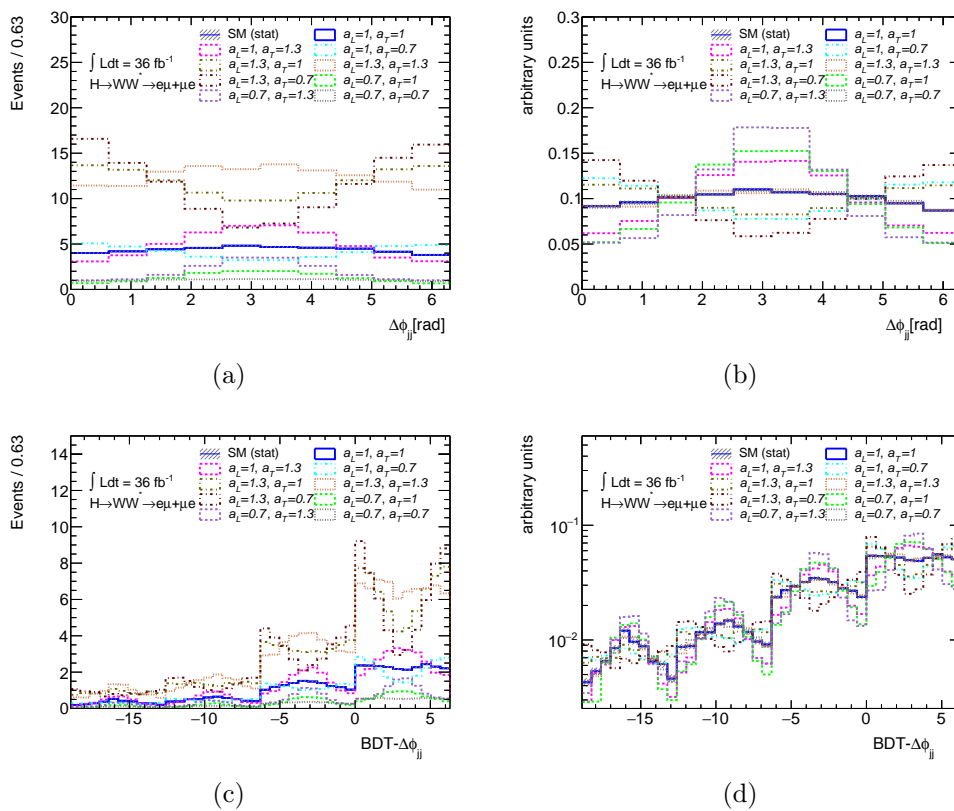
FIGURE 7.23: Figures 7.23(a) and 7.23(b) show the $\Delta\phi_{jj}$ distribution in the SR, after the $Z \to \tau\tau$ veto, for different (a_L, a_T) pairs: the black solid line is the SM case where $a_L = a_T = 1$, while the colored dotted lines are the 8 BSM cases with $\pm30\%$ variations. The distributions in the plot on the left are normalized to the number of events, while on the right to unity to better show the shape differences. Instead, Figures 7.23(c) and 7.23(d) show the BDT-$\Delta\phi_{jj}$ distribution in the SR, after the $Z \to \tau\tau$ veto, also in this case for different (a_L, a_T) values, employing the same color notation. In this case as well, the distributions in the plot on the left are normalized to the number of events, while on the right to unity.

the signal region, in the control regions and in the WW validation region is given in Figures 7.24. An overall good agreement is observed between data and MC predictions.

The final discriminant for the study of the Higgs couplings to polarized vec-

(a) $\Delta\phi_{jj}$ in the Top CR

(b) $\Delta\phi_{jj}$ in the $Z \rightarrow \tau\tau$ CR

(c) $\Delta\phi_{jj}$ in the WW VR
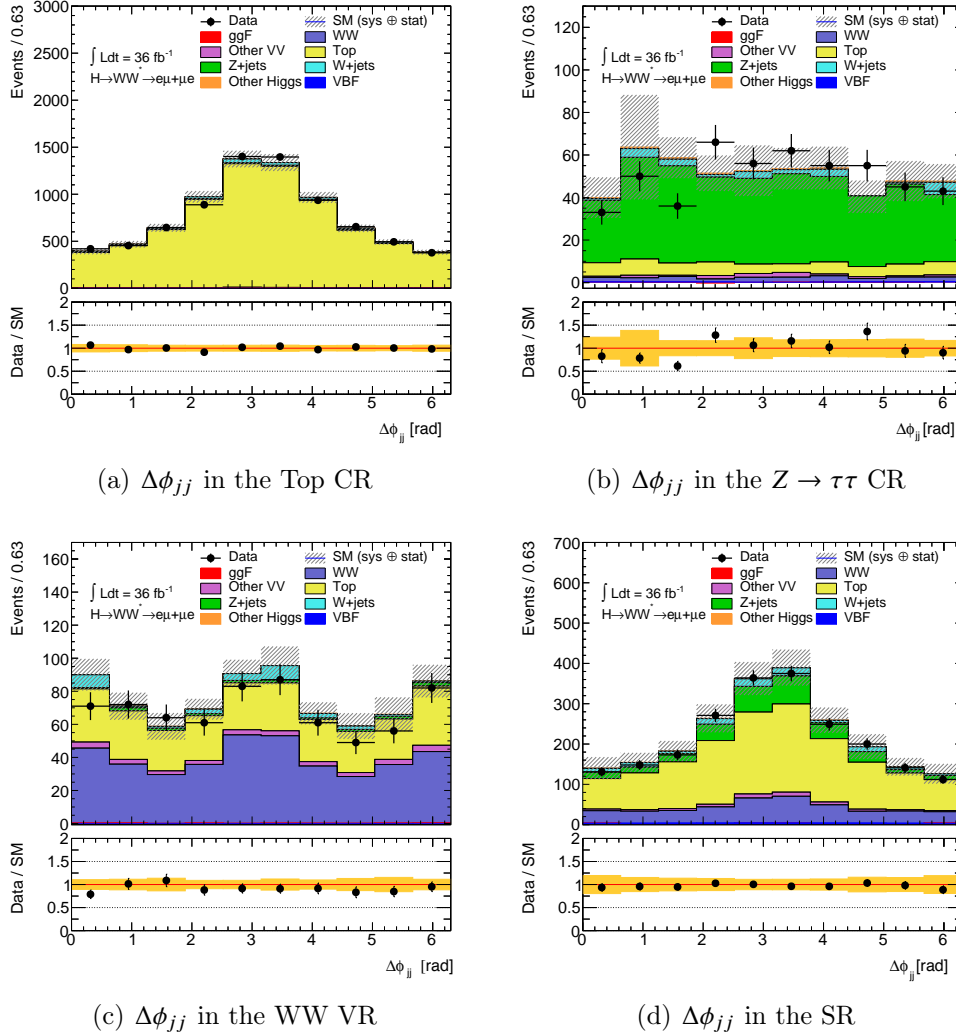
(d) $\Delta\phi_{jj}$ in the SR

FIGURE 7.24: Pre-fit distribution of $\Delta\phi_{jj}$ in the various control/validation regions and in the signal region. In the plots, the top and $Z \rightarrow \tau\tau$ backgrounds are re-scaled with pre-fit normalization factors. The bottom plots show the ratio between the data and the MC. In all plots the error bands include statistic and experimental systematic uncertainties.

tor bosons is the convolution of the BDT output and of the $\Delta\phi_{jj}$ distribution. This quantity shows the $\Delta\phi_{jj}$ distribution in each one of the four BDT bins: the lower BDT bins are on the left-hand side of the distributions, the higher on the right-hand side. The mapping between the bin numbers of the unrolled $BDT - \Delta\phi_{jj}$ distribution and the corresponding BDT, $\Delta\phi_{jj}$ intervals is given in Table 7.14. The distribution in the VBF SR for the different polarized
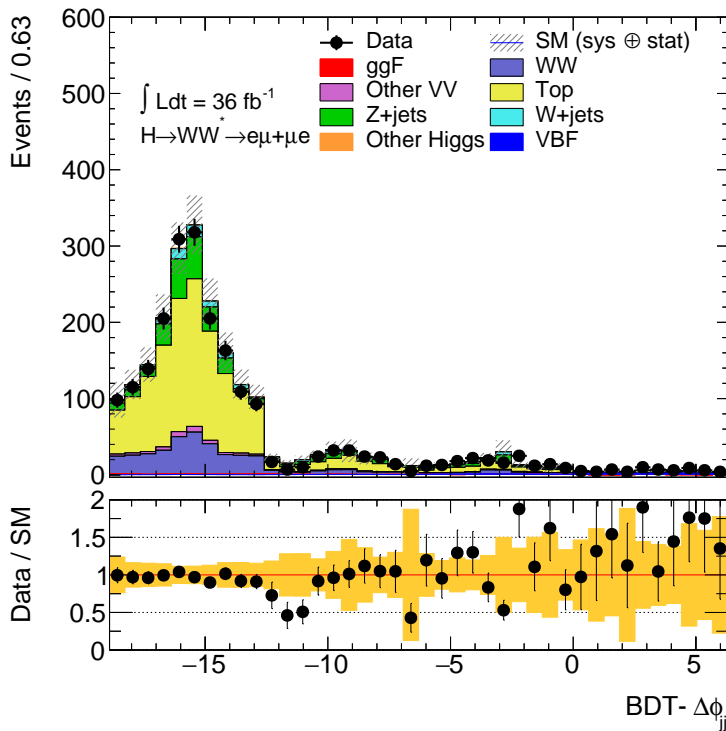
FIGURE 7.25: Pre-fit distribution of the BDT-$\Delta\phi_{jj}$ variable in the VBF SR. The bottom plot shows the data/MC ratio and the yellow band represents the statistic and experimental systematic uncertainty.

samples is shown in Figures 7.23(c), normalized to the number of events, and in Figure 7.23(d), normalized to unity. In all four BDT bins the differences in the $\Delta\phi_{jj}$ distribution for the various BSM scenarios are still visible, especially in the highest two bins, that are signal enriched-ones. Figure 7.25 shows, instead, the pre-fit distribution in the VBF SR for the SM signal, all the background processes and the data. Only statistic and experimental systematics are shown in the plot. With the addition of theory uncertainties, discussed in Section 7.8.2, the data-MC ratio will be fully covered by the errors.

As it will be discussed in Chapter 8, for the measurement of the VBF cross-section the shape of the BDT output, shown in Figure 7.22(b), is employed to fit to the data, while, for the polarized couplings studies the convolution of the BDT distribution and of $\Delta\phi_{jj}$ (Fig. 7.25) is used.

Bin number	x-axis value	BDT response	$\Delta\phi_{jj}$
1. bin	$-18.9 < x < -18.27$	$-1.00 < BDT < 0.26$	$0.0\pi < \Delta\phi_{jj} < 0.2\pi$
2. bin	$-18.27 < x < -17.64$	$-1.00 < BDT < 0.26$	$0.2\pi < \Delta\phi_{jj} < 0.4\pi$
3. bin	$-17.64 < x < -17.01$	$-1.00 < BDT < 0.26$	$0.4\pi < \Delta\phi_{jj} < 0.6\pi$
4. bin	$-17.01 < x < -16.38$	$-1.00 < BDT < 0.26$	$0.6\pi < \Delta\phi_{jj} < 0.8\pi$
5. bin	$-16.38 < x < -15.75$	$-1.00 < BDT < 0.26$	$0.8\pi < \Delta\phi_{jj} < 1.0\pi$
6. bin	$-15.75 < x < -15.12$	$-1.00 < BDT < 0.26$	$1.0\pi < \Delta\phi_{jj} < 1.2\pi$
7. bin	$-15.12 < x < -14.49$	$-1.00 < BDT < 0.26$	$1.2\pi < \Delta\phi_{jj} < 1.4\pi$
8. bin	$-14.49 < x < -13.86$	$-1.00 < BDT < 0.26$	$1.4\pi < \Delta\phi_{jj} < 1.6\pi$
9. bin	$-13.86 < x < -13.23$	$-1.00 < BDT < 0.26$	$1.6\pi < \Delta\phi_{jj} < 1.8\pi$
10. bin	$-13.23 < x < -12.6$	$-1.00 < BDT < 0.26$	$1.8\pi < \Delta\phi_{jj} < 2.0\pi$
11. bin	$-12.6 < x < -11.97$	$0.26 < BDT < 0.61$	$0.0\pi < \Delta\phi_{jj} < 0.2\pi$
12. bin	$-11.97 < x < -11.34$	$0.26 < BDT < 0.61$	$0.2\pi < \Delta\phi_{jj} < 0.4\pi$
13. bin	$-11.34 < x < -10.71$	$0.26 < BDT < 0.61$	$0.4\pi < \Delta\phi_{jj} < 0.6\pi$
14. bin	$-10.71 < x < -10.08$	$0.26 < BDT < 0.61$	$0.6\pi < \Delta\phi_{jj} < 0.8\pi$
15. bin	$-10.08 < x < -9.45$	$0.26 < BDT < 0.61$	$0.8\pi < \Delta\phi_{jj} < 1.0\pi$
16. bin	$-9.45 < x < -8.82$	$0.26 < BDT < 0.61$	$1.0\pi < \Delta\phi_{jj} < 1.2\pi$
17. bin	$-8.82 < x < -8.19$	$0.26 < BDT < 0.61$	$1.2\pi < \Delta\phi_{jj} < 1.4\pi$
18. bin	$-8.19 < x < -7.56$	$0.26 < BDT < 0.61$	$1.4\pi < \Delta\phi_{jj} < 1.6\pi$
19. bin	$-7.56 < x < -6.93$	$0.26 < BDT < 0.61$	$1.6\pi < \Delta\phi_{jj} < 1.8\pi$
20. bin	$-6.93 < x < -6.3$	$0.26 < BDT < 0.61$	$1.8\pi < \Delta\phi_{jj} < 2.0\pi$
21. bin	$-6.3 < x < -5.67$	$0.61 < BDT < 0.86$	$0.0\pi < \Delta\phi_{jj} < 0.2\pi$
22. bin	$-5.67 < x < -5.04$	$0.61 < BDT < 0.86$	$0.2\pi < \Delta\phi_{jj} < 0.4\pi$
23. bin	$-5.04 < x < -4.41$	$0.61 < BDT < 0.86$	$0.4\pi < \Delta\phi_{jj} < 0.6\pi$
24. bin	$-4.41 < x < -3.78$	$0.61 < BDT < 0.86$	$0.6\pi < \Delta\phi_{jj} < 0.8\pi$
25. bin	$-3.78 < x < -3.15$	$0.61 < BDT < 0.86$	$0.8\pi < \Delta\phi_{jj} < 1.0\pi$
26. bin	$-3.15 < x < -2.52$	$0.61 < BDT < 0.86$	$1.0\pi < \Delta\phi_{jj} < 1.2\pi$
27. bin	$-2.52 < x < -1.89$	$0.61 < BDT < 0.86$	$1.2\pi < \Delta\phi_{jj} < 1.4\pi$
28. bin	$-1.89 < x < -1.26$	$0.61 < BDT < 0.86$	$1.4\pi < \Delta\phi_{jj} < 1.6\pi$
29. bin	$-1.26 < x < -0.63$	$0.61 < BDT < 0.86$	$1.6\pi < \Delta\phi_{jj} < 1.8\pi$
30. bin	$-0.63 < x < 0.0$	$0.61 < BDT < 0.86$	$1.8\pi < \Delta\phi_{jj} < 2.0\pi$
31. bin	$0.0 < x < 0.63$	$0.86 < BDT < 1.00$	$0.0\pi < \Delta\phi_{jj} < 0.2\pi$
32. bin	$0.63 < x < 1.26$	$0.86 < BDT < 1.00$	$0.2\pi < \Delta\phi_{jj} < 0.4\pi$
33. bin	$1.26 < x < 1.89$	$0.86 < BDT < 1.00$	$0.4\pi < \Delta\phi_{jj} < 0.6\pi$
34. bin	$1.89 < x < 2.52$	$0.86 < BDT < 1.00$	$0.6\pi < \Delta\phi_{jj} < 0.8\pi$
35. bin	$2.52 < x < 3.15$	$0.86 < BDT < 1.00$	$0.8\pi < \Delta\phi_{jj} < 1.0\pi$
36. bin	$3.15 < x < 3.78$	$0.86 < BDT < 1.00$	$1.0\pi < \Delta\phi_{jj} < 1.2\pi$
37. bin	$3.78 < x < 4.41$	$0.86 < BDT < 1.00$	$1.2\pi < \Delta\phi_{jj} < 1.4\pi$
38. bin	$4.41 < x < 5.04$	$0.86 < BDT < 1.00$	$1.4\pi < \Delta\phi_{jj} < 1.6\pi$
39. bin	$5.04 < x < 5.67$	$0.86 < BDT < 1.00$	$1.6\pi < \Delta\phi_{jj} < 1.8\pi$
40. bin	$5.67 < x < 6.3$	$0.86 < BDT < 1.00$	$1.8\pi < \Delta\phi_{jj} < 2.0\pi$

TABLE 7.14: Mapping between the bin numbers of the unrolled $BDT - \Delta\phi_{jj}$ distribution and the corresponding BDT, $\Delta\phi_{jj}$ intervals.

7.8   Systematic uncertainties

Both measurements of the VBF cross-section and of the couplings to polarized vector bosons are affected by systematic uncertainties arising from various sources. These systematic uncertainties can be split in two categories: *experimental* uncertainties associated to the experimental measurements, such as reconstruction, identification and trigger efficiencies and the scale and resolution of energy and momentum and *theoretical* uncertainties arising form the modeling of the backgrounds and signal processes. The first ones are discussed in Section 7.8.1, while the second ones in Section 7.8.2.

7.8.1   Experimental uncertainties

The main sources of experimental uncertainties are due to inefficiencies in the identification and in the reconstruction of the physical objects and to detector limitations. A summary of these uncertainties is given in Table 7.15, while the effect of the main experimental ones on the signal region yields is given in Table 7.16.

Jet uncertainties: Jet uncertainties can be split in two main components: jet energy scale (JES) and jet energy resolution (JER) uncertainties. The first ones are a collection of several uncertainties measured as a function of the jet p_T and $|\eta|$ using dedicated methods [147]. The uncertainties considered in this analysis are derived from various dijet-p_T-balance measurements and from in-situ calibration techniques. The jet calibration results can be affected by the presence of nearby jets and pile-up contributions. As well, the different response of the calorimeter to gluon and light quark jets, the modeling of b-hadron decays and presence of neutrinos in heavy-flavor hadron decays, can alter the JES predictions. A good agreement is found in the measurements of the JER in data and in simulation [148]. Therefore, no corrections are applied to simulated jets but the impact of the JER uncertainties on the measurements is estimated with a smearing procedure on the transverse momenta of the simulated jets, that depends on the p_T and $|\eta|$ of the jet.
An uncertainty on the performances of the JVT cut is also assigned. The JVT is corrected to the data using $Z \to \mu\mu$+jets events. This uncertainty is estimated as a function of the jet p_T and separate uncertainties are considered for central ($|\eta| < 2.4$) and forward jets ($2.4 < |\eta| < 4.5$).

b-**tagging uncertainties:** Data-to-simulation scale factors are calculated to correct the performances of the MV2c10 algorithm for simulated *b*-, *c*- and light-flavor jets. These factors are obtained using combinatorial likelihood methods, tag-and-probe, D^* and the negative tag methods as described in [149]. For each jet-flavor, the uncertainties of these scale factors are described by independent eigenvectors, that also take into account their correlations. Furthermore, an uncertainty is assigned on the *b*-tagging of the τ jets; another uncertainty, instead, covers the extrapolation effects for high-p_{T} jets.

Pile-up: The uncertainty is calculated by modifying the default value of the data scale factor for the pileup $< \mu >$, varying it up and down by a factor equal to the scale factor uncertainty, and re-evaluating the re-weighting factors.

Lepton uncertainties: The tag-and-probe method in $Z \to \ell\ell$ events is used to estimate the uncertainties on reconstruction and identification of the leptons and on trigger efficiencies. Correction factors are calculated to make the simulation prediction agree to the data. The $Z \to \ell\ell$ events are also used to estimate the uncertainties on the lepton momentum and energy scales and resolutions.

E_T^{miss} **uncertainties:** The uncertainties associated to the scaling and smearing of the leptons and jet energies and momenta also affect the calculation of the missing transverse momentum. This has to be taken into account in the E_T^{miss} calculation as an uncertainty. Moreover, the presence of low-p_{T} pile-up jets and underlying event activity give rise to uncertainties on the soft term components.

Luminosity: The integrated luminosity is estimated from a preliminary calibration of the luminosity scale using van der Meer beam-separation scans, following a methodology detailed in Ref. [150]. The scans were performed in August 2015 and May 2016 using 3.2 fb^{-1} data collected in 2015 and 2.6 fb^{-1} data from 2016, for a total of 5.8 fb^{-1}. The uncertainties on the luminosity values for 2015 and 2016 are 2.1% and 3.7%, respectively. The uncertainty on the total luminosity is 2.0%, obtained by combining the single uncertainties as uncorrelated.

Systematic uncertainty	Description
Object	
Luminosity	uncertainty on total integrated luminosity
Pileup Reweighting	uncertainty on pileup reweighting
Electrons	
EL_EFF_Trigger_Total_1NPCOR_PLUS_UNCOR	trigger efficiency uncertainty
EL_EFF_Reco_Total_1NPCOR_PLUS_UNCOR	reconstruction efficiency uncertainty
EL_EFF_ID_CorrUncertaintyNP (0 to 14)	ID efficiency uncertainty splits in 15 components
EL_EFF_ID_SIMPLIFIED_UncorrUncertaintyNP (0 to 15)	ID efficiency uncertainty splits in 16 components
EL_EFF_Iso_Total_1NPCOR_PLUS_UNCOR	isolation efficiency uncertainty
EG_SCALE_ALLCORR	
EG_SCALE_E4SCINTILLATOR	
EG_SCALE_LARTEMPERATURE_EXTRA2015PRE	energy scale uncertainty
EG_SCALE_LARTEMPERATURE_EXTRA2016PRE	
EG_SCALE_LARCALIB_EXTRA2015PRE	
EG_RESOLUTION_ALL	energy resolution uncertainty
Muons	
MUON_EFF_TrigStatUncertainty	trigger efficiency uncertainty
MUON_EFF_TrigSystUncertainty	
MUON_EFF_STAT	reconstruction and ID efficiency
MUON_EFF_SYS	uncertainty for muons with $p_\mathrm{T} > 15$ GeV
MUON_ISO_STAT	isolation efficiency uncertainty
MUON_ISO_SYS	
MUON_TTVA_STAT	track-to-vertex association efficiency uncertainty
MUON_TTVA_SYS	
MUON_ID	momentum resolution uncertainty from inner detector
MUON_MS	momentum resolution uncertainty from muon system
MUON_SCALE	momentum scale uncertainty
Jets	
JES_EffectiveNP_1	
JES_EffectiveNP_2	
JES_EffectiveNP_3	
JES_EffectiveNP_4	energy scale uncertainty from
JES_EffectiveNP_5	the in situ analyses splits into 8 components
JES_EffectiveNP_6	
JES_EffectiveNP_7	
JES_EffectiveNP_8restTerm	
JES_SingleParticle_HighPt	energy scale uncertainty
	from the behavior of high-p_T jets
JES_PunchThrough_MC15	energy scale uncertainty
	for punch-through jets
JES_BJES_Response	energy scale uncertainty on b-jets
JES_Flavor_Response	energy scale uncertainty
	on samples' flavor response
JES_Flavor_Composition	energy scale uncertainty
	on flavor composition
JES_Pileup_RhoTopology	energy scale uncertainty
	on pile-up (density ρ)
JES_Pileup_PtTerm	energy scale uncertainty on pile-up (pt term)
JES_Pileup_PtTerm	energy scale uncertainty on pile-up (pt term)
JES_Pileup_OffsetNPV	energy scale uncertainty on pile-up (NPV dependent)
JES_Pileup_OffsetNPV	energy scale uncertainty on pile-up (NPV dependent)
JES_Pileup_OffsetMu	energy scale uncertainty on pile-up (mu dependent)
JES_Pileup_OffsetMu	energy scale uncertainty on pile-up (mu dependent)
JES_EtaIntercalibration_NonClosure	energy scale uncertainty on eta-intercalibrations (non-closure)
JES_EtaIntercalibration_NonClosure	energy scale uncertainty on eta-intercalibrations (non-closure)
JES_EtaIntercalibration_TotalStat	energy scale uncertainty on eta-intercalibrations (statistics/method)
JES_EtaIntercalibration_TotalStat	energy scale uncertainty on eta-intercalibrations (statistics/method)
JES_EtaIntercalibration_Modeling	energy scale uncertainty on eta-intercalibration (modeling)
JES_EtaIntercalibration_Modeling	energy scale uncertainty on eta-intercalibration (modeling)
JER_SINGLE_NP	energy resolution uncertainty
JvtEfficiency	JVT efficiency uncertainty
FT_EFF_Eigen_B	b-tagging efficiency uncertainties ("BTAG_MEDIUM"): 3
FT_EFF_Eigen_C	components for b jets, 4 for c jets and 5 for light jets
FT_EFF_Eigen_L	
FT_EFF_Eigen_extrapolation	b-tagging efficiency uncertainty on the extrapolation to high-p_T jets
FT_EFF_Eigen_extrapolation_from_charm	b-tagging efficiency uncertainty on tau jets
MET	
MET_SoftTrk_ResoPara	track-based soft term related longitudinal resolution uncertainty
MET_SoftTrk_ResoPerp	track-based soft term related transverse resolution uncertainty
MET_SoftTrk_Scale	track-based soft term related longitudinal scale uncertainty

TABLE 7.15: Summary of the experimental systematic uncertainties.

Systematic uncertainty	yield variation [%]
FT_EFF_Eigen_B_0	9.69
JER	4.82
JES_Flavor_Comp	2.57
FT_EFF_Eigen_B_1	2.47
JES_EtaInter_Model	1.72
FT_EFF_Eigen_B_2	1.59
HWW_FakeFactor_mu_EWSUBTR	1.44
MUON_EFF_SYS	1.10
JES_PU_PtTerm	1.03
FT_EFF_Eigen_Light_0	0.91
JES_Flavor_Resp	0.78
MET_SoftTrk_ResoPerp	0.76
MET_SoftTrk_Scale	0.64
FT_EFF_Eigen_C_0	0.60
MET_SoftTrk_ResoPara	0.51
JES_EtaInter_NonClosure	0.48
EL_EFF_ID_CorrUncertainty_NP14	0.47
HWW_FakeFactor_mu_SAMPLECOMPOSITION	0.43
JES_EffectiveNP_1	0.42
JES_PU_OffsetMu	0.42
HWW_FakeFactor_el_EWSUBTR	0.41
PRW_DATASF	0.41
FT_EFF_Eigen_Light_2	0.36
MUON_ISO_SYS	0.34
JES_EtaInter_Stat	0.33
JES_PU_Rho	0.32
JES_EffectiveNP_2	0.29
MUON_EFF_STAT	0.28
JVT	0.26
EL_EFF_ID_CorrUncertainty_NP13	0.25
EL_EFF_Reco_TOTAL_1NPCOR_PLUS_UNCOR	0.24
MUON_MS	0.23
JES_PU_OffsetNPV	0.21
JES_EffectiveNP_5	0.19
EG_SCALE_ALLCORR	0.19
EL_EFF_Iso_TOTAL_1NPCOR_PLUS_UNCOR	0.18
MUON_EFF_TrigSystUncertainty	0.18
HWW_FakeFactor_el_SAMPLECOMPOSITION	0.17
JES_EffectiveNP_6	0.17
JES_BJES	0.16
FT_EFF_Eigen_Light_1	0.15
JES_EffectiveNP_7	0.13
MUON_ID	0.12
EL_EFF_TRIG_TOTAL_1NPCOR_PLUS_UNCOR	0.12
MUON_TTVA_STAT	0.12
JES_EffectiveNP_4	0.12
MUON_SCALE	0.10
MUON_EFF_TrigStatUncertainty	0.10
EG_RESOLUTION_ALL	0.08
EL_EFF_ID_CorrUncertainty_NP12	0.07
MUON_TTVA_SYS	0.07
EL_EFF_ID_CorrUncertainty_NP11	0.07
EL_EFF_ID_CorrUncertainty_NP6	0.06
EG_SCALE_LARCALIB_EXTRA2015PRE	0.06
FT_EFF_Eigen_Light_3	0.06
EL_EFF_ID_UncorrUncertainty_NP8	0.06
JES_EffectiveNP_3	0.05
EL_EFF_ID_UncorrUncertainty_NP6	0.05

TABLE 7.16: Effect of the experimental systematic uncertainties on the SR yields. Uncertainties with effect below 0.05% are omitted.

7.8.2   Theory uncertainties

In this section, uncertainties related to the modeling of the relevant background and signal processes are discussed. These are related to the choice of the matrix element and parton shower generators, the choice of the PDF sets and the choice of the QCD renormalization and factorization scales. These uncertainties are evaluated on the expected signal and background yields (*normalization uncertainty*) in the signal region and, for some of the backgrounds, also in the control regions. Furthermore, *shape uncertainties* on the modeling of the BDT response, for the VBF cross-section analysis, and on the BDT-$\Delta\phi_{jj}$ distribution, for the W bosons polarization one, are evaluated in the signal region. However, for brevity, only the shape uncertainties on the BDT-$\Delta\phi_{jj}$ distribution will be shown in this section .

The uncertainties coming from the choice of the matrix element generator are calculated by comparing the predictions of the nominal MC generator of a given process to those of an alternative one. QCD scale uncertainties are instead estimated by changing the renormalization and factorization scales μ_R and μ_F by a factor 2.0 from the central value $(\mu_R, \mu_F) = (1.0, 1.0)$. The PDF uncertainties are evaluated by comparing the event yields of the nominal MC with alternative predictions that make use of a different PDF set, i.e. comparing, for example, the prediction of the PDF NNPDF to those of the CT14 or MMHT2014 or PDF4LHC sets. Furthermore, every nominal PDF set contains a set of internal variations that represent another source of uncertainty. This is evaluated taking the standard variation of the event yields of the single PDF internal variations. The final PDF uncertainty is the largest variation emerging from these comparisons.

In the statistical treatment, discussed in more detail in Chapter 8, signal and control regions are fitted simultaneously and the Top an $Z \rightarrow \tau\tau$ backgrounds normalization factors are extrapolated from the control region to the signal region using extrapolation factors. The final evaluation of the theoretical uncertainties is therefore performed on the extrapolation from the CR to the SRs as well as on the modeling of the $BDT - \Delta\phi_{jj}$ shape used in the fit. In this section, however, the reported uncertainties are evaluated on the normalization of the SR, and, when statistically significant, on the CRs. The fitting code then automatically propagates these uncertainties on the extrapolation factors.

7.8.2.1 Modeling uncertainties on the combined top-quark background

Several sources of modeling uncertainties are considered for the combined $t\bar{t}$ and Wt backgrounds:

- The uncertainties arising from the choice of the matrix element generator and the associated matching to the parton shower are estimated by comparing event yields and shapes of the convoluted BDT-$\Delta\phi_{jj}$ distribution obtained with the $t\bar{t}$ sample generated by POWHEG-Box+PYTHIA 8 to those obtained from a sample generated using SHERPA v.2.2.1, shown in Figure 7.26(a). Instead, the matrix element uncertainties on the Wt production, shown in Figure 7.27(a), are calculated by comparing the predictions of POWHEG-Box + HERWIG 7 to those of MAD-GRAPH5_AMC@NLO + HERWIG 7.

- The dependences on the fragmentation and parton shower modeling (PS model) are estimated interfacing the POWHEG-Box generator to PYTHIA 8 and HERWIG 7 to produce two different $t\bar{t}$ samples. The results obtained with these samples are compared, see Figure 7.26(b), and their difference is assigned as a systematic uncertainty. For the single-top process, parton shower model uncertainties are estimated comparing POWHEG-Box + PYTHIA 6 and POWHEG-Box + HERWIG 7, shown in Figure 7.27(b).

- An uncertainty is also assigned to study the impact of an increased or decreased amount of initial and final state radiation (ISR/FSR) produced in association to the $t\bar{t}$ system and as well for the single-top process. For the $t\bar{t}$ process, two further samples are produced with POWHEG-Box + PYTHIA 8, where the settings of the renormalization and factorization scales μ_R and μ_F as well as the so-called radiation scale parameter `hdamp`, which controls the p_{T} of the first additional emission, have been adjusted to cover the experimental uncertainties on previous N^{jet} and gap fraction measurements [151]. The scales μ_R and μ_F are shifted up (down) by a factor of 2 (0.5), while the `hdamp` parameter is set to 3.0 times the top-quark mass for the sample corresponding to a decreased amount of radiation and to 1.5 times the top-quark mass for the sample corresponding to an increased amount of radiation. As these two samples contain already a variation of μ_R and μ_F, no additional uncertainty on the QCD scales is considered for the $t\bar{t}$ background. The comparison

Source of uncertainty	VBF SR [%]	Top CR [%]
ME Gen. ($t\bar{t}$)	±7.4	±1.3
PS model ($t\bar{t}$)	±4.3	±3.3
ISR/FSR ($t\bar{t}$)	±0.6	±3.1
ME+PS (Wt)	±0.9	±0.03
PS model (Wt)	±2.0	±1.5
ISR/FSR (Wt)	±0.5	±0.8
DR vs DS scheme (Wt)	±1.0	±0.5

TABLE 7.17: Normalization uncertainties for the $t\bar{t}$ and Wt backgrounds in the VBF SR and in the Top CR.

is given in Figure 7.26(c). Also for the single-top one, two additional samples produced with POWHEG-Box + PYTHIA 6 are studied in order to estimate the impact of an increased or decreased amount of ISR and FSR, see Figure 7.27(c).

- In the nominal Wt samples, the diagram removal (DR) approach is used to handle the interference between the $t\bar{t}$ and Wt final states, which exist starting from NLO. Alternative samples including the diagram subtraction (DS) scheme are used as well and their comparison is shown in Figure 7.27(d).

A summary of the modeling uncertainties on the combined $t\bar{t}$ and Wt backgrounds is presented in Table 7.17, that shows the overall normalization uncertainties in the SR and the top-quark control regions.

7.8.2.2   Modeling uncertainties on the WW background

The WW theory uncertainties are estimated on the total yields in the VBF signal region and on the shape of the convoluted BDT-$\Delta\phi_{jj}$ distribution (BDT output) for the polarization studies (for the cross-section measurement) in the SR. Due to the low MC statistics available for the nominal and alternative generators, that can limit an accurate estimation of the theory systematic uncertainties causing artificial fluctuations, the calculation of all the WW theory uncertainties is performed at truth level.

- The combined matrix element and parton shower model (ME + PS) uncertainties on the WW background is calculated by comparing the nominal SHERPA v2.2.2 sample with MADGRAPH5_AMC@NLO v2.3.3 + PYTHIA 8. This alternative sample contains diagrams with up-to one additional parton associated to the diboson system at NLO precision in

(a) $t\bar{t}$ Matrix Element

(b) $t\bar{t}$ Parton Shower

(c) $t\bar{t}$ ISR/FSR
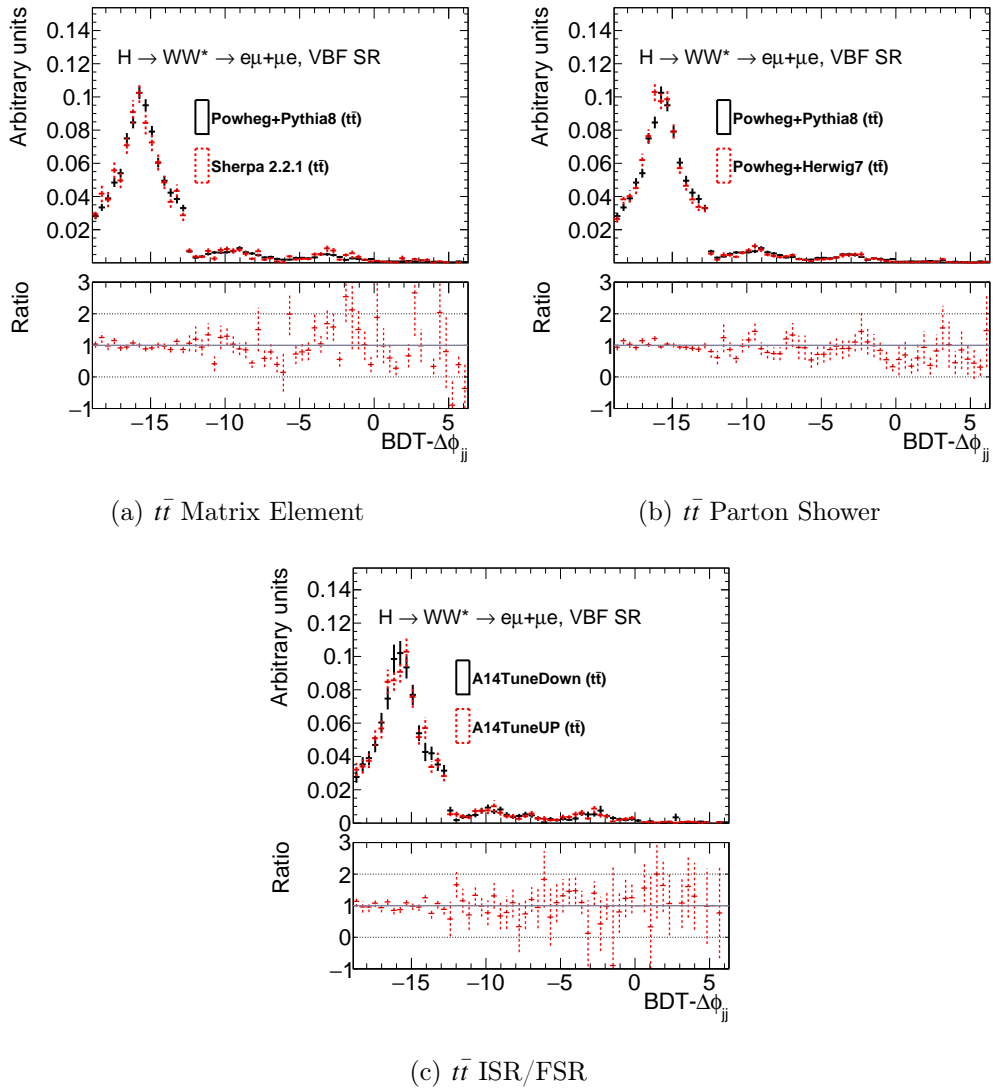
FIGURE 7.26: Shape comparison for the BDT-$\Delta\phi_{jj}$ distribution, for the matrix element, parton shower, ISR/FSR in the VBF SR for the $t\bar{t}$ background. The bottom plot shows the ratio of the variation histogram to the nominal one. The errors shown are statistical only.

QCD, and at LO, diagrams including the emission of a second parton. Overlaps between partonic configurations produced during the simulation of the matrix element and the parton shower are removed using the FxFx merging [152]. This comparison is shown in Figure 7.28(a).

- The uncertainty on the QCD scales is computed by varying the values of the renormalization and factorization scales by a factor of 2.0 or 0.5 with respect to the nominal value, shown in Fig 7.28(b).

(a) *Wt* Matrix Element

(b) *Wt* Parton Shower

(c) *Wt* ISR/FSR

(d) *Wt* DR/DS
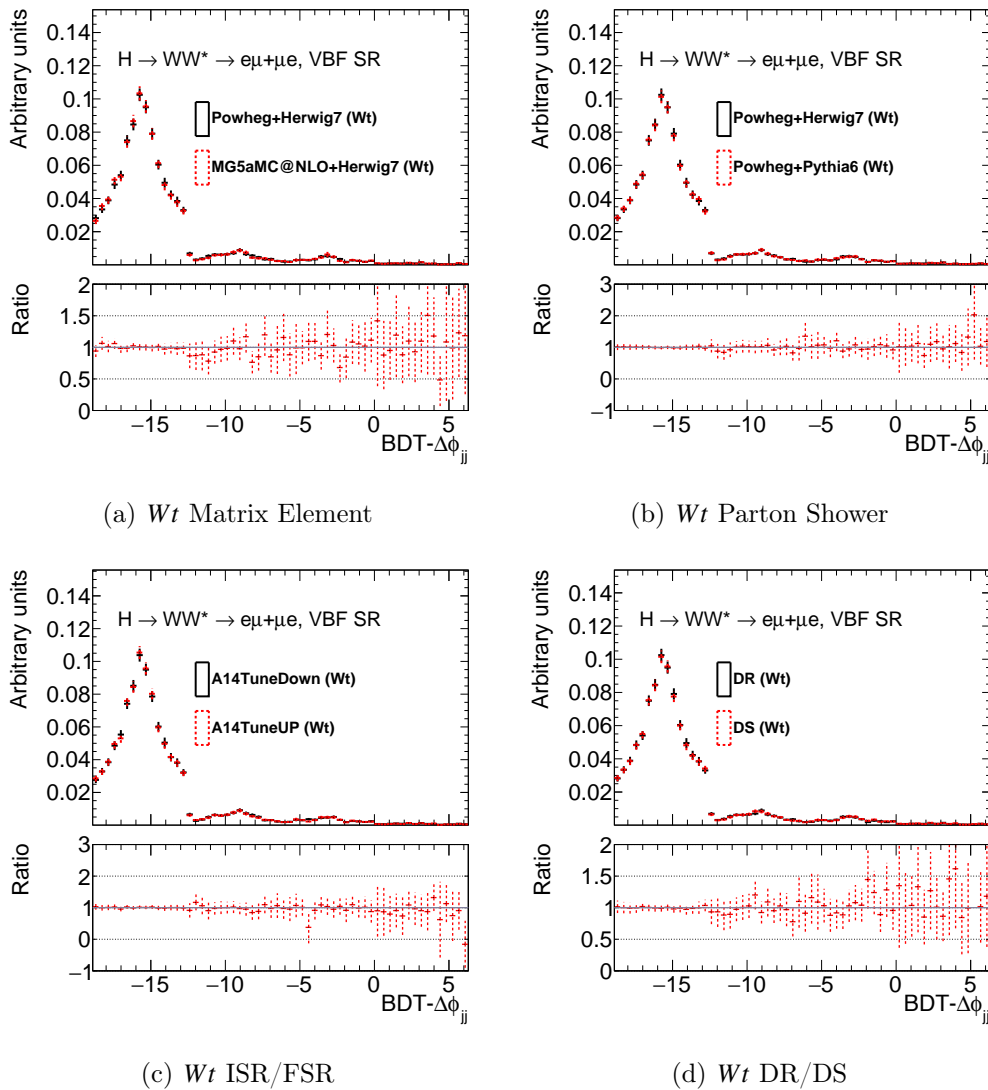
FIGURE 7.27: Shape comparison for the BDT-$\Delta\phi_{jj}$ distribution, for the matrix element, parton shower, ISR/FSR, DR/DS schemes in the VBF SR for the *Wt* background. The bottom plot shows the ratio of the variation histogram to the nominal one. The errors shown are statistical only.

- The NNPDF3.0 NNLO PDF set is used for both the hard-process calculation and the parton shower. As PDF uncertainty, the envelope of the internal NNPDF uncertainties and the comparison between the NNPDF and the MMHT2014 (CT14) PDF sets is taken, see Figure 7.28(c).

- Additional uncertainties on the modeling of the parton shower within SHERPA cover effects related to variations of the resummation scale as well as recoil and matching schemes:

    - The uncertainties based on the choice of the scale μ_Q that controls

Source of uncertainty	VBF SR
	[%]
ME Gen. +PS	±6.9
QCD scale	+20.4/-15.5
PDF	±1.16
CKKW	±2.2
Resummation scale μ_Q	±5.3

TABLE 7.18: Normalization uncertainties for the WW background in the VBF SR.

the resummation of soft gluon emissions, are evaluated by shifting the value of the resummation scale μ_Q up (down) by a factor of 2.0 (0.5) with respect to the nominal value. The final uncertainty is evaluated as the difference between these two variations (Figure 7.28(d)).

– The nominal CKKW (Catani-Krauss-Kuhn-Webber) matching scale Q_{cut} for the SHERPA diboson samples is set to 20GeV, while also alternative samples have been provided for which the matching scales are set to 15GeV and 30GeV, respectively. The comparison between the up and down variations of the CKKW matching scale is shown in Figure 7.28(e).

The summary of the *WW* theory uncertainties and their effect in the VBF SR is shown in Table 7.18.

7.8.2.3 Modeling uncertainties on the $Z \to \tau\tau$ background

The modeling uncertainties on the $Z \to \tau\tau$ + jets background are listed in Table 7.19, showing the overall normalization uncertainties in the respective SR and the $Z \to \tau\tau$ control region. Due to the limited statistics of the MC samples, only normalization uncertainties are taken into account for this background. Uncertainties for the ME and PS are evaluated comparing the nominal SHERPA sample with the predictions of MADGRAPH5_AMC@NLO + PYTHIA 8. QCD variations are estimated by varying the factorization and renormalization scales of a factor 2 by their nominal value. As PDF uncertainty, the comparison between the NNPDF and the MMHT2014 and CT14 PDF sets has been computed.

Source of uncertainty	VBF SR	$Z \rightarrow \tau\tau$ CR
	[%]	[%]
ME Gen. (MG5)	±1.1	±24.4
QCD	±-6.2/+1.2	±-0.9/+5.1
PDF	±0.3	±0.4

TABLE 7.19: Normalization uncertainties for the $Z \rightarrow \tau\tau$ background in the VBF SR and in the $Z \rightarrow \tau\tau$ CR.

7.8.2.4   Modeling uncertainties on the ggF background

For the ggF background, the systematic uncertainties, arising from the choice of the matrix element generator, are estimated by comparing the predictions of the nominal generator MADGRAPH5_AMC@NLO to those of the POWHEG MiNLO generator. This uncertainty has been calculated at reconstruction level, taking the relative difference in the final yields after the VBF selection. Figure 7.29(a) shows the effect on the BDT-$\Delta\phi_{jj}$ distribution in the SR, while the normalization uncertainty is given in Table 7.20.

The perturbative uncertainties on the ggF signal in the VBF analysis are estimated with the Stewart-Tackmann method (ST) [153], that takes as input the inclusive 2-jet and inclusive 3-jet cross-sections, $\sigma_{\geq 2}$ and $\sigma_{\geq 3}$. In order to define those cross-sections, the nominal VBF selection has been applied, with the exception of the CJV. Thanks to this cut, it is indeed possible to define the jet inclusive and exclusive regions as follows:

- Two jets inclusive region ($\geq$ 2 jets): no requirement on the third jet (i.e. no CJV cut).

- Two jets exclusive region (= 2jets): defined when the CJV (<20 GeV) cut is applied.

- Three jets inclusive region ($\geq$ 3 jets): defined reversing the CJV cut, CJV>20 GeV.

If the uncertainties are calculated considering only the variations of the μ_R and μ_F scales, there is a resulting underestimation of the size of the systematic effect due to accidental cancellations between the scale dependence of the perturbative series and Sudakov effects from the jet veto. The method proposed by Stewart-Tackmann is, instead, more reliable since it takes into account higher order contributions that are not negligible. This method uses fixed-order calculations to evaluate uncertainties in the exclusive jet cross-sections: it is based on the assumption that the scale uncertainties on the

Source of uncertainty	VBF SR
	[%]
ME Gen.	±4
ST QCD scale	±24.4
PDF (Internal)	±0.4
PDF set	±8.9
PS	±5.9

TABLE 7.20: Normalization uncertainties for the ggF background in the VBF SR.

inclusive multi-jet cross-sections $\sigma_{\geq 2j}$ and $\sigma_{\geq 3j}$, are uncorrelated and it is therefore possible to propagate them to the exclusive jet bins:

$$\sigma_N = \sigma_{\geq N} - \sigma_{\geq N+1}. \tag{7.19}$$

The uncertainty $\Delta\sigma_N$ on σ_N due to perturbative scale uncertainties can be obtained following:

$$\Delta\sigma_N^2 = \Delta\sigma_{\geq N}^2 + \Delta\sigma_{\geq N+1}^2, \tag{7.20}$$

where $\Delta\sigma_{\geq N}$ and $\Delta\sigma_{\geq N+1}$ are inclusive cross-section uncertainties.

The QCD scale uncertainties have been therefore estimated with MADGRAPH5_AMC@NLO + PYTHIA 8, that is at NLO precision for $\sigma_{\geq 2}$ and LO for $\sigma_{\geq 3}$. The normalization and the shape uncertainties for the BDT - $\Delta\phi_{jj}$ distributions have been calculated in the SR.

The ST uncertainty on the normalization of the VBF SR is shown in Table 7.20. The shape uncertainty is determined by normalizing to the nominal cross-section in the 2-jet and 3-jet inclusive regions and then calculating the ST uncertainty bin-by-bin: the envelope of the ST shape uncertainty is shown in Figure 7.29(b).

The error on the PDF is estimated at first evaluating the internal NNPDF3.0 PDF uncertainty, defined as the standard deviation of the 100 PDF uncertainty variations. The final uncertainty is given as the envelope of these internal variations and the largest one between the nominal PDF set with MMHT2014 and the CT14 PDFs (Figure 7.29(c)).

The parton shower uncertainty has been estimated by comparing the predictions of MADGRAPH5_AMC@NLO + PYTHIA 8 and MADGRAPH5_AMC@NLO + HERWIG, shown in Figure 7.29(d).

The normalization uncertainties are summarized in Table 7.20.

Source of uncertainty	VBF SR
	[%]
QCD scale	±1.2
PDF (Internal)	±0.2
PDF set	±1.8
PS (ptMaxFudge)	±15.6

TABLE 7.21: Normalization uncertainties for the VBF signal
in the VBF SR.

7.8.2.5   Uncertainties on the VBF signal modeling

The uncertainties on MADGRAPH5_AMC@NLO predictions for the VBF signal are evaluated at truth level.

The uncertainty on the QCD scales is computed by varying the values of the renormalization and factorization scales by a factor of 2.0 or 0.5 with respect to the nominal value, as is shown in Fig 7.30(a).

The PDF uncertainties are instead calculated taking the envelope of the internal variations for the NNPDF3.0 set and the maximum difference between NNPDF3.0, CT10 and MMHT14 PDF sets (shown in Fig. 7.30(b)).

The uncertainty arising from the parton-shower modeling, also accounting for LO/NLO differences, is estimated by halving/doubling the `ptMaxFudge` parameter described in Section 5.3. The associated uncertainty is shown in Figure 7.30(c).

The summary of the uncertainties due to the VBF signal modeling in the signal region is given in Table 7.21.

(a) Matrix Element

(b) QCD scales

(c) PDF uncertainty

(d) Resummation scale

(e) CKKW
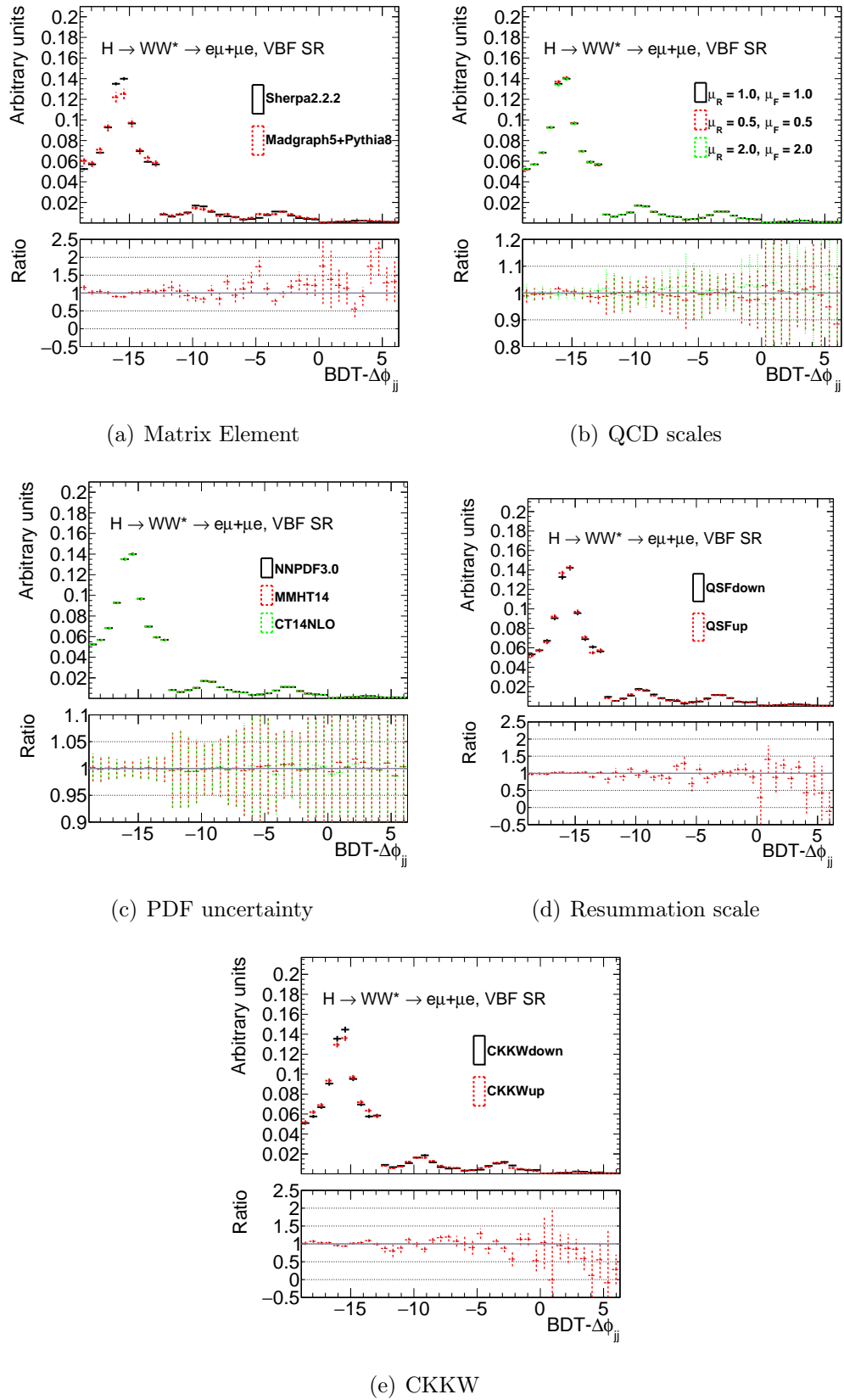
FIGURE 7.28: Shape comparisons for the BDT-$\Delta\phi_{jj}$ distribution, for the matrix element, QCD, PDF, resummation scale and CKKW in the VBF SR for the *WW* background. The bottom plot shows the variation of the alternative prediction with respect to the nominal one. The errors shown are statistical only.

(a) Matrix Element

(b) QCD

(c) PDF sets

(d) Parton Shower
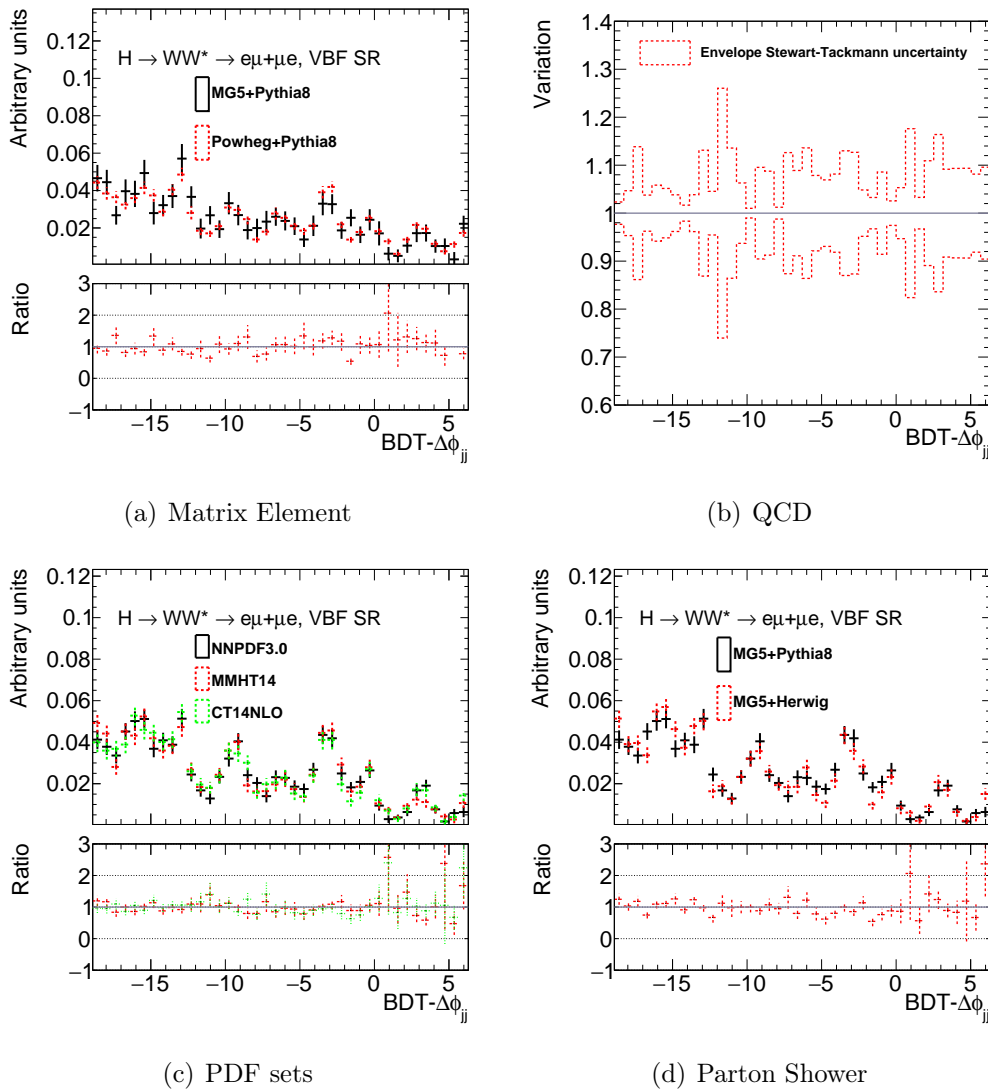
FIGURE 7.29: In Figure 7.29(a) the comparison between the nominal MADGRAPH5_AMC@NLO sample (in red) and alternative Powheg one (in black) is shown after the $Z \rightarrow \tau\tau$ veto at reconstruction level. Figure 7.29(b) shows the envelope of the bin-by-bin ST uncertainty in the VBF SR. The last two figures, Figure 7.29(c) and 7.29(d), show, respectively, the comparisons among different PDF sets for the MADGRAPH5_AMC@NLO sample, and the prediction obtained with different parton shower generators (PYTHIA 8 vs HERWIG) at truth level. In all the figures, the plot on the bottom shows the variation of the alternative prediction with respect to the nominal one. The errors shown are statistical only.

(a) QCD

(b) PDF sets

(c) Parton Shower
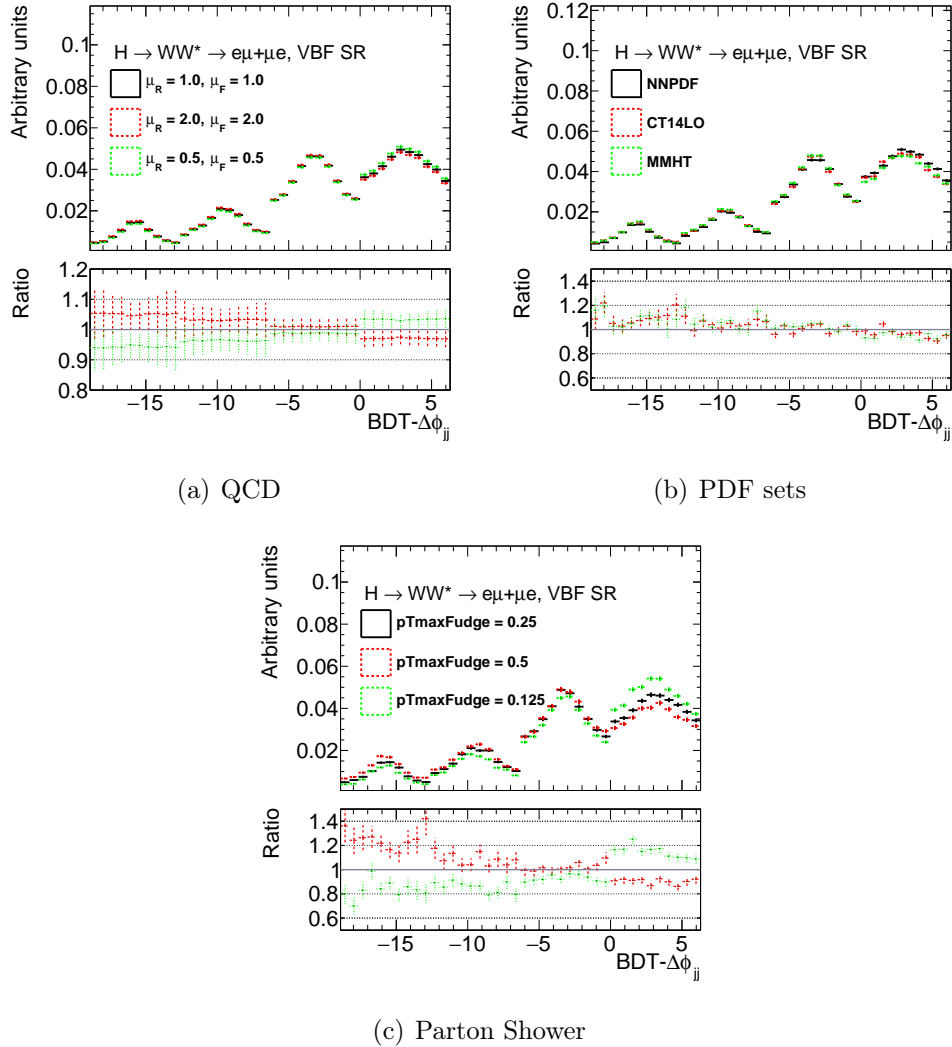
FIGURE 7.30: In Fig. 7.30(a) the comparison between the nominal QCD scale $\mu_R = \mu_F = 1$ and the variations $\mu_R = \mu_F = 2/\mu_R = \mu_F = 0.5$ for the nominal MADGRAPH5_AMC@NLO sample in the VBF SR is shown. In Fig. 7.30(b) the comparison between NNPDF3.0 and the alternative PDF sets (CT14LO and MMHT14) is given. Fig. 7.30(c) shows the comparison between the sample showered with `pTmaxFudge` = 0.25 its up/down variations. The bottom plots give the ratio between the nominal case and the alternatives. The errors shown are statistical only.

7.8.3   Uncertainties on the fakes estimation

There are different sources of systematic uncertainty arising from the calculation of the fake factor described in Section 7.2.1. The first one is the statistical uncertainty on the fake factor estimation, that includes both data and MC statistical uncertainties.

Furthermore, considering that the fake factor is measured in the Z+jets control sample and is applied to the W+jets control sample, an uncertainty has to be added that takes into account the differences in jet kinematics and heavy flavor fraction in these two samples, that may cause differences in the fake factors. This *Sample Composition* differences result in discrepancies in the jet kinematics and in the FF estimation. Therefore, to account for this, correction factors, derived from MC, are used, with a systematic uncertainty calculated comparing different Monte Carlo generators.

Moreover, another uncertainty is due to the real lepton contamination from multi-leptons in the Z+jets data sample (*EW subtraction*). This is estimated by varying the EW background, up and down of a 10%, subtracted in the Z+jets sample and re-computing the FF. A summary of the effect of these three uncertainties is given in Table 7.22.

Kinematic region ($|\eta|$ and p_T range)	Statistical	EW Subtraction	Sample Composition	Total
Electron:				
$0.0 < |\eta| < 1.5$				
$15 - 20$ GeV	27	13	32	44
$20 - 25$ GeV	25	16	32	44
$25 - 35$ GeV	23	16	13	31
$35 - 1000$ GeV	26	33	13	44
$1.5 < |\eta| < 2.5$				
$15 - 20$ GeV	26	13	32	43
$20 - 25$ GeV	54	16	32	65
$25 - 35$ GeV	27	16	13	34
$35 - 1000$ GeV	32	33	13	47
Muon:				
$0.0 < |\eta| < 2.5$				
$15 - 20$ GeV	11	9	23	27
$20 - 25$ GeV	24	17	23	37
$25 - 1000$ GeV	76	143	23	163

TABLE 7.22: Summary of systematic uncertainties (quoted as percentages) on the Z+jets fake factor measurement, binned in η and p_T. The *Statistical*, *EW subtraction* and *Sample composition* uncertainties are presented. From Reference [134].

7.8.4 Uncertainty for the m_{jj} mis-modeling

A mis-modeling is observed in the m_{jj} distribution at the VBF pre-selection, after the b-jet veto. As it visible from Figure 7.31(a), the MC appears to overestimate the data. To correct this mis-modeling a re-weighting procedure is applied to the total background prediction to obtain a data-MC agreement. The resulting change in the BDT-$\Delta\Phi_{jj}$ shape of the total background in the VBF signal region reveals the impact of this mis-modeling on the final discriminant. Bin-per-bin scale factors are therefore computed in the VBF SR at pre-selection, in order to re-weight the MC prediction to match the data. These scale factors are not applied to the nominal distribution but are only used to compute an uncertainty on the m_{jj} modeling. Figure 7.31(b) shows the BDT-$\Delta\Phi_{jj}$ shape for the total background before (black) and after reweighing (red), using the weights calculated at pre-selection level.
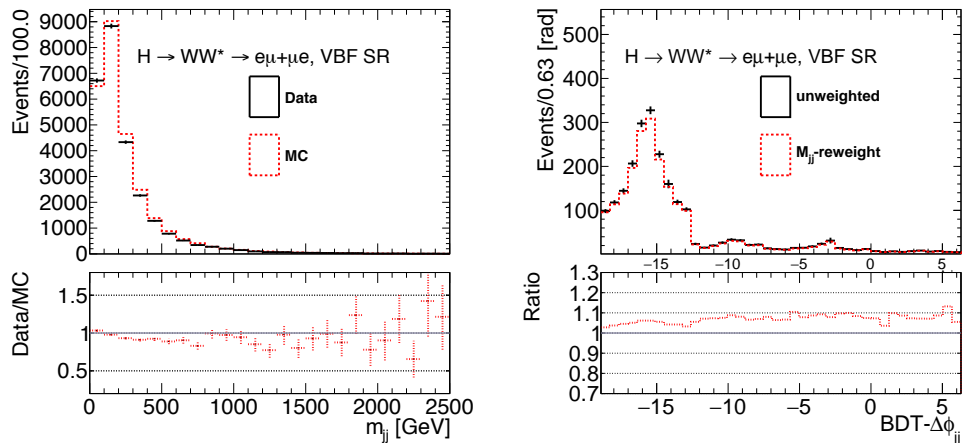
(a) m_{jj} before re-weighting   (b) BDT-$\Delta\Phi_{jj}$ before/after re-weighting

FIGURE 7.31: Distribution of m_{jj} in the $e\mu+\mu e$ before reweighting in the VBF pre-selection and the comparison between the BDT-$\Delta\Phi_{jj}$ before and after the re-weighting is applied in the VBF SR. The bottom plots show the ratio between the nominal case and the variations. The errors shown are statistical only.

In order to account for this mis-modeling a shape systematic is applied in the VBF SR for all the background processes and added as an additional nuisance parameter to the final fit, as explained in Chapter 8.

Statistical interpretation and results

The description of the statistical methods employed for the polarized couplings analysis and for the VBF cross-section extraction is outlined in this chapter. Maximum likelihood fits are performed to the data and the significance on the coupling parameters is estimated.

This chapter starts with a brief outline of the fitting methodology. The analytical morphing method, employed to model the signal and its dependence on the couplings parameters, is also described. More detailed descriptions of the fitting procedures can be found in References [154–156], while for the morphing method on References [157–159]. Finally, results on the $H \to WW^* \to \ell\nu\ell\nu$ cross-section measurement and on the polarized couplings parameters are presented.

8.1   Statistical procedure

Given a set of measurements $x = x_1,...,x_N$ resulting from the outcome of an experiment, the probability of these data given an hypothesis H is defined as $P(x|H)$. If $P(x|H)$ is a function of the hypothesis H, then it is referred to as the *likelihood* of H. Since the hypothesis can depend on several parameters θ, called *nuisance* parameters (NP), and on the so-called *parameter of interest* μ, the likelihood can be expressed as

$$L(\mu,\theta) = P(x|\mu,\theta). \tag{8.1}$$

Two different hypotheses are tested against the data: the *null hypothesis H_0*, which is the hypothesis that sees the Standard Model predictions as true, and the *alternative hypothesis H_1*, that implies the presence of effects coming from new physics. With these two definitions, a *test statistic* can be built: this is a quantity, estimated from the data, that can evaluate the probability of the observed result with respect to the null or to the alternative hypothesis.

The *parameter of interest* (POI) is a free parameter of the alternative hypothesis, that in the null one can be either fixed or can be not present at all; in a typical ATLAS analysis this parameter can be the signal strength, defined as the ratio of the measured cross-section over the SM prediction or a coupling parameter, such as, for example, the longitudinal or the transverse polarized coupling. Instead, with the term *nuisance parameters* (NP) are called those parameters that are related to the effects of statistic and systematic uncertainties or to the normalization factors of specific backgrounds in given control regions.

8.1.1   The likelihood function

In order to build the likelihood function, a few considerations have to be made. The first one is that the data, in each bin of the input distribution, follow a Poisson probability distribution function. The second one is that, in the fit, it is necessary to add a parametrization that takes into account the background treatment in the control regions: normalization factors from the fitted background rates in the control regions have to be propagated to the signal and to the other control regions.

Therefore, the likelihood can be parametrized as follows:

$$\mathscr{L}(\mu, \mu_b) = P(N_{SR}|\mu s_{\text{SR}} + \mu_b b_{\text{SR}}) \times P(N_{CR}|\mu_b b_{\text{CR}}) \tag{8.2}$$

In this equation s_{SR}, $b_{\text{SR/CR}}$ are the expected number of signal and background events in the SR and CR, respectively; N_{SR} and N_{CR} are the number of observed events in the signal and in the control regions, μ is the signal strength and μ_b is the background normalization factor.

This simple formulation of the likelihood can be expanded according to the different measurements of each analysis. For the study of the polarized coupling and of the VBF cross-section measurement, it is necessary to take into account the lepton flavors in the final state and the number of bins of the input distribution. The strength parameters of the backgrounds μ_b are applied to the top-quark and $Z \rightarrow \tau\tau$ backgrounds, while the other minor

backgrounds, whose predictions are not constrained in a control region, do not present floating strength parameters, but are anyhow considered in the Poisson expectations. Therefore, the full likelihood can be written as

$$\mathscr{L}(\mu, \vec{\theta}) = \{ \prod_{i=e\mu,\mu e} \prod_{j=0}^{N_{BDT-\Delta\phi_{jj}}\text{bins}} P(N_{ij}|\mu s_{ij} + \sum_{n}^{N_{\text{bkg}}} b_{ij}) \}$$

$$\times \{ \prod_{c=1}^{N_{\text{CR}}} P(N_c|\mu s_c + \sum_{n}^{N_{\text{bkg}}} b_{cn}) \} \times \{ \prod_{i=1}^{N_\theta} N(\tilde{\theta}_i|\theta_i) \}. \tag{8.3}$$

The last term $N(\tilde{\theta}_i|\theta_i)$ represents the constraints related to the presence of nuisance parameters: both the signal and background expected values are functions of the nuisance parameters θ and the form of the constraint depends on the nature of the nuisance parameters themselves.

For nuisance parameters related to systematic variations, the constraint follows a Gaussian distribution [155]:

$$Gaussian(\tilde{\theta}|\theta, \sigma) = \frac{1}{\sqrt{2\pi\sigma^2}} e^{-\frac{(\tilde{\theta}-\theta)^2}{2\sigma^2}}. \tag{8.4}$$

The maximum likelihood estimation of θ can be identified with the global observable $\tilde{\theta}$; by convention, θ is usually scaled such that the distribution is centered at zero and has unit variance, $G(\tilde{\theta}|0, 1)$. For the systematics that only affect the normalization of the input distribution, the dependency on θ can be determined by shifting θ of ± 1. Instead, for shape systematics, a model that interpolates bin-by-bin between the histograms is built, performing a vertical linear interpolation to estimate the variation: the content of each bin is modified thanks to a linear function, that interpolates between the nominal bin content value and the values at $\theta = \pm 1$.

The statistical uncertainties are related to statistical fluctuations in each bin of the input distribution and to the background normalization factors. These follow a Poisson distribution:

$$Poisson(\tilde{\theta}|\theta\lambda) = \frac{(\theta\lambda)^{\tilde{\theta}} e^{-\theta\lambda}}{\tilde{\theta}!}, \tag{8.5}$$

where λ is a constant typically taken as the nominal value of $\tilde{\theta}$. The nominal value of θ is equal to 1, such that $\tilde{\theta}$ varies around $\theta\lambda$.

One single nuisance parameter θ can affect multiple signal and background rates in a correlated way, but not all of them can affect each rate: for example, the WW QCD theoretical systematic uncertainty will not affect the top

background.

Only shape systematics with statistically significant variations must be taken into account: shape variations affected by poor MC statistics can produce convergence issues in the fit.

8.1.2   Test statistic

The test statistic, mentioned previously, can be performed constructing the *profile likelihood ratio*:

$$\lambda(\mu) = \frac{L(\mu, \hat{\hat{\vec{\theta}}}(\mu))}{L(\hat{\mu}, \hat{\vec{\theta}})} \ . \tag{8.6}$$

In this equation, the term at the numerator is the profiled likelihood, in which $\hat{\hat{\vec{\theta}}}$ is the value of $\vec{\theta}$ that maximizes the likelihood for the specified μ (conditional maximum-likelihood). Instead, at the denominator, $\hat{\mu}$ and $\hat{\vec{\theta}}$ are the values that maximize in absolute the likelihood function (unconditional maximum-likelihood). From Eq. (8.6), it follows that $0 \leq \lambda \leq 1$. A good agreement between the data and the estimation of μ is achieved when λ is close to 1. For convenience, the test-statistic is re-written taking the logarithm of the ratio:

$$t_\mu = -2 \ln \lambda(\mu) \tag{8.7}$$

In this re-formulation, higher values of t_μ are matched to larger incompatibility between μ and the data. The level of agreement of the observed data with a given hypothesis can be computed estimating the *p*-value. This is defined as the probability, under the tested hypothesis, to observe a deviation at least as extreme or more as the observed deviation. The tested hypothesis is excluded if the estimated *p*-value is below a threshold. The *p*-value in particle physics is usually translated into an equivalent significance Z. The *p*-value can also be seen as the area under the Gaussian curve that is at the left from the mean of Z-sigmas:

$$Z = \Phi^{-1}(1 - p), \tag{8.8}$$

where Φ^{-1} is the inverse of the cumulative distribution of the Gaussian. Typically, to claim a discovery, the null hypothesis is rejected with significance of at least 5σ, that is a p-value of $p = 2.87 \times 10^{-7}$. Instead, the convention for excluding an alternative hypothesis is to set a threshold for *p*-value of 0.05, corresponding to 95% confidence level (2σ).

8.2 The analytical Lagrangian morphing technique

The analytical Lagrangian morphing [157–159] is a method implemented to handle signal models with a dependency on a large quantity of coupling parameters, providing, in a multi-dimensional space of parameters, a continuous description of a physical signal observable. In the case of the polarized couplings analysis, this physical signal observable can be identified as the BDT-$\Delta\phi_{jj}$ distribution. A basic interpolation technique would be limited to the phase-space covered by the samples given as input for the interpolation. The morphing technique does something more advanced, allowing the extrapolation outside the boundaries of the input samples. Let's consider a physical observable T, that can be, for example, the BDT-$\Delta\phi_{jj}$ distribution. Its dependence on a set of non-SM couplings $\vec{g}_{\text{target}}$ can be described by the morphing function:

$$T_{\text{out}}(\vec{g}_{\text{target}}) = \sum_i w_i(\vec{g}_{\text{target}}; \vec{g}_i)T_{\text{in}}(\vec{g}_i). \qquad (8.9)$$

In this equation, the input $BDT-\Delta\phi_{jj}$ distributions T_{in} obtained for different coupling configurations $\vec{g}_i$ are linearly combined, and the resulting output distribution T_{out} presents the correct shape and cross-section predictions for a given $\vec{g}_{\text{target}}$. Assuming that there is a proportionality between the value of a physical observable and the squared matrix element of the considered process:

$$T \propto \mathscr{M}^2, \qquad (8.10)$$

the target variable can be obtained by combining the samples T_{in} weighted by w_i. These weights are function of the coupling parameters in the matrix element $\mathscr{M}$. Here, T represents anything that can be obtained from the matrix element, such as a MC sample.

The only requirements of the morphing technique are a minimal number of input configurations, that depends on the number of the BSM couplings $\vec{g}_{\text{target}}$, and that the differential cross-section of the studied process can be written as a polynomial in terms of coupling parameters.

Given a physics process, in order to build the morphing function, the matrix element has to be squared. Denoting with p the operators that appear only in the production vertex, with d the ones in the decay vertex and with s

the ones that are shared between both vertices and assuming that the two vertices are uncorrelated, that is the case for a scalar intermediate particle, it follows that:

$$\left|\mathcal{M}(\vec{g})\right|^2 = \underbrace{\left(\sum_{x \in p,s} g_x \mathcal{O}(g_x)\right)^2}_{\text{production}} \cdot \underbrace{\left(\sum_{x \in d,s} g_x \mathcal{O}(g_x)\right)^2}_{\text{decay}}. \tag{8.11}$$

Furthermore, the matrix element has to be expanded to a 4th degree polynomial in the coupling parameters.

$$\left|\mathcal{M}(\vec{g})\right|^2 = \sum_{i=1}^{N} X_i \cdot P_i(\vec{g}). \tag{8.12}$$

In this equation $P_i(\vec{g})$ is a 4th degree polynomial of $\vec{g}$, while X_i is a pre-factor linked to the input distribution. Given Eq 8.10, the input distributions can be generated at fixed parameter points $\vec{g}_i$

$$T_{\text{in},i} \propto \left|\mathcal{M}(\vec{g}_i)\right|^2. \tag{8.13}$$

The morphing function can therefore be written as:

$$T_{\text{out}}(\vec{g}) = \sum_{i=1}^{N} \underbrace{\left(\sum_{j=1}^{N} A_{ij} P_j(\vec{g})\right)}_{w_i(\vec{g})} T_{\text{in},i}. \tag{8.14}$$

$$= \vec{P}(\vec{g}) \cdot A\vec{T}. \tag{8.15}$$

In the previous equation, the second line rewrites the first one in matrix notation. The matrix A has to be evaluated to obtain the morphing function. Since the output distribution has to match the input one at fixed input parameters,

$$T_{\text{out}}(\vec{g}_i) = T_{\text{in},i} \qquad \text{for} \qquad i = 1, \ldots, N, \tag{8.16}$$

this can be formulated in matrix notation as

$$A \cdot \left(P_j(\vec{g}_i)\right)_{ij} = \mathbb{1} \quad \Leftrightarrow \quad A \cdot G = \mathbb{1}. \tag{8.17}$$

The condition $\det(G) \neq 0$ has to be fulfilled to obtain the unique solution $A = G^{-1}$.

The number of input samples depends on the number of coupling parameters in the production and in the decay vertices [158, 159]:

$$
\begin{aligned}
N = \ & \frac{n_p \left(n_p + 1\right)}{2} \cdot \frac{n_d \left(n_d + 1\right)}{2} + \binom{4 + n_s - 1}{4} \\
& + \left(n_p \cdot n_s + \frac{n_s \left(n_s + 1\right)}{2}\right) \cdot \frac{n_d \left(n_d + 1\right)}{2} \\
& + \left(n_d \cdot n_s + \frac{n_s \left(n_s + 1\right)}{2}\right) \cdot \frac{n_p \left(n_p + 1\right)}{2} \\
& + \frac{n_s \left(n_s + 1\right)}{2} \cdot n_p \cdot n_d + \left(n_p + n_d\right) \binom{3 + n_s - 1}{3}.
\end{aligned}
\tag{8.18}
$$

In this formula, n_p stands for the number of couplings appearing only in production, n_d only in decay and n_s is the number of shared coupling in both in production and decay. For the polarization analysis, the number of parameters affecting only the production process is $n_p = 0$, the ones affecting only the decay process is $n_d = 0$, while there are two parameters present both in the production and the decay, e.g. a_L and a_T, which give $n_s = 2$. Therefore the number of input samples will be:

$$
N_{\mathrm{VBF}} = \binom{4 + n_s - 1}{4},
\tag{8.19}
$$

The result of eq. 8.19 determines the need of $N = 5$ samples in order to model this physics case. The samples that have been chosen as a basis have the following values for the $(a_L,\ a_T)$ pairs: (1,1), (1.3,0.7), (0.7,1.3), (1,1.3), (1.3,1).

8.2.1 Morphing validation

A validation of the morphing method has been performed by comparing the expected $\Delta\phi_{jj}$ distribution from the morphing method with the same distribution as obtained directly from the matrix element generator. This check has been carried out for the following combinations of a_L and a_T values: (0.7,0.7), (1.3,1.3), (0.7,1), (1,0.7). The results are shown in Figure 8.1. The comparison shows that the differences among the morphed and the validation distributions are compatible within the statistical fluctuations, as expected.
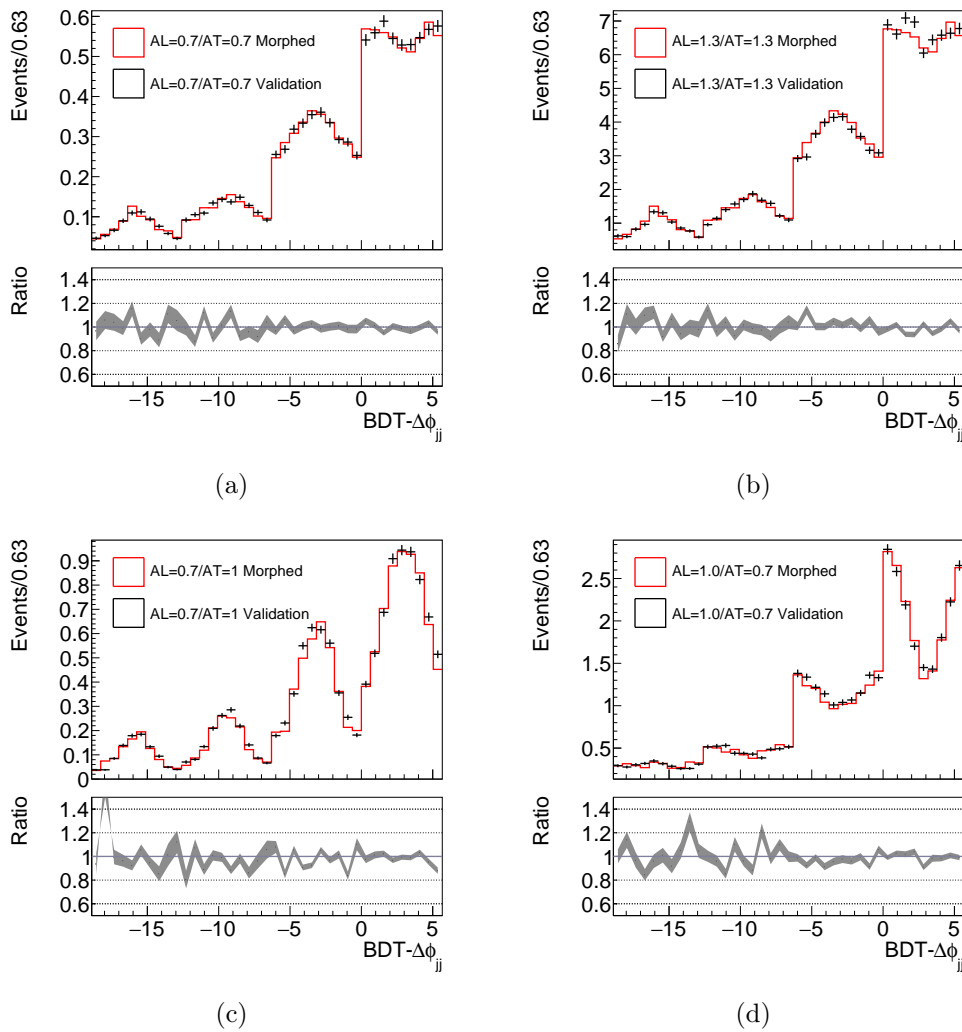
FIGURE 8.1: Comparison of the morphed $\Delta\phi_{jj}$ distribution with the one obtained from the generator (labeled as validation) for four different choices of the a_L and a_T parameters. The validation curve shows the statistical error from the Monte Carlo generator. The bottom plots show the ratio of the morphed to the validation distribution and the statistical error.

8.2.2   Uncertainty on the morphing method

As mentioned in the previous section, five input samples are given as input to the morphing function. A way to estimate the uncertainty on the model is to compare the morphing performances with different combinations of the input samples. Therefore, four different bases have been chosen:

- Base 1: the a_L and a_T pairs that form this basis are: (1,1), (1.3,0.7), (0.7,1.3), (1,1.3), (1.3,1). This has been chosen as default basis, as mentioned in the previous section.

- Base 2: the a_L and a_T pairs that form this basis are: (1,1), (1.3,0.7), (0.7,1.3), (1,0.7), (0.7,1).

- Base 3: the a_L and a_T pairs that form this basis are: (1,1), (1.3,0.7), (0.7,1.3), (1.3,1), (0.7,1).

- Base 4: the a_L and a_T pairs that form this basis are: (1,1), (1.3,0.7), (0.7,1.3), (1,0.7), (1,1.3).

The (a_L, a_T) point to morph has been chosen such that $a_L \neq a_T$, so that the shape of $\Delta\phi_{jj}$ is different wrt the SM one (the SM point is always given as input to the morphing function), and relatively close to the SM point: the selected point is therefore (a_L, a_T)=(1.2,1.0).

The shape comparison for the BDT-$\Delta\phi_{jj}$ distribution at this morphed point is shown in Figure 8.2 for the over-mentioned bases. As shown in the bottom plot, the variations of the alternative bases 2, 3 and 4 with respect to the default one (base 1) are rather small, of the order of a few percent. The normalization uncertainty is found to be negligible, since lower than 1%. Tests changing the morphed point have been performed, all showing consistent results.

These small shape differences have been added as a shape uncertainty on the signal sample in the final likelihood fit.
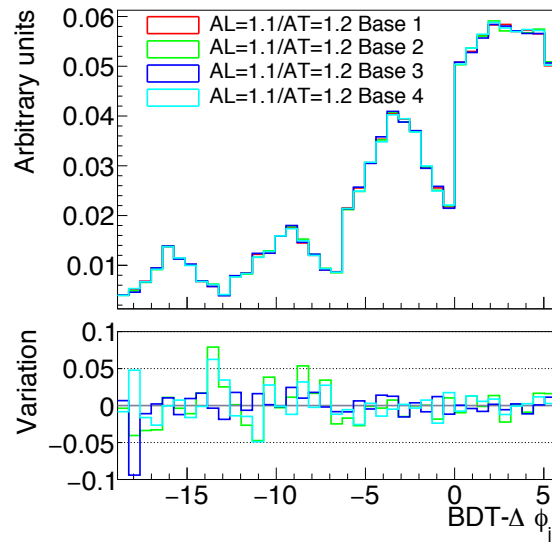

FIGURE 8.2: Comparison of the BDT-$\Delta\phi_{jj}$ distributions, normalized to unity, at the morphed point $a_L = 1.2$ $a_T = 1.1$ for different basis of the input samples. The lower panel shows the variation among bases 2, 3 and 4 with respect to base 1.

8.3 Results on the $H \to WW^* \to \ell\nu\ell\nu$ cross-section measurement

The cross-section measurement has been performed building signal regions in different N_{jet} categories. Events with zero-jets and with one-jet ($N_{\text{jet}} = 0$ and $N_{\text{jet}} = 1$) match the ggF production mode, while events with at least two jets ($N_{\text{jet}} \geq 2$) the VBF one [160, 161].

The event selection is summarized in Table 8.1. The same pre-selection, described more in detail in Section 7.5, is applied to both ggF and VBF channels. As already mentioned in Chapter 7, the polarized coupling analysis and the VBF cross-section measurement present the same selection, but the likelihood fit is performed on different quantities. Therefore, the selection for the SR and the CRs for the VBF analysis is detailed in Chapter 7.

For the ggF categories, a short description of the analysis is outlined below, as a simultaneous fit of the ggF and VBF signal is performed.

In order to reject the $t\bar{t}$ and Wt backgrounds, events containing b-jets are vetoed. Furthermore, in the $N_{\text{jet}} = 0$ category, cuts are applied on the opening angle between the di-lepton system and the transverse missing energy, $\Delta\phi(\ell\ell, E_T^{\text{miss}}) > \pi/2$, to remove potential pathological events in which the E_T^{miss} points in the direction of the lepton pair. Moreover, the transverse momentum of the di-lepton system, $p_T^{\ell\ell}$, is required to be at least 30 GeV to reject $Z \to \tau\tau$ events.

In the $N_{\text{jet}} = 1$ category, a lower bound on the maximum value of m_T^ℓ is required in order to reject $Z/\gamma* \to \tau\tau$ background, since processes with at least one real W boson typically present a large value of m_T^ℓ for at least one of the two leptons.

In the ggF $N_{\text{jet}} = 0$ and $N_{\text{jet}} = 1$ selection, eight signal regions are built by splitting $m_{\ell\ell}$ in two bins, $m_{\ell\ell} < 30$ GeV and $m_{\ell\ell} \geq 30$ GeV, and the sub-leading lepton p_T in $p_T^{\text{sublead}} < 20$ GeV and $p_T^{\text{sublead}} \geq 20$ GeV.

To constrain the predictions of the main background processes, control regions are built for the WW (only for $N_{\text{jet}} \leq 1$), for the $t\bar{t}/Wt$ and for Z/γ^* backgrounds, respectively.

The discriminating variable between the signal and the background processes for the ggF categories is the di-lepton transverse mass, defined in Equation 7.2. The post-fit m_T distribution for $N_{\text{jet}} \leq 1$ category is shown in Figure 8.3(a), while Figure 8.3(b) shows the post-fit VBF BDT distribution for the $N_{\text{jet}} \geq 2$ category.

A maximum likelihood fit is performed simultaneously in all SRs and CRs

Category	$N_{\text{jet.}(p_T > 30 \text{ GeV})} = 0$ **ggF**	$N_{\text{jet.}(p_T > 30 \text{ GeV})} = 1$ **ggF**	$N_{\text{jet.}(p_T > 30 \text{ GeV})} \geq 2$ **VBF**
Preselection	Two isolated, different-flavour leptons ($\ell = e, \mu$) with opposite charge $p_T^{\text{lead}} > 22$ GeV , $p_T^{\text{sublead}} > 15$ GeV $m_{\ell\ell} > 10$ GeV		
	$p_T^{\text{miss}} > 20$ GeV		
Background rejection		$N_{b\text{-jet}} = 0$	
	$\Delta\phi(\ell\ell, E_T^{\text{miss}}) > \pi/2$ $p_T^{\ell\ell} > 30$ GeV	$\max\left(m_T^\ell\right) > 50$ GeV $m_{\tau\tau} < m_Z - 25$ GeV	
$H \to WW^* \to e\nu\mu\nu$ topology	$m_{\ell\ell} < 55$ GeV $\Delta\phi_{\ell\ell} < 1.8$		central jet veto outside lepton veto
Discriminant variable	m_T		BDT
BDT input variables			$m_{jj}, \Delta y_{jj}, m_{\ell\ell}, \Delta\phi_{\ell\ell}, m_T, \eta_\ell^{\text{centrality}}, \sum_{\ell,j} m_{\ell j}, p_T^{\text{tot}}$

TABLE 8.1: Signal region event selection for different jet categories for the cross-section measurements.

in order to extract the ggF and VBF cross-sections. The measured cross-sections times branching fractions, $\sigma_{\text{ggF}} \cdot \mathscr{B}_{H \to WW^*}$ and $\sigma_{\text{VBF}} \cdot \mathscr{B}_{H \to WW^*}$, are found to be:

$$
\begin{aligned}
\sigma_{\text{ggF}} \cdot \mathscr{B}_{H \to WW^*} &= 11.4^{+1.2}_{-1.1}(\text{stat.})^{+1.2}_{-1.1}(\text{theo syst.})^{+1.4}_{-1.3}(\text{exp syst.}) \text{ pb} \\
&= 11.4^{+2.2}_{-2.1} \text{ pb} \\
\sigma_{\text{VBF}} \cdot \mathscr{B}_{H \to WW^*} &= 0.50^{+0.24}_{-0.22}(\text{stat.}) \pm 0.10(\text{theo syst.})^{+0.12}_{-0.13}(\text{exp syst.}) \text{ pb} \\
&= 0.50^{+0.29}_{-0.28} \text{ pb.}
\end{aligned}
$$

These values are in agreement, within their uncertainties with the cross-section times branching fraction values predicted by the SM: 10.4 ± 0.6 pb and 0.81 ± 0.02 pb for, respectively, ggF and VBF [162].

Figure 8.4 shows two-dimensional contours of $\sigma_{\text{ggF}} \cdot \mathscr{B}_{H \to WW^*}$ and $\sigma_{\text{VBF}} \cdot \mathscr{B}_{H \to WW^*}$ at the 68% (in blue) and 95% (in red) confidence level: the black cross is the best-fit value, while the red marker shows the SM prediction. The measurements are in good agreement with respect to the SM predictions.

The results are also given in terms of signal strength, μ, that is defined as the ratio of the measured signal yield to the SM predictions. The signal strengths for ggF and VBF are found to be:

$$
\begin{aligned}
\mu_{\text{ggF}} &= 1.10^{+0.10}_{-0.09}(\text{stat.})^{+0.13}_{-0.11}(\text{theo syst.})^{+0.14}_{-0.13}(\text{exp syst.}) \\
&= 1.10^{+0.21}_{-0.20} \\
\mu_{\text{VBF}} &= 0.62^{+0.29}_{-0.27}(\text{stat.})^{+0.12}_{-0.13}(\text{theo syst.}) \pm 0.15(\text{exp syst.}) \\
&= 0.62^{+0.36}_{-0.35}.
\end{aligned}
$$

The observed (expected) significance for the ggF and VBF signals is found to be, respectively, of 6.0 (5.3) and 1.8 (2.6) standard deviations.

The breakdown of the main uncertainties on the measured $\sigma_{\text{ggF}} \cdot \mathscr{B}_{H \to WW^*}$ and $\sigma_{\text{VBF}} \cdot \mathscr{B}_{H \to WW^*}$ is shown in Table 8.2. For the ggF channel, the main
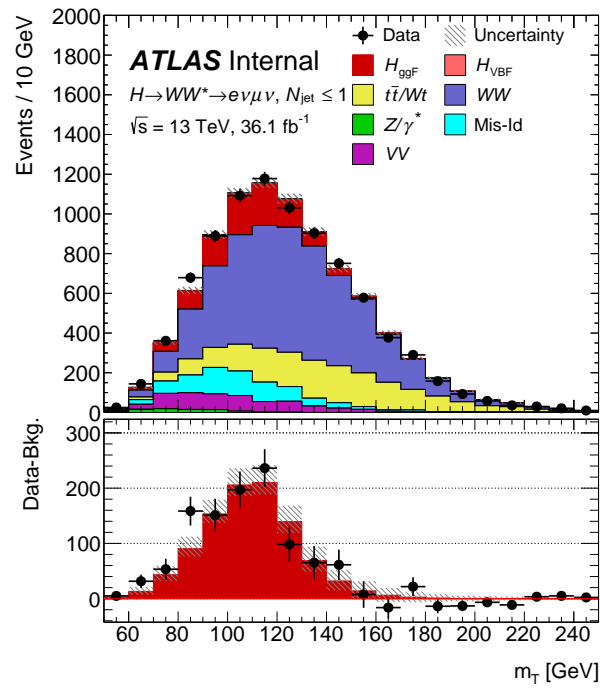
(a)
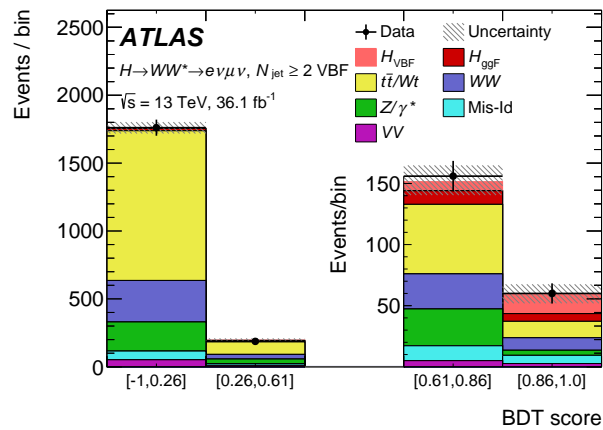
(b)

FIGURE 8.3: Post-fit distributions of the combined transverse mass for $N_{jet} \le 1$ (Fig. 8.3(a)) and of the BDT for $N_{jet} \ge 2$ (Fig. 8.3(b)). In Figure 8.3(a) the difference between the data and the estimated background compared to the distribution for a SM Higgs boson is shown in the bottom panel. In both plots, the total uncertainty is shown as an hatched band.

source is arising from the modeling of in the non-resonant WW background and on the mis-identified leptons. For the For the $N_{jet} \ge 2$ region, among the main uncertainties there is, as well, the modeling of the WW background and of the ggF signal. A large impact on the total uncertainty, especially for the
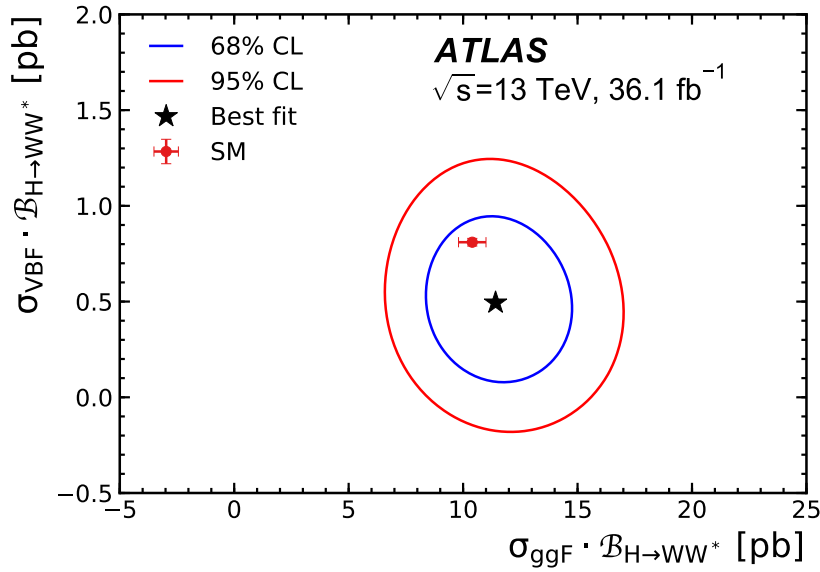
FIGURE 8.4: Two-dimensional likelihood contours of $\sigma_{\text{ggF}} \cdot \mathcal{B}_{H \rightarrow WW^*}$ vs. $\sigma_{\text{VBF}} \cdot \mathcal{B}_{H \rightarrow WW^*}$ at 68% (blue curve) and 95% (red curve) confidence level. The best fit value is shown by the black cross, while the SM prediction by the red marker.

VBF measurement, is due to the statistical uncertainty of the MC simulation.

Source	$\Delta\sigma_{\text{ggF}} \cdot \mathcal{B}_{H \rightarrow WW^*}$ [%]	$\Delta\sigma_{\text{VBF}} \cdot \mathcal{B}_{H \rightarrow WW^*}$ [%]
Data statistics	10	46
CR statistics	7	9
MC statistics	6	21
Theoretical uncertainties	10	19
ggF signal	5	13
VBF signal	<1	4
WW	6	12
Top-quark	5	5
Experimental uncertainties	8	9
b-tagging	4	6
Modelling of pile-up	5	2
Jet	2	2
Lepton	3	<1
Misidentified leptons	6	9
Luminosity	3	3
TOTAL	18	57

TABLE 8.2: Main sources of uncertainties for $\sigma_{\text{ggF}} \cdot \mathcal{B}_{H \rightarrow WW^*}$ and $\sigma_{\text{VBF}} \cdot \mathcal{B}_{H \rightarrow WW^*}$. The total uncertainty differs from the sum in quadrature of the single components because of the presence of correlations between the individual entries.

8.4   Results on the polarized couplings measurement

As previously mentioned, polarized studies follow the same SR and CRs selection as for the VBF cross-section measurement. The details of this selection are shown in Chapter 7, together with the description of the input distribution for the maximum likelihood fit.

The results are expressed, as discussed in Chapter 2, in terms of two scalar parameters a_L and a_T and in terms of pseudo-observables κ_{WW} and ϵ_{WW} (see Section. 2.4.2).

The longitudinal coupling a_L is mainly sensitive to the event rates, while the distribution of $\Delta\phi_{jj}$ changes if $a_L \neq a_T$. Similarly, κ_{WW} is sensitive to the total rates (since $\kappa_{WW} \simeq a_L$), while ϵ_{WW}, being proportional to a_L-a_T, reflects changes in the shape of the $\Delta\phi_{jj}$ distribution.

Maximum likelihood fits that take into account the shape of the input distribution and as well the total event rates are performed.

To model the signal and its dependence on the coupling parameters, the analytical morphing method is used; the input distribution to the likelihood fits is the convolution of the BDT output and $\Delta\phi_{jj}$, $BDT - \Delta\phi_{jj}$, shown in Figure 7.25.

Profiled likelihood scans over a_L and a_T (and as well over the POs) are performed. A scan over different values of the POI is performed with dedicated fits for every single point.

The signal region and background control regions defined in Chapter 7 are used as input for the fit; the SR is binned in $BDT - \Delta\phi_{jj}$, while, in the CRs, no shape information is used.

To evaluate the expected median sensitivity the *Asimov dataset* is employed: this method makes use of an artificial dataset in which all observed quantities are set equal to their expected values [154].

8.4.1   Results in terms of a_L and a_T couplings

Maximum likelihood fits over a_L and a_T have been performed in one or two dimensions. One-dimensional scans have been carried out by profiling one coupling parameter while keeping the other one constant and equal to its SM value, while two-dimensional scans by simultaneously fitting both parameters. From these fits, the top and $Z \rightarrow \tau\tau$ backgrounds normalization factors could

be extracted as mentioned in Section 7.6. These NFs are found to be:

$$NF_{Z \to \tau\tau} = 0.89 \pm 0.19(tot) \tag{8.20}$$

$$NF_{Top} = 0.99 \pm 0.06(tot) \tag{8.21}$$

The results of the 1D-likelihood scans are shown in Figure 8.5 and 8.6,

(a) Shape+rate fit   (b) Shape-only fit

FIGURE 8.5: Expected and observed shape+rate and shape-only likelihood fits on profiled a_L, while a_T is kept constant at its SM value.
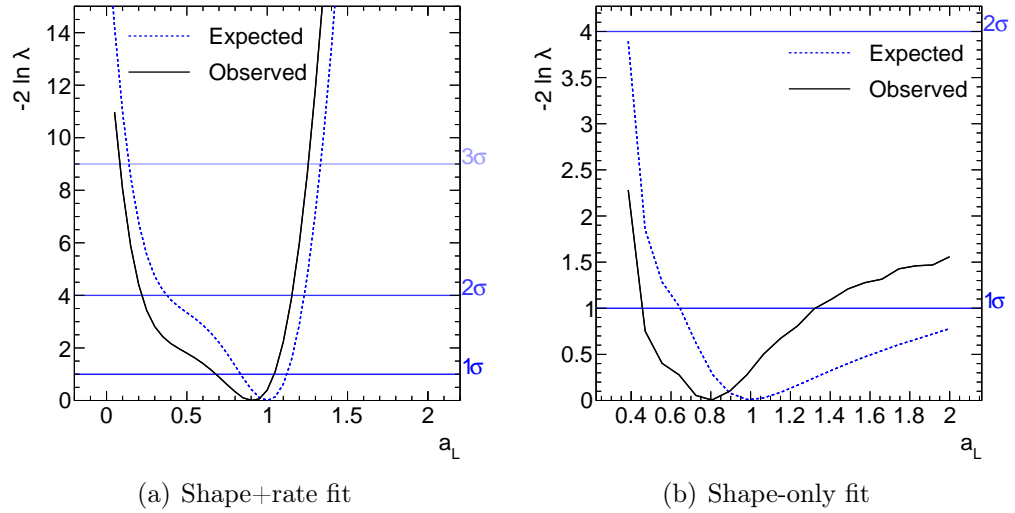

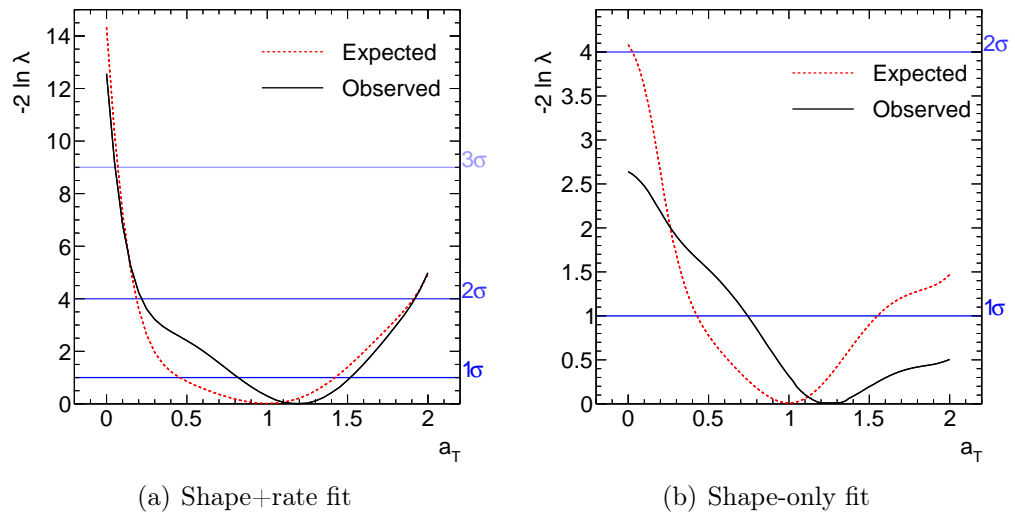(a) Shape+rate fit   (b) Shape-only fit

FIGURE 8.6: Expected and observed shape+rate and shape-only likelihood fits on profiled a_T, while a_L is kept constant at its SM value.

including all systematics. For the longitudinal coupling, both the shape and rate scan and the shape-only one are shown, in respectively, Figure 8.6(a) and Figure 8.6(b). The dashed lines indicate the expected likelihood curve, while the solid ones correspond to the observed. The largest sensitivity to a_L stems from the information on normalization, reaching as higher boundary $2(3)\sigma$ for $a_L \sim 1.15(1.3)$ and as lower boundary $2(3)\sigma$ for $a_L \sim -0.2(-0.1)$. From the shape-only fit to a_L a lower sensitivity is achieved in the observed result, almost hitting 1σ for values of $a_L \sim -0.45$ and ~ 1.3.

The sensitivity to a_T comes predominantly from the shape information, as the cross-section undergoes a minimal change with a_T. As a consequence, the exclusion increases only slightly while adding the normalization information. In the shape+normalization fit, the observed sensitivity to the a_T parameter becomes greater than $2(3)\sigma$ for a_T values lower than $\sim -0.2(-0.1)$ and greater than ~ 1.9, as shown in Figure 8.6(a). Lower sensitivity is observed in shape-only fit, reaching 1σ at $a_T \sim -0.7$, as shown in Figure 8.6(b). The observed and expected best fit values for both shape+rate and shape-only fits over a_L and a_T are summarized in Table 8.3. A good agreement, within the uncertainties, between the expected values and the observed results is achieved.

The results of a simultaneous shape+rate likelihood scan over both the a_L

POI	Fit	Expected	Observed
a_L	shape+rate ($a_T =1$)	$1.00^{+0.12}_{-0.17}$	$0.91^{+0.14}_{-0.23}$
a_L	shape ($a_T =1$)	$1.00^{+1.36}_{-0.35}$	$0.80^{+0.56}_{-0.35}$
a_T	shape+rate($a_L =1$)	$1.00^{+0.43}_{-0.54}$	$1.19^{+0.33}_{-0.37}$
a_T	shape ($a_L =1$)	$1.00^{+0.56}_{-0.57}$	$1.25^{+1.53}_{-0.51}$

TABLE 8.3: Expected and observed best-fit values of a_L and a_T from profiled fits. When profiling one of the two POIs, the other one is kept constant at its SM value.

and a_T coupling parameters are depicted in Figure 8.7. Contours at 1σ (68% CL), 2σ (95% CL), 3σ (99.73% CL), 4σ (99.993% CL) and 5σ (99.999% CL) are shown, together with the expected SM value and the best fit point. The asymmetry in the contours is due to the asymmetric behavior of the cross-section and of the $\Delta\phi_{jj}$ distribution. More details on the $\Delta\phi_{jj}$ distribution and on the expected rates can be found in Appendix A. A good agreement

between the SM predictions and observed best-fit point is achieved.
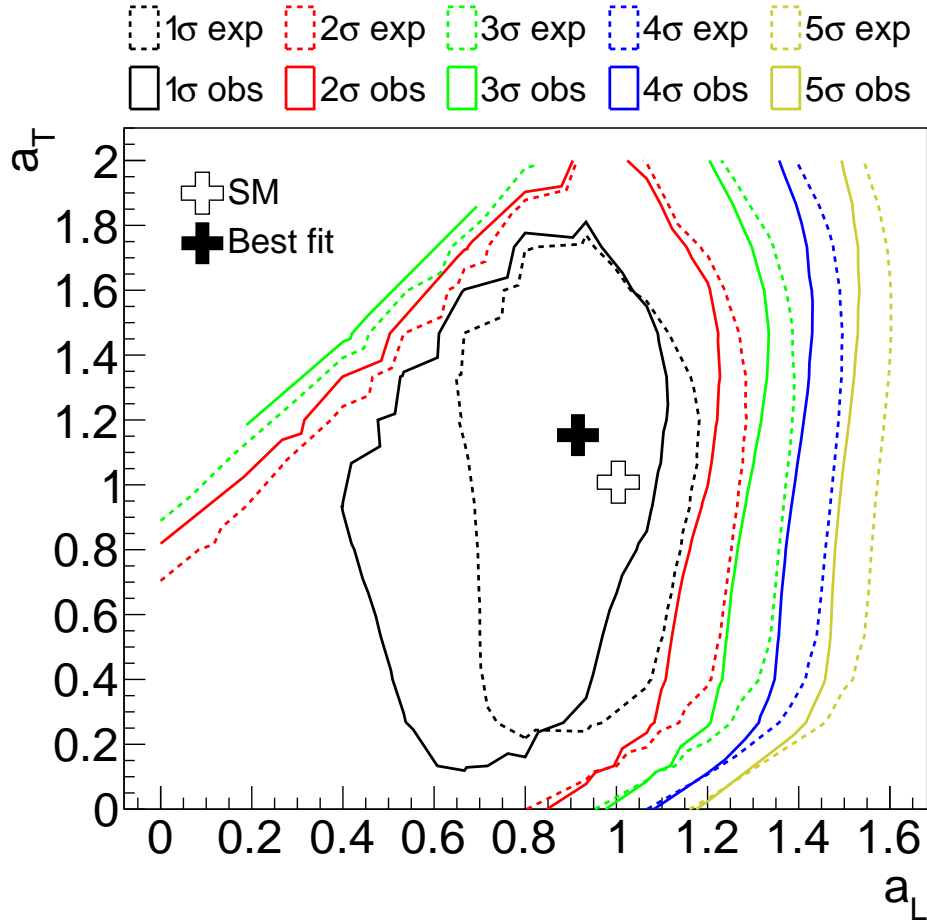
FIGURE 8.7: Expected and observed maximum likelihood fit over a_L and a_T. Both normalization and shape are taken into account in the fit. Statistical and systematical uncertainties are included. The concentric curves represent, respectively, from the innermost to the outermost one, the contours at 1σ (68% CL), 2σ (95% CL), 3σ (99.73% CL), 4σ (99.993% CL) and 5σ (99.999% CL). The expected SM value and the best fit point are also shown.

8.4.2 Results in terms of pseudo-observables

As shown in Section 2.4.2, the coupling parameters a_L and a_T are mapped in POs as:

$$a_L \simeq \kappa_{WW} \qquad a_L - a_T \simeq -\frac{m_H^2}{2m_W^2}\varepsilon_{WW} \qquad (8.22)$$

With this mapping, the SM values are at $\kappa_{WW} = 1$ and $\varepsilon_{WW} = 0$.

The results of the 1D-likelihood scans are shown in Fig 8.8. In Figure 8.8(a) the observed (black solid line) and expected (green dashed line) scans over the κ_{WW} observable, while ε_{WW} is set to 0, are shown. This is similar to the a_L one, shown in Figure 8.5(a), apart from a lower sensitivity on the left-hand side of the scan: this difference is due to the fact that in this case a_L-a_T is set to zero, while in Figure 8.5(a) a_T is set to 1. A upper boundary on κ_{WW} can be set at $2(3)\sigma$ for $\kappa_{WW} \sim 1.15(1.3)$. Figure 8.8(b) shows the shape+rate scan over ε_{WW}, while keeping $\kappa_{WW} = 1$. The magenta line corresponds to the expected likelihood, while the black solid line to the observed one. A higher sensitivity is obtained, as expected, from this fit with respect to the a_T one, since the difference in shape arises when $a_L \neq a_T$. An upper limit on ε_{WW} can be set at $2(3)\sigma$ for $\varepsilon_{WW} \sim 0.8(0.9)$, and a lower one at 2σ for $\varepsilon_{WW} \sim -0.9$. The observed and expected best fit values for both shape+rate fits over κ_{WW} and ε_{WW} are summarized in Table 8.4. A good agreement, within the uncertainties, between the expected values and the observed ones is found.

(a) Shape+rate - $\varepsilon_{WW} = 0$ (b) Shape+rate fit - $\kappa_{WW} = 1$
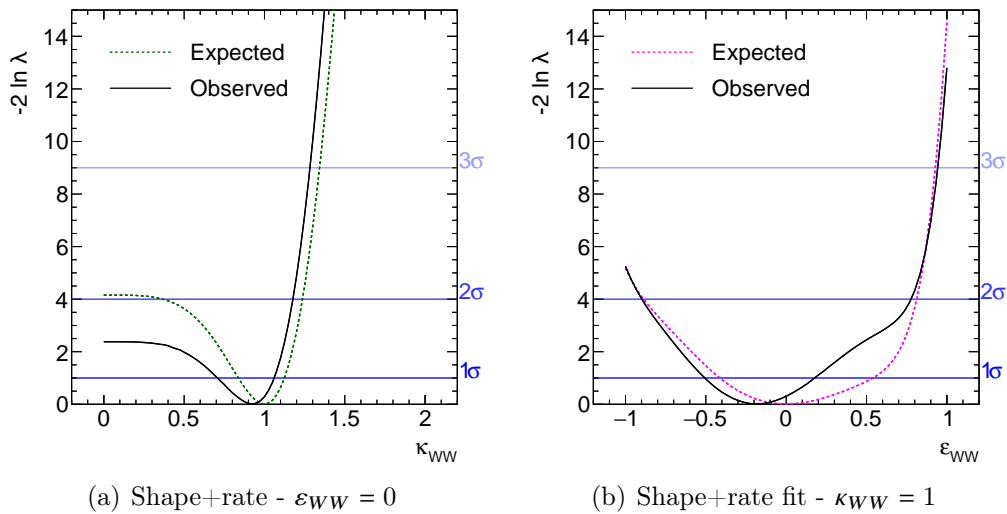
FIGURE 8.8: Expected and observed likelihood scans for over the κ_{WW} and ε_{WW} observables.

The simultaneous scan over both the κ_{WW} and ε_{WW} observables is shown in Figure 8.9. Contours at 1σ (68% CL), 2σ (95% CL), 3σ (99.73% CL), 4σ (99.993% CL) and 5σ (99.999% CL) are shown, together with the expected SM value and the best fit point. A good agreement between the SM predictions and observed best-fit point is achieved.
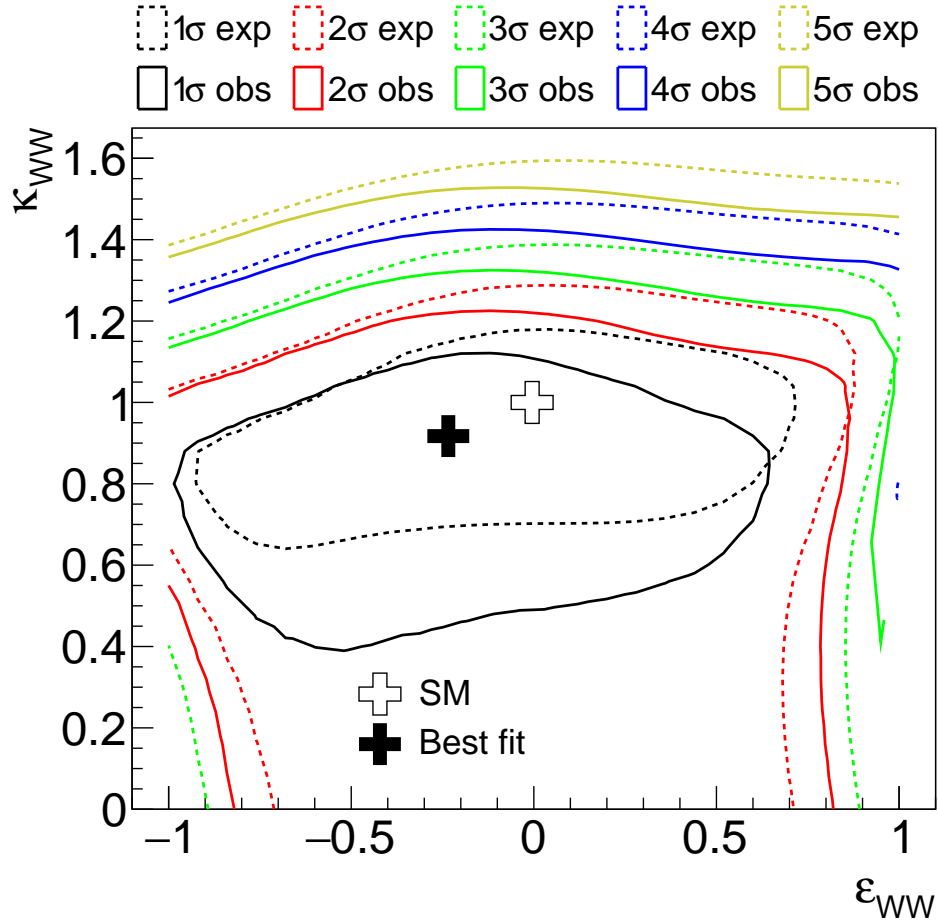
FIGURE 8.9: Expected and observed maximum likelihood fit over the pseudo-observables κ_{WW} and ε_{WW}. Both normalization and shape are taken into account in the fit. Statistical and systematical uncertainties are included. The concentric curves represent, respectively, from the innermost to the outermost one, the contours at 1σ (68% CL), 2σ (95% CL), 3σ (99.73% CL), 4σ (99.993% CL) and 5σ (99.999% CL). The expected SM value and the best fit point are also shown.

POI	Fit	Expected	Observed
κ_{WW}	shape+rate ($\varepsilon_{WW} = 0$)	$1.00^{+0.13}_{-0.16}$	$0.92^{+0.14}_{-0.28}$
ε_{WW}	shape+rate ($\kappa_{WW} = 1$)	$0.00^{+0.54}_{-0.42}$	$-0.18^{+0.36}_{-0.32}$

TABLE 8.4: Expected and observed best fit values of κ_{WW} and ε_{WW} from 1D-fits.

8.5   Breakdown of the systematics

The ranking of the uncertainties for the fits over a_L and a_T is shown in Table 8.5. The breakdowns are estimated by comparing the unconditional fit, in which all the systematics are floating, with the conditional one, in which the studied parameter is fixed to its best-fit value. They are obtained as follows:

$$Breakdown = \sqrt{\sigma^2_{uncond} - \sigma^2_{cond}}. \qquad (8.23)$$

The main source of uncertainty for the longitudinal coupling a_L arises from the theoretical uncertainties, while the a_T coupling is instead dominated by statistical uncertainties from data. In both cases, the largest theory uncertainties are due to the modeling of the $BDT - \Delta\phi_{jj}$ distribution for the top-quark and WW backgrounds. For the top-quark background the largest systematics arise from the shape uncertainty on the matrix element (~5% on a_L, ~9% on a_T), on the initial/final state radiation (~5% on a_L, ~6% on a_T) and on the parton shower (~4% on a_L, ~2% on a_T) described in Section 7.8.2.1. The presence of correlations between the single uncertainties causes the total uncertainty to differ from the sum in quadrature of the single components. The CR is not constraining these large shape uncertainties because, having only one bin, it only constrains the normalization ones. Also the largest contributions to the WW uncertainties are from shape uncertainties. For this background, the main ones are caused by the generator choice (~4% on a_L, ~4% on a_T) and the modeling and QCD scales (~3% on a_L, ~4% on a_T), described in Section 7.8.2.2. Furthermore, another source is the modeling of the VBF signal, due to the large parton shower normalization uncertainty (~4% on a_L, ~5% on a_T). This uncertainty, however, takes into account, as explained in Section 7.8.2.5, the discrepancy between NLO and LO calculations. A rather large impact is due to uncertainties arising from the mis-identified leptons, while the main experimental uncertainties are due to the jet energy scales and resolution (JES and JER) and pile-up. The data statistical uncertainties and the fake factor ones in the future will of course benefit from more statistics: for the a_T coupling, about 120 fb^{-1} of integrated luminosity will be necessary to make the systematics uncertainty dominant over data.

Source	a_L [%]	a_T [%]
Data statistics	11	31
Total systematics	14	17
Theoretical uncertainties	12	14
Top theoretical uncertainties	7	7
WW theoretical uncertainties	6	6
VBF theoretical uncertainties	4	6
ggF theoretical uncertainties	4	3
Z+jets theoretical uncertainties	2	3
Experimental systematic uncertainties	6	6
Jet	2	5
Pile-up	< 1	3
b-tagging	1	2
Misidentified leptons	4	2
Leptons	< 1	< 1
Monte Carlo statistics	2	6
Background statistics	2	6
Signal statistics	< 1	< 1
Background normalizations	< 1	< 1

TABLE 8.5: Observed uncertainties on a_L and a_T. For each sub-category only the most important sources are listed.

8.6 Conclusions

The Higgs boson cross-section results, from a measurement performed with 36.1 fb^{-1} of integrated luminosity in the ggF and VBF production channels, have been described in this chapter. The cross-sections times the $H \to WW^*$ branching ratio are measured to be $11.4^{+2.2}_{-2.1}$ pb and $0.50^{+0.29}_{-0.28}$ pb for ggF and VBF, respectively. A significance of 6σ is reached in the ggF channel and the cross-section measurement is performed in the $N_{\text{jet}} = 0$ and $N_{\text{jet}} = 1$ topologies. The main uncertainties are caused by the modeling of the dominant WW background. The experimental ones are mainly due to the tagging of b-quarks and to the mis-identification of the leptons.

The $N_{\text{jet}} \geq 2$ case, that targets the VBF production mechanism, presents a lower significance of 1.8σ. The cross-section measurement in this channel is still limited by statistics, the main source of uncertainty. Theory systematics follows and, similarly to ggF, these are mainly due to the modeling of the WW background, where SHERPA 2.2.2 is compared with MAD-GRAPH5_AMC@NLO . Future analysis will certainly benefit from a better understanding of the MC generators used for this process. Furthermore, if a dedicated control region will be built, more data will help in constraining this background.

Another source arises from the modeling of the ggF signal: in the two jet exclusive region a large uncertainty is caused by the QCD scales. Moreover, the fake factor estimation gives a large contribution. This channel will certainly profit from a larger dataset. With approximately 200 fb^{-1} of integrated luminosity, the statistical uncertainties will eventually become smaller than the theoretical ones.

The focus of this thesis is on the first measurement of the Higgs couplings to polarized vector bosons ever performed. Results are presented in terms of the couplings parameters a_L and a_T and in terms of pseudo-observables. Considering both the shape of the $\Delta\phi_{jj}$ distribution and the total rates, the observed values of the longitudinal and transversal couplings are $a_L = 0.91^{+0.14}_{-0.23}$ and $a_T = 1.19^{+0.33}_{-0.37}$. The results are in agreement with the SM predictions within the uncertainties. Overall, a better sensitivity is obtained for the longitudinal coupling than for the transversal one. The main uncertainties on a_L are due to the modeling of the main backgrounds, WW and $t\bar{t}$, and on the VBF signal. The transversal coupling measurement is instead still limited by statistics. However, with at least 120 fb^{-1} of integrated luminosity the theoretical uncertainties will become dominant. Therefore, this study will certainly benefit from the full Run 2 dataset: with four times the actual integrated luminosity, better exclusion limits will be set. Exclusion limits at 95% CL could be set on a_L variations larger than 20% and on a_T variations larger than 40%, considering both shape and total rates. More details are given in Appendix B.

Nonetheless, also other improvements should be taken into account. It should be worth investigating other variables sensitive to the polarization, such as the angular correlations between the Higgs decay products with the Cabibbo-Maksymowicz variables [163]. Those angles, for which the description can be found in Ref. [164], are known to be sensitive to the spin of the decaying resonance (in our case, the Higgs boson) and therefore could also carry information on the polarization. These have not been studied in this thesis because of the difficulty to reconstruct the Higgs rest frame in the $H \rightarrow WW^* \rightarrow \ell\nu\ell\nu$ channel. A way around the problem should be to reconstruct the Higgs rest frame in the $H \rightarrow WW^* \rightarrow \ell\nu\ell\nu$ channel following the method in Ref. [165] or perform the analysis in the VBF $H \rightarrow ZZ^*$ channel, where the Higgs boson rest frame can be fully reconstructed.

Morphing the $\Delta\phi_{jj}$ distribution

To fully understand the results shown in Chapter 8, the behavior of the shape of the azimuthal angle between the tagging jets has to be studied. With the MC samples produced, however, it is not possible to entirely cover the coupling parameter space in a_L and a_T. Therefore, the analytic morphing method, explained in Section 8.2, is employed to model such distribution. Figure A.1 shows the morphed number of events as a function of the coupling parameters a_L and a_T in the VBF SR (at the $Z \rightarrow \tau\tau$ veto). Instead, in
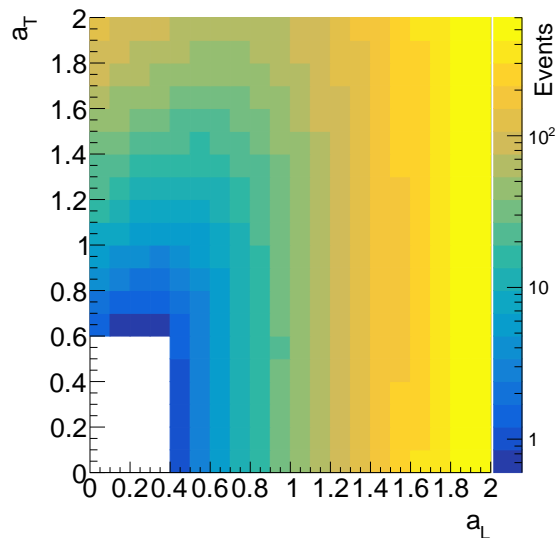

FIGURE A.1: Morphed number of events as a function of the coupling parameters a_L and a_T in the VBF SR. The white area in the plot correspond to bins with a zero-value of the morphed number of events.

Figure A.2 and A.3 are given the $\Delta\phi_{jj}$ distribution changing either a_L or a_T, while keeping the other coupling to its SM value. On the left hand side the

distributions normalized to the number of events in the VBF SR are shown, while on the right hand side normalized to unity.

The trend of the total rates and the differences in shape changing a_L and a_T are helpful to understand the 1D and 2D likelihood scans presented in Section 8.4.

(a) $0 \leq a_L \leq 1$

(b) $0 \leq a_L \leq 1$

(c) $1 \leq a_L \leq 2$

(d) $1 \leq a_L \leq 2$
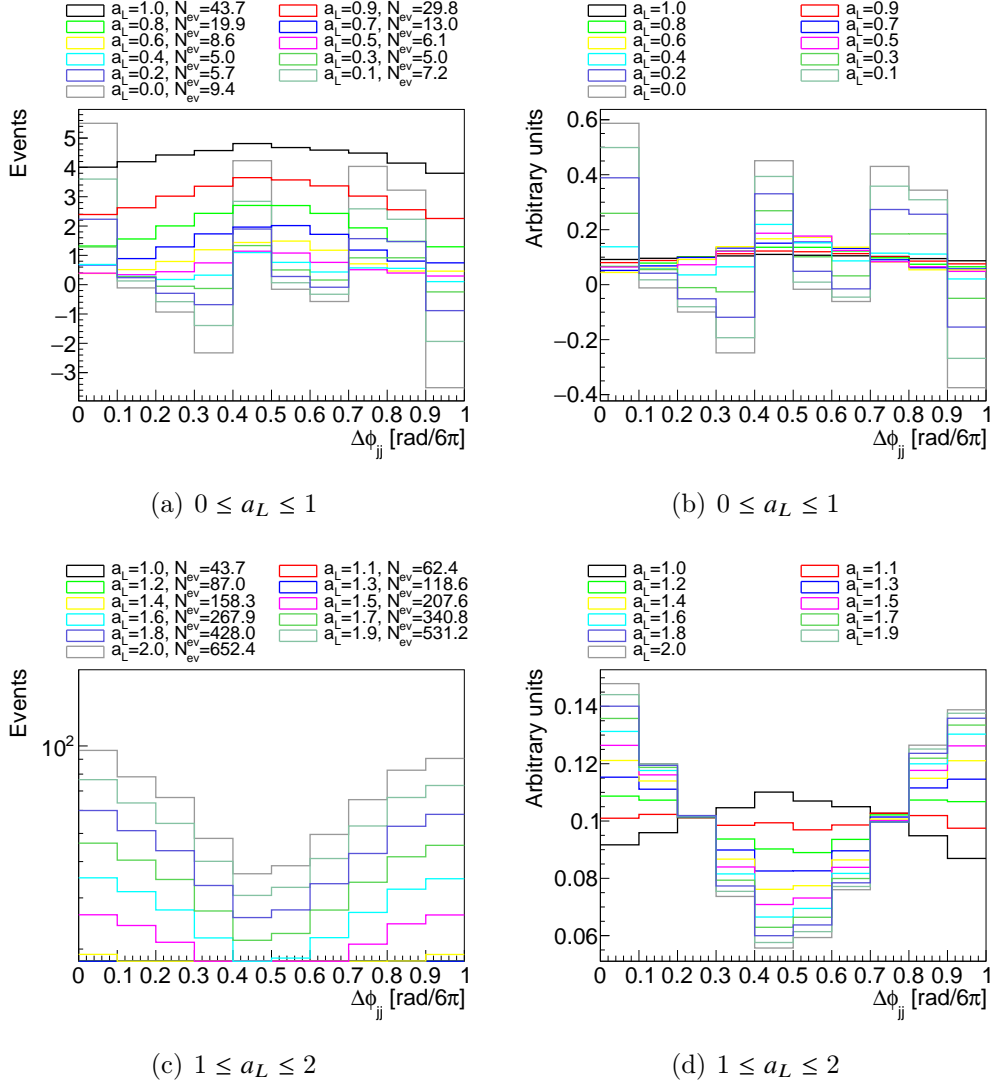
FIGURE A.2: Morphed $\Delta\phi_{jj}$ distributions changing a_L while keeping at the SM value ($a_T = 1$).

(a) $0 \le a_T \le 1$

(b) $0 \le a_T \le 1$
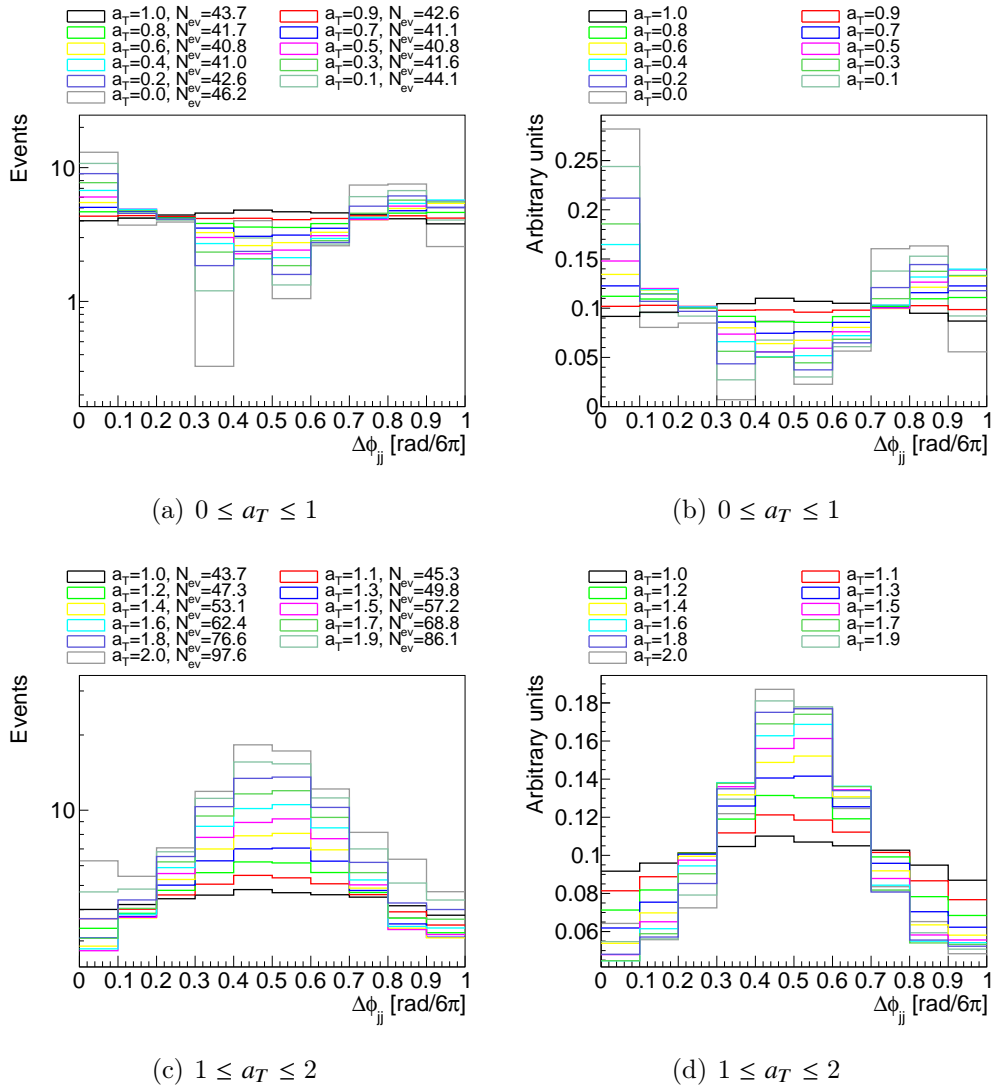
(c) $1 \le a_T \le 2$

(d) $1 \le a_T \le 2$

FIGURE A.3: Morphed $\Delta\phi_{jj}$ distributions changing a_T while keeping at the SM value ($a_L = 1$).

Prospects

In this appendix, profile likelihood scans are shown at four times higher integrated luminosity $(150 fb^{-1})$. In this way, a rough estimate of the sensitivity to a_L and a_T with the full Run 2 dataset can be done. From Figures B.1, that show the expected shape+rate and shape-only profile fits on a_L and a_T at $150 fb^{-1}$ of integrated luminosity, upper and lower limits can be set. Variations larger than $\pm 20\%$ on the longitudinal coupling can be excluded at 2σ considering both shape and rate. If only the shape is taken into account, 2σ are reached on the lower bound, at approximately $a_L = $ -0.55. Variations on a_T larger than 40% will be excluded at 2σ considering both shape and rate. In the shape-only fit, the 2σ are hit at approximately $a_T = $-0.65 and $a_T = $0.9.
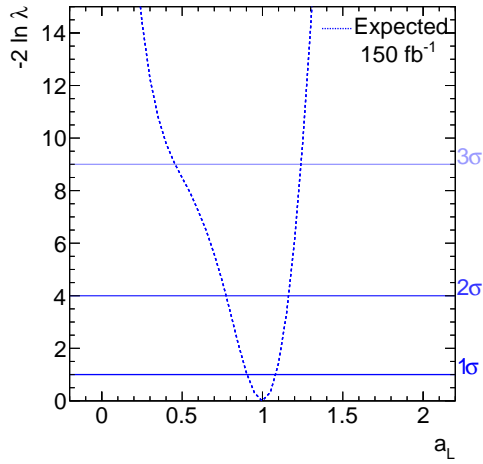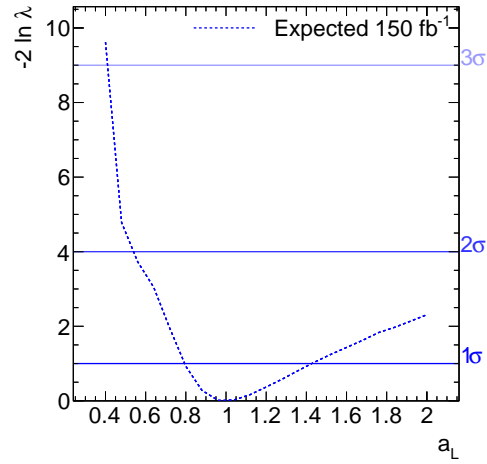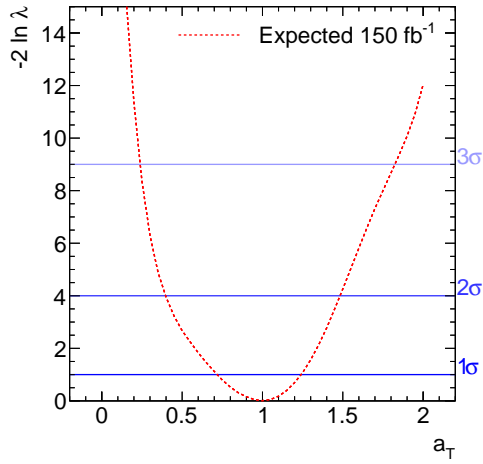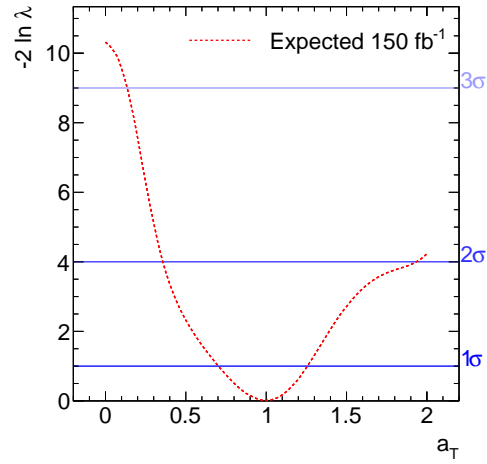
(a) Shape+rate fit on a_L

(b) Shape-only fit on a_L

(c) Shape+rate fit on a_T

(d) Shape-only fit on a_T

FIGURE B.1:   Expected shape+rate and shape-only likeli-
hood fits at $150 fb^{-1}$ of integrated luminosity on profiled a_L
(Fig. B.1(a) and B.1(b)) and a_T (Fig. B.1(c) and B.1(d)), while
the other POI is kept constant at its SM value.

Bibliography

[1] ATLAS Collaboration. *Technical Design Report for the ATLAS Inner Tracker Strip Detector*. Tech. rep. CERN-LHCC-2017-005. ATLAS-TDR-025. Geneva: CERN, 2017.

[2] M. Aaboud et al. *Measurements of gluon-gluon fusion and vector-boson fusion Higgs boson production cross-sections in the $H \rightarrow WW^* \rightarrow e\nu\mu\nu$ decay channel in pp collisions at $\sqrt{s} = 13$ TeV with the ATLAS detector*. In: (2018).

[3] M. Thomson. *Modern Particle Physics*. Cambridge University Press, 2013.

[4] A. Djouadi. *The Anatomy of electro-weak symmetry breaking. I: The Higgs boson in the standard model*. In: *Phys. Rept.* 457 (2008), pp. 1–216.

[5] S. Dittmaier and M. Schumacher. *The Higgs Boson in the Standard Model - From LEP to LHC: Expectations, Searches, and Discovery of a Candidate*. In: *Prog. Part. Nucl. Phys.* 70 (2013), pp. 1–54.

[6] W. Hollik. "Quantum field theory and the Standard Model". In: *High-energy physics. Proceedings, 17th European School, ESHEP 2009, Bautzen, Germany, June 14-27, 2009*. 2010.

[7] G. Aad et al. *Observation of a new particle in the search for the Standard Model Higgs boson with the ATLAS detector at the LHC*. In: *Phys. Lett.* B716 (2012), pp. 1–29.

[8] G. Aad et al. *A particle consistent with the Higgs Boson observed with the ATLAS Detector at the Large Hadron Collider*. In: *Science* 338 (2012), pp. 1576–1582.

[9] S. Chatrchyan et al. *Observation of a new boson at a mass of 125 GeV with the CMS experiment at the LHC*. In: *Phys. Lett.* B716 (2012), pp. 30–61.

[10] S. Glashow. *Partial Symmetries of Weak Interactions.* In: *Nucl.Phys.* 22 (1961), pp. 579–588.

[11] S. Weinberg. *A Model of Leptons.* In: *Phys.Rev.Lett.* 19 (1967), pp. 1264–1266.

[12] A. Salam. *Weak and Electromagnetic Interactions.* In: *Conf.Proc.* C680519 (1968), pp. 367–377.

[13] G. 't Hooft and M. Veltman. *Regularization and Renormalization of Gauge Fields.* In: *Nucl.Phys.* B44 (1972), pp. 189–213.

[14] C. Patrignani et al. *Review of Particle Physics.* In: *Chin. Phys.* C40.10 (2016), p. 100001.

[15] Y. Fukuda et al. *Evidence for oscillation of atmospheric neutrinos.* In: *Phys. Rev. Lett.* 81 (1998), pp. 1562–1567.

[16] R. Aaij et al. *Observation of the resonant character of the $Z(4430)^-$ state.* In: *Phys. Rev. Lett.* 112.22 (2014), p. 222002.

[17] M. Ablikim et al. *Observation of a Charged Charmoniumlike Structure in $e^+e^- \to \pi^+\pi^- J/\Psi$ at $\sqrt{s} = 4.26$ GeV.* In: *Phys. Rev. Lett.* 110 (2013), p. 252001.

[18] R. Aaij et al. *Observation of $J/\psi p$ Resonances Consistent with Pentaquark States in $\Lambda_b^0 \to J/\psi K^- p$ Decays.* In: *Phys. Rev. Lett.* 115 (2015), p. 072001.

[19] C. N. Yang and R. L. Mills. *Conservation of Isotopic Spin and Isotopic Gauge Invariance.* In: *Phys. Rev.* 96 (1 1954), pp. 191–195.

[20] S. P. Martin. *A Supersymmetry primer.* In: (1997). [Adv. Ser. Direct. High Energy Phys.18,1(1998)], pp. 1–98.

[21] J. F. Gunion and H. E. Haber. *The CP conserving two Higgs doublet model: The Approach to the decoupling limit.* In: *Phys. Rev.* D67 (2003), p. 075019.

[22] G. C. Branco et al. *Theory and phenomenology of two-Higgs-doublet models.* In: *Phys. Rept.* 516 (2012), pp. 1–102.

[23] G. F. Giudice et al. *The Strongly-Interacting Light Higgs.* In: *JHEP* 06 (2007), p. 045.

[24] *LHC Higgs Cross Section WG Picture Gallery.* URL: https://twiki.cern.ch/twiki/bin/view/LHCPhysics/LHCHXSWGCrossSectionsFigures.

[25] M. Aaboud et al. *Measurement of the Higgs boson mass in the $H \rightarrow ZZ^* \rightarrow 4\ell$ and $H \rightarrow \gamma\gamma$ channels with $\sqrt{s} = 13$ TeV pp collisions using the ATLAS detector*. In: (2018).

[26] G. Aad et al. *Determination of spin and parity of the Higgs boson in the $WW^* \rightarrow e\nu\mu\nu$ decay channel with the ATLAS detector*. In: *Eur. Phys. J.* C75.5 (2015), p. 231.

[27] G. Aad et al. *Study of the spin and parity of the Higgs boson in diboson decays with the ATLAS detector*. In: *Eur. Phys. J.* C75.10 (2015). [Erratum: Eur. Phys. J.C76,no.3,152(2016)], p. 476.

[28] J. Brehmer, J. Jaeckel, and T. Plehn. *Polarized WW Scattering on the Higgs Pole*. In: *Phys.Rev.* D90.5 (2014), p. 054023.

[29] A. M. Sirunyan et al. *Observation of electroweak production of same-sign W boson pairs in the two jet and two same-sign lepton final state in proton-proton collisions at $\sqrt{s} = 13$ TeV*. In: *Phys. Rev. Lett.* 120.8 (2018), p. 081801.

[30] G. Aad et al. *Evidence for Electroweak Production of $W^\pm W^\pm jj$ in pp Collisions at $\sqrt{s} = 8$ TeV with the ATLAS Detector*. In: *Phys. Rev. Lett.* 113.14 (2014), p. 141803.

[31] ATLAS Collaboration. *Observation of electroweak $W^\pm Z$ boson pair production in association with two jets in pp collisions at $\sqrt{s} = 13 TeV$ with the ATLAS Detector*. Tech. rep. ATLAS-CONF-2018-033. Geneva: CERN, 2018.

[32] CMS Collaboration. *Measurement of electroweak WZ production and search for new physics in pp collisions at sqrt(s) = 13 TeV*. Tech. rep. CMS-PAS-SMP-18-001. Geneva: CERN, 2018.

[33] B. W. Lee, C. Quigg, and H. B. Thacker. *Weak interactions at very high energies: The role of the Higgs-boson mass*. In: *Phys. Rev. D* 16 (5 1977), pp. 1519–1531.

[34] K. Cheung, C.-W. Chiang, and T.-C. Yuan. *Partially Strong WW Scattering*. In: *Phys. Rev.* D78 (2008), p. 051701.

[35] R. Contino et al. *Effective Lagrangian for a light Higgs-like scalar*. In: *JHEP* 07 (2013), p. 035.

[36] K. Hagiwara, R. Szalapski, and D. Zeppenfeld. *Anomalous Higgs boson production and decay*. In: *Phys. Lett.* B318 (1993), pp. 155–162.

[37]   K. Hagiwara et al. *Low-energy effects of new interactions in the elec-troweak boson sector*. In: *Phys. Rev.* D48 (1993), pp. 2182–2203.

[38]   D. Z. Marco Sekulla. *Contribution of effective operators to a_L and a_T*. Personal communication. 2017.

[39]   M. Gonzalez-Alonso et al. *Pseudo-observables in Higgs decays*. In: *Eur. Phys. J.* C75 (2015), p. 128.

[40]   A. Greljo et al. *Pseudo-observables in electroweak Higgs production*. In: *Eur. Phys. J.* C76.3 (2016), p. 158.

[41]   G. Isidori. *Matching between PO and a_L, a_T*. Personal communication. 2017.

[42]   W. W. Armstrong et al. *ATLAS: Technical proposal for a general-purpose p p experiment at the Large Hadron Collider at CERN*. In: (1994).

[43]   ATLAS Collaboration. *The ATLAS Experiment at the CERN Large Hadron Collider*. In: *Journal of Instrumentation* 3.08 (2008), S08003.

[44]   O. S. Brüning et al. *LHC Design Report*. CERN Yellow Reports: Monographs. Geneva: CERN, 2004.

[45]   L. Evans and P. Bryant. *LHC Machine*. In: *JINST* 3 (2008), S08001.

[46]   S. Chatrchyan et al. *The CMS Experiment at the CERN LHC*. In: *JINST* 3 (2008), S08004.

[47]   LHCb Collaboration. *The LHCb Detector at the LHC*. In: *Journal of Instrumentation* 3.08 (2008), S08005.

[48]   K. Aamodt et al. *The ALICE experiment at the CERN LHC*. In: *JINST* 3 (2008), S08002.

[49]   J. Haffner. *The CERN accelerator complex. Complexe des accélérateurs du CERN*. In: (2013). General Photo.

[50]   ATLAS Collaboration. *Luminosity Results Run 2*. URL: https://twiki.cern.ch/twiki/bin/view/AtlasPublic/LuminosityPublicResultsRun2.

[51]   J. Pequenao. "Computer generated image of the whole ATLAS detector". 2008.

[52]   J. Pequenao. "Computer generated image of the ATLAS inner detector". 2008.

[53]   J. Schieck. *Track-based alignment for the ATLAS Inner Detector Tracking System*. In: *JINST* 7 (2012), p. C01012.

[54] M Capeans et al. *ATLAS Insertable B-Layer Technical Design Report.* Tech. rep. CERN-LHCC-2010-013. ATLAS-TDR-19. 2010.

[55] N. Wermes and G Hallewel. *ATLAS pixel detector: Technical Design Report.* Technical Design Report ATLAS. Geneva: CERN, 1998.

[56] ATLAS Collaboration. *ATLAS inner detector: Technical Design Report, 1.* Technical Design Report ATLAS. Geneva: CERN, 1997.

[57] S. Haywood et al. *ATLAS inner detector: Technical Design Report, 2.* Technical Design Report ATLAS. Geneva: CERN, 1997.

[58] R. Nisius. *End-cap modules for the ATLAS SCT.* In: *Nuclear Instruments and Methods in Physics Research Section A: Accelerators, Spectrometers, Detectors and Associated Equipment* 530.1 (2004). Proceedings of the 6th International Conference on Large Scale Applications and Radiation Hardness of Semiconductor Detectors, pp. 44 –49.

[59] A. Abdesselam and T. Akimoto. *The Barrel Modules of the ATLAS SemiConductor Tracker.* Tech. rep. ATL-INDET-PUB-2006-005. ATL-COM-INDET-2006-009. CERN-ATL-COM-INDET-2006-009. Geneva: CERN, 2006.

[60] F. Campabadal et al. *Design and performance of the ABCD3TA ASIC for readout of silicon strip detectors in the ATLAS semiconductor tracker.* In: *Nuclear Instruments and Methods in Physics Research Section A: Accelerators, Spectrometers, Detectors and Associated Equipment* 552.3 (2005), pp. 292 –328.

[61] T. A. T. collaboration. *The ATLAS Transition Radiation Tracker (TRT) proportional drift tube: design and performance.* In: *Journal of Instrumentation* 3.02 (2008), P02013.

[62] J. Pequenao. "Computer Generated image of the ATLAS calorimeter". 2008.

[63] ATLAS Collaboration. *ATLAS liquid-argon calorimeter: Technical Design Report.* Technical Design Report ATLAS. Geneva: CERN, 1996.

[64] ATLAS Collaboration. *ATLAS tile calorimeter: Technical Design Report.* Technical Design Report ATLAS. Geneva: CERN, 1996.

[65] ATLAS Collaboration. *ATLAS muon spectrometer: Technical Design Report.* Technical Design Report ATLAS. Geneva: CERN, 1997.

[66] M. Aaboud et al. *Performance of the ATLAS Trigger System in 2015.* In: *Eur. Phys. J.* C77.5 (2017), p. 317.

[67]   E. Simioni et al. *Topological and Central Trigger Processor for 2014 LHC luminosities*. Tech. rep. ATL-DAQ-PROC-2012-041. Geneva: CERN, 2012.

[68]   M. Shochet et al. *Fast TracKer (FTK) Technical Design Report*. Tech. rep. CERN-LHCC-2013-007. ATLAS-TDR-021. ATLAS Fast Tracker Technical Design Report. 2013.

[69]   The ATLAS TDAQ Collaboration. *The ATLAS Data Acquisition and High Level Trigger system*. In: *Journal of Instrumentation* 11.06 (2016), P06008.

[70]   G. Apollinari et al. *High-Luminosity Large Hadron Collider (HL-LHC): Preliminary Design Report*. CERN Yellow Reports: Monographs. Geneva: CERN, 2015.

[71]   ATLAS Collaboration. *Letter of Intent for the Phase-II Upgrade of the ATLAS Experiment*. Tech. rep. CERN-LHCC-2012-022. LHCC-I-023. Geneva: CERN, 2012.

[72]   ATLAS Collaboration. *Technical Design Report for the ATLAS Inner Tracker Pixel Detector*. Tech. rep. CERN-LHCC-2017-021. ATLAS-TDR-030. Geneva: CERN, 2017.

[73]   ATLAS Collaboration. *ATLAS Phase-II Upgrade Scoping Document*. Tech. rep. CERN-LHCC-2015-020. LHCC-G-166. Geneva: CERN, 2015.

[74]   ATLAS Collaboration. *Expected Performance of the ATLAS Inner Tracker at the High-Luminosity LHC*. Tech. rep. ATL-PHYS-PUB-2016-025. Geneva: CERN, 2016.

[75]   ATLAS Collaboration. *Expected performance for an upgraded ATLAS detector at High-Luminosity LHC*. Tech. rep. ATL-PHYS-PUB-2016-026. Geneva: CERN, 2016.

[76]   W. Lu et al. *Development of the ABCStar front-end chip for the ATLAS silicon strip upgrade*. In: *Journal of Instrumentation* 12.04 (2017), p. C04017.

[77]   URL: https://telescopes.desy.de/Main_Page.

[78]   H. Jansen et al. *Performance of the EUDET-type beam telescopes*. In: *EPJ Tech. Instrum.* 3.1 (2016), p. 7.

[79]   D. D. S. Kulis. http://skulis.web.cern.ch/skulis/telescope/. 2014.

[80] M. G.-S. et al. *The FE-I4 pixel readout integrated circuit*. In: *Nuclear Instruments and Methods in Physics Research Section A: Accelerators, Spectrometers, Detectors and Associated Equipment* 636.1, Supplement (2011), S155 –S159.

[81] C. E. *EUDAQ Software User Manual. E. Corrin*. In: *EUDET-Memo-2010-01* (2010).

[82] *Project Specification v4.3 Project Name: ABC130 ASIC*. 2013. URL: https://indico.cern.ch/event/227566/attachments/374699/521269/ABC130_DRAFT_Specification04_3.pdf.

[83] J. Kaplon. *The ABCN front-end chip for ATLAS Inner Detector Upgrade*. In: (2008).

[84] Y. U. et al. *Development of n in p large-area silicon microstrip sensors for very high radiation environments ATLAS12 design and initial results*. In: *Nuclear Instruments and Methods in Physics Research Section A: Accelerators, Spectrometers, Detectors and Associated Equipment* (2014).

[85] A. Bulgheroni et al. *EUTelescope: Tracking Software*. In: *EUDET-Memo-2007-20* (2007).

[86] *Millepede II*. http://www.desy.de/ kleinwrt/MP2/doc/html/index.html.

[87] C. Kleinwort. *General broken lines as advanced track fitting method*. In: *Nuclear Instruments and Methods in Physics Research Section A: Accelerators, Spectrometers, Detectors and Associated Equipment* 673 (2012), pp. 107 –110.

[88] R. Peschke. "Characterisation of the ATLAS ITK Strips Front-End Chip and Development of EUDAQ 2.0 for the EUDET-Style Pixel Telescopes". Universität Hamburg, Diss., 2016. Dr. Hamburg: Universität Hamburg, 2017.

[89] R. Mori. Personal communication. 2015.

[90] M. H. et al. *Alibava : A portable readout system for silicon microstrip sensors*. In: (2007).

[91] M. A. Dobbs et al. "Les Houches guidebook to Monte Carlo generators for hadron collider physics". In: *Physics at TeV colliders. Proceedings, Workshop, Les Houches, France, May 26-June 3, 2003*. 2004, pp. 411–459.

[92]   L. N. Lipatov. *The parton model and perturbation theory.* In: *Sov. J. Nucl. Phys.* 20 (1975). [Yad. Fiz.20,181(1974)], pp. 94–102.

[93]   V. N. Gribov and L. N. Lipatov. *Deep inelastic e p scattering in perturbation theory.* In: *Sov. J. Nucl. Phys.* 15 (1972). [Yad. Fiz.15,781(1972)], pp. 438–450.

[94]   G. Altarelli and G. Parisi. *Asymptotic Freedom in Parton Language.* In: *Nucl. Phys.* B126 (1977), pp. 298–318.

[95]   P. M. Nadolsky et al. *Implications of CTEQ global analysis for collider observables.* In: *Phys. Rev.* D78 (2008), p. 013004.

[96]   F. D. Aaron et al. *Combined Measurement and QCD Analysis of the Inclusive e+- p Scattering Cross Sections at HERA.* In: *JHEP* 01 (2010), p. 109.

[97]   A. D. Martin et al. *Parton distributions for the LHC.* In: *Eur. Phys. J.* C63 (2009), pp. 189–285.

[98]   R. D. Ball et al. *Parton distributions with LHC data.* In: *Nucl. Phys.* B867 (2013), pp. 244–289.

[99]   R. D. Ball et al. *Parton distributions with QED corrections.* In: *Nucl. Phys.* B877 (2013), pp. 290–320.

[100] J. M. Campbell, J. W. Huston, and W. J. Stirling. *Hard Interactions of Quarks and Gluons: A Primer for LHC Physics.* In: *Rept. Prog. Phys.* 70 (2007), p. 89.

[101] G. D. S. Bethke and G. Salam. *Quantum chromodynamics.* URL: `http://pdg.lbl.gov/2015/reviews/rpp2015-rev-qcd.pdf;%%`.

[102] R. K. Ellis, W. J. Stirling, and B. R. Webber. *QCD and Collider Physics.* Cambridge monographs on particle physics, nuclear physics, and cosmology. Photography by S. Vascotto. Cambridge: Cambridge Univ. Press, 2003.

[103] J. Alwall et al. *MadGraph 5 : Going Beyond.* In: *JHEP* 06 (2011), p. 128.

[104] J. Alwall et al. *A Standard format for Les Houches event files.* In: *Comput. Phys. Commun.* 176 (2007), pp. 300–304.

[105] S. Frixione et al. *Matching NLO QCD computations with Parton Shower simulations: the POWHEG method.* In: *JHEP* 0711 (2007), p. 070.

[106] T. Gleisberg et al. *Event generation with SHERPA 1.1.* In: *JHEP* 0902 (2009), p. 007.

[107] T. Sjostrand et al. *A Brief Introduction to PYTHIA 8.1*. In: *Comput. Phys. Commun.* 178 (2008), pp. 852–867.

[108] G. Corcella, et al. *HERWIG 6.5 release note*. In: (2002).

[109] N. D. Christensen and C. Duhr. *FeynRules - Feynman rules made easy*. In: *Comput. Phys. Commun.* 180 (2009), pp. 1614–1641.

[110] P. de Aquino et al. *ALOHA: Automatic Libraries Of Helicity Amplitudes for Feynman Diagram Computations*. In: *Comput. Phys. Commun.* 183 (2012), pp. 2254–2263.

[111] ATLAS Collaboration. *Performance of the ATLAS Inner Detector Track and Vertex Reconstruction in the High Pile-Up LHC Environment*. Tech. rep. ATLAS-CONF-2012-042. Geneva: CERN, 2012.

[112] R. Fruhwirth. *Application of Kalman filtering to track and vertex fitting*. In: *Nucl. Instrum. Meth.* A262 (1987), pp. 444–450.

[113] T. Cornelissen et al. *The new ATLAS track reconstruction (NEWT)*. In: *Journal of Physics: Conference Series* 119.3 (2008), p. 032014.

[114] ATLAS Collaboration. *Early Inner Detector Tracking Performance in the 2015 data at $\sqrt{s}$ = 13 TeV*. Tech. rep. ATL-PHYS-PUB-2015-051. Geneva: CERN, 2015.

[115] ATLAS Collaboration. *Vertex Reconstruction Performance of the ATLAS Detector at $\sqrt{s}$ = 13 TeV*. Tech. rep. ATL-PHYS-PUB-2015-026. Geneva: CERN, 2015.

[116] W. Lampl et al. *Calorimeter Clustering Algorithms: Description and Performance*. Tech. rep. ATL-LARG-PUB-2008-002. ATL-COM-LARG-2008-003. Geneva: CERN, 2008.

[117] G. Aad et al. *Topological cell clustering in the ATLAS calorimeters and its performance in LHC Run 1*. In: *Eur. Phys. J.* C77 (2017), p. 490.

[118] M. Cacciari, G. P. Salam, and G. Soyez. *The Anti-k(t) jet clustering algorithm*. In: *JHEP* 04 (2008), p. 063.

[119] M. Aaboud et al. *Jet energy scale measurements and their systematic uncertainties in proton-proton collisions at $\sqrt{s}$ = 13 TeV with the ATLAS detector*. In: *Phys. Rev.* D96.7 (2017), p. 072002.

[120] ATLAS collaboration. *Tagging and suppression of pileup jets*. In: (2014).

[121]   M. H. Klein, F. Rubbo, and A. Schwartzman. *Forward Jet Vertex Tagging: A new technique for the identification and rejection of forward pileup jets.* Tech. rep. ATL-COM-PHYS-2015-723. Geneva: CERN, 2015.

[122]   A. Hoecker et al. *TMVA - Toolkit for Multivariate Data Analysis.* In: *ArXiv Physics e-prints* (2007).

[123]   ATLAS collaboration. *JVT Public Plots for ICHEP 2016.* 2016. URL: https://atlas.web.cern.ch/Atlas/GROUPS/PHYSICS/PLOTS/JETM-2016-011/.

[124]   ATLAS Collaboration. *Forward Jet Vertex Tagging: A new technique for the identification and rejection of forward pileup jets.* Tech. rep. ATL-PHYS-PUB-2015-034. Geneva: CERN, 2015.

[125]   M. Aaboud et al. *Identification and rejection of pile-up jets at high pseudorapidity with the ATLAS detector.* In: *Eur. Phys. J.* C77.9 (2017). [Erratum: Eur. Phys. J.C77,no.10,712(2017)], p. 580.

[126]   G. Aad et al. *Performance of b-Jet Identification in the ATLAS Experiment.* In: *JINST* 11.04 (2016), P04008.

[127]   ATLAS Collaboration. *Calibration of ATLAS b-tagging algorithms in dense jet environments.* Tech. rep. ATLAS-CONF-2016-001. Geneva: CERN, 2016.

[128]   ATLAS Collaboration. *b-tagging efficiency calibration from 2015+2016 data on lepton+jets $t\bar{t}$ events.* 2017. URL: http://atlas.web.cern.ch/Atlas/GROUPS/PHYSICS/PLOTS/FTAG-2017-003/.

[129]   ATLAS Collaboration. *Electron identification measurements in ATLAS using $\sqrt{s} = 13$ TeV data with 50 ns bunch spacing.* Tech. rep. ATL-PHYS-PUB-2015-041. Geneva: CERN, 2015.

[130]   T. G. Cornelissen et al. *The global χ^2 track fitter in ATLAS.* In: *Journal of Physics: Conference Series* 119.3 (2008), p. 032013.

[131]   ATLAS Collaboration. *Improved electron reconstruction in ATLAS using the Gaussian Sum Filter-based model for bremsstrahlung.* Tech. rep. ATLAS-CONF-2012-047. Geneva: CERN, 2012.

[132]   ATLAS Collaboration. *Electron efficiency measurements with the ATLAS detector using the 2015 LHC proton-proton collision data.* Tech. rep. ATLAS-CONF-2016-024. Geneva: CERN, 2016.

[133] ATLAS Collaboration. *Electron efficiency measurements in 2015 data.* 2015. URL: `https://atlas.web.cern.ch/Atlas/GROUPS/PHYSICS/ PLOTS/EGAM-2015-006/index.html`.

[134] K. Becker et al. *Optimisation note of the ggF+VBF analysis in $H \rightarrow WW^*$ using 36 fb^{-1} of data collected with the ATLAS detector at $\sqrt{s} =$ 13 TeV.* Tech. rep. ATL-COM-PHYS-2017-1089. Geneva: CERN, 2017.

[135] G. Aad et al. *Muon reconstruction performance of the ATLAS detector in proton–proton collision data at $\sqrt{s}$ =13 TeV.* In: *Eur. Phys. J.* C76.5 (2016), p. 292.

[136] ATLAS Collaboration. *Performance of missing transverse momentum reconstruction with the ATLAS detector using proton-proton collisions at $\sqrt{s}$ = 13 TeV.* Tech. rep. ATL-COM-PHYS-2016-407. Geneva: CERN, 2016.

[137] G. Aad et al. *Observation and measurement of Higgs boson decays to WW^* with the ATLAS detector.* In: *Phys. Rev.* D92.1 (2015), p. 012006.

[138] G. Aad et al. *Study of (W/Z)H production and Higgs boson couplings using $H \rightarrow WW^*$ decays with the ATLAS detector.* In: *JHEP* 08 (2015), p. 137.

[139] ATLAS Collaboration. *Measurements of the Higgs boson production cross section via Vector Boson Fusion and associated WH production in the $WW^* \rightarrow \ell\nu\ell\nu$ decay mode with the ATLAS detector at $\sqrt{s} = 13$ TeV.* Tech. rep. ATLAS-CONF-2016-112. Geneva: CERN, 2016.

[140] T. Plehn, D. L. Rainwater, and D. Zeppenfeld. *A Method for identifying $H \rightarrow \tau^+\tau^- \rightarrow e^\pm\mu^\mp p_T$ at the CERN LHC.* In: *Phys. Rev.* D61 (2000), p. 093005.

[141] C. G. Lester and D. J. Summers. *Measuring masses of semiinvisibly decaying particles pair produced at hadron colliders.* In: *Phys. Lett.* B463 (1999), pp. 99–103.

[142] URL: `https://atlas-caf.web.cern.ch/`.

[143] F. Pedregosa et al. *Scikit-learn: Machine Learning in Python.* In: *Journal of Machine Learning Research* 12 (2011), pp. 2825–2830.

[144] T. Chen and C. Guestrin. "XGBoost: A Scalable Tree Boosting System". In: *Proceedings of the 22Nd ACM SIGKDD International Conference on Knowledge Discovery and Data Mining.* KDD '16. San Francisco, California, USA: ACM, 2016, pp. 785–794.

[145] A. Justel, D. Peña, and R. Zamar. *A multivariate Kolmogorov-Smirnov test of goodness of fit*. In: 35 (Oct. 1997), pp. 251–259.

[146] C. Adam-Bourdarios et al. "The Higgs boson machine learning challenge". In: *Proceedings of the NIPS 2014 Workshop on High-energy Physics and Machine Learning*. Vol. 42. Proceedings of Machine Learning Research. PMLR, 2015, pp. 19–55.

[147] ATLAS Collaboration. *Jet energy measurement and its systematic uncertainty in proton-proton collisions at $\sqrt{s}$ = 7 TeV with the ATLAS detector*. In: *Eur.Phys.J.* C75.1 (2015), p. 17.

[148] ATLAS Collaboration. *Jet energy resolution and selection efficiency relative to track jets from in-situ techniques with the ATLAS Detector Using Proton-Proton Collisions at a Center of Mass Energy $\sqrt{s}$ = 7 TeV*. In: *ATLAS-CONF-2010-054* ().

[149] ATLAS Collaboration. *Calibration of the performance of b-tagging for c- and light-flavour jets in the 2012 ATLAS data*. In: *ATLAS-CONF-2014-046* ().

[150] G. Aad et al. *Improved luminosity determination in pp collisions at sqrt(s) = 7 TeV using the ATLAS detector at the LHC*. In: *Eur. Phys. J.* C73.8 (2013), p. 2518.

[151] ATLAS Collaboration. *Studies on top-quark Monte Carlo modelling for Top2016*. Tech. rep. ATL-PHYS-PUB-2016-020. Geneva: CERN, 2016.

[152] R. Frederix and S. Frixione. *Merging meets matching in MC@NLO*. In: *JHEP* 12 (2012), p. 061.

[153] I. W. Stewart and F. J. Tackmann. *Theory Uncertainties for Higgs and Other Searches Using Jet Bins*. In: *Phys. Rev.* D85 (2012), p. 034011.

[154] G. Cowan et al. *Asymptotic formulae for likelihood-based tests of new physics*. In: *Eur. Phys. J.* C71 (2011). [Erratum: Eur. Phys. J.C73,2501(2013)], p. 1554.

[155] K. Cranmer et al. *HistFactory: A tool for creating statistical models for use with RooFit and RooStats*. Tech. rep. CERN-OPEN-2012-016. New York: New York U., 2012.

[156] I. Narsky and F. C. Porter. *Statistical analysis techniques in particle physics*. Weinheim, Germany: Wiley-VCH, 2014.

[157] M. Baak et al. *Interpolation between multi-dimensional histograms using a new non-linear moment morphing method.* In: *Nucl. Instrum. Meth.* A771 (2015), pp. 39–48.

[158] A. Kaluza et al. *A morphing technique for signal modelling in a multidimensional space of coupling parameters.* Tech. rep. ATL-COM-PHYS-2015-457. Geneva: CERN, 2015.

[159] L. Brenner. "Character profile of the Higgs boson". PhD thesis. Amsterdam U., 2017.

[160] ATLAS Collaboration. *Measurements of gluon-gluon fusion and vector-boson fusion Higgs boson production cross-sections in the $H \rightarrow WW^* \rightarrow e\nu\mu\nu$ decay channel in pp collisions at $\sqrt{s} = 13$ TeV with the ATLAS detector.* Tech. rep. arXiv:1808.09054. Geneva: CERN, 2018.

[161] A. K. Becker et al. *Measurements of the Higgs boson production cross section via ggF and VBF in $H \rightarrow WW^* \rightarrow l\nu l\nu$ with 36.1 fb^{-1} of data collected with the ATLAS detector at $\sqrt{s} = 13$ TeV.* Tech. rep. ATL-COM-PHYS-2017-1094. Geneva: CERN, 2017.

[162] LHC Higgs Cross Section Working Group. *Handbook of LHC Higgs Cross Sections: 4. Deciphering the Nature of the Higgs Sector.* In: (2016).

[163] N. Cabibbo and A. Maksymowicz. *Angular Correlations in K_{e4} Decays and Determination of Low-Energy $\pi - \pi$ Phase Shifts.* In: *Phys. Rev.* 137 (2B 1965), B438–B443.

[164] S. Bolognesi et al. *On the spin and parity of a single-produced resonance at the LHC.* In: *Phys. Rev.* D86 (2012), p. 095031.

[165] R. Z. Aben. "Spinning the Higgs: Spin and parity measurement of the discovered Higgs-like boson in the $H \rightarrow WW \rightarrow \ell\nu\ell\nu$ decay mode". 2015.

Summary

The Standard Model (SM) is the theoretical framework at the basis of particle physics. It gives a description of the fundamental particles and their interactions. Elementary particles acquire their mass thanks to the spontaneous breaking of the electroweak symmetry and thanks to the introduction of a complex Higgs field. The *Brout-Englert-Higgs mechanism* adds to the theory a new particle, the Higgs boson. However, its mass is a free parameter and is therefore not predicted. With the discovery of the Higgs boson in 2012 by the ATLAS and CMS collaborations, its mass has been found to be approximately 125 GeV. Other properties, such as spin and CP, have been extensively studied, disclosing the SM-like spin-0 and CP-even nature of the Higgs boson. The SM has revealed itself successful in describing most of the observed particle physics phenomena, but, for example, it does not include neutrino oscillations and it fails in explaining the presence of dark matter and dark energy in the universe. A strategy to search for Beyond Standard Model (BSM) physics is to use LHC data to search for deviations from the SM. The study of the Higgs boson properties can either further confirm its SM-like nature or may open doors to new physics. For example, there are BSM theories that foresee the existence of more than one Higgs boson.

There are some features of this intriguing particle that have not been studied yet. One of those, that is discussed in this thesis, is how it couples to longitudinally and transversally polarized vector bosons. The SM predicts the longitudinal coupling parameter (a_L) and the transversal one (a_T) to be equal and finely-tuned in order to restore unitarity in the scattering of electroweak W bosons. If an anomalous coupling is observed, this would hint at new physics in the interactions between the Higgs and the vector bosons.

In the present thesis, these couplings are studied in the case in which the Higgs is produced via vector boson fusion (VBF) and decays into the $WW^* \to e\nu\mu\nu$ final state. VBF production has a very distinctive signature,

characterized by two forward jets with large invariant mass, presence of missing transverse energy and two opposite-sign leptons that must lay in the rapidity gap between the two tagging jets. The Higgs to WW^* decay channel suffers from the presence of large backgrounds. The largest arise from the production of top-quark pairs, from continuum $WW^* \to \ell\nu\ell\nu$ production and Drell-Yan events in association with two jets.

The analysis, presented in this thesis, is performed with the data collected by the ATLAS experiment during 2015 and 2016, corresponding to an integrated luminosity of 36.1 fb^{-1}.

To disentangle the signal from the backgrounds, a boosted decision tree (BDT) classifier is built, exploiting kinematic distributions that reflect the characteristic signature of the VBF topology and of the decay products.

Anomalies in the longitudinal or transversal coupling directly affect the production cross-section, which presents a strong dependence on the longitudinal coupling and a mild one on the transversal one. The kinematic distributions of the two leading jets are not only related to the intrinsic structure of the VBF production vertex, but carry also information about the polarization. In particular, the shape of the distribution of the angle between the two leading jets in the plane perpendicular to the beam ($\Delta\phi_{jj}$) is sensitive to BSM effects. In order to distinguish the VBF SM signal from the backgrounds, while being sensitive at the same time to possible BSM values of the a_L and a_T couplings, the BDT output distribution is convoluted with the $\Delta\phi_{jj}$ one.

Maximum likelihood fits are performed on these coupling parameters, exploiting the shape of the BDT-$\Delta\phi_{jj}$ distribution and the total rates. When profiling one coupling at the time, the observed best values of the longitudinal and transversal coupling parameters are found to be $a_L = 0.91^{+0.14}_{-0.23}$ and $a_T = 1.19^{+0.33}_{-0.37}$, respectively. These results are in agreement with the SM predictions ($a_L = a_T = 1$) within the errors. The main uncertainties on the longitudinal coupling arise from the modeling of the dominant backgrounds, while the transversal coupling measurement is limited by data statistics.

The measured cross section times branching fractions obtained from 36.1 fb^{-1} of integrated luminosity in the $H \to WW^* \to \ell\nu\ell\nu$ decay channel are also presented. For the gluon-gluon fusion channel the result is $\sigma_{\mathrm{ggF}} \cdot \mathscr{B}_{H \to WW^*} = 11.4^{+2.2}_{-2.1}$ pb, while, for vector boson fusion, one obtains $\sigma_{\mathrm{VBF}} \cdot \mathscr{B}_{H \to WW^*} = 0.50^{+0.29}_{-0.28}$ pb. In both cases, the measured cross sections are consistent with the SM predictions within the errors.

Samenvatting

Het Standaardmodel (SM) is het theoretisch raamwerk dat de basis van de deeltjesfysica vormt. Het geeft een beschrijving van de fundamentele deeltjes en hun interacties. Elementaire deeltjes krijgen hun massa dankzij de spontane breking van de elektrozwakke wisselwerking en dankzij de introductie van een complex Higgs-veld. Het *Brout-Englert-Higgsmechanisme* voegt een nieuw deeltje aan de theorie toe: Het Higgsboson. Echter is hiervan de massa een vrije parameter en is daarom niet voorspeld. Met de ontdekking van het Higgsboson in 2012 door de ATLAS en CMS collaboraties is ontdekt dat de massa ongeveer 125 GeV is. Andere eigenschappen, zoals spin en CP, zijn uitgebreid getest, waaruit de SM-achtige spin-0 en CP-even kwaliteiten van het Higgsboson zijn bevestigd.

Het SM is succesvol gebleken in het beschrijven van de waargenomen fenomenen in de deeltjesfysica. Maar het bevat bijvoorbeeld geen neutrino-oscillaties en kan niet de aanwezigheid van donkere materie en donkere energie in het universum verklaren. Een strategie om naar fysica buiten het Standaardmodel (BSM) te zoeken is om LHC data te bestuderen voor afwijkingen van het SM. De studie naar de eigenschappen van het Higgsboson kan verder zijn SM-achtige kwaliteiten bevestigen of de deur openen naar nieuwe fysica. Er zijn bijvoorbeeld BSM-theorieën die het bestaan van meer dan één Higgsboson voorspellen.

Er zijn enkele eigenschappen van dit deeltje die nog niet zijn onderzocht. Eén hiervan, die in dit proefschrift besproken zal worden, is hoe het koppelt met longitudinaal en transversaal gepolariseerde vectorbosonen. Het SM voorspelt dat de longitudinale (a_L) en transversale (a_T) koppelingsparameters gelijk en fijn afgesteld zullen zijn om de unitariteit in de verstrooiing van elektrozwakke W-bosonen te herstellen. Als een abnormale koppeling wordt geobserveerd, zou dit een hint zijn naar nieuwe fysica in de interacties tussen de Higgs- en vectorbosonen.

In dit proefschrift zijn deze koppelingen bestudeerd in het geval waarin de Higgs is geproduceerd via vector boson fusion (VBF) en vervalt naar de $WW^* \rightarrow e\nu\mu\nu$ final state. VBF-productie is duidelijk te herkennen aan zijn twee voorwaarts-gerichte jets met een grote invariante massa, de aanwezigheid van ontbrekende transversale energie, en de twee tegenovergesteld-geladen leptonen de zich moeten bevinden in de rapiditeits-holte tussen de twee eerder genoemde jets. Het verval van Higgs naar WW^* lijdt onder de aanwezigheid van grote achtergronden. De grootste van deze achtergronden komt van de productie van top quark-paren, van continuum $WW^* \rightarrow \ell\nu\ell\nu$ productie en van Drell-Yan events geassocieerd met twee jets.

De analyse gepresenteerd in dit proefschrift is gedaan met de data verzameld door het ATLAS-experiment gedurende 2015 en 2016, wat overeenkomt met een geïntegreerde luminositeit van 36.1 fb^{-1}.
Om het signaal van de achtergronden te ontkoppelen, wordt een boosted decision tree (BDT) gebruikt, welke gebruik maakt van kinematische distributies die de karakteristieke eigenschappen van de VBF-topologie en haar vervalproducten reflecteren.
Abnormaliteiten in de longitudinale of transversale koppeling hebben een directe invloed over de cross-sectie van de productie, hetgeen een sterke afhankelijkheid van de longitudinale koppeling en een zwakkere van de transversale koppeling introduceert. De kinematische distributie van de twee leidende jets is niet alleen gerelateerd aan de intrinsieke structuur van de VBF-productie vertex, maar bevatten ook informatie over de polarisatie. In het bijzonder is de vorm van de distributie van de hoek tussen de twee leidende jets in het vlak loodrecht aan de beam ($\Delta\phi_{jj}$) gevoelig voor BSM-effecten.
Om het VBF SM-signaal van de achtergronden te onderscheiden, maar ook gevoelig te zijn voor mogelijke BSM-waarden van de a_L and a_T koppelingen, is de distributie van de BDT-output opgerold met die van $\Delta\phi_{jj}$.
De maximum-likelihood-fit is toegepast op deze koppelingsparameters, wat gebruik maakt van de vorm van de BDT-$\Delta\phi_{jj}$ distributie en de totale hoeveelheden. Als een koppeling apart wordt onderzocht, zijn de waargenomen beste waarden voor de longitudinale en transversale koppelingsparameters respectievelijk $a_L = 0.91^{+0.14}_{-0.23}$ en $a_T = 1.19^{+0.33}_{-0.37}$. Deze resultaten zijn in overeenstemming met de SM-voorspellingen van ($a_L = a_T = 1$) binnen de foutmarges. De voornaamste onzekerheden op de longitudinale koppeling komen van het modelleren van de dominante achtergronden, terwijl de meting van de transversale koppeling gelimiteerd is door de statistiek van de data.

De gemeten cross-secties maal branching fracties verkregen van een geïntegreerde luminositeit van 36.1 fb^{-1} in het $H \rightarrow WW^* \rightarrow \ell\nu\ell\nu$ vervalskanaal zijn ook gepresenteerd. Voor het gluon-gluon fusiekanaal is het resultaat $\sigma_{\mathrm{ggF}} \cdot \mathscr{B}_{H \rightarrow WW^*} = 11.4^{+2.2}_{-2.1}$ pb, en voor vector boson fusion is dit $\sigma_{\mathrm{VBF}} \cdot \mathscr{B}_{H \rightarrow WW^*} = 0.50^{+0.29}_{-0.28}$ pb. In beide gevallen zijn de gemeten cross-secties in overeenstemming met het Standaardmodel binnen de foutmarges.